

Die approbierte Originalversion dieser
Dissertation ist in der Hauptbibliothek der
Technischen Universität Wien aufgestellt und
zugänglich.

<http://www.ub.tuwien.ac.at>



The approved original version of this thesis is
available at the main library of the Vienna
University of Technology.

<http://www.ub.tuwien.ac.at/eng>



TECHNISCHE
UNIVERSITÄT
WIEN

Vienna University of Technology

DISSERTATION

Static and Dynamic Modelling of Lightweight Floating Platforms Supported by Flexible Air Chambers

ausgeführt zum Zwecke der Erlangung des akademischen Grades eines Doktors der
technischen Wissenschaften unter der Leitung von

O.Univ.Prof. Dipl.-Ing. Dr.techn. F. G. Rammerstorfer
E317

Institut für Leichtbau und Struktur-Biomechanik

eingereicht an der Technischen Universität Wien
bei der Fakultät für Maschinenwesen und Betriebswissenschaften

von

Dipl.-Ing. Florian Toth
Matrikelnummer 0525414
Mollardgasse 70A/4
1060 Wien

Wien, 1. Juli 2014

Florian Toth

Einige schätzen die Bücher nach ihrer Dicke; als seien sie geschrieben, die Arme, nicht die Köpfe daran zu üben.

Gárcian

Kurzfassung

Eine neuartig Schwimmplattform für Solarkraftwerke wurde vorgestellt. Die Schwimmplattform besteht aus einem plattenförmigen Rahmenwerk, das durch zylindrische Luftkammern getragen wird. Die Kammern werden durch die Plattform-Platte, eine flexible Membran, und die Wasseroberfläche gebildet. Ballast am unteren Ende der Membran sorgt auch bei Seegang für die Luftdichtheit der offenen Luftkammern.

Numerische Homogenisierung wurde verwendet um die ebene, periodische Rahmenstruktur in eine äquivalente Plattenstruktur überzuführen, um die Komplexität des mechanischen Modells zu reduzieren. Ein Verfahren zur Bestimmung der Steifigkeit der äquivalenten Platte basierend auf der Einheitszelle der periodischen Struktur wurde vorgestellt. Die Berechnung lokaler Feldvariablen in den Einheitszellen basierend auf Analyseergebnisse der homogenisierten Platte, die sogenannte Lokalisierung, wurde erläutert. Ein Verfahren, um ein auf Einheitszellenebene definiertes Versagenskriterium in den Raum der globaler Schnittkräfte zu übertragen wurde entwickelt. Dieses bietet eine Reduzierung des Rechenaufwands durch die Anwendung einer vorab berechneten Versagensfläche der Einheitszelle.

Das Verhalten der Schwimmplattform unter Wellenerregung wurde durch ein mechanisches Modell beschrieben. Eine numerisch effiziente Modellierung mit einer minimalen Anzahl an Eingabeparametern, welche dennoch alle wichtigen Effekte berücksichtigte, wurde speziell für den Entwurf von Schwimmplattformen entwickelt. Die flexible Platte wurde mittels der Methode der Finiten Elemente modelliert. Die Luftkammern, welche Wasseroberfläche und der Platte koppeln, wurden durch lineare Federn unter Berücksichtigung der Membranflexibilität und der Kompressibilität der Luft idealisiert. Die durch Druckschwankungen in den Luftkammern auftretenden hydrodynamischen Reaktionskräfte wurden durch ein akustisches Sub-Modell der umgebenden Flüssigkeit mit freier Oberfläche bestimmt. Auf diese Weise konnte die komplexen Fluid-Struktur-Interaktion über ein äquivalentes Feder-Masse-Dämpfer System berücksichtigt werden. Die Erregerkräfte aufgrund von Oberflächenwellen wurden aus der linearen Wellentheorie ermittelt. Die numerisch ermittelten Eigenschwingungsformen und Übertragungsfunktionen wurden durch Modellversuche validiert. Experimente in regelmäßigen und unregelmäßigen Wellen dienten zur Ermittlung der Übertragungsfunktionen. Das Ibrahim Zeitbereichsverfahren wurde eingesetzt, um die Eigenschwingungsformen, Eigenfrequenzen und Dämpfungsfaktoren frei schwimmender Plattformen experimentell zu bestimmen.

Eine einzelne Luftkammer zeigt eine statische Instabilität: Es kommt zum globalen Ausknicken, und damit zum Verlust der Tragfähigkeit, wenn ein kritischer Innendruck überschritten wird. Diese Instabilität wurde rechnerisch und experimentell untersucht. Als Grund für die Instabilität konnte die unsymmetrische Druckverteilung, die an der

Wasserlinie einer leicht geneigten Luftkammern auftritt und ein Biegemoment erzeugt, identifiziert werden.

Schließlich wurde ein Prototyp-Design für das Mittelmeer vorgestellt. Das Verhalten der Plattform in unregelmäßigen Wellen wurde basierend auf Wahrscheinlichkeitstheorie untersucht, um die Machbarkeit des vorgeschlagenen Entwurfs zu demonstrieren.

Abstract

A novel concept for a floating platform usable as a solar power plant was presented. The floating platform consists of a plate-like frame structure which is supported by cylindrical air chambers. The chambers are formed by the platform-plate, a flexible membrane, and the water surface. Ballast weights at the bottom end of the membrane ensure the air-tightness of the open air chambers even during conditions with high waves.

Computational homogenisation was used to reduce the plane-periodic frame structure to an equivalent plate structure in order to reduce the complexity of the mechanical model. Thick plate properties, were computed based on the unit cell of the periodic structure. The localisation procedure for computing local field variables in the unit cells based on the analysis results of the homogenised plate was explained. A procedure to directly evaluate a failure criterion defined on unit cell level based on global section forces was developed. This procedure offers a reduction of the computational cost by pre-computing the failure surface of the unit cell.

A mechanical model of the floating platform under wave forcing was developed. The model is computationally very efficient and has a minimal number of input parameters, yet incorporates all important effects, making it suitable for preliminary design. The finite element method was used to model the deformable platform-plate. The supporting air chambers, coupling water surface and plate, were idealised by linear springs taking the flexibility of the membrane and the compressibility of the air into account. The hydrodynamic reaction forces arising due to pressure oscillations in the air chambers were determined by an acoustic sub-model of the surrounding fluid with free surface. In this way the complex fluid-structure-interaction could be accounted for by the use of equivalent spring-mass-daspot elements. Excitation forces from surface gravity waves were obtained from linear wave theory. The natural modes and transfer functions computed by the developed model were experimentally validated by model tests. Tests were carried out in regular and irregular waves to obtain transfer functions. The Ibrahim time domain method was employed to determine free floating oscillation modes, natural frequencies and damping factors experimentally.

A single air chamber shows a static instability: It globally buckles if a critical internal pressure is exceeded, resulting in the loss of load carrying capacity. This instability phenomenon was investigated computationally and experimentally. The reason for the instability was determined to be the unsymmetrical pressure distribution arising at the waterline of slightly inclined air chambers. This creates a bending moment which leads to global buckling of the chamber.

Finally, a prototype design suitable for the Mediterranean Sea was presented. The behaviour of the platform in irregular seas was evaluated based on probabilistic theory, confirming the feasibility of the proposed design.

Acknowledgements

This work was carried out under the framework of the doctoral college *Energy Systems 2030* (ENSYS2030) of the Vienna University of Technology. Additional financial support was provided through the Austrian Research Promotion Agency (FFG) in the form of its Research Studios Austria (RSA) program funding the studio *HelioFloat* aimed at developing offshore solar power plants. I gained valuable insights through the cooperation with the other two PhD students involved in the project, Ewelina Rupnik and Christian Diendorfer. The tireless effort of Prof. M. Haider acting as a project coordinator and thesis co-advisor is gratefully acknowledged.

The work at the Institute of Lightweight Design and Structural Biomechanics (ILSB) has always been enjoyable for me, owing to a large part to the friendly atmosphere. Special thanks go to my long-term office mates Herr Bilik and Andreas Reisinger who kept spirits up*. All members of the institute, amongst others Helmut Böhm, Dieter Pahr, Benedikt Daum, Heinz Pettermann, Jakob Gager and Melanie Todt were always available for fruitful discussions. Despite his tight schedule my advisor, Prof. F. G. Rammerstorfer, was always available to give guidance when needed, which is gratefully acknowledged. Amongst other things he instructed me in the art of precise and correct formulation of scientific statements.

Of course, this thesis could not have been completed without the support of friends and family. I'm happy my parents supported my wish to study engineering. Their generous support made it possible to complete my studies in a short time and enabled me to spend a year at the Royal Institute of Technology (KTH) in Sweden. I'm grateful for having good friends who always supported me morally through intensive months of working and writing. Finally, I wish to thank Sandrine for her loving support. I'm honoured that you're such an important part of my life.

*by complaining so much about their work that yours does not seem hard any more

Contents

1	Introduction	1
1.1	Offshore Solar Power Plants	1
1.2	Scope of the Thesis	3
2	Dynamic Model	4
2.1	Modelling Assumptions	4
2.2	Axial Stiffness of the Air Chambers	6
2.3	Hydrodynamic Excitation by Waves	7
2.4	Hydrodynamic Reaction Forces	9
2.4.1	Acoustic Theory	10
2.4.2	Equivalent Model	12
2.4.3	Non-Dimensional Representation of Quantities	14
2.4.4	The Relation of the Damping Constant to the Radiated Wave Energy	14
2.4.5	Computational Models	15
2.4.6	Results	21
2.5	Equations of Motion	28
2.5.1	Equations of Motion for a Rigid Plate	28
2.5.2	Treatment of the Deformable Plate by Finite Elements	29
2.6	Model Output	30
2.6.1	Natural Frequencies and Oscillation Modes	30
2.6.2	Steady State Solution of the Equations of Motion	31
2.6.3	Transfer Functions	32
2.6.4	Chamber Pressure	33
2.6.5	Axial Tension in the Cylindrical Membrane	33
2.7	Model Validation	35
2.7.1	Impact of Input Parameters	35
2.7.2	Natural Frequencies, Oscillation Modes and Damping Parameters	37
2.7.3	Transfer Functions	41
2.8	Conclusion	44
3	Static Stability of a Single Air Chamber	45
3.1	Description of the Mechanical System	45
3.2	Simulation Model	46
3.2.1	Modelling Assumptions	46
3.2.2	Element Type and Mesh Size	48
3.2.3	Imperfections	49

3.2.4	Analysis Procedure	51
3.3	Experiments	51
3.4	Results	52
3.4.1	The Buckling Process	52
3.4.2	Critical Pressure	54
3.4.3	Critical Bending Moment	55
3.5	Conclusion	59
4	Homogenisation and Localisation	60
4.1	Plate Theory	61
4.2	Equivalent Stiffness Properties for Plain Periodic Structures	62
4.2.1	Unit Cells with Periodic Boundaries	62
4.2.2	Transverse Shear Stiffness	63
4.3	Localisation	63
4.4	Failure Criteria Defined in Terms of Global Section Forces	64
4.4.1	Using Radial Paths to Determine Points of the Failure Surface	65
4.4.2	Assessment of the Failure Criterion for a Section Force Combination	66
4.5	Validation of the Homogenisation Method	75
4.5.1	Global Displacements	75
4.5.2	Stress Localisation	76
4.6	Conclusion	78
5	Experimental Testing	79
5.1	Froude's Scaling Law	79
5.2	Scale Models	80
5.2.1	Design of Equivalent Models	80
5.2.2	Description of the Scale Models	82
5.3	Behaviour of the Platform in Waves	82
5.3.1	Test Setup	83
5.3.2	Measurement of Displacements and Deformations	85
5.3.3	Regular Wave Experiments	89
5.3.4	Experiments in Irregular Waves	91
5.4	Measurement of Natural Frequencies and Oscillation Modes	96
5.4.1	Theory of the Ibrahim Time Domain Method	97
5.4.2	Assessment of the Identification Quality	98
5.4.3	Automatic Mode Sorting	100
5.5	Summary	101
6	Geometric Non-Linear Effects in Plates	102
6.1	Equations for Large Deflections of Plates	102
6.2	Homogeneous, Isotropic Plates	103
6.3	Periodic Plate-Like Structures	106
6.4	Conclusion	109

7	Design of a Prototype Platform	110
7.1	Environmental Conditions	110
7.2	Overall Dimensions of the Floating Platform	112
7.3	Load Cases	113
7.3.1	Static Equilibrium	113
7.3.2	Quasi-Static Wave	113
7.3.3	Irregular Wave Spectrum	114
7.4	Results and Discussion	116
7.4.1	Gravity Loading	116
7.4.2	Evaluation of the Irregular Wave Load Cases	117
7.4.3	Quasi-Static Wave Load Case	125
7.5	Conclusion	127
	Bibliography	129
	Appendix A Water Waves	135
A.1	Linear Surface Gravity Waves	135
A.2	Representation of an Irregular Seaway	136
A.3	Wave Energy	137
A.4	Commonly Used Wave Spectra	138
	Appendix B Additional Experimental Results	140
B.1	Small Model	140
B.2	Large Model	140
B.2.1	Wave Heading 0°	141
B.2.2	Wave Heading 22.5°	144
B.2.3	Wave Heading 45°	147
	Appendix C Miscellaneous Mechanics	150
C.1	Static Air Pressure in the Chambers	150
C.2	Chamber Stiffness and Wave Height	150
C.3	Pressure Measurement by a Water Column	151
C.4	Homogeneous, Isotropic, Linear-Elastic Shells	153
C.5	Natural Frequencies of a Cylindrical Domain	153
	Appendix D Miscellaneous Mathematics	156
D.1	Fourier Series and Fourier Transform	156
D.2	Discrete Form of the Fourier Transform	157
D.3	Power Spectral Density	158
D.4	Integral over One Oscillation Period	159
D.5	Numerical Integration of Narrow-Band Spectra	160
D.6	Definition of a Cartesian Coordinate System	161
D.7	Coordinate Transformation	161
D.8	Euler Angles	162
D.9	Nullspace	164
D.10	Single Value Decomposition	164
D.11	N-Dimensional Polar Coordinates	165

Chapter 1

Introduction

Renewable energy sources are becoming increasingly important due to increases in energy demand and the desire to replace fossil fuels [25, 32]. Solar power offers great potential to satisfy this demand. To date, solar thermal electricity (STE) and solar photovoltaic electricity (PV) are competitive against oil-fuelled electricity in sunny areas [31]. PV systems are more flexible and have recently shown a dramatic decrease in price [51]. On the other hand, STE is attractive because it allows time shifted electricity production by the means of thermal storage [31]. STE systems today are based on concentrating solar power (CSP), i.e. use optical devices to focus the sunlight. Thus, they require large areas with high overall direct normal irradiation (DNI). As such areas are scarce in Europe, the idea of offshore solar power plants emerged. Compared to traditional land based systems, such floating solar power plates promise additional advantages like ample available space, sun tracking around a vertical axis, and efficient cooling.

1.1 Offshore Solar Power Plants

As general requirement for offshore solar power plants, large areas for the concentrator fields must be provided by a floating platform. This floating platforms must be designed in order to withstand the harsh ocean environment. State of the art offshore floating platforms, as used for example as oil/gas drilling rigs or floating production, storage and offloading units (FPSO) can be built in order to withstand even the most severe sea states. However, typical dimensions of such platforms are about 100x100 m with area loads of several tons per square meter. Therefore, such platforms are deemed too expensive for floating solar power plants.

Floating platforms designed to cover large areas on the ocean, i.e. very large floating structures (VLFS), have been a topic of interest for several decades. Traditional target applications include floating airports or offshore cities [78, 80]. Again such structures must be able to carry several tons per square meter and are, thus, expensive to build.

The payload requirements for solar collectors are fundamentally different, allowing novel platform concepts. Parabolic pre-stressed concentrators [65, 69] or PV modules have a mass per area of only about 25 kg/m². This allows the use of large, flexible air chamber to support the platform. It has been shown that air cushion support can substantially decrease wave induced strains in offshore structures [75, 77]. However, previous research was focused on the analysis of air chambers with comparatively stiff walls [10, 30, 41, 53],

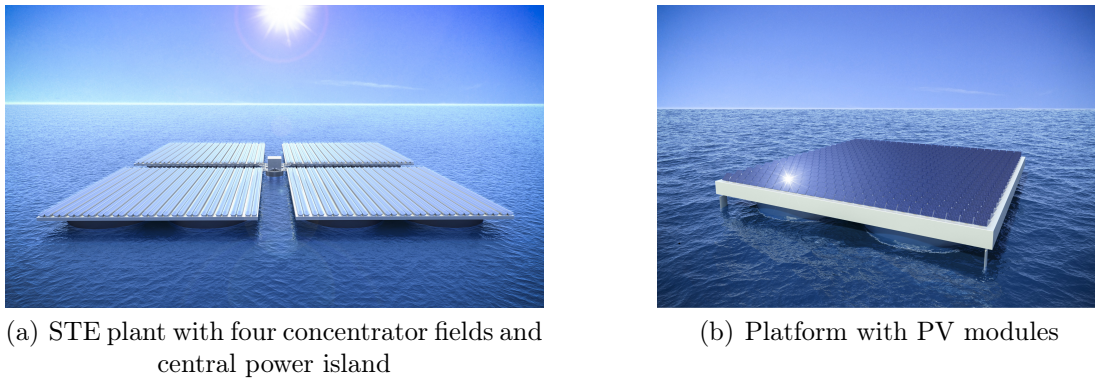


Figure 1.1: Possible designs for offshore floating power plants.

which are a necessity to sustain high payloads. A novel, patented [23] design for a light weight floating platform supported by open, flexible air chambers is investigated in this thesis. Figure 1.1 shows how solar power plants based on this novel design might look like. A joint thesis by Diendorfer [13] describes the concept of offshore solar power plants in more detail, also giving an extensive review of similar concepts. He also tackles issues like optical and overall efficiency of concentrating systems, optimal sun tracking, and site selection [13], for which this thesis gave input.

The floating platform carrying the concentrator system consists of a large, plate-like structure supported by a number of cylindrical air cushions, which are attached below the plate and are open to the water at the bottom. One such air cushion is formed by the platform-plate, the wall of the cylindrical membrane and the water surface. The cylindrical membrane, in the following termed *skirt*, is sufficiently ballasted and long to stay submerged in all wave conditions. Figure 1.2 shows a cross section of such a platform. In order to achieve static stability of the global structure at least three independent chambers are necessary. The static air pressure in the chambers is self regulating and determined by the weight of the platform and the area of the cut water plane. It provides an homogeneous, continuous support for the plate-structure. Therefore, the structure may be constructed in a very light and cost effective way. Another advantage of the air chambers is the attenuation of wave forcing onto the platform-plate. The amount of air in the chambers can be used to control the draught of the platform.

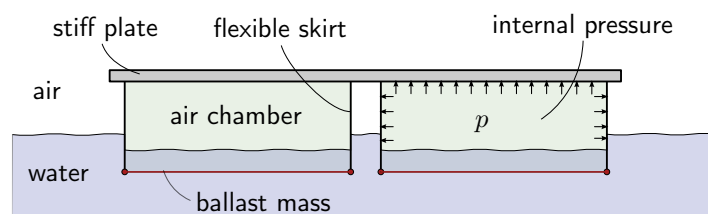


Figure 1.2: Sketch of an air chamber supported floating platform.

1.2 Scope of the Thesis

The aim of this thesis is to shed light on the complex behaviour of floating platforms supported by open, flexible air chambers. The prediction of wave induced motions and forces is crucial for the design of the floating platform itself and for the design of a concentrator system mounted on the platform as a payload.

Accurate predictions can only be expected of a mechanical model if all important effects are accounted for. These include fluid flow with a free surface in an unbounded domain, i.e. surface gravity waves, interacting with air chambers, formed of a highly flexible membrane, containing a compressible fluid (air). Additionally, the air chambers are interacting with a plate-like, periodic frame structure composed of several thousands of beams. Techniques exist to tackle each of the mentioned phenomena separately in great detail, but no solution which tackles all phenomena in combination is known to date. Although this coupling is possible in principle, it would lead to a complicated, computationally very demanding model, which would not be useful for early design stages where the impact of a lot of input parameters is still unknown. Therefore, a simplified model with a minimal amount of input parameters, yet incorporating all important interaction effects, is developed.

Computational homogenisation is used to reduce the periodic frame structure to a mechanically equivalent plate. An air chamber supports the platform-plate by its internal pressure, which depends on the volume of the air chamber. The volume (and, consequently, pressure) change is governed by the position of the platform-plate, the water surface inside the chamber, and the flexibility of the bounding membrane and can be modelled by a linear spring. Rising pressure in an air chamber will lead to a displacement of the free water surface inside the chamber. In order to quantify the resulting displacement the hydrostatic and hydrodynamic reaction forces must be known. They may be obtained by modelling the water as an acoustic fluid with a free surface, and can simply be described by a combination of a spring, mass, and dashpot with frequency dependant properties. The floating platform can, hence, efficiently be described by a deformable plate coupled to a system of spring, mass and dashpot elements. The approaching wave field may be described by linear wave theory and acts as a forcing to the mechanical system. The resulting model can be used to describe the behaviour of the floating platform in waves from an arbitrary direction through its transfer functions.

In order to validate the model predictions, experiments in wave tanks were performed. Natural frequency measurements, as well as experiments in regular and irregular waves to determine the transfer functions were performed and analysed. Despite the simplicity of the mechanical model good agreement with experimental observations was obtained.

During the testing of the first models an unexpected static instability of a single air chamber was discovered. If the vertical load on an air chamber, i.e. the internal pressure, increases a critical limit the air chamber buckles sideways and loses its load carrying capacity. As such an instability can lead to a catastrophic failure of the overall platform the instability phenomenon is investigated computationally and experimentally.

Finally, the developed dynamic model of the floating platform and the homogenisation procedure is combined with probabilistic theory to describe a platform in irregular waves. This allows the evaluation of a proposed design for a floating solar power plant in the Mediterranean Sea.

Chapter 2

Dynamic Model

In the design process of the floating platform the impact of water waves on its behaviour is of outermost interest. The wave induced motions impact the optical efficiency of a concentrator system mounted on the platform. Therefore, the behaviour of the floating platform in waves must be determined in order to allow for site-selection based on local wave data and solar irradiation maps. For the structural design wave induced motions and forces must be determined for the dimensioning of the platform elements. Especially for the early design stage a model with a low number of input parameters, which correctly describes the platform behaviour and allows for a determination of principal design parameters, like platform size, number and arrangement of air chambers, skirt and platform stiffness, etc., is of interest.

2.1 Modelling Assumptions

In order to derive a simple dynamic model of the described floating platform strong simplifications are necessary. For a fast and efficient model it is not possible to take the complex interaction effects between flexible membrane, free water surface and pressurized air into account. Nevertheless, if a simplified model that captures the basic properties of the dynamic system can be found, such a model is of great value. The fundamental assumptions used in the derivation of the dynamic model are

- linearity in terms of
 - wave theory (i.e. Airy waves) and
 - assumed small structural displacements and rotations,
- the volume of the air chambers is dependent on
 - the internal water surface elevation and
 - the circumferential stiffness of the skirt material,
- ideal gas in air chambers,
- chamber membrane is linear elastic,
- platform structure is treated as a homogeneous plate,
- only vertical forcing on the plate is considered.

Figure 2.1 shows an illustration of the modelling concept.

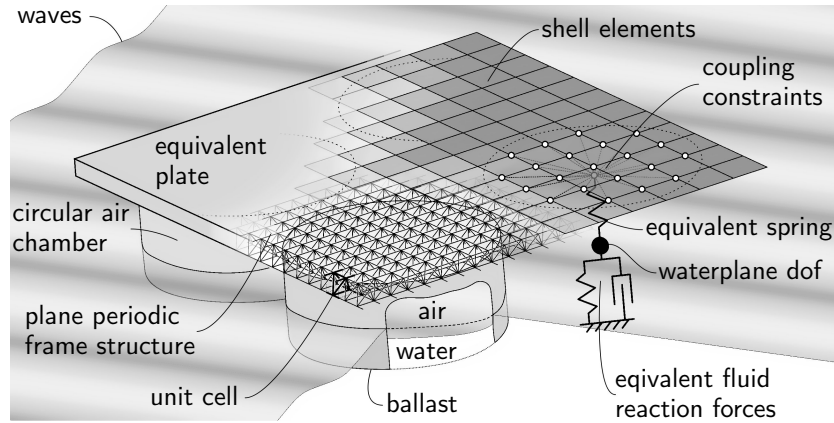


Figure 2.1: Illustration of the modelling concept.

Linear wave theory is a common and useful assumption in offshore engineering, which is applicable for waves with small amplitudes compared with their wavelength [9]. Small amplitude responses are expected, and the equations of motion are, therefore, posed as a linearisation around the static equilibrium.

The volume of an air chamber is defined by an additional degree of freedom at the waterplane, which describes the average water elevation of the chamber footprint. This degree of freedom is forced by the approaching waves. The wave forcing based on linear wave theory is detailed in Section 2.3. Hydrodynamic reaction forces are taken into account by the use of an added mass formulation, as described in more detail in Section 2.4. The air in the chambers can, in the given pressure regime, be treated as an ideal gas. Together with the assumption on the linear elastic behaviour of the membrane material, the axial compressibility of the air chambers can be modelled by linear springs, as explained in more detail in Section 2.2.

Only vertical forcing on the plate is considered, because especially the pitch and roll motion are of interest for the optical efficiency of a concentrator system mounted on the platform. The axial stiffness of the skirt is not taken into account, and the skirt is assumed to remain in tension at all times. Therefore, the skirt mass and the additional mass at the lower end of the skirt are treated as concentrated masses on the plate. The validity of this assumption must be evaluated for each particular design and wave condition based on the computation results, according to Section 2.6.5. If the membrane does not remain in tension the amount of ballast on the lower end of the skirt must be increased.

In a first step the platform-plate will be treated as rigid, because this allows for a semi-analytical treatment of the resulting four equations of motion. This simple model already allows for valuable insights in the platform behaviour. In a next step the plate will be discretised by means of the finite element method (FEM) and hence treated as flexible. The homogenisation of the periodic frame structure into an equivalent deformable plate is treated in Chapter 4.

2.2 Axial Stiffness of the Air Chambers

The axial stiffness of an air chamber will be derived for a cylindrical chamber of linear elastic material filled with an ideal gas. End effects are neglected, i.e. membrane theory is used to prescribe the skirts behaviour, and the membrane is assumed to remain under circumferential tension. The validity of this assumption must be checked once the computation of the platform under specified wave conditions is complete (see Section 2.6.4). All relations will be presented as linearised around an equilibrium position. The cylinder, and the used symbols are depicted in Fig. 2.2.

Assuming a reversible adiabatic process the pressure change Δp due to a change of volume ΔV can be written as

$$\Delta p = p_1 - p_0 = p_0 \left[\left(\frac{V_0}{V_0 + \Delta V} \right)^\gamma - 1 \right] \approx -p_0 \gamma \frac{\Delta V}{V_0}, \quad (2.1)$$

where indices donate the different states and γ is the ratio of specific heats. The relation has been linearised for small volume changes. Using the stress strain relationship for thin membranes with thickness t_s , Youngs's modulus E_s and Poisson's ratio ν_s in polar coordinates

$$\epsilon_{\phi\phi} = \frac{1}{E_s} (\sigma_{\phi\phi} + \nu_s \sigma_{zz}), \quad (2.2)$$

together with the relation for pressure vessels

$$\Delta \sigma_{\phi\phi} \approx \frac{r_0}{t_s} \Delta p, \quad (2.3)$$

and neglecting the axial tension, i.e. setting $\sigma_{zz} = 0$, one can write

$$\frac{\Delta r}{r_0} \approx \frac{1}{E_s} \frac{r_0}{t_s} \Delta p. \quad (2.4)$$

Linearising the volume change for small changes of radius Δr and small changes of hight Δh gives

$$\Delta V = r_0^2 \pi \Delta h + 2r_0 h_0 \Delta r. \quad (2.5)$$

Combining Eqs. (2.1), (2.4) and (2.5) yields the equation

$$\Delta p = -p_0 \gamma \left(1 + \frac{2\gamma r_0 p_0}{t_s E_s} \right)^{-1} \frac{\Delta h}{h_0}, \quad (2.6)$$

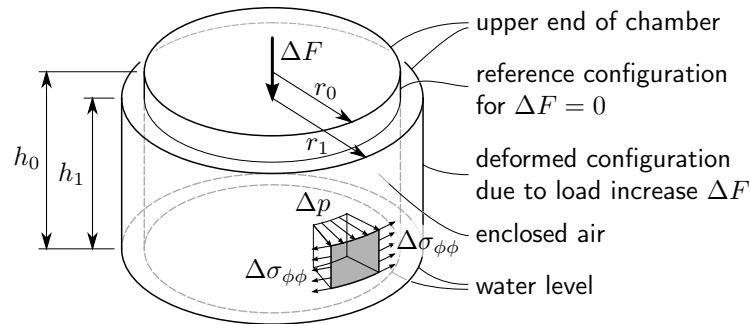


Figure 2.2: Axial stiffness of a cylindrical air chamber.

which can be multiplied by the cylinder footprint area to obtain the desired axial spring stiffness of a flexible air chamber

$$k_c = p_0 \gamma \left(1 + \frac{2\gamma r_0 p_0}{t_s E_s} \right)^{-1} \frac{r_0^2 \pi}{h_0}. \quad (2.7)$$

The term in parentheses in Eq. (2.7) accounts for the flexibility of the membrane. It can decrease the axial stiffness of the chamber by several orders of magnitude, in comparison to a cylinder with rigid walls, and approaches unity for high membrane stiffness.

2.3 Hydrodynamic Excitation by Waves

The water waves are assumed to travel underneath the platform without being impacted by the presence of the flexible air chambers. As the air chamber is bounded by the water surface, any surface displacement will change the volume of the chamber. The water surface elevation can be described by an appropriate wave theory. Due to the assumption of linear waves, one can use the so called Airy wave theory, derived in detail for example by Holthuijsen [26] or briefly in Appendix A.1.

The vertical surface elevation η of a point $\mathbf{x} = [x, y]^T$ at time t for Airy waves is described by

$$\eta(\mathbf{x}, t) = a \cos(\mathbf{k}\mathbf{x} - \omega t), \quad (2.8)$$

where a is the wave amplitude and λ the wave length. The two-dimensional (2D) wave number vector \mathbf{k} will be defined as

$$\mathbf{k} = k \begin{bmatrix} \cos \alpha \\ \sin \alpha \end{bmatrix}, \quad (2.9)$$

where α is the wave direction depicted in Fig. 2.3b. The classical one-dimensional wave number k is the length of the 2D wave number vector \mathbf{k} . For water depths larger than two times the wave length, deep water assumptions can be used with good accuracy. The dispersion relation between wave number and angular wave frequency ω for deep water waves

$$\omega^2 = gk, \quad (2.10)$$

connects both quantities by the acceleration of gravity g . The dynamic pressure in the wave field is given by

$$p_d(\mathbf{x}, z, t) = a \rho g e^{-kz} \cos(\mathbf{k}\mathbf{x} - \omega t), \quad (2.11)$$

where ρ is the water density.

Assuming vertical skirt walls which are immobile, but allow the waves to pass without interaction, the volume in such an air chamber is dependant on the instantaneous water surface elevation. The change in volume due to the travelling wave train can be calculated by integrating the wave elevation over the footprint area of an air chamber yielding

$$\Delta V(t) = \iint_A \eta(\mathbf{x}, t) dA = \int_{p_x-r}^{p_x+r} \int_{p_y-r}^{p_y+r} a \cos(\mathbf{k}\mathbf{x} - \omega t) dy dx, \quad (2.12)$$

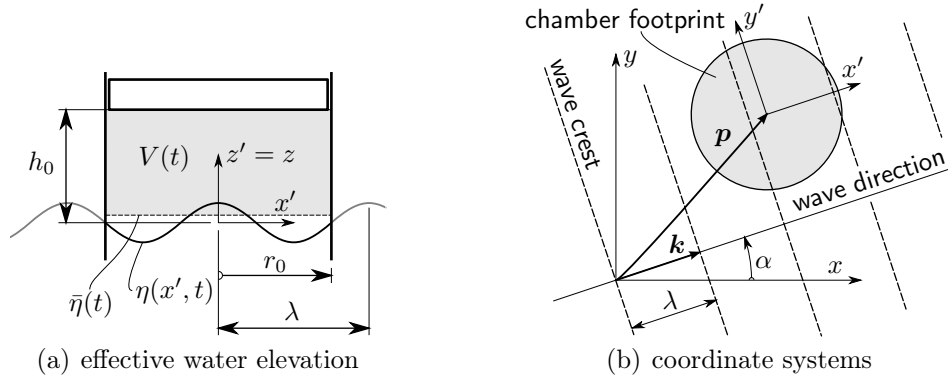


Figure 2.3: Effective water elevation in an air chamber (a) and used coordinate systems for integration of the free surface (b).

where r is the radius of the circular footprint area with its centre at $\mathbf{p} = [p_x, p_y]^T$. One can define an equivalent water elevation

$$\bar{\eta} = \frac{\Delta V}{r^2 \pi}, \quad (2.13)$$

which is proportional to the volume change. The equivalent water elevation is depicted in Fig. 2.3a.

In the following we will define a coordinate transformation into a cartesian system with one axis parallel to the wave direction (see Fig. 2.3b), denoted by the prime symbol, which simplifies the above integral in Eq. (2.12). The transformation equations in matrix form are

$$\begin{bmatrix} x \\ y \end{bmatrix} = \begin{bmatrix} \cos \alpha & \sin \alpha \\ -\sin \alpha & \cos \alpha \end{bmatrix} \begin{bmatrix} x' \\ y' \end{bmatrix} + \begin{bmatrix} p_x \\ p_y \end{bmatrix}. \quad (2.14)$$

Combining Eqs. (2.9) and (2.12) to (2.14) and some simplification yields

$$\bar{\eta}(t) = \int_{-r}^r \int_0^{\sqrt{r^2 - x'^2}} a \cos(kx' + \underbrace{k(p_x \cos \alpha + p_y \sin \alpha)}_{\varphi_p} - \omega t) dy' dx'. \quad (2.15)$$

Abbreviating the position dependent phase shift in the cosine function as φ_p , carrying out the integration for y' , and noting the symmetry of the integrand one obtains

$$\begin{aligned} \bar{\eta}(t) &= \frac{2a}{r^2 \pi} \int_{-r}^r \sqrt{r^2 - x'^2} \cos(kx' + \varphi_p - \omega t) dx' \\ &= a \frac{2J_1(kr)}{kr} \cos(\varphi_p - \omega t), \\ &= a h(kr) \cos(\varphi_\lambda(kr) + \varphi_p - \omega t) \end{aligned} \quad (2.16)$$

where J_1 is a Bessel functions of the first kind. The above equation describes the time dependant equivalent surface elevation $\bar{\eta}$ (see also Fig. 2.3a) of an arbitrarily located circular air chamber with radius r . The function h defined as

$$h(kr) = \left| \frac{2J_1(kr)}{kr} \right|, \quad (2.17)$$

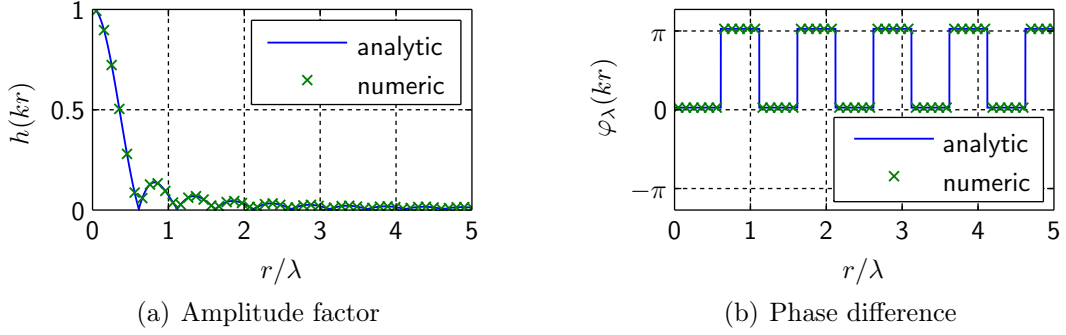


Figure 2.4: Height ratio and phase difference of the effective surface elevation inside an air chamber.

represents a multiplication factor for the reference wave. Multiplying the reference wave amplitude with h one obtains the oscillation amplitude of the equivalent surface elevation in the chamber. The phase shift of the equivalent surface elevation with respect to the reference wave is given by

$$\varphi_\lambda(kr) = \begin{cases} 0, & J_1(kr) \geq 0 \\ \pi, & J_1(kr) < 0 \end{cases}. \quad (2.18)$$

The functions h and φ_λ can also be obtained by a numerical integration of Eq. (2.15) for a range of time instances and wave frequencies with $\varphi_{p,i}$ set to zero. The result is depicted in Fig. 2.4.

The force required to obtain the effective surface elevation is equal to the integral of the dynamic pressure on the water surface over the footprint area of the chamber. As the water elevation, Eq. (2.8), and the dynamic pressure at the surface, Eq. (2.11) with $z = 0$, are related by the constant factor ρg , the total vertical excitation force can be written directly as

$$F(t) = \rho g \bar{\eta}(t) = a \rho g h(kr) \cos(\varphi_\lambda(kr) + \varphi_p - \omega t). \quad (2.19)$$

The forcing is still harmonic with the angular frequency of the wave. The amplitude is proportional to the amplitude factor $h(kr)$, which is dependent on the ratio between chamber radius and wavelength. It rapidly decreases from the limit value of one for waves much longer than the chamber radius until it is almost negligible for waves shorter than the chamber diameter (see Fig. 2.4a). The phase difference depends both on the position of the air chamber with respect to the reference location of the wave and on the wavelength which causes a jumps of the phase by π if $J_1(kr) < 0$ (see Fig. 2.4b).

2.4 Hydrodynamic Reaction Forces

The elevation of the water surface inside an air chamber is prescribed by a degree of freedom. Movement of this degree of freedom will cause reaction forces of the water. For the sake of simplicity, let us imagine a massless, circular cylinder with vertical axis and its lower end immersed in the fluid. Obviously, displacing the cylinder downwards will result in an increase of the buoyancy force. This hydrostatic force can be simply

obtained by integrating the hydrostatic pressure in the fluid over the wetted body surface. Additionally, accelerating the cylinder in axial direction will cause reaction forces, despite the cylinder being massless. These forces are caused by the surrounding fluid, and are the hydrodynamic reaction forces being the topic of this section.

2.4.1 Acoustic Theory

As the hydrodynamic forces are of interest for steady state, periodic motion, they can be obtained by using acoustic theory.

2.4.1.1 Governing Equations

If the fluid can be considered as inviscid the viscous terms of the Navier-Stokes equations may be neglected. Considering only small motions the equilibrium equations for a fluid particle can be written as

$$\frac{\partial p}{\partial \mathbf{x}} + \rho_f \ddot{\mathbf{u}}_f = \mathbf{0}, \quad (2.20)$$

where p is the dynamic pressure in the fluid, \mathbf{x} is the spacial position of the particle, $\ddot{\mathbf{u}}_f$ is the acceleration of the particle and ρ_f is the density of the fluid. The convection term has been neglected, which is usually considered sufficiently accurate for steady fluid velocities up to Mach 0.1 [12]. The constitutive behaviour is considered as inviscid and compressible relating the bulk modulus of the fluid, K_f , and the dynamic pressure by

$$p = -K_f \frac{\partial}{\partial \mathbf{x}} \cdot \mathbf{u}_f, \quad (2.21)$$

where $\frac{\partial}{\partial \mathbf{x}} \cdot \mathbf{u}_f = \epsilon_V$ denotes the volumetric strain.

If the speed of sound is constant in the medium, the above equations can be combined into a single equation, the acoustic wave equation,

$$\nabla^2 p - \frac{1}{c_f^2} \frac{\partial^2 p}{\partial t^2} = 0 \quad \text{or}, \quad (2.22)$$

$$\frac{\partial^2 \dot{\mathbf{u}}}{\partial t^2} - c_f^2 \nabla^2 \dot{\mathbf{u}} = 0, \quad (2.23)$$

where $c_f = \sqrt{K_f/\rho_f}$ denotes the speed of sound in the acoustic medium. In above equation ∇^2 denotes the Laplace operator*.

The acoustic equations are linear differential equations and can be solved by the finite element method. In the current work the software package ABAQUS has been used. Here the acoustic pressure at the finite element nodes is computed [12].

* The Laplace operator, also commonly denoted by Δ , is the divergence ($\nabla \cdot$) of the gradient ∇f . Thus, it may also be written as $\frac{\partial}{\partial x_1} + \dots + \frac{\partial}{\partial x_n}$, i.e. the sum of all unmixed second order partial derivatives with respect to the Cartesian coordinates x_i .

2.4.1.2 Boundary Conditions

To solve the acoustic equations for a specific problem, appropriate boundary conditions must be specified. Apart from cases where the nodal pressure is prescribed directly, the boundary conditions are formulated in terms of the boundary traction defined as

$$T(\mathbf{x}) = -\mathbf{n} \cdot \ddot{\mathbf{u}}_f, \quad (2.24)$$

where \mathbf{n} denotes the outward normal vector at the boundary.

Stationary Rigid Wall or Symmetry Plane: If nodal values are not constrained, i.e. no boundary traction is specified, this corresponds to a stationary rigid wall or a symmetry plane (Neumann condition). This can be seen from Eq. (2.24): zero traction enforces zero outwards acceleration, hence an immobile wall or symmetry plane.

Acoustic Structural Boundary: If the acoustic medium should be directly coupled to the motion of a solid, so called *acoustic interface elements* can be used. These elements couple the accelerations of the structure directly to the acoustic pressure. For this purpose they possess four degrees of freedom (DoF) per node (one pressure DoF and three displacement DoFs). The coupling is accomplished by shared nodes between acoustic, interface and structural elements.

Free Surface: On the free surface the restoring force due to gravity can be introduced by the use of appropriate boundary conditions. This enables the modelling of low amplitude, i.e. linear, surface gravity waves. The correct restoring force is enforced by setting the surface traction in the normal direction to

$$T_{fr}(\mathbf{x}) = \frac{1}{\rho_f g} \ddot{p}, \quad (2.25)$$

where g denotes the acceleration of gravity. The above relation can be imposed directly on faces of acoustic elements in ABAQUS by the specification of a boundary admittance and respectively boundary impedance [12]. In order to directly obtain information on the displacement of the free surface, acoustic interface elements, in conjunction with membrane elements and appropriate boundary conditions to impose the surface tractions, can be used. The surface traction formulated in terms of the displacement DoFs corresponds to a displacement dependent pressure on the membrane face. This is enforced in ABAQUS by the use of element foundations (see the *FOUNDATION keyword) [12].

Radiation Boundary: When modelling a structure oscillation in an unbounded fluid domain, it is necessary to specify boundary conditions that permit the created waves to pass unhindered into infinity. This is usually done by imposing a radiation condition of the form

$$\lim_{x \rightarrow \infty} \left(\frac{\partial p}{\partial x} - i \frac{1}{v} \frac{\partial p}{\partial t} \right) = 0, \quad \text{with } v = \frac{\omega}{k}. \quad (2.26)$$

Here, $i = \sqrt{-1}$ stands for the imaginary quantity, and ω is the circular frequency of the oscillation, and k the corresponding wave number. Above condition can be derived from

the the general condition of radiation [84], which was first published by Sommerfeld [63]. It is implemented in ABAQUS for sound waves in so called *infinite elements*, which can be placed on the appropriated boundaries. In this case the parameter v , termed *real speed of the radiation wave* by Xing [84], is equal to the speed of sound ($v = c_f$).

However, for surface gravity waves, the condition must be adapted. The real speed of the radiation wave in this case must correspond to the phase velocity of the surface waves

$$c_p = \frac{\omega}{k} = \frac{g}{\omega}. \quad (2.27)$$

In above relation the dispersion relation for deep water waves has been used. Setting the speed of sound in the infinite medium equal to the required speed of radiation yields the required bulk modulus on the infinite elements

$$K_{f,inf} = \rho_f \left(\frac{g}{\omega} \right)^2. \quad (2.28)$$

The density in the infinite elements remains equal to the density in the adjacent fluid elements. The bulk modulus of the infinite elements is frequency dependent and must be adapted to the excitation frequency in steady state dynamic procedures. With acoustic infinite elements with material properties altered in the prescribed way, reflection coefficients as low as 10% can be achieved in ABAQUS for two-dimensional surface gravity waves.

2.4.2 Equivalent Model

For the case of a rigid body oscillating in a fluid the resulting fluid forces can be written in the from

$$f_{h,k} = A_{kj}\ddot{\eta}_j + B_{kj}\dot{\eta}_j, \quad (2.29)$$

where η_j denotes the degrees of freedom of the rigid body [17]. The coefficients A_{kj} and B_{kj} are termed added mass and damping coefficients. In general they are functions of the oscillation frequency and body shape, and other factors like the vicinity of a free surface or finite water depth can have an impact too.

Observing the structure of the above equation, the equivalence to a mass-dashpot system is apparent. The hydrostatic restoring forces, which are proportional to the displacement of the rigid body, can be modelled as a linear spring. The fluid forces on an oscillating immersed body can, therefore, be modelled by an equivalent mass-spring-dashpot system for ever degree of freedom. Figure 2.5 shows a sketch of floating body conducting vertical oscillations, and a mechanically equivalent mass-spring-dashpot system.

In the current case the hydrodynamic forces of a body in vertical motion are of interest. If the body is axially symmetric, only vertical forces will arise. Therefore, only two (A_{33} and B_{33}) of the in general 2×36 coefficients are of interest. In order to illustrate the similarity to the mass-spring-dashpot system they will be termed m_a and c in the following.

In order to compute the parameters of the equivalent system, i.e. the added mass and damping coefficients, the following procedure can be used. An acoustic finite element model of the fluid surrounding the floating body is created. Appropriate boundary conditions at the free surface, the infinite boundaries and at the body surface are employed. A

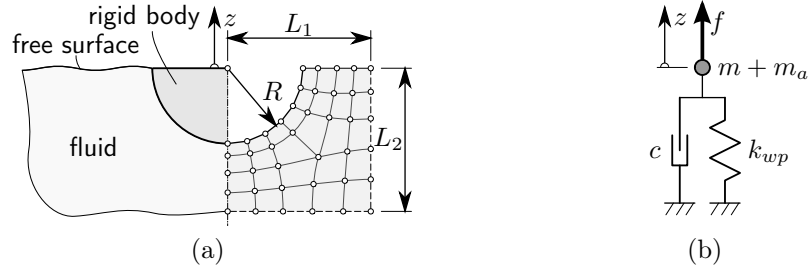


Figure 2.5: Floating cylinder with its axis in the waterplane (a), and equivalent mass-spring-dashpot system for vertical oscillatory motion (b).

forced oscillation of the body is prescribed and the resulting reaction forces are calculated in a steady state dynamic analysis for all frequencies of interest. The prescribed harmonic excitation can be written in the form

$$z(t) = \text{Re}\{\hat{z}e^{i\omega t}\}, \quad (2.30)$$

where \hat{z} is the complex valued excitation. The equation of motion for the equivalent system (depicted in Figure 2.5b) reads

$$(m + m_a)\ddot{z} + c\dot{z} + k_{wp}z = f, \quad (2.31)$$

where m donates the structural mass of the body and f the reaction force. The steady state solution is obtained by using the above Ansatz, Eq. (2.30), for the displacement and an equivalent Ansatz for the reaction force. Inserting them into the equation and regrouping the terms yields

$$[-\omega^2 m_a + i\omega c] \hat{z} = \underbrace{\hat{f} - [k_{wp} - m\omega^2] \hat{z}}_{\hat{f}_h}. \quad (2.32)$$

It can be seen that the hydrodynamic force, \hat{f}_h , is obtained from the computed reaction force, \hat{f} , by subtraction of the hydrostatic contribution, $k_{wp}\hat{z}$, created by a modelled waterplane stiffness and the inertial contribution, $-m\omega^2\hat{z}$, created by the structural mass, m , of the rigid body. The added mass and damping constant determine the magnitude of the real and imaginary part of the complex valued hydrodynamic force divided by the complex valued excitation. They are related by

$$m_a = \text{Re}\left\{-\frac{1}{\omega^2} \frac{\hat{f}_h}{\hat{z}}\right\}, \quad (2.33)$$

$$c = \text{Im}\left\{\frac{1}{\omega} \frac{\hat{f}_h}{\hat{z}}\right\}. \quad (2.34)$$

The hydrodynamic force is obtained from the computed reaction force, \hat{f} , by

$$\hat{f}_h = \hat{f} - (k_{wp} - m\omega^2) \hat{z}, \quad (2.35)$$

where the hydrostatic contribution, $k_{wp}\hat{z}$, created by a modelled waterplane stiffness and the inertial contribution, $-m\omega^2\hat{z}$, created by the structural mass, m , of the rigid body have been subtracted.

2.4.3 Non-Dimensional Representation of Quantities

It is useful to represent results in a non-dimensional form in order to allow for their applicability to physically similar problems. The appropriate similarity law for the problem class of surface gravity waves is the Froude scaling law [9]. As long as acoustic effects remain negligible, Froude scaling remains appropriate. To represent the oscillation frequency f , the non-dimensional quantity R/λ is used. Here λ is the wavelength of linear surface gravity waves in deep water. It is related to the wave frequency by the dispersion relation

$$\omega^2 = g \frac{2\pi}{\lambda}, \quad \text{with} \quad \omega = 2\pi f. \quad (2.36)$$

The added mass and damping constants are made non-dimensional by

$$C_a = \frac{m_a}{\rho_f S_f}, \quad (2.37)$$

$$C_d = \frac{c}{\rho_f \omega S_f}, \quad (2.38)$$

to obtain the added mass coefficient C_a and the damping coefficient C_d . To comply with the general three-dimensional case, the above relations are written in terms of a characteristic volume, S_f , of the body. For the two-dimensional problem treated in Section 2.4.5.1 the characteristic volume, in this case a characteristic area, is chosen as $\pi R^2/4$. For the axially symmetric problem of a single air chamber treated in Section 2.4.5.2, the volume of a semi-sphere with the same radius as the circular air chamber is used.

2.4.4 The Relation of the Damping Constant to the Radiated Wave Energy

The damping in the acoustic system is the result of wave energy radiated to infinity. The dashpot in the equivalent system should be designed such that the dissipated energy is equal to the energy contained in the surface gravity waves. This energy based consideration offers an alternate way to determine the damping parameter of the equivalent system.

The energy per surface area contained in surface gravity waves is related to the wave amplitude, a , by

$$E_s = \frac{\rho_f g}{2} a^2. \quad (2.39)$$

New waves on the unperturbed water surface are created with the group velocity, which equals the energy transport velocity. For the case of deep water waves the group velocity is

$$c_g = \frac{c_p}{2} = \frac{gT}{2\pi}, \quad (2.40)$$

where T denotes the wave period. Hence, the amount of energy dissipated per period can be computed by the product of wave energy per surface area and created wave surface.

Another possibility to compute the dissipated energy is to evaluate the work done at the boundary of the domain during one period. The work done during one period at the

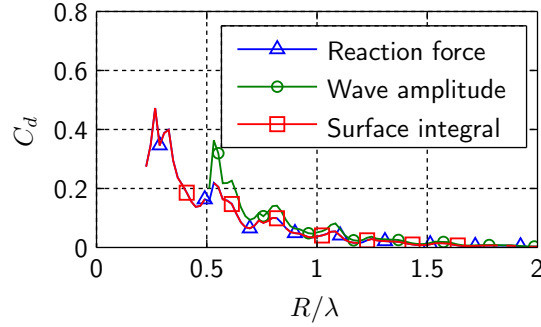


Figure 2.6: Comparison of the determination methods for the damping coefficient.

boundary surface A is

$$W = \int_0^T \int_A p \dot{\mathbf{u}} \mathbf{n} dA dt, \quad (2.41)$$

where $\dot{\mathbf{u}}$ is the fluid particle velocity, and \mathbf{n} the outwards normal vector at the boundary[†].

Comparison of the determination methods for the damping parameter showed excellent agreement between the methods (see Fig. 2.6). The reason for the deviation of the values obtained from the wave amplitude is the presence of reflected waves in the wave field.

2.4.5 Computational Models

2.4.5.1 Validation Model

As a validation model for the proposed computation approach the case of an infinite, circular cylinder with its axis in the waterplane is chosen. The case of vertical oscillations is considered. Results for this problem are given for example by Faltinsen [17].

A sketch of the problem and of the corresponding finite element model is shown in Fig. 2.5a. The radius R of the cylinder was chosen as 1 m and the size of the computational domain $L_1 = L_2$ as 10 m. As an acoustic medium water at room temperature with the material properties $\rho_f = 998.2 \text{ kg/m}^3$ and $K_f = 2.2 \text{ GPa}$ was assumed. Acoustic interface elements and membrane elements were used at the free surface and at the body edge, respectively. The bending stiffness and density of the membrane elements were chosen so small that their impact on the overall system is negligible. The displacement degrees of freedom of the nodes of the cylinder edge were constraint to the displacement of a reference node, thereby creating a rigid body. The gravitational restoring force on the free surface was modelled as a displacement dependent pressure, as described earlier. Due to symmetry only one symmetric half has to modelled. The pressure DoFs in the symmetry plane were left free, to create a symmetry boundary condition. On the other vertical boundary infinite acoustic elements were placed with material properties set in order to absorb surface gravity waves, as described earlier. On the lower horizontal boundary standard acoustic infinite elements were placed.

[†]For a steady state dynamic analysis both p and $\dot{\mathbf{u}}$ are represented by complex values. See Appendix D.4 for a description on how to evaluate the integral over one oscillation period.

The validation model was used to investigate the influence of the different model parameters on the computed added mass and damping constants. Most of the results will be presented in non-dimensional form, as described in Section 2.4.3. For the current two-dimensional problem the characteristic volume is replaced by a characteristic area, which is chosen as $\pi R^2/4$.

Observing the diagram of the computed added mass coefficient in Fig. 2.7, a decaying oscillation is visible. This oscillation is not present in the reference solution published by Faltinsen [17]. The reason for the oscillations was identified to be the infinite boundary condition. A portion of the free surface wave created by the oscillating structure is reflected back into the domain. The resulting wave system is composed of an incident wave travelling away from the structure towards the infinite boundary, and a reflected wave travelling in the opposite direction. The amplitudes of both waves can be determined by the spatially varying amplitude of the resulting wave system. The reflection coefficient of the boundary, defined as the ratio between the amplitude of the reflected wave a_r and the amplitude of the incident wave a_i , can be computed by

$$\frac{a_r}{a_i} = \frac{a_{max} - a_{min}}{a_{max} + a_{min}}, \quad (2.42)$$

where a_{max} denotes the maximum, and a_{min} the minimum amplitude of the compound wave system. A reflection coefficient of 10 to 15% was determined throughout the investigated frequency range. The reflected wave influences the reaction force from which the added mass coefficient is computed, causing the oscillations in the result. The frequencies at which minima and maxima occur in the computed results could be identified as the frequencies at which constructive and destructive interference between the incident and radiated wave fields arise. The corresponding wavelengths for constructive and destructive interference are

$$\lambda_c = \frac{2}{n} (L_1 - R) \quad \text{and} \quad \lambda_d = \frac{4}{2n + 1} (L_1 - R) \quad \text{for} \quad n = 0, 1, \dots, \quad (2.43)$$

where the indices c and d denote constructive and destructive interference, respectively. The so computed frequencies are marked in Fig. 2.7 as continuous lines for constructive interferences and dashed lines for destructive interference. It can be seen that they correspond well with the minima and maxima.

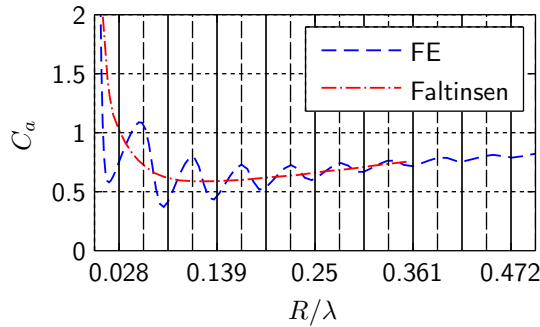


Figure 2.7: Comparison of the added mass computed from the acoustic model and the solution published by Faltinsen [17].

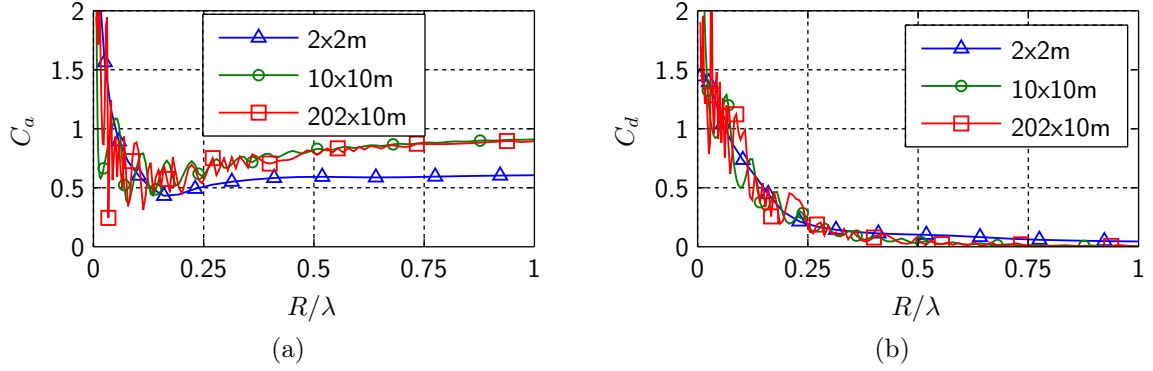


Figure 2.8: Added mass coefficient (a) and damping coefficient (b) for different sizes ($L_1 \times L_2$) of the computational domain.

The frequencies at which minima and maxima occur depend on the size of the computational domain, according to Eq. (2.43). Figure 2.8 shows a comparison of computation results for different sizes of the computational domain. For a larger domain more interferences are present in the investigated frequency range. In fact the interferences are so dense on the frequency axis that the oscillation can not be resolved, which explains the edge shape of the curve. The curve for the small domain size shows no oscillation at all, but severely deviates from the other two curves. This can be explained by the close vicinity of the infinite boundary, which perturbs the simulation results.

A remedy against the undesired oscillations is to fit a function to the computed results. The fit is computed for the non-dimensional quantities. The fit functions for the added mass and damping coefficients are

$$C_a(x) = a_0 + \sum_{i=1}^2 a_i x^{-\frac{1}{i+1}} e^{b_i x}, \quad (2.44a)$$

$$C_d(x) = c_1 x^{c_2} e^{c_3 x}. \quad (2.44b)$$

The chosen function for the added mass coefficient satisfies the theoretical conditions

$$\lim_{x \rightarrow 0} C_a(x) = \infty \quad \text{and} \quad \lim_{x \rightarrow \infty} C_a(x) = a_0 = \text{const.} \quad (2.45)$$

For the damping coefficient the theoretical limits

$$\lim_{x \rightarrow 0} C_d(x) = 0 \quad \text{and} \quad \lim_{x \rightarrow \infty} C_d(x) = 0, \quad (2.46)$$

are likewise met, ensuring that physically reasonable functions are computed. In the non-linear fitting algorithm the weights correcting for an equal distribution of the data values along the x -axis, i.e. the frequency-axis, are used. The computed parameters of the fitting functions can be found in Table 2.1, whereas Fig. 2.9 shows a plot of the computed fitting functions as well as the data from the finite element analysis and values from the literature. It can be seen that excellent agreement can be obtained between the computed fitting functions and the results from the literature.

The last phenomenon investigated is the impact of the bulk modulus of the acoustic medium. It can be seen in Fig. 2.10 that no major differences exist if the bulk modulus

	(a)		(b)
a_0	0.9272	c_1	1.747
a_1	1.24	c_2	1.362e-06
b_1	-3.382	c_3	-9.148
a_2	-2.071		
b_2	-3.603		

Table 2.1: Computed parameters of the fitting functions: (a) Equation (2.44a) for the added mass coefficient; (b) Equation (2.44b) for the damping coefficient.

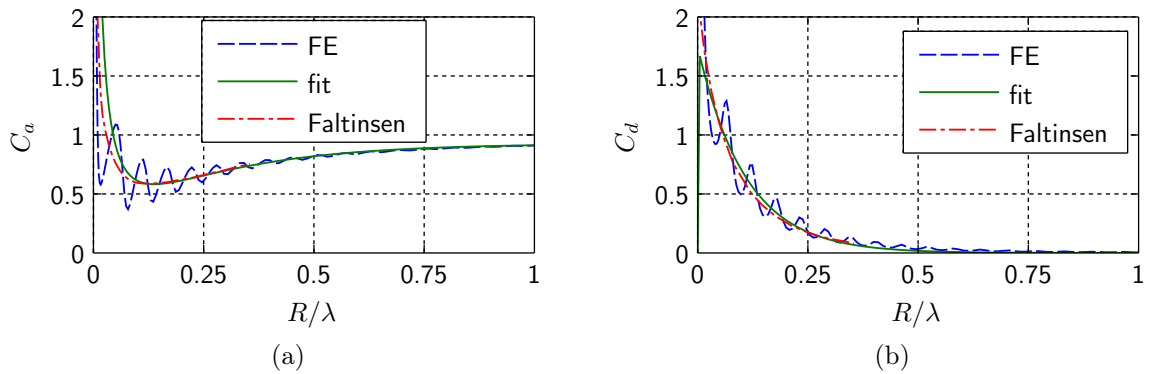


Figure 2.9: Comparison of the fit to the data computed by the FE analysis, with results given by Faltinsen [17] for the added mass coefficient (a) and the damping coefficient (b).

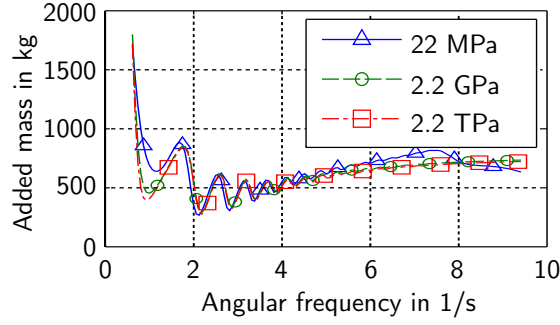


Figure 2.10: Computed added mass constant for different values of the bulk modulus.

is increased from the reference value of 2.2 GPa, hence compressibility effects have no impact. On the other hand, if the bulk modulus is decreased, differences, especially in the high frequency regime, appear. This differences can be explained by standing acoustic waves in the domain.

2.4.5.2 Model of a Single Air Chamber

The aim of this model is to determine the hydrodynamic forces acting onto the water surface of a cylindrical air chamber. The air chamber is formed by a horizontal plane, a cylindrical membrane, and the water surface. The internal pressure is only slightly above the atmospheric pressure outside the chamber, so the static water level difference can be neglected. Due to pressure oscillations in the chamber, the internal water surface will be displaced. The magnitude of this displacement is governed by the hydrodynamic reaction forces, which are computed by the acoustic finite element (FE) model. The parameters of an equivalent spring-mass-dashpot system can be derived from the results of the FE model, as described above.

Figure 2.11 shows a sketch of the structural acoustic finite element model of the investigated configuration. In order to reduce the modelling and computational effort an axially symmetric model is used. At the bottom of the acoustic domain infinite acoustic elements are used. The natural boundary condition in the symmetry axis is enforced automatically by leaving the pressure degrees of freedom unconstrained. At the second vertical boundary the material properties of the used infinite acoustic elements are modified in order to absorb surface gravity waves as described in Section 2.4.1.2. The restoring forces at the free surface are modelled by a displacement dependent pressure onto massless membrane elements which are coupled to the acoustic elements by acoustic interface elements as described in more detail in Section 2.4.1.2. For the acoustic structural interface at the vertical skirt acoustic interface elements are used at both sides. In order to allow for different pressure values at both sides of the membrane a second set of nodes is created (at the same location), and only the displacements are coupled by constraint equations. The skirt itself is modelled by shell elements of appropriate thickness with linear elastic material properties. At the top end of the skirt, only the x -displacements are coupled between the acoustic interface nodes and the shell nodes. In this way the vertical motion of the shell elements can be constrained.

Linear steady state dynamic analyses are performed at specified frequencies. The

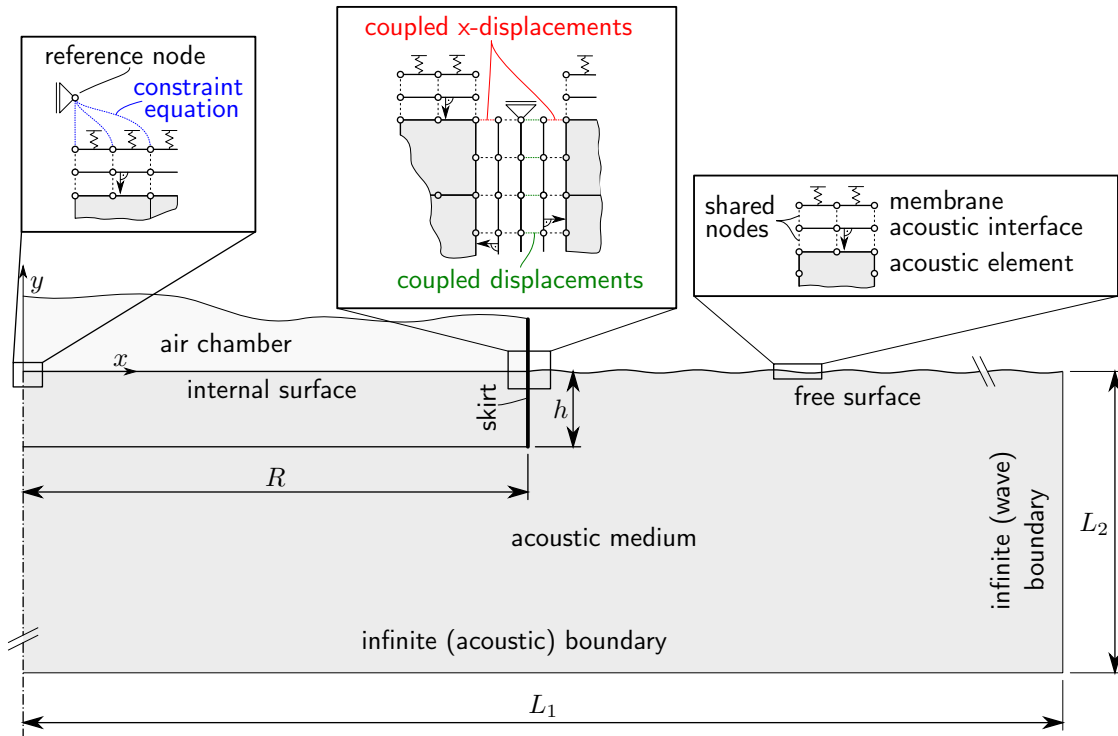


Figure 2.11: Sketch of the finite element model of the air chamber showing all important boundary conditions and coupling equations.

system is excited by defining the displacement of a reference node, which is coupled to the internal surface in two different ways. In the first model the y -displacements are simply set equal, thereby creating a rigid body. In the second model a constraint equation is used which leaves the shape of the surface elevation free, but enforces constant pressure onto the surface if the reference node is displaced.

In order to study the influence of the flexibility of the skirt, three different models are investigated. In the first model represents an infinitely compliant, massless skirt simply by omitting the shell elements and coupling of the pressure degrees of freedom. The second model represents the other extreme of a rigid skirt. It is created by omitting the shell elements and leaving the pressure degrees of freedom free at both sides, thereby modelling an immobile, rigid wall. The third model represents the actual skirt as described above with a thickness of 4 mm, and a linearly elastic material with a Young's modulus of 1.0 GPa and Poisson's ratio of 0.3, and a density of 1000 kg/m^3 .

Two different models were created to investigate the scaling effects. The first model was created in the model scale with an air chamber radius of $R = 0.9 \text{ m}$ and a skirt depth of $h = 13.3 \text{ cm}$. For this model the infinite boundary was chosen as circular with a radius of 15 m, and the material properties were set to make it surface gravity wave absorbing. Only the cases of rigid and infinitely compliant, massless skirt were computed. The second model was created in the prototype scale with a chamber radius of 67.5 m and a skirt depth of 10 m. The shape of the domain was chosen as depicted in Fig. 2.11 with $L_1 = 200 \text{ m}$ and $L_2 = 150 \text{ m}$.

2.4.6 Results

In the first part of this section a number of results comparing the different modelling strategies will be presented. A discussion more focused on the physical phenomena will follow at a later point together with the determination of non-dimensional formulations for the added mass and damping coefficients.

2.4.6.1 Differences between Modelling Strategies

The excitation method, i.e. prescribed harmonic forcing or prescribed harmonic displacement, for the dynamical system does not influence the computed added mass and damping coefficients. This can be seen from Fig. 2.12, where both forcing methods are compared for a model with rigid internal surface and infinitely flexible, massless skirt.

The mesh size should be chosen in such a way that a minimum of 10 nodes per wavelength are present. As the free surface waves have much smaller wavelength than the acoustic waves they govern the mesh size. The mesh can be more coarse towards the bottom of the domain. Figure 2.13 shows a comparison of results obtained on two different meshes. It can be seen that the coarse mesh is already sufficiently fine.

Comparing results obtained on the model and on the prototype scale shows that the used Froude scaling is appropriate. Figures 2.14 to 2.16 show a comparison of results obtained for computations done on the prototype and model length scales. The curves for the model scale show the characteristic oscillatory pattern caused by constructive and destructive interferences of the reflected surface gravity waves (as explained in Section 2.4.5.1). For the prototype scale this pattern shows a longer wavelength, which is caused by the smaller non-dimensional domain size of this model. Furthermore, due to the large absolute size of the domain, acoustic modes can also be present in the investigated frequency regime. Due to this reason results on the model scale will be used in the following fitting of analytic expressions for the added mass and damping coefficients.

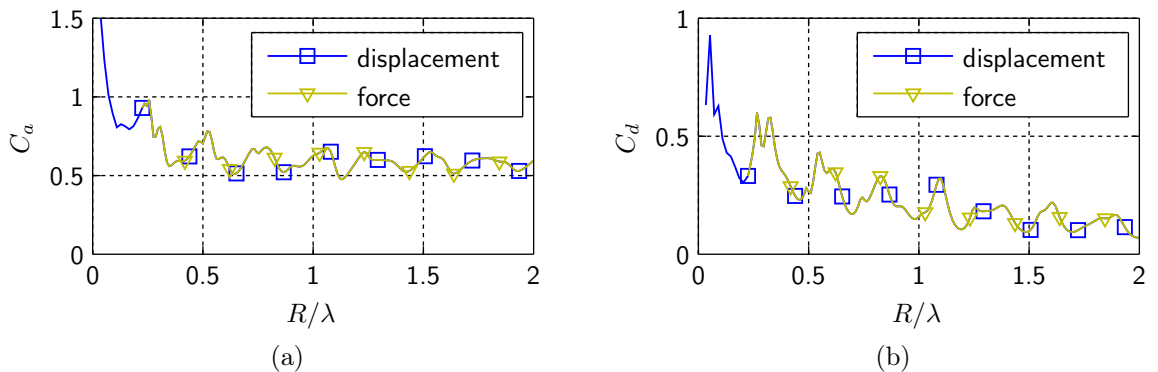


Figure 2.12: Comparison of force and displacement controlled excitation for a model on the prototype scale with rigid internal surface and infinitely flexible, massless skirt. The diagrams show the computed added mass coefficients (a) and damping coefficients (b).

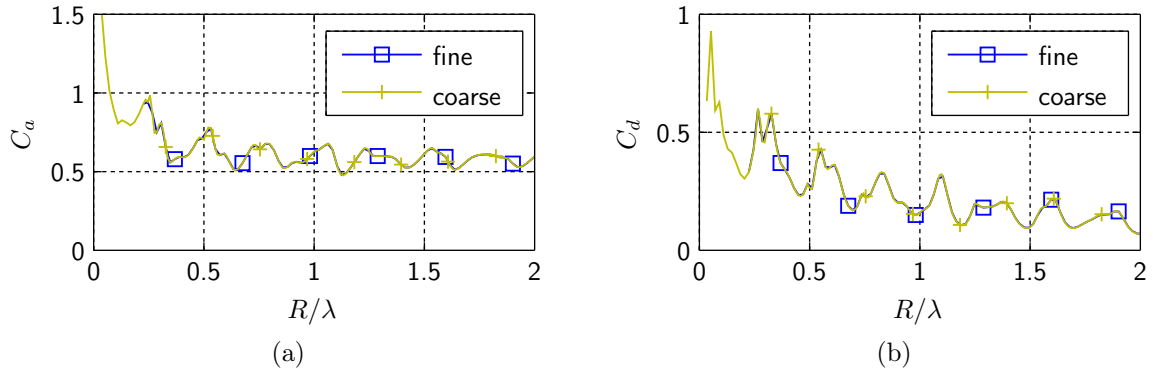


Figure 2.13: Comparison of different mesh sizes (2000 and 20,000 elements) for a model on the prototype scale with rigid internal surface and infinitely flexible, massless skirt. The diagrams show the computed added mass coefficients (a) and damping coefficients (b).

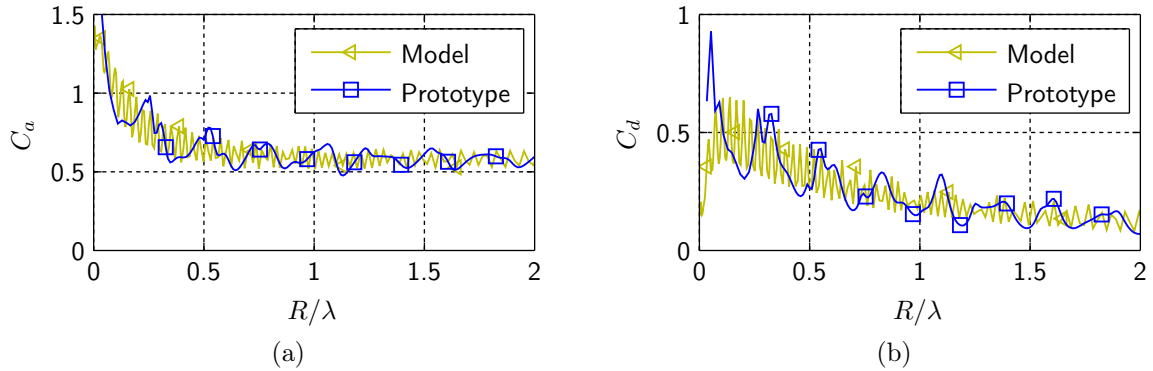


Figure 2.14: Comparison of results obtained for models of different length scales with rigid internal surface and infinitely flexible, massless skirt. The diagrams show the computed added mass coefficients (a) and damping coefficients (b).

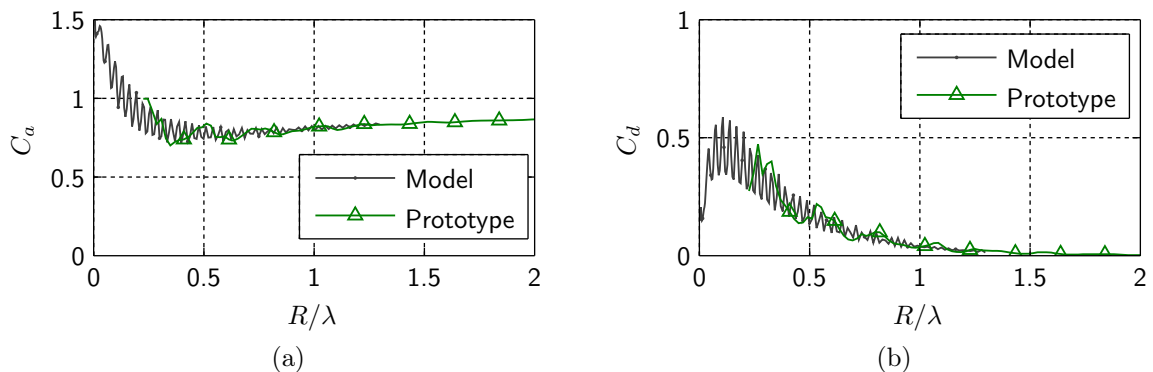


Figure 2.15: Comparison of results obtained for models of different length scales with rigid internal surface and rigid skirt. The diagrams show the computed added mass coefficients (a) and damping coefficients (b).

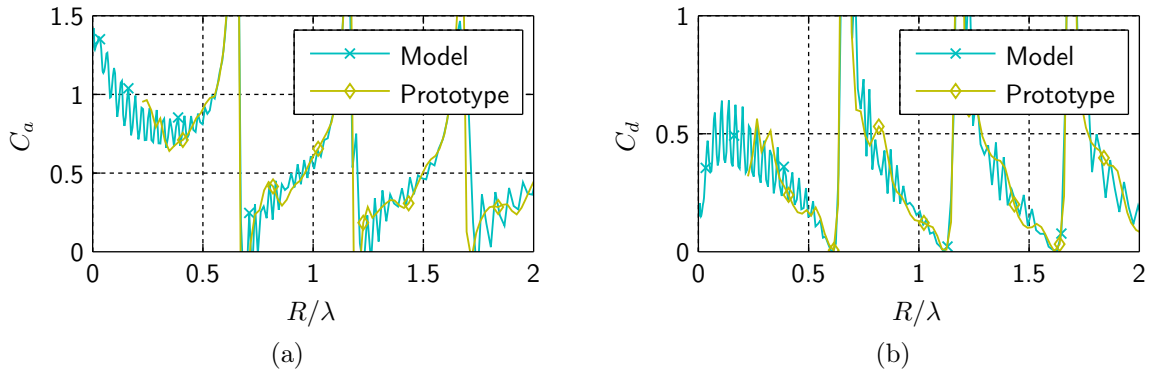


Figure 2.16: Comparison of results obtained for models of different length scales with free internal surface and infinitely flexible, massless skirt. The diagrams show the computed added mass coefficients (a) and damping coefficients (b).

2.4.6.2 Physical Phenomena

The flexibility of the skirt is a key parameter in the design of an air chamber supported platform. The two limit cases, an infinitely flexible, massless skirt, and a rigid, immobile skirt, are compared with a realistic, elastic skirt. In Fig. 2.17 it can be seen that the elastic skirt is very close to the limit case of an infinitely flexible, massless skirt. This might be explained by the high density of the acoustic medium, which causes the inertial forces in the fluid to be large compared to the elastic forces in the skirt.

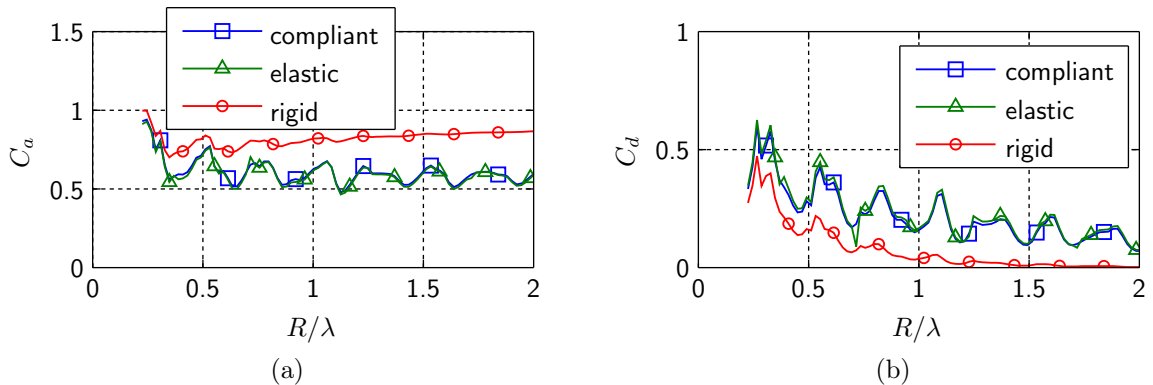


Figure 2.17: Comparison of the impact of the skirt flexibility. Results were obtained on the prototype scale for rigid internal surface. The diagrams show the computed added mass coefficients (a) and damping coefficients (b).

Another interesting phenomenon concerns the free surface in the chamber. Comparing the added mass and damping coefficients obtained by models with rigid internal surface and free internal surface, as shown in Fig. 2.18 for the model scale and infinitely flexible, massless skirt, large differences are visible. The added mass coefficient for a free internal surface shows poles, i.e. vertical tangents, at certain frequencies. Approaching this frequencies the value of the added mass coefficient tends to positive or negative infinity, depending on the direction. The damping coefficients show a similar behaviour; they tend

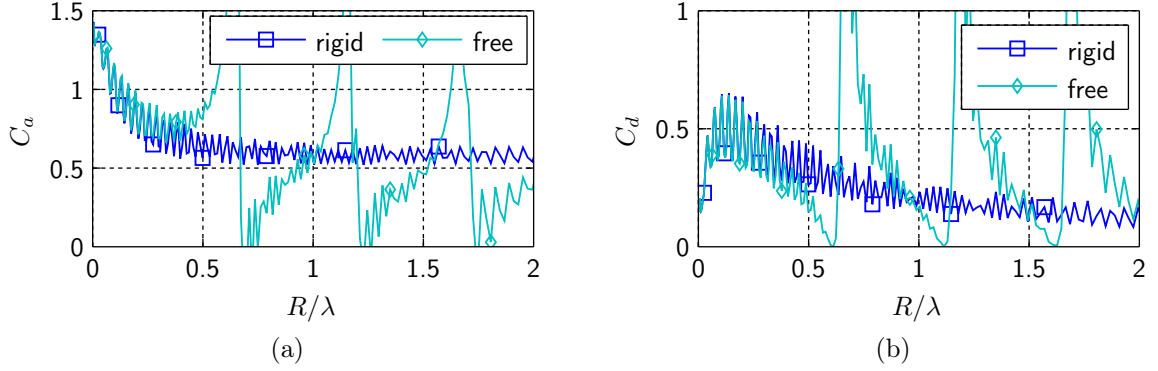


Figure 2.18: Comparison of free internal surface and rigid internal surface. The results were obtained on the model scale and the skirt was treated infinitely flexible and massless. The diagrams show the computed added mass coefficients (a) and damping coefficients (b).

to infinity at the same frequencies. The frequencies of the poles can be identified as the natural frequencies of a circular tank. More precisely, they correspond to the frequencies of the axially symmetric modes. For the behaviour of the equivalent system infinite added mass or damping coefficients mean that there will be zero response for forced excitation. This behaviour is explained as follows: if the system is excited exactly at a natural frequency it must respond at the corresponding natural mode shape. The axially symmetric modes, however, show now effective displacement of the free surface, and, hence, no displacement of the equivalent model degree of freedom. For an air chamber used to support a floating platform this will mean that the air chamber will absorb the wave energy at its natural frequencies and not transmit vertical forces via the pressurized air to the platform. More information on the natural frequencies and mode shapes of liquid in circular cylinders is presented in Appendix C.5.

2.4.6.3 Expressions for the Added Mass and Damping Coefficients

Analytic expressions for the added mass and damping coefficients were obtained by a non-linear least squares fits to the computed results on the model scale. In this manner it is possible to get rid of the oscillations caused by waves reflected by the infinite boundary. The fits were computed in the non-dimensional space, with a constant density of data points along the R/λ -axis. Except for very low frequencies it does not matter if the fit is computed from data obtained from the model or from the prototype scale. In the following, all fits will be computed from data obtained on the model scale.

Rigid Internal Surface: For the case of a rigid internal surface the expressions

$$C_{a,r}(x) = c + \sum_{i=1}^2 a_i x^{-\frac{1}{i+1}} e^{b_i x}, \quad \text{with } b_i \leq 0, \quad (2.47a)$$

$$C_{d,r}(x) = \sum_{i=1}^2 k_i x^{p_i} e^{d_i x}, \quad \text{with } d_i \leq 0 \leq p_i, \quad (2.47b)$$

were used. The obtained coefficients are given in Table 2.2 for the case of an infinitely flexible, massless skirt. For the case of the rigid skirt the coefficients are noted in Table 2.3. The corresponding curves are depicted in Fig. 2.19.

Free Internal Surface: Different expressions are needed for the fitting functions in the case of the free internal surface. The functions must represent the poles at the appropriate locations. For the added mass coefficient the fit is computed for the difference between the results for a rigid and a free internal surface as

$$C_{a,f}(x) = C_{a,r}(x) - \bar{C}_a(x). \quad (2.48)$$

The used fitting function for the difference is

$$\bar{C}_a(x) = \frac{\prod_{i=1}^{N-1} x - z_i}{\prod_{i=1}^N x - x_i} kx^p, \quad (2.49)$$

where the parameters k and p were determined by the non-linear least squares algorithm, and the locations of the zeroes z_i and the locations of the poles x_i were given. Both are noted in Table 2.4. Together with the expressions from the previous section the formulation for the added mass coefficient is now complete. The added mass coefficient is shown in the graph in Fig. 2.19a.

For the damping coefficient the fit is computed directly to the data from the acoustic model. The used fit function is

$$C_{d,f}(x) = \left| \frac{\prod_{i=1}^N x - z_i}{\prod_{i=1}^N x - x_i} \sum_{i=1}^2 k_i x e^{d_i x} \right|, \quad \text{with } d_i \leq 0, \quad (2.50)$$

where the parameters k_i , p_i and d_i were chosen to fit the expression to the data, and the poles and zeroes were set according to their location. The obtained values can be found in Table 2.5 and a graph of the curve is displayed in Fig. 2.19b.

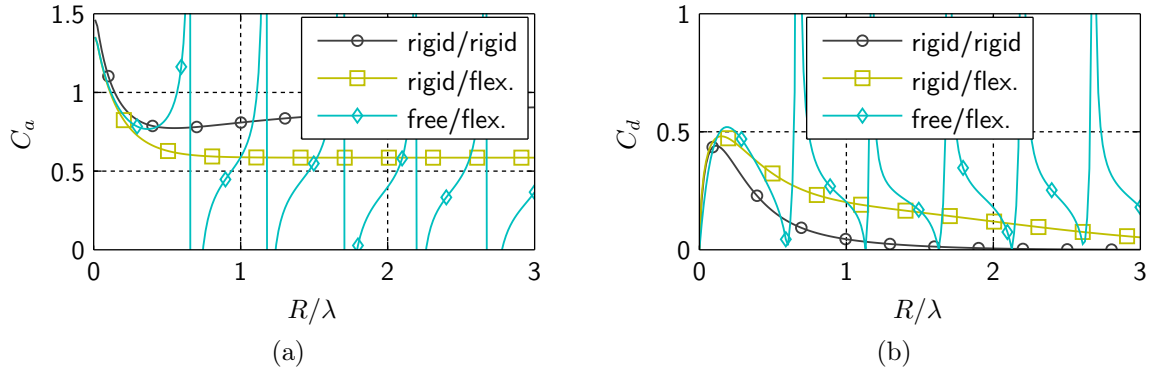


Figure 2.19: Comparison of result from models for different internal-surface/skirt combinations. The diagrams show the computed added mass coefficients (a) and damping coefficients (b).

(a)				(b)			
i	a_i	b_i	c	i	k_i	p_i	d_i
			0.5855				
1	-0.1823	-8.149		1	7.621	0.7053	-1.575
2	-0.5561	-5.353		2	-8.888	0.9557	-1.867

Table 2.2: Computed parameters of the fitting functions for the case of an infinitely flexible, massless skirt: (a) Equation (2.47a) for the added mass coefficient; (b) Equation (2.47b) for the damping coefficient.

(a)				(b)			
i	a_i	b_i	c	i	k_i	p_i	d_i
			0.9392				
1	-0.2081	-0.4215		1	9.543	0.7965	-3.275
2	0.5854	-4.605		2	-11.85	1.097	-3.624

Table 2.3: Computed parameters of the fitting functions for the case of a rigid skirt: (a) Equation (2.47a) for the added mass coefficient; (b) Equation (2.47b) for the damping coefficient.

(a)		(b)		
k	0.1625	i	z_i	x_i
p	1.219	1	1.0	0.67
		2	1.52	1.17
		3	2.1	1.695
		4	2.56	2.196
		5	3.1	2.68
		6	3.61	3.18
		7	4.11	3.96
		8	4.617	4.2
		9	5.12	4.7
		10		5.123

Table 2.4: Parameters of the fitting function for the added mass, Eq. (2.49), for the case of an infinitely flexible, massless skirt: (a) Fitted coefficients; (b) Locations of poles and zeros.

(a)			(b)		
i	k_i	d_i	i	z_i	x_i
1	0.45	-0.6	1	0.599	0.67
2	10.0	-5.31	2	1.13	1.17
			3	1.627	1.695
			4	2.125	2.196
			5	2.615	2.68
			6	3.129	3.18
			7	3.61	3.96
			8	4.11	4.2
			9	4.617	4.7
			10	5.12	5.123

Table 2.5: Parameters of the fitting function for the damping coefficient, Eq. (2.50), for the case of an infinitely flexible, massless skirt: (a) Fitted coefficients; (b) Locations of poles and zeroes.

2.5 Equations of Motion

The relations for the air chambers and the free surface must now be coupled with equations of motion for the plate structure. For the sake of simplicity the plate will be assumed as rigid in the first step. This results in a coupled system of three equations of motion (EoM) for the plate and one EoM per air chamber. The system can then be solved directly in a semi-analytical procedure.

In a second step a flexible plate will be modelled by the means of the finite element method. The system matrices are generated and solved by the code *ABAQUS*. Air chambers and hydrodynamics are taken into account by a combination of spring, mass and dashpot elements.

2.5.1 Equations of Motion for a Rigid Plate

The equations of motions are defined by a balance of momentum for the plate, yielding Eq. (2.51a) to Eq. (2.51c). Posing the momentum balance in vertical direction for the effective water level in chamber i yields the remaining equations of motion, Eq. (2.51d). The resulting coupled system is

$$\left(m + \sum_i m_{s,i} \right) \ddot{z} = \sum_i k_{c,i} (z + p_{y,i} r_x - p_{x,i} r_y - z_i), \quad (2.51a)$$

$$\left(J_x + \sum_i p_{y,i} m_{s,i} \right) \ddot{r}_x = \sum_i p_{y,i} k_{c,i} (z + p_{y,i} r_x - p_{x,i} r_y - z_i), \quad (2.51b)$$

$$\left(J_y + \sum_i p_{x,i} m_{s,i} \right) \ddot{r}_y = \sum_i p_{x,i} k_{c,i} (z + p_{y,i} r_x - p_{x,i} r_y - z_i), \quad (2.51c)$$

$$m_{a,i} \ddot{z}_i = F_i(t) + k_{c,i} (z + p_{y,i} r_x - p_{x,i} r_y - z_i) - k_{wp,i} z_i - c_{d,i} \dot{z}_i. \quad (2.51d)$$

Refer to Fig. 2.20 for a description of the used symbols in above equations.

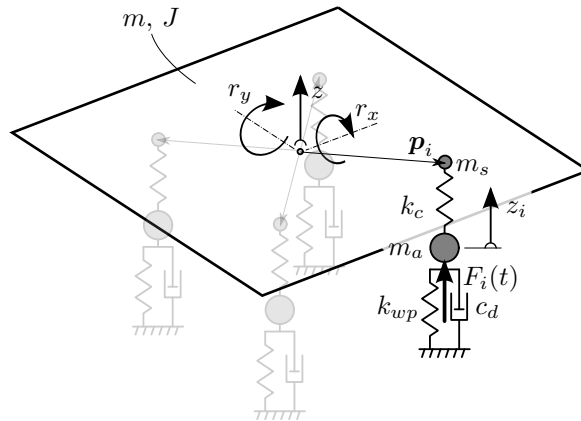


Figure 2.20: The rigid plate with mass m and moment of inertia J has three forces degrees of freedom; vertical displacement z and the rotations r_x and r_y . The vector $\mathbf{p}_i = [p_{x,i}, p_{y,i}]^T$ defines the centre of a circular chamber, where the mass of the skirt m_s is concentrated.

The plate and the effective water level in the chambers are coupled by the pressure in the chambers, modelled by linear springs with stiffness k_c . The derivation of the spring stiffness is described in Section 2.2. Inertial forces arising when changing the effective water level are modelled via the added mass concept by a mass dashpot combination, as explained in detail in Section 2.4. The buoyancy forces arising when displacing the effective water level can be modelled as linear springs, using the water plane stiffness of a floating body. For a circular air chamber with radius r the water plane stiffness is defined as

$$k_{wp} = \rho_w g r^2 \pi, \quad (2.52)$$

where ρ_w is the water density and g is the gravitational acceleration. The effective water level is forced by the dynamic pressure at the free surface, $F(t)$, which was calculated in Section 2.3.

The equations of motion derived (2.51) can be written in matrix form giving

$$\mathbf{M}\ddot{\mathbf{x}} + \mathbf{D}\dot{\mathbf{x}} + \mathbf{K}\mathbf{x} = \mathbf{f}(t), \quad (2.53)$$

where \mathbf{M} is the mass matrix including added mass contributions, \mathbf{K} is the stiffness matrix, \mathbf{D} is the damping matrix, and $\mathbf{f}(t)$ is a time dependant forcing vector. The vector of unknowns $\mathbf{x} = [z, r_x, r_y, z_1, \dots, z_n]^T$ contains the degrees of freedom.

2.5.2 Treatment of the Deformable Plate by Finite Elements

The deformable plate can be conveniently treated by the finite element method. In the present work the code *ABAQUS* was used. The plate is assumed as quadratic and homogeneous. It was discretised using 4-noded thick shell elements, with mass and stiffness properties defined explicitly in terms of a mass per area and stiffness matrices including transverse shear terms.

An air chamber is modelled by a linear spring, subsequently called chamber-spring, with appropriate stiffness (see Section 2.2). The node at the upper end is coupled to the plate nodes within the radial distance in the following manner: The vertical displacement of the spring node is coupled to the weighted mean of the vertical displacements of the plate nodes. The weights are proportional to the 'nodal area'[‡] resulting in a constant pressure distribution onto the plate. The lower node of the chamber-spring represents the mean water elevation in the chamber. Horizontal degrees of freedom are constrained (i.e. set to zero) leaving the vertical DoF as the waterplane-DoF. Here a concentrated mass and a spring and dashpot element against the inertial system are used to account for hydrostatic and hydrodynamic forces, respectively. The water plane stiffness is computed according to Eq. (2.52). The added mass and dashpot properties derived in Section 2.4 are frequency dependent. Therefore, a separate model is created for every considered angular frequency. For the determination of the natural frequencies these properties are updated in an iterative manner.

The system matrices created by the FE program are analogous to Eq. (2.51), however the vector of unknowns now contains the nodal degrees of freedom. The equations of motion can be solved in different routines to compute natural frequencies and oscillation modes or the steady state response.

[‡] The nodal area for a particular node is $\sum_i A_i/n_i$, where A_i is the area and n_i the number of nodes. The index i stands for the elements connected to the considered node.

2.6 Model Output

The model can be used to compute the natural frequencies and mode shapes of floating platforms with an arbitrary number and position of air chambers. In the FE model the flexibility of the plate can be taken into account. The response of the platform in regular waves can be computed for arbitrary wave directions and frequencies. Transfer functions for all model DoFs, i.e. plate displacements and water plane displacements, are obtained directly from the model. Additionally, these direct transfer functions can be used to compute the transfer functions for derived quantities like chamber pressure, skirt tension and plate velocities and accelerations.

2.6.1 Natural Frequencies and Oscillation Modes

2.6.1.1 Free Oscillation

The free oscillation eigenvalue problem is obtained by setting the forcing vector to zero and disregarding the damping matrix in (2.53). Inserting a harmonic Ansatz like

$$\mathbf{x}(t) = \hat{\mathbf{x}}e^{i\omega t}, \quad (2.54)$$

yields the free oscillation eigenvalue problem

$$(\mathbf{K} - \omega^2 \mathbf{M}) \mathbf{z} = \mathbf{0}, \quad (2.55)$$

which can be solved for the eigenvalues ω_j^2 , representing the angular natural frequencies ω_j and the corresponding eigenvectors \mathbf{z}_j , representing oscillation mode shapes.

2.6.1.2 Complex Eigenvalue Extraction

The damped natural frequencies of the system can be computed by solving the eigenvalue problem

$$(\mu^2 \mathbf{M} + \mu \mathbf{C} + \mathbf{K}) \phi_R = 0, \quad (2.56)$$

of the mechanical system. The above eigenvalue problem is solved by ABAQUS by a subspace projection method. The system matrices are projected onto the subspace of un-damped eigenvectors obtained from Eq. (2.55). The damped natural frequencies and damping ratio[§] can be computed from the k-th eigenvalue by

$$\omega_{d,k} = \text{Im } \mu_k, \quad (2.57)$$

$$\zeta_k = -\frac{\text{Re } \mu_k}{\sqrt{\text{Re } \mu_k^2 + \text{Im } \mu_k^2}}. \quad (2.58)$$

The natural frequencies of the un-damped system are related to the natural frequencies of the damped system by $\omega_{d,k} = \omega_{n,k} \sqrt{1 - \zeta_k^2}$, hence the un-damped natural frequency can be directly obtained from the k-th eigenvalue of the damped system by

$$\omega_{n,k} = \sqrt{\text{Re } \mu_k^2 + \text{Im } \mu_k^2}. \quad (2.59)$$

[§]The damping ratio reported by ABAQUS is defined differently: $\text{DAMP RATIO} = -2 \frac{\text{Re } \mu}{\text{Im } \mu}$.

Because the mass and damping matrix in Eq. (2.56) are frequency dependent, an iterative procedure must be used to solve the eigenvalue problem: The system matrices are evaluated for a starting frequency and the eigenvalues are computed. The damped natural frequency of the k -th mode is used as a new starting frequency and the eigenvalue problem is solved again. This is done until convergence is obtained. The procedure needs to be applied to every mode separately.

2.6.2 Steady State Solution of the Equations of Motion

For harmonic forcing the right hand side of the equations of motion (2.53) can be written in the form

$$f_k(t) = f_k \cos(\phi_k + \omega t) = \text{Re} \left\{ \hat{f}_k e^{i\omega t} \right\}, \quad (2.60)$$

where \hat{f}_k is a complex valued quantity describing amplitude and phase of the oscillatory force by its absolute value and argument, respectively. Commonly, it is implicitly assumed that the actual time signal only consists of the real part of the complex valued expression $\hat{f}_k e^{i\omega t}$. Adopting this convention, the forcing vector is written as

$$\mathbf{f}(t) = \hat{\mathbf{f}} e^{i\omega t}, \quad (2.61)$$

where the complex valued components of the amplitude vector $\hat{\mathbf{f}} = [\hat{f}_1, \dots, \hat{f}_n]^T$ represent the magnitude and phase of the harmonic forces acting on the n DoFs of the model. Inserting a harmonic Ansatz, like Eq. (2.54), into the differential equation (2.53) yields

$$(-\omega^2 \mathbf{M} + i\omega \mathbf{D} + \mathbf{K}) \hat{\mathbf{x}} = \hat{\mathbf{f}}, \quad (2.62)$$

which can be solved for the steady state response $\hat{\mathbf{x}}$ by inversion of the system matrix.

The eigenvectors of the free oscillation eigenvalue problem (2.55), i.e. the oscillation modes, can be used to express the displacement vector as

$$\mathbf{x} = \sum_{j=1}^n q_j \mathbf{z}_j, \quad (2.63)$$

where n is the number of degrees of freedom of the system and q are the modal coordinates. The above relation can be written in matrix notation as

$$\mathbf{x} = \mathbf{Z} \mathbf{q}, \quad (2.64)$$

which represents a change of coordinate basis from natural coordinates \mathbf{x} to modal coordinates \mathbf{q} . The columns of the transformation matrix \mathbf{Z} contain the eigenvectors \mathbf{z}_j . Inserting the transformation relation into (2.53) and pre-multiplying by \mathbf{Z}^T leads to

$$\underbrace{\mathbf{Z}^T \mathbf{M} \mathbf{Z}}_{\mathbf{M}_m} \ddot{\mathbf{q}} + \underbrace{\mathbf{Z}^T \mathbf{D} \mathbf{Z}}_{\mathbf{D}_m} \dot{\mathbf{q}} + \underbrace{\mathbf{Z}^T \mathbf{K} \mathbf{Z}}_{\mathbf{K}_m} \mathbf{q} = \mathbf{Z}^T \mathbf{f}(t), \quad (2.65)$$

which can be solved equivalently to (2.53) to obtain the steady state solution. The modal mass matrix, \mathbf{M}_m , and the modal stiffness matrix, \mathbf{K}_m , are diagonal. Additional damping, not modelled by the dashpot elements, may be taken into account by adding

to the diagonal terms of the modal damping matrix. The modal damping matrix, \mathbf{D}_m , will not be diagonal except, if proportional damping is assumed. Its diagonal terms $2\omega_j\zeta_j$ are then defined by the modal damping factors ζ_j . The modal damping factors can be determined experimentally, for example by the Ibrahim Time Domain Method [29]. Therefore, experiments can be used to check the validity of the damping matrix resulting from the dashpot elements, and if necessary to correct it in a reasonable way.

Due to the frequency dependence of the forcing, the added mass and the hydrodynamic damping, forcing vector, mass and damping matrix must be computed for each frequency. For each wave frequency one inversion of the system matrix is necessary to obtain the steady state response.

The equations of motion formulated in the modal degrees of freedom (2.65) can be solved equivalently as described above for (2.53). For the case of rigid plate model, the EoMs are solved in terms of modal coordinates. It should be noted, that the modal basis can either be selected based on the free floating modes calculated with the mass matrix corresponding to $\omega = 0$, or based on the mass matrix corresponding to the wave frequency. In the latter approach complex modes may arise due to negative added masses. Both methods were compared for the rigid plate model in an example case which showed no significant difference, as can be seen in Fig. 2.21.

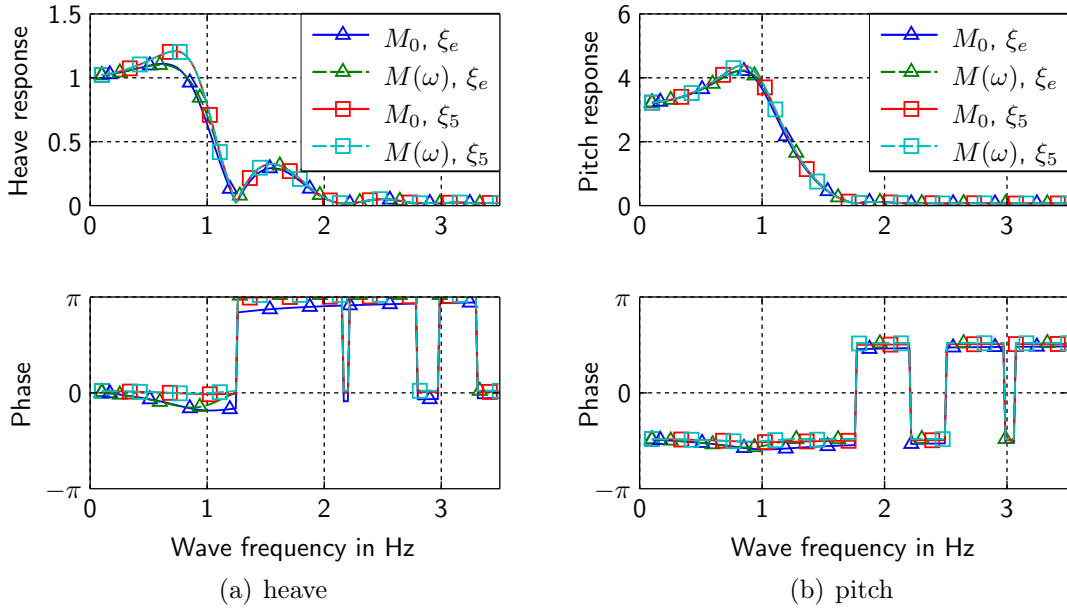


Figure 2.21: Comparison of the computed response for different formulations of the modal basis and different damping values.

2.6.3 Transfer Functions

For a linear, time invariant system under harmonic forcing the Laplace variable can be reduced to $i\omega$. Solving the EoMs by Laplace transformation is then equivalent to the use of a harmonic Ansatz. The transfer function is obtained by dividing the complex values output, i.e. the displacement vector, by the complex valued input, i.e. the complex

representation of the reference wave. The reference wave with unit amplitude is evaluated at the position $[0, 0]^T$. Inserting into Eq. (2.8) and using a harmonic Ansatz (2.54) shows that the complex representation is unity. Hence, the complex valued transfer function is equal to the computed response for a reference wave with unit amplitude.

Commonly the complex valued transfer function is displayed in form of the so called gain, i.e. the absolute value of the transfer function, and the phase shift, i.e. the argument of the complex value. Both quantities are displayed in dependence of the excitation frequency. In marine engineering the gain is commonly called response amplitude operator (RAO) [3, 9].

2.6.4 Chamber Pressure

The pressure oscillations in the air chambers during steady state operation is represented by the spring force in the dynamic model. For the model of the deformable plate the spring forces can be output directly by *ABAQUS*. In the case of the semi-analytical, rigid plate model, it can be calculated from the spring elongation prescribed by the model DoFs by

$$\Delta p_{c,i}(t) = \Delta \hat{p}_{c,i} e^{i\omega t} = \underbrace{\frac{k_{c,i}}{r_i^2 \pi} (\hat{z} + p_{y,i} \hat{r}_x - p_{x,i} \hat{r}_y - \hat{z}_i)}_{\Delta \hat{p}_c} e^{i\omega t}, \quad (2.66)$$

where \hat{z} , \hat{r}_x , \hat{r}_y , and \hat{z}_i are the complex valued steady state response amplitudes for a wave with unit amplitude. For waves with different amplitudes the pressure can be linearly scaled.

The amplitude of the pressure oscillation $|\Delta \hat{p}_c|$ must be smaller than the static pressure in the chamber for all relevant wave conditions. If the pressure oscillations were larger than the static pressure in the chamber, the circumferential tension stress state in the membrane would be lost. Compression stresses in the very thin membrane would immediately lead to wrinkling.

2.6.5 Axial Tension in the Cylindrical Membrane

To prevent instabilities of the skirt deformation states, i.e. buckling or wrinkling, the cylindrical membrane must remain in tension in all space directions at all times. To simplify the analysis, friction forces will not be considered. Considering the rather low viscosity of water this simplifying assumption seems to be justified. A sketch of the considered system is shown in Fig. 2.22. The equation of motion for a segment of length $r d\varphi$ of the ballast ring reads

$$(dm_b + dm_a) \ddot{u}_b = -dm_b \left(1 - \frac{\rho_w}{\rho_b} \right) g + F_m, \quad (2.67)$$

where dm_b is the mass of the ring segment, dm_a is the hydrodynamic added mass associated with the ring segment, ρ_b is the mass density of the ballast material and F_m is the axial tension force in the membrane per circumferential length unit. The added mass of

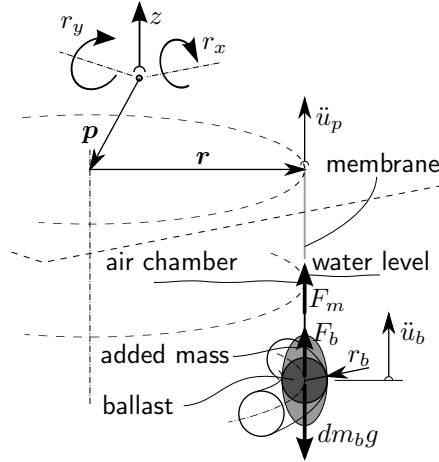


Figure 2.22: Acceleration of the plate and added mass of the ballast.

the ring segment is assumed constant and calculated by

$$dm_a = \rho_w \underbrace{\frac{m_b}{\rho_b 2r\pi^2}}_{r_b^2} \pi dl, \quad (2.68)$$

where $dl = r d\varphi$ is the length of the ring segment.

If, for the moment, the membrane is assumed as axially rigid (for the sake of simplicity), it follows that the membrane remains in axial tension if the downwards acceleration of any point at the upper limit of the skirt (at the plate) is smaller than the maximum downwards acceleration the ballast mass could reach, if it were free ($F_m = 0$). An axially rigid membrane requires the vertical plate accelerations and the vertical accelerations of the ballast mass to be equal ($\ddot{u}_p = \ddot{u}_b$). For the membrane to remain under axial tension $F_m > 0$ must hold. Inserting those requirements into Eq. (2.67) yields the maximum allowed plate acceleration for the membrane to remain in axial tension as

$$\ddot{u}_{p,max} = \frac{dm_b}{dm_b + dm_a} \left(1 - \frac{\rho_w}{\rho_b}\right) g = \frac{\rho_b - \rho_w}{\rho_w + \rho_b} g, \quad (2.69)$$

where Eq. (2.68) has been used to obtain the final expression. It can be seen that higher mass density of the ballast material increases the maximum allowable acceleration. The theoretical limit for infinite density is the gravitational acceleration.

For the semi-analytical, rigid-plate model the acceleration of the plate in vertical direction at the intersection with the skirt can be computed for the solution of the equations of motion, Eq. (2.53). It is determined by

$$\ddot{u}_p = [\hat{z} + (p_y + r \sin \varphi) \hat{r}_x - (p_x + r \cos \varphi) \hat{r}_y] \omega^2 e^{i\omega t}, \quad (2.70)$$

where φ is an angle between 0 and 2π . The acceleration must be computed for all chambers, and a sufficient number of angular positions φ . In the case of the FE model of the deformable plate the accelerations can be output directly by the FE code or simply computed from the displacements by

$$\ddot{u}(t) = \frac{d^2}{dt^2} \hat{u} e^{i\omega t} = \underbrace{-\omega^2 \hat{u}}_{\hat{a}} e^{i\omega t}. \quad (2.71)$$

2.7 Model Validation

In order to validate the developed computational model comparison with experimental results is necessary. All comparisons are obtained with computational models directly prescribing the experimental model. Therefore, scaling effects do not impact the validation. Two different models, a small 1x1 m model and a larger 4x4 m model, were built and tested. The conducted experiments are described in more detail in Chapter 5 with details about the models in Section 5.2.

Additionally to comparisons with experiments the impact of different input parameters for the computational model, like modal damping, plate stiffness, etc., on the results are discussed in the following.

2.7.1 Impact of Input Parameters

2.7.1.1 Added Mass Formulation

In Section 2.4 formulations for the hydrodynamic added mass were developed. Expressions for two different cases were give. In the first case, the internal free surface was modelled as free, which leads to infinite added mass and damping coefficients at the natural frequencies of the free surface. If the hydrodynamic coefficients are obtained from a model where the free surface is treated like a rigid disk, these natural frequencies do not arise. Figure 2.23 shows the computed rigid body response for the two different added mass formulations. The response amplitude only shows minor differences, i.e. it has additional zeros at the natural frequencies of the internal free surface for the respective added mass formulation. The location of the zeros can be found more easily by looking for jumps in the phase.

2.7.1.2 Additional Modal Damping

The dashpot elements modelling the hydrodynamic reaction forces are the only source of damping in the system. However, they only account for radiation damping arising if the free surface in the chambers is displaced. The dashpot elements alone lead to modal damping factors of about 0.25, which is lower than experimentally obtained values, especially for the heave mode. Additional sources of damping, like viscous effects or damping in the air chambers, is accounted for by introducing an additional modal damping. Figure 2.24 shows the impact of additional modal damping on the rigid body response in head waves. It can be seen, that with modal damping values of about 0.2 the measured response is matched very well.

2.7.1.3 Rigid Plate Assumption

The rigid plate assumption can be used with good accuracy even for flexible plates as long as the deformations remain small. This will be the case if not more than two chambers are in line with respect to the wave direction, as for example for a four-chamber arrangement under 0° wave heading. For this loading scenarios all chambers maintain a positive pressure, counteracting the gravity forcing on the plate. Figure 2.25 shows a comparison of the computed transfer functions for the rigid body response of the small model in head waves (0° heading). No significant difference can be seen between rigid and deformable

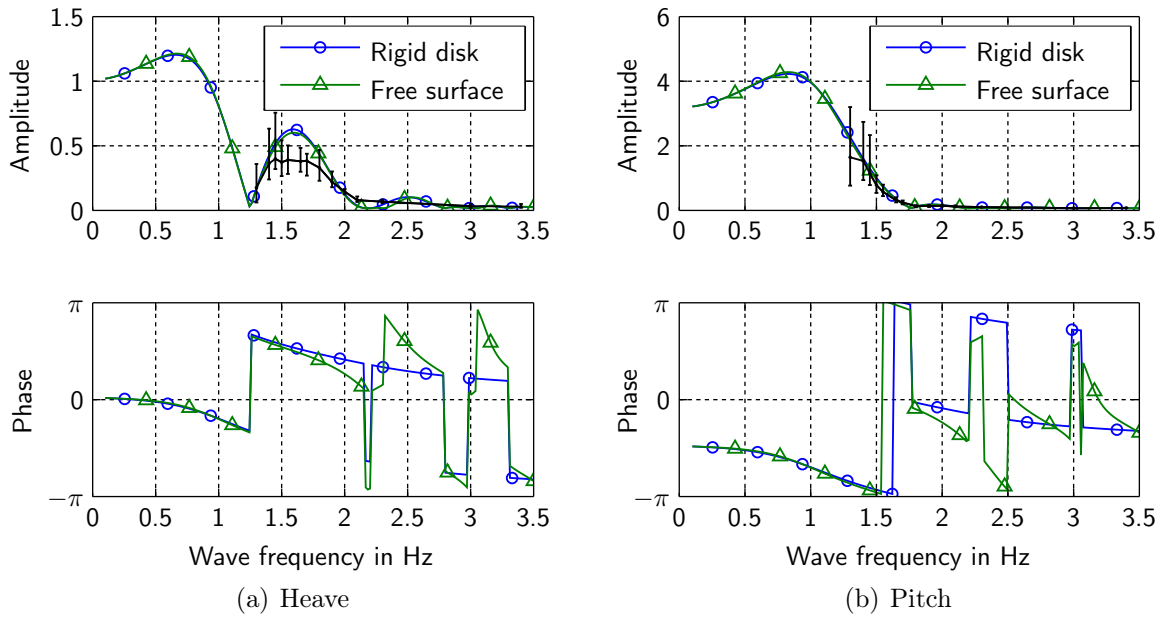


Figure 2.23: Comparison of the different added mass formulations for a simulation of the small experimental platform. An additional modal damping of 10% was assumed. Experimental results are shown in black with errorbars representing the 95% confidence intervals computed from all measurement runs.

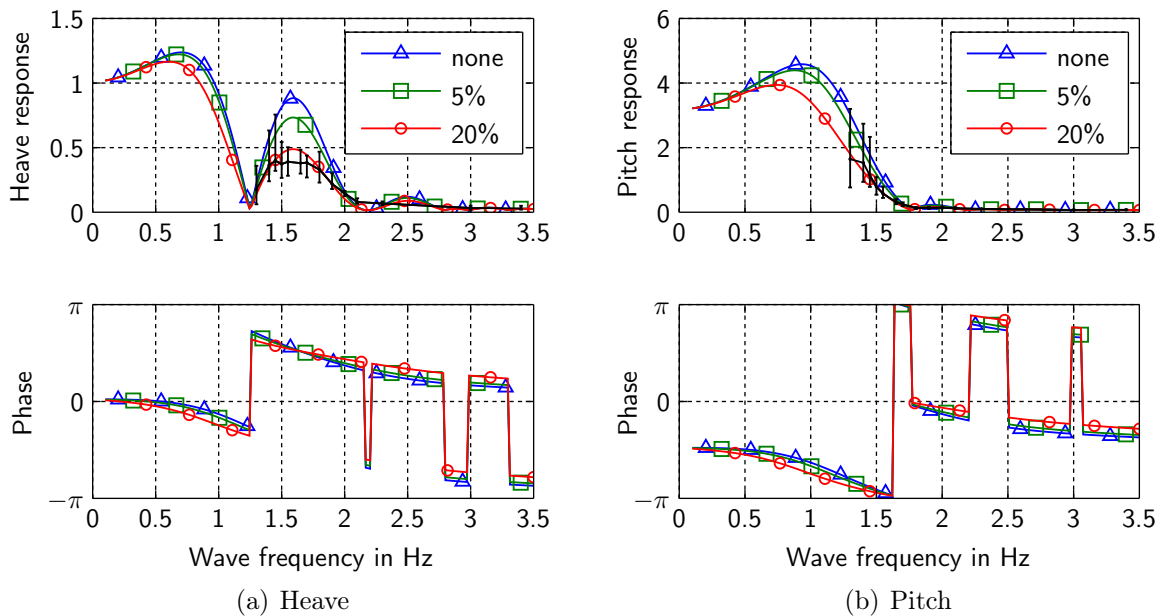


Figure 2.24: Comparison of the different additional modal damping values for the small model. The added mass formulation for rigid internal surface and infinitely flexible membrane was used. Experimental results are shown in black with error bars representing the 95% confidence intervals computed from all measurement runs.

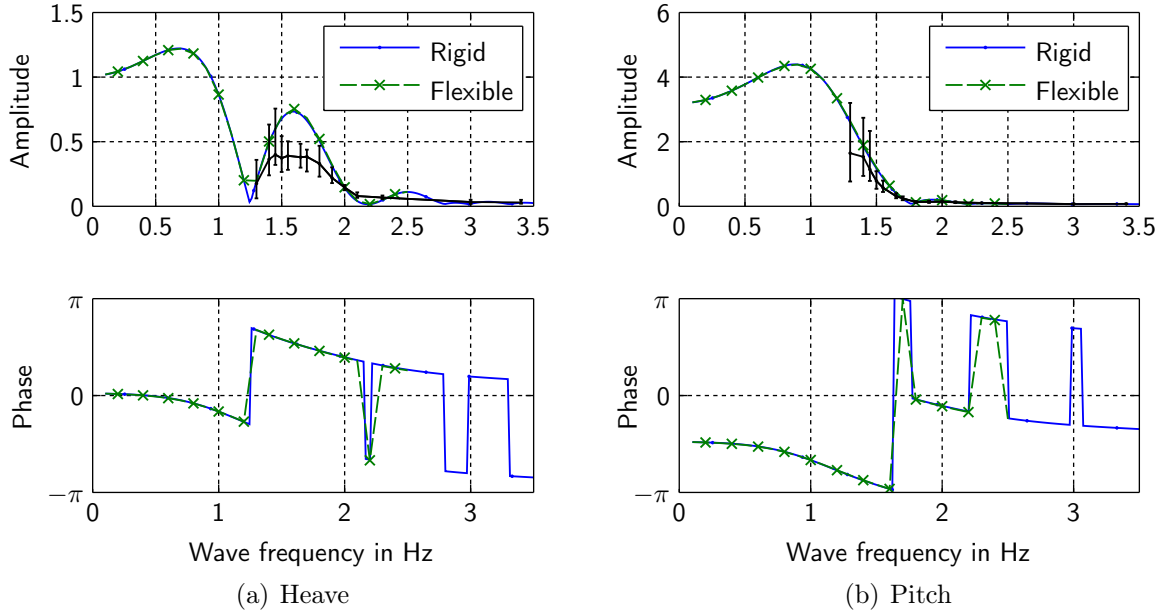


Figure 2.25: Comparison of results obtained for a rigid plate and for a flexible plate for the small model. Experimental results are shown in black with errorbars representing the 95% confidence intervals computed from all measurement runs.

plate model. However, for an arrangement with more than two chambers in line with respect to the wave direction, the wave forcing can lead to severe bending moments on the plate. If the plate is stiff enough to justify the assumption of a rigid plate, the dynamic pressure oscillation amplitudes in the chambers are likely to exceed the static pressure, and hence lead to a loss of the internal overpressure. If this is the case the modelling of the air chambers by linear springs is not valid any more. For flexible chambers negative internal pressure would lead to wrinkling of the membrane. Therefore, in reality negative pressures in the chambers cannot arise. The plate should be modelled as flexible, especially for lightweight structures, for arrangements with more than three chambers. If a rigid plate model is used, the computed amplitudes of the dynamic pressure oscillations must be compared against the static pressure to ensure the validity of the linear model.

2.7.2 Natural Frequencies, Oscillation Modes and Damping Parameters

The Ibrahim time domain (ITD) method allows the measurement of natural frequencies, mode shapes and modal damping parameters without the measurement of the excitation [16]. It is described in more detail in Section 5.4, and was applied to the small experimental model. The extracted mode shapes are displayed in Fig. 2.27, and the corresponding natural frequencies and damping parameters can be found in Table 2.6. An equivalent computational model was used to calculate the complex eigenvalues of the coupled system. The computed mode shapes are displayed in Fig. 2.28, and Table 2.7 contains the corresponding eigenvalues.

Generally good agreement between experiments and computations could be obtained.

However, the computed natural frequencies differ by 20 to 30% for the modes dominated by the added mass, i.e. the pitch/roll, heave and first bending mode. On the other hand, the natural frequency of the second bending mode agrees very well with experimental data. The computed damping ratios agree reasonably well with the experimentally determined ones. They pass the t-test with a significance level of 1%. The boxplots in Fig. 2.26 show a comparison between computed and experimentally determined natural frequencies and damping ratios.

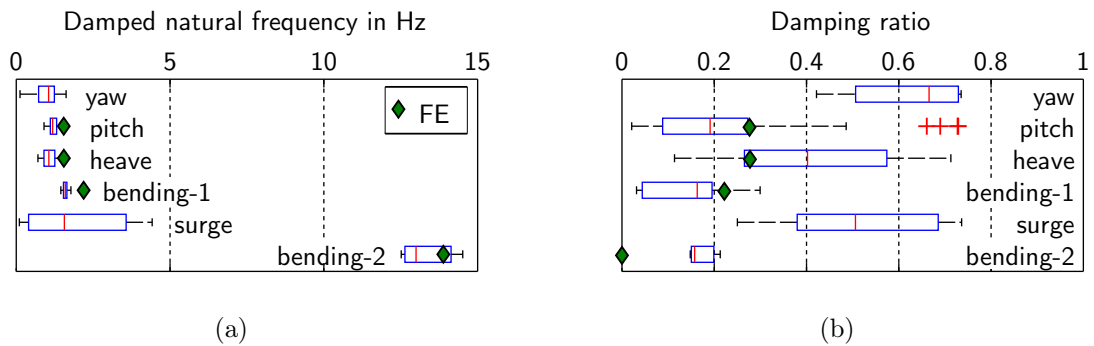


Figure 2.26: Comparison of experimentally identified and computed modes in terms of damped natural frequencies (a) and damping ratios (b). The experimental results are shown as boxplots.

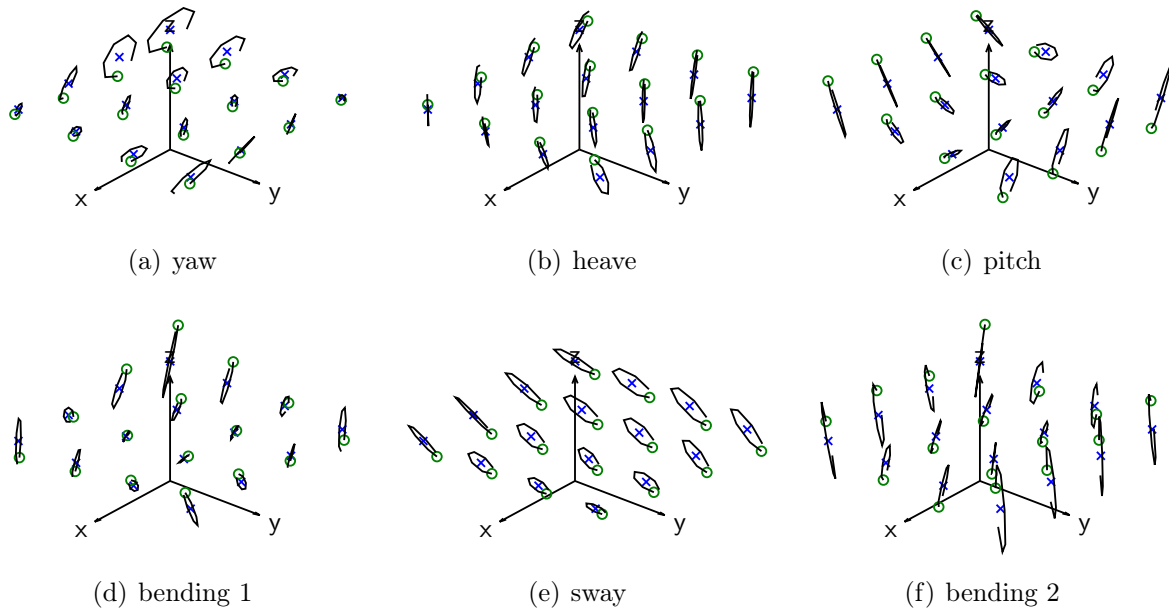


Figure 2.27: Experimentally determined modes of the small experimental model; The mode shapes were obtained by averaging all identified modes.

Mode	$\text{Re } \mu$	$\text{Im } \mu$	f_n in Hz	ζ	N
yaw	-4.55 (± 2.11)	6.09 (± 3.19)	1.23 (± 0.57)	0.62 (± 0.13)	6
pitch/roll	-1.97 (± 2.22)	7.55 (± 0.89)	1.28 (± 0.22)	0.23 (± 0.20)	35
heave	-3.17 (± 1.56)	6.91 (± 1.49)	1.23 (± 0.24)	0.40 (± 0.18)	16
bending-1	-1.48 (± 1.00)	10.04 (± 0.63)	1.62 (± 0.11)	0.14 (± 0.10)	8
surge	-6.59 (± 4.97)	12.00 (± 9.48)	2.21 (± 1.67)	0.51 (± 0.16)	26
bending-2	-14.89 (± 4.37)	83.84 (± 6.56)	13.56 (± 1.15)	0.17 (± 0.04)	3

Table 2.6: Mean eigenvalues of the identified modes of the small experimental model as well as derived parameters (un-damped natural frequency and damping ratio). The values in parentheses are the standard deviation of the N identified eigenvalues.

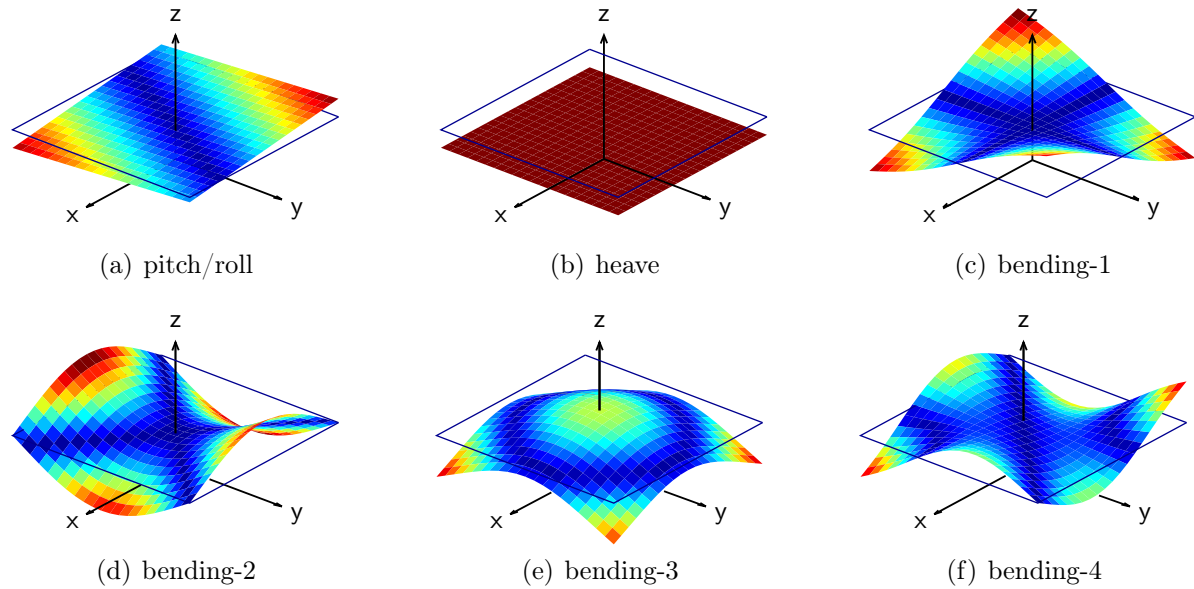


Figure 2.28: Mode shapes for the small model computed by ABAQUS. The corresponding natural frequencies and damping factors can be found in Table 2.7.

Mode	$\text{Re } \mu$	$\text{Im } \mu$	f_n in Hz	ζ
pitch/roll	-2.7888	9.6965	1.6058	0.2764
heave	-2.8070	9.7228	1.6106	0.2774
bending-1	-3.1316	13.7650	2.2468	0.2218
bending-2	0.0	87.2424	13.8851	0.0
bending-3	0.0	107.9324	17.1780	0.0
bending-4	0.0	155.0185	24.6720	0.0

Table 2.7: Eigenvalues of the small model computed iteratively by ABAQUS. Corresponding mode shapes are displayed in Fig. 2.28.

2.7.3 Transfer Functions

2.7.3.1 Rigid Body Response

The computed and experimentally determined rigid body response for heave, pitch and roll are compared in Figs. 2.29, 2.30 and 2.31, respectively. The computed heave response matches the measured one, both in amplitude and phase, very well. Comparing the measured rotational responses with computation results show an overestimation of the response. The predicted response amplitudes are generally too low. The predicted phase shift on the other hand again matches well. When comparing the phase shift it should be taken into account that a difference of 2π between two values makes them appear far apart in the graph, but actually means equal phase shift.

2.7.3.2 Pressure Response

The computed dynamic pressure oscillations in the chambers in response to wave forcing is compared to experimentally measured values in Fig. 2.32. Generally the computational model overestimates the pressure response. The pressure amplitudes are minimal for wave headings of 0° and maximal for wave headings of 45° . The difference in amplitude is almost one order of magnitude. This somewhat puts the excellent agreement between computation and experiments for the 0° case into perspective: In the experiment exact placement of the platform at 0° heading is not possible, which leads to higher measured pressures. The computed response amplitudes are qualitatively in good agreement with the experimental results, both zeros and maxima are at the correct locations. The phase response of all measured transfer functions agree reasonably well with the numerical simulations.

2.7.3.3 Deformation Response

Figure 2.33 shows a comparison of the computed and experimentally determined modal deformation response. Again very good qualitative agreement is achieved, especially in the amplitude response. The magnitude of the response amplitude is slightly overestimated by the computational model in the case of a wave heading of 45° . For this wave direction the dominating deformation is represented by the first plate twist mode. In the analysis of the experimental results also magnitudes of higher twist modes arise. As they are almost in phase the amplitudes may be added to obtain the total amplitude. For the case of 0° wave direction (see Fig. 2.33a) the response is dominated by the bending mode. Due to inexact placement of the model in the tank, also twist deformations are measured experimentally. Therefore, the measured deformations are higher.

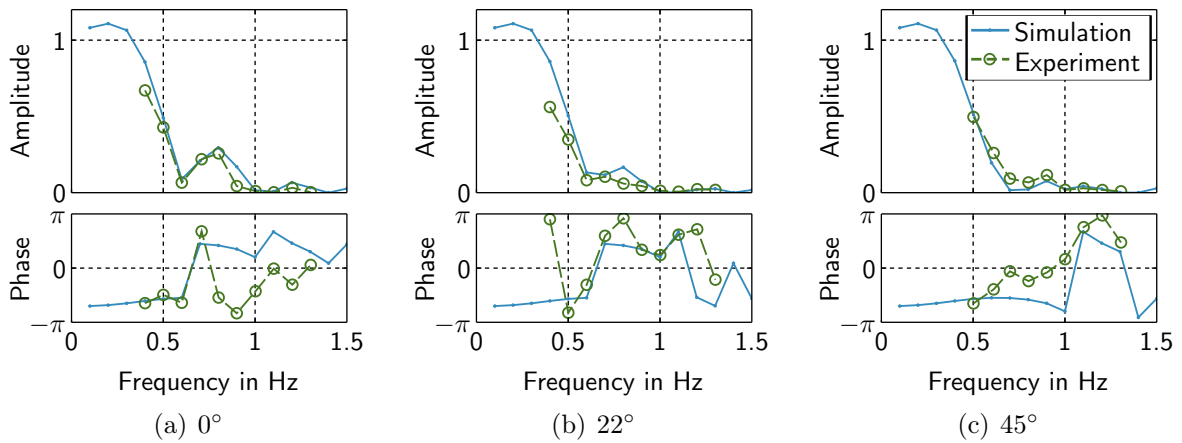


Figure 2.29: Normalised heave response of the large model for different wave headings.

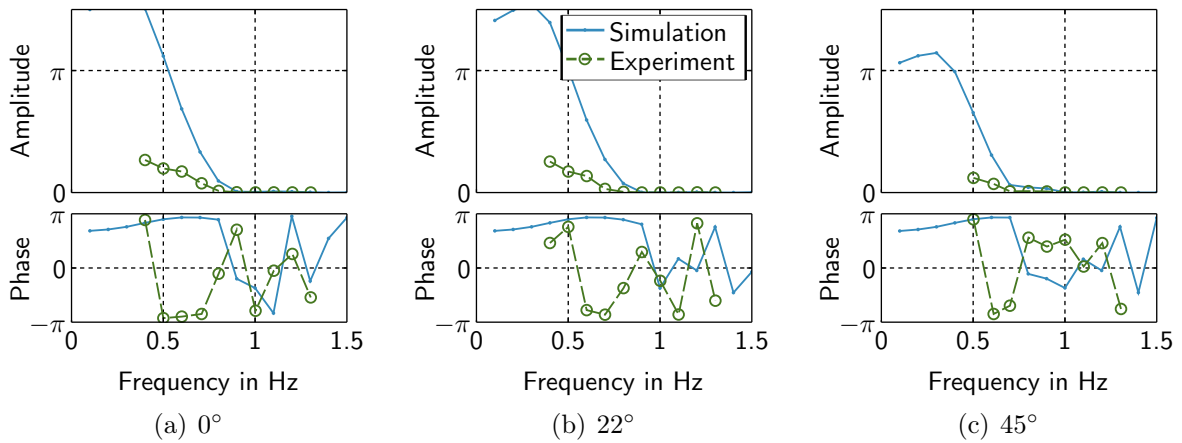


Figure 2.30: Normalised pitch response of the large model for different wave headings.

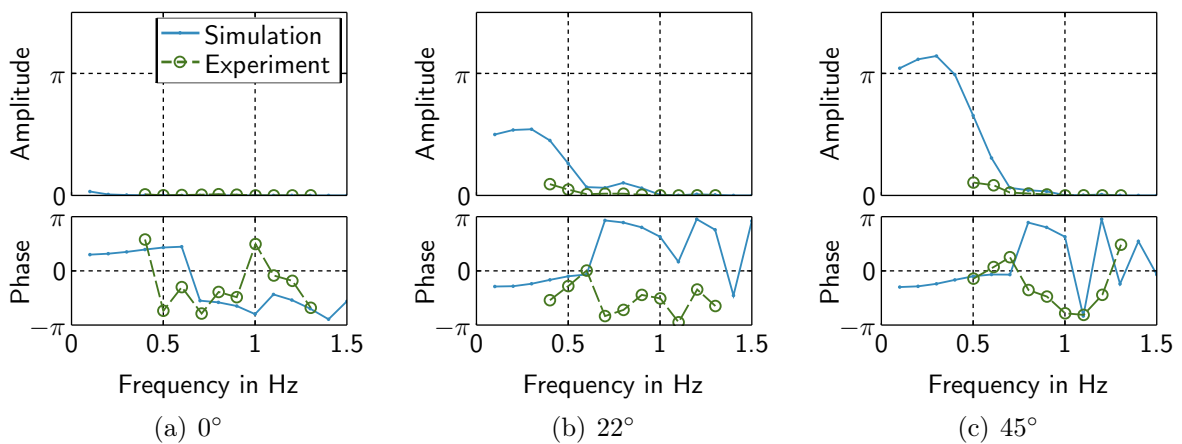


Figure 2.31: Normalised roll response of the large model for different wave headings.

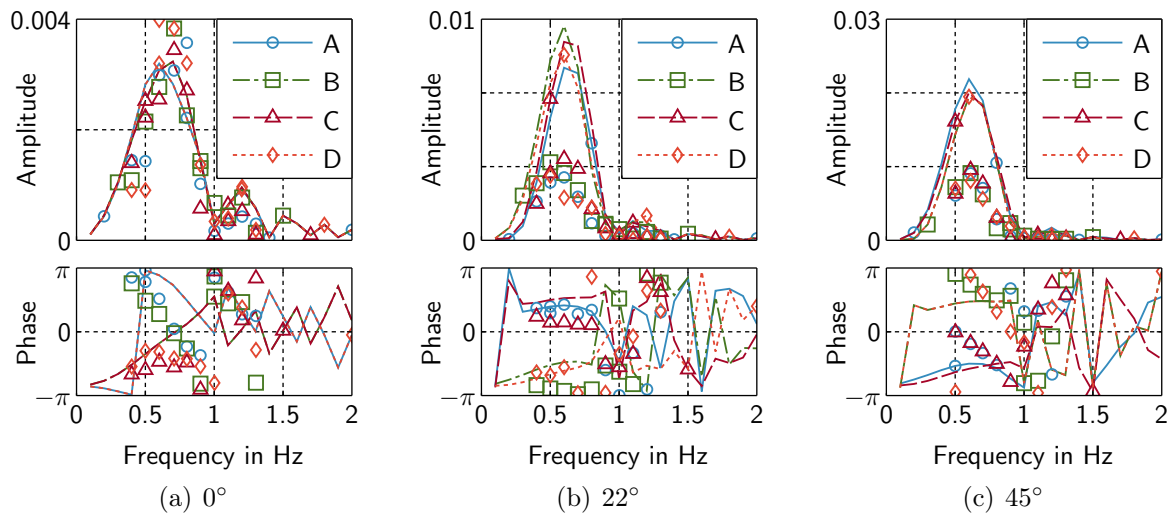


Figure 2.32: Normalised pressure response in the four chambers (A,B,C,D) of the large model for different wave headings. Experimentally obtained values are shown by markers.

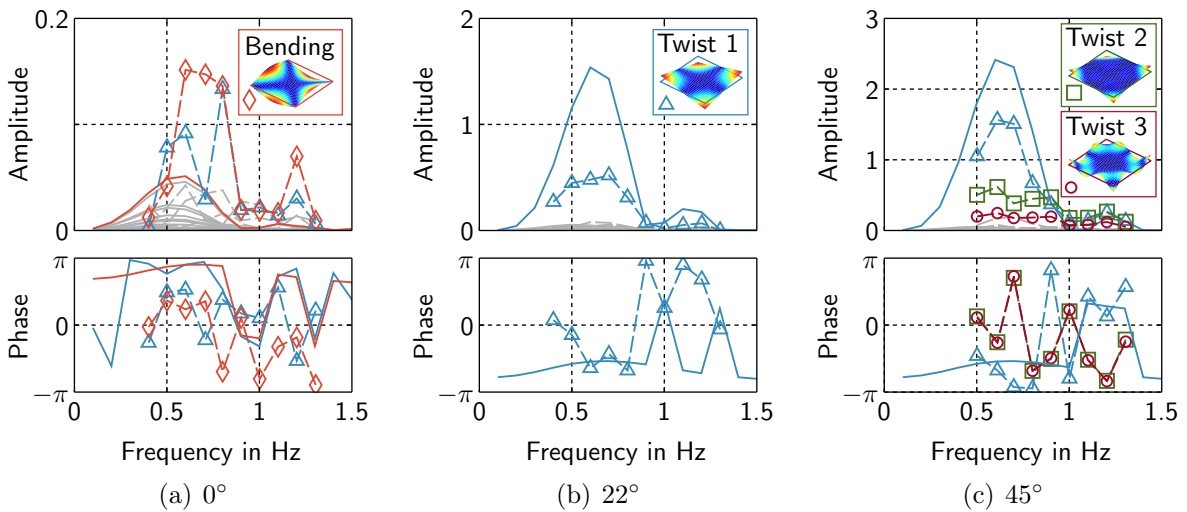


Figure 2.33: Normalised modal deformation response of the large model for different wave headings. Simulation results are displayed as solid lines and measurements as dashed lines with markers. Corresponding modes are shown in the same color.

2.8 Conclusion

Since the proposed modelling strategy is based on carefully performed simplifications, the amount of input parameters is minimal, and results can be obtained rapidly. It has been shown that the model is able to predict the natural frequencies of an air cushion supported floating platform reasonably well. The model can also accurately predict the heave and pitch response of such a floating platform. Especially the extrema in the heave response are located at the correct frequencies by the calculation model. This leads to the conclusion that the computed vertical forcing is correct in terms of the dependence of the force amplitude on the ratio between chamber size and wave length. The position of minima in the pitch response depends on the chamber locations with respect to each other, and will be correct if the dispersion relation holds. The pressure oscillations in the chambers and the plate deformations can be predicted with reasonable accuracy. For all predicted response quantities excellent qualitative agreement with measurement results was obtained.

The main aim of the model is to calculate response amplitude operators that can be used in the efficiency estimation of a concentrator system for a solar power plant. For such a system the pitch/roll response of the platform is the main influence factor. The sway motion also has an effect on the positioning accuracy of the mirrors and, therefore, on the optical efficiency. It is not incorporated in the current model, however extensions based on the current modelling strategy seem possible. Response amplitude operators can be computed for arbitrary wave directions, which make a precise efficiency calculation for the concentrator system based on wave directional wave spectra possible.

Chapter 3

Static Stability of a Single Air Chamber

Considering a single air chamber, the internal pressure is a function of the vertically applied load. Due to the opening on the bottom of the air chamber the water level inside is lower than outside. The vertical load on the platform can be increased up to a certain level, at which the air chamber shows a global instability. The instability commences with the formation of wrinkles at the upper support and finally results in a global buckling of the air chamber, as depicted in Fig. 3.1. As the buckled configuration has lost all its load carrying capacity such an instability could lead to the failure of an air chamber supported floating platform. In the following this instability will be investigated theoretically as well as experimentally.

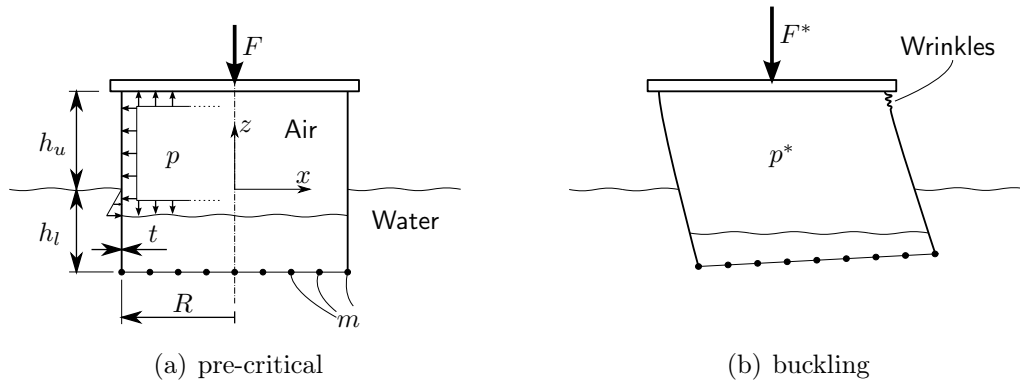


Figure 3.1: Sketch of a single air chamber in a pre-critical (a) and post-critical (b) configuration.

3.1 Description of the Mechanical System

A thin flexible material is used to form a cylindrical air chamber. The flexible cylinder, subsequently called *skirt*, is attached to a stiff plate at its upper end. The lower end of the skirt is ballasted by weights and submerged in water. Thereby an air chamber is formed. If the plate is translated downwards, the air in the chamber is compressed and the water level inside the chamber changes to a value corresponding to the hydrostatic pressure, while the outer water level remains the same. The skirt above the external water

line is now in a state of constant internal pressure. The internal pressure at the external water line linearly decreases with the depth to a value of zero at the internal water line. Here the free water surface requires an equilibrium between air pressure in the chamber and hydrostatic pressure in the fluid. The acting forces on the membrane are depicted in Fig. 3.1a.

Instead of translating the top plate to increase the pressure, the same configuration could be obtained by regulating the amount of air in the chamber. In fact, for the investigated configuration, the stiffness of the water plane ($\rho_w g$) is much smaller than the axial stiffness of the air in the chamber (p_0/h_u). This means, that the compressibility of the air in the chamber can be neglected.

The stress state in the skirt will be dominated by the internal overpressure in the air chamber, creating tensile stresses in circumferential direction. The magnitude of the circumferential tensile stress depends on the internal pressure, the membrane thickness and the radius of the chamber. The difference to a conventional pressure vessel is the stress in axial direction. The air chamber is bounded by the free water surface at the bottom. Therefore, no axial stresses are introduced into the membrane due to internal pressure. The constant axial stress acting in the membrane is caused by the weights at the bottom of the skirt.

The constrained deformations at the top of the skirt will cause a disturbance in the otherwise uniform stress field on the membrane. This local disturbance decays with increasing distance from the clamped boundary.

3.2 Simulation Model

3.2.1 Modelling Assumptions

The aim of the current study is to find the static stability limit of the skirt structure loaded by internal pressure. Therefore, the mechanical problem is treated as a static problem. Dynamic phenomena, as observed in the experiments after the stability limit was exceeded, were not taken into account.

For the skirt material, high density polyethylene, linear elastic material behaviour with a Young's modulus of 1.0 GPa, a Poisson's ratio of 0.45, and a density of 950 kg/m³ is assumed. The water has a very similar density of 998.2 kg/m³ at room temperature [14].

The compressibility of the air in the chamber is not taken into account. This is possible because the stiffness of the water plane is much lower than the axial stiffness of the air chamber. Therefore, the air in the chamber is modelled by an internal pressure distribution. The internal pressure is increased in a static non-linear incremental iterative analysis. It is modelled as a position dependent follower force onto the shell elements. The pressure value is dependent on the vertical coordinate z and the artificial time t by

$$p(z, t) = \begin{cases} k_p t, & \text{if } z \geq 0 \\ k_p t + \rho_w g z, & \text{if } -\frac{k_p t}{\rho_w g} < z < 0, \\ 0, & \text{otherwise} \end{cases} \quad (3.1)$$

where k_p is a factor suitably chosen to linearly relate the artificial time to a pressure value. The above relation can be implemented in the finite element code as an space and

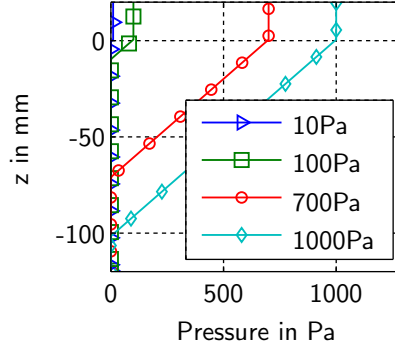


Figure 3.2: Pressure on the membrane depending on the vertical coordinate for different internal pressure levels.

time dependent pressure force. The used pressure function from Eq. (3.1) is depicted in Fig. 3.2.

Although the mass of the skirt is very small compared to the mass of the additional weights, gravity is modelled as a mass dependent nodal force for all skirt nodes in the negative z -direction. The buoyancy of completely submerged skirt parts is neglected because of the small density difference between skirt material and water.

The additional weights are modelled as nodal forces acting in the negative z -direction at nodes located at the original water line. This is necessary because convergence problems arise if the vertical force is introduced at the end of the skirt in case of a initial plate axis inclined with respect to the horizontal direction. This can be explained by local instabilities in the skirt caused by compressive stresses in the thin shell. For the lead weights the buoyancy forces are taken into account. The nodal force is computed by

$$F_m = \frac{mg}{N_c} \left(1 - \frac{\rho_w}{\rho_m} \right), \quad (3.2)$$

where N_c is the number of nodes around the circumference, m the mass of all weights, and ρ_m their density.

Fig. 3.3 shows a sketch of the finite element model. The upper edge of the skirt is clamped, i.e. all degrees of freedom of nodes located at the upper edge are constrained to zero. All other nodes are left free. The length of the submerged part of the skirt h_l is limited to 70 mm in the FE-model to decrease the number of nodes. This is possible because totally submerged elements are unloaded. Furthermore the stability limit is expected below an internal pressure of 700 Pa, which corresponds to a water level difference of approximately 70 mm.

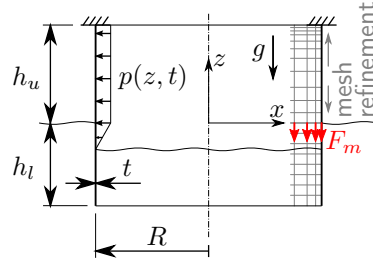


Figure 3.3: Sketch of the finite element model.

3.2.2 Element Type and Mesh Size

The skirt is modelled as thin shell elements with bilinear interpolation function. The shell thickness is $13\ \mu\text{m}$. Membrane elements cannot be used because no equilibrium solution can be found by the solver. This is caused by the sharp change of loading at the water line and by the fact that the skirt is not constrained in axial direction.

In order to find an appropriate mesh size a convergence study was conducted. The model for this convergence study was as perfect circular cylinder with a radius of 196 mm and a height of 209 mm. The upper end was clamped and the cylinder was loaded by internal pressure. Loads due to gravity and the additional weights at the bottom of the skirt were taken into account. A non-linear analysis with incrementally increasing internal pressure was conducted. Shell elements with bilinear interpolation were used. The mesh was refined towards the clamped edge in axial direction of the cylinder. Table 3.1 shows details of the node numbers of investigated meshes.

The unloaded natural frequencies of the structure lightly decrease if the mesh is refined. This can be explained by the more stiff behaviour of large elements compared to small elements. The first five computed natural frequencies for the unloaded configuration for the different meshes are depicted in Fig. 3.4a. The relative error with respect to the finest mesh is depicted in Fig. 3.4b: It is smaller than 0.2% for meshes with more than 80,000 nodes. The computation time increases exponentially with the number of nodes.

	N_c	N_h	total
Mesh 1	160	25	4,000
Mesh 2	200	32	6,400
Mesh 3	360	54	19,440
Mesh 32	720	108	77,760
Mesh 34	1,440	216	311,040
Mesh 4	600	75	45,000
Mesh 5	1080	120	129,600
Mesh 6	1200	154	184,800

Table 3.1: Number of nodes of the investigated meshes. The total number of nodes is the product of the nodes along the circumference, N_c , and the number of axial nodes, N_h .

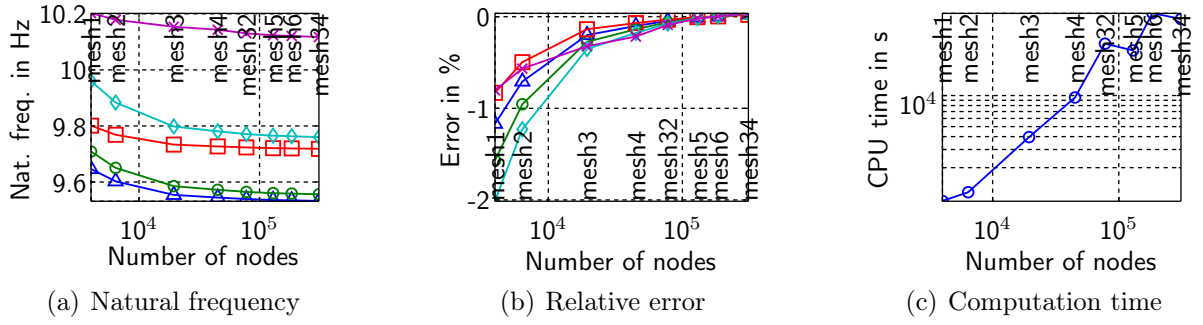


Figure 3.4: Impact of the mesh size: (a) unloaded natural frequencies decrease when refining the mesh; (b) error of the unloaded natural frequencies with respect to the finest mesh; (c) computation time increases exponentially with the number of nodes.

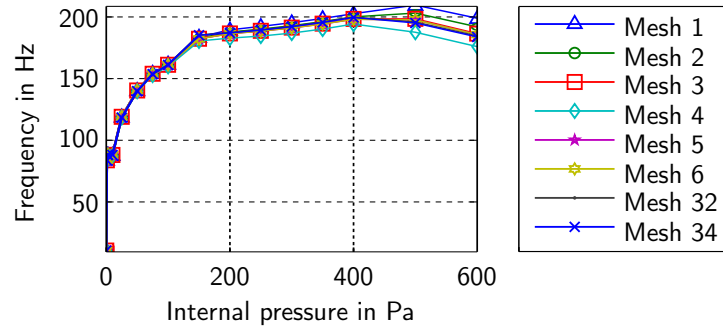


Figure 3.5: Dependence of the lowest natural frequency on the internal pressure for different meshes. The mesh parameters can be found in Table 3.1.

Therefore, the number of nodes should be as low as possible while maintaining sufficient accuracy.

The natural frequencies increase if the structure is loaded by internal pressure. This is shown for the lowest natural frequency for different meshes in Fig. 3.5. The differences between the meshes are increasing with increasing internal pressure. It can also be observed that the natural frequency starts to decrease for internal pressure larger than 400 Pa. This is an indication for an instability.

In the finite element model 720 nodes around the circumference and 181 nodes in axial direction were chosen. This corresponds to *Mesh 32* from Table 3.1. The node spacing in axial direction is constant for elements below $z = 15$ mm.

3.2.3 Imperfections

in order to trigger buckling, i.e. deviation from the trivial equilibrium path, imperfections are introduced. Two types of imperfections, as well as a combination of both, were investigated. The first imperfection is a rotation of the perfect cylinder around the y -axis.

The second imperfection is a deviation from the perfect circular cylinder in the form of a combination of the free oscillation modes. Following Leissa [42], the oscillation mode

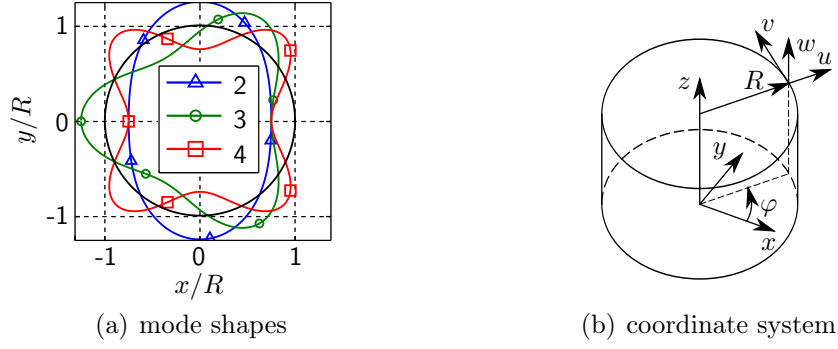


Figure 3.6: Low-frequency mode shapes for thin walled, infinitely long circular cylinders (a) for different values of n ; and coordinate system used to compute the mode shapes (b).

shapes for a thin walled, infinite cylinder are given by

$$u = C \cos(n\varphi) \cos(\omega t), \quad (3.3)$$

$$v = B \sin(n\varphi) \cos(\omega t), \quad (3.4)$$

where u and v are the radial and tangential coordinates of the coordinate system depicted in Fig. 3.6b. The constants B and C for the different modes are obtained by solving

$$\begin{bmatrix} n^2 - \Omega^2 & n \\ n & 1 + \frac{h^2}{12R^2}(1 - n^2)^2 - \Omega^2 \end{bmatrix} \begin{bmatrix} B \\ C \end{bmatrix} = \begin{bmatrix} 0 \\ 0 \end{bmatrix}, \quad \text{for } n = 1, 2, \dots, \quad (3.5)$$

where h is the thickness of the shell. Hence, they are the components of the eigenvector corresponding to the eigenvalue Ω^2 , which is related to the natural frequency ω by

$$\Omega = \frac{\rho(1 - \nu^2)}{E} R^2 \omega^2. \quad (3.6)$$

The mode shapes for the lower frequency modes for $n = 2, 3, 4$ are depicted in Fig. 3.6a.

For the analysis a linear combination of the 2nd and 3rd oscillation mode was used. The combination ratio was kept constant as 5 to 1. The maximum modal displacement was then scaled to different ratios of the radius R . Figure 3.7 shows the shape of the linear combination as well as local radius and curvature.

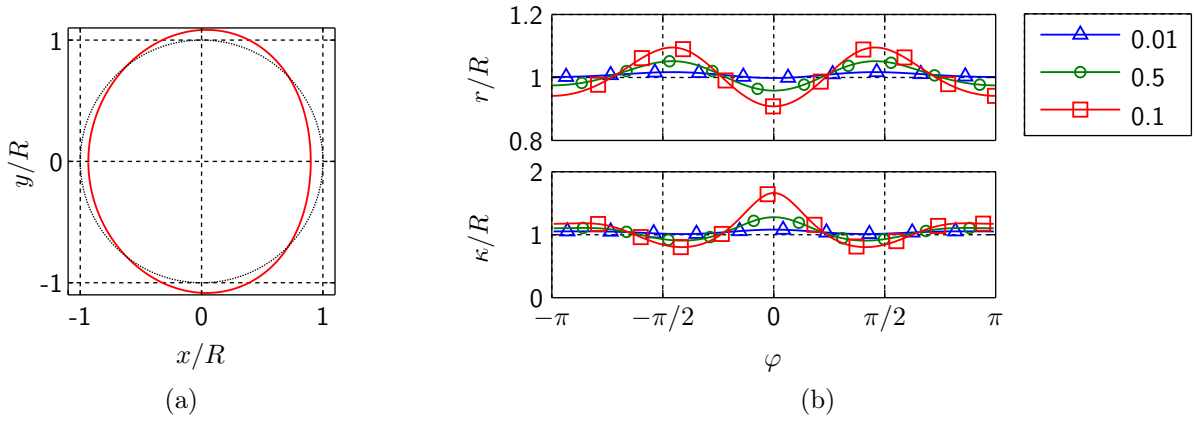


Figure 3.7: Shape of the cross section of the imperfect cylinder: (a) Linear combination of mode 2 and 3 (5:1) scaled to a maximum modal displacement of $0.1R$; (b) Radial coordinate r and local curvature κ of at the cross section points for different scales.

3.2.4 Analysis Procedure

An static analysis in which the pressure was increased in an incremental iterative way. The analysis was conducted up to internal pressure levels of 700 Pa or terminated before of no convergence could be obtained. This is usually the case at the stability limit.

3.3 Experiments

Experimental tests were performed with skirts manufactured from high density polyethylene (PE-HD) bags. The bags had a thickness of $13\mu\text{m}$ and were cylindrical with a diameter of 1216 mm and a height of 225 mm when the bottom was cut off. The upper end of the skirt was fixed onto a conical ring which was glued to a plate to ensure a defined shape of the upper support. The position of the plate with respect to the horizontal plane could be adjusted by three vertical screws. At the lower end of the skirt 16 lead weights were fixed around the circumference. Tests with two different masses (3 g and 6.8 g) were performed. The pressure in the air chamber can be measured by a water column as described in more detail in Appendix C.3. The height of the water level was measured visually on a scale with an accuracy of approximately 0.5 mm. Fig. 3.8 shows an annotated photo of the measurement setup and corresponding dimensions. The air chamber was slowly pressurized trough a valve in the top plate by air from a compressor.

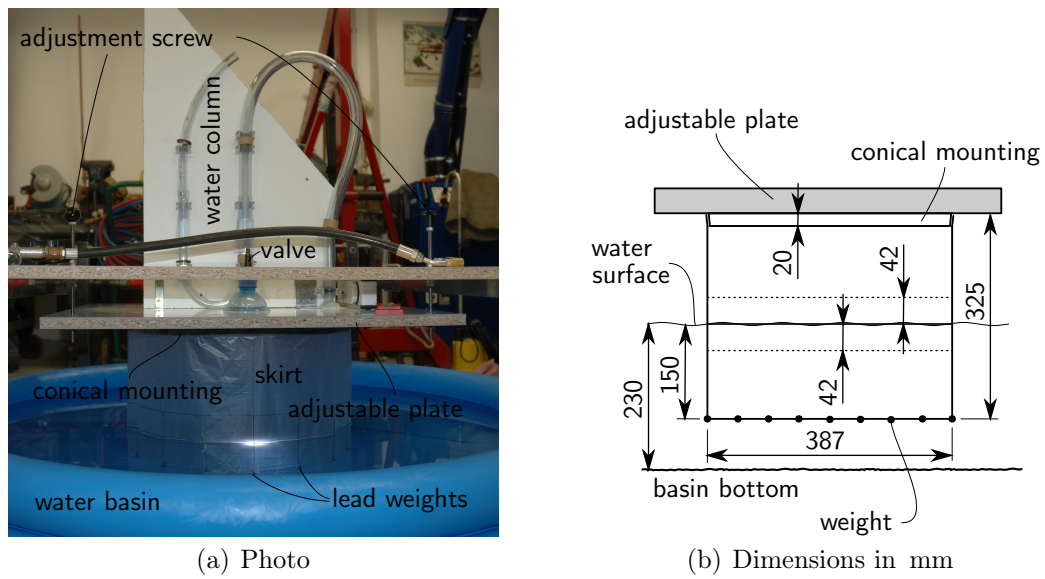


Figure 3.8: Picture of the measurement setup (a) and corresponding dimensions (b).

3.4 Results

3.4.1 The Buckling Process

A first sign of the instability can be detected by observing the upper edge of the cylinder. On one side small wrinkles appear. This local instability is followed by a global bending of the cylinder around the upper support if the internal pressure is further increased. The process is visualised in Fig. 3.9 for one FE-model and in Fig. 3.10 and Fig. 3.11 for the experiments. Fig. 3.12 shows a sequence of photos from the global buckling process. In the experiments the dynamic characteristic of the post buckling behaviour must be taken into account. Due to the large amount of water that must be moved together with the submerged membrane, the internal pressure can exceed the critical pressure if it is increased too fast.

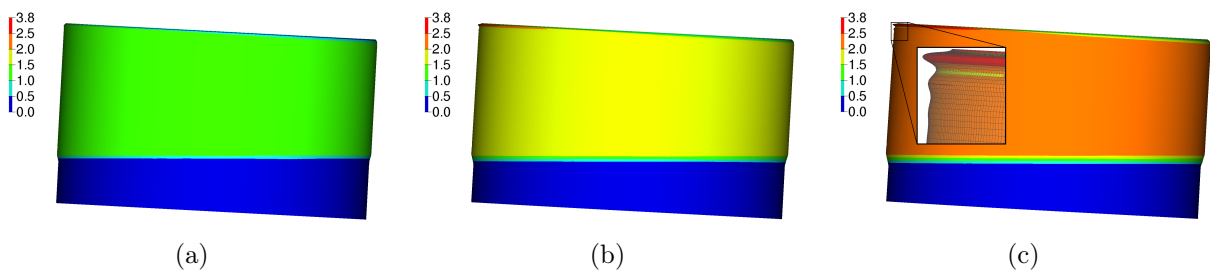


Figure 3.9: Contour plot of the maximum von-Mises equivalent stress in MPa for the perfect cylinder inclined 3° at a waterline of 155 mm at different values of the internal pressure: (a) 75 Pa; (b) 118 Pa; (c) 148 Pa. Displacements are displayed scaled by a factor of 10.

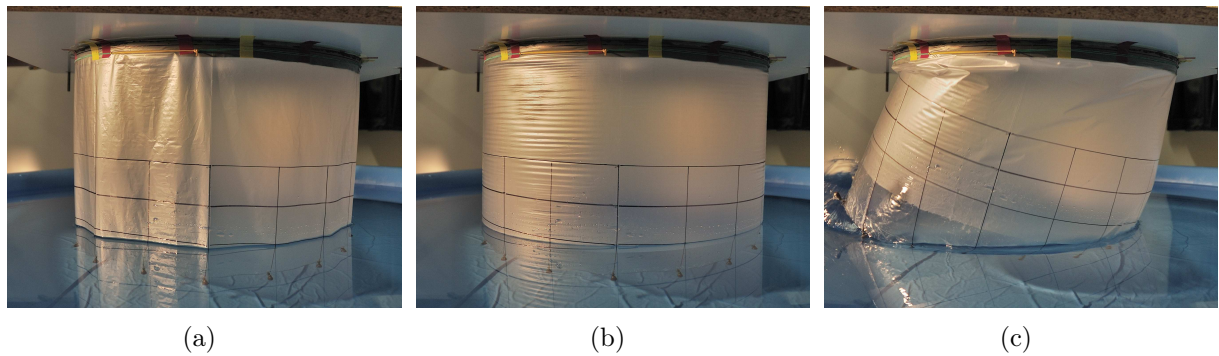


Figure 3.10: Photos of the experiment of a perfect cylinder inclined 2° at a waterline of 197 mm ballasted with a mass of 48 g at the bottom at different pressure levels: (a) unpressurised; (b) subcritical; (c) supercritical.

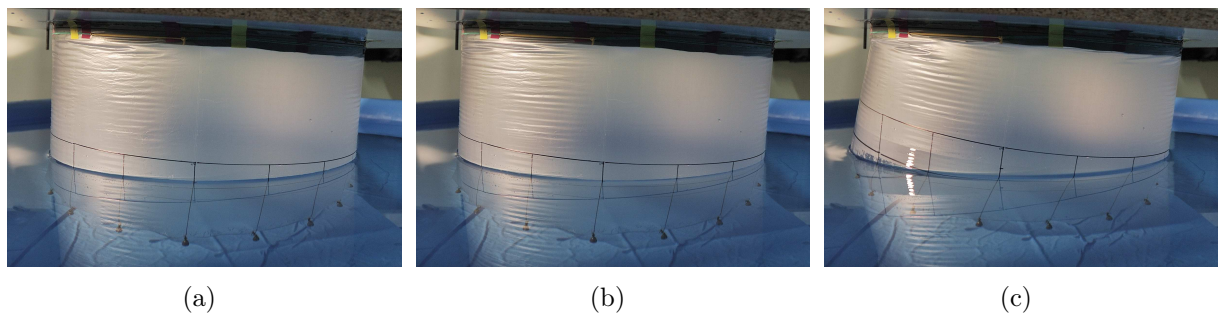


Figure 3.11: Photos of the experiment of a perfect cylinder inclined 3° at a waterline of 134 mm ballasted with a mass of 48 g at the bottom at different pressure levels: (a) low; (b) high; (c) critical.

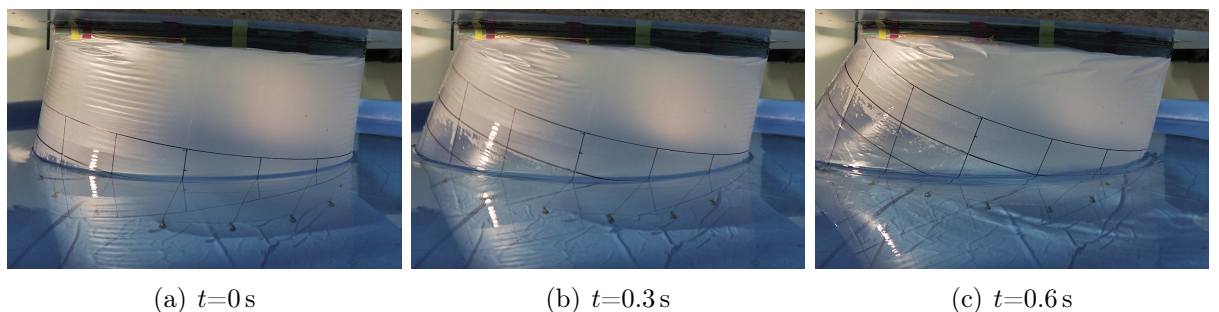


Figure 3.12: Photos of the global buckling process of a perfect cylinder inclined 3° at a waterline of 134 mm ballasted with a mass of 48 g at the bottom at different pressure levels.

3.4.2 Critical Pressure

The critical pressure is defined as the internal pressure at which the global instability occurs. It was experimentally measured for a number of configurations. In the FE-model the critical pressure was obtained as the pressure at which the solver does not converge any more. Comparisons between computational and experimental results are displayed in Fig. 3.13. It can be seen that the critical pressure is predicted very well by the FE-model. For perfect cylinders the critical pressure decreases with increasing inclination of the cylinder and with increasing mass at the lower edge.

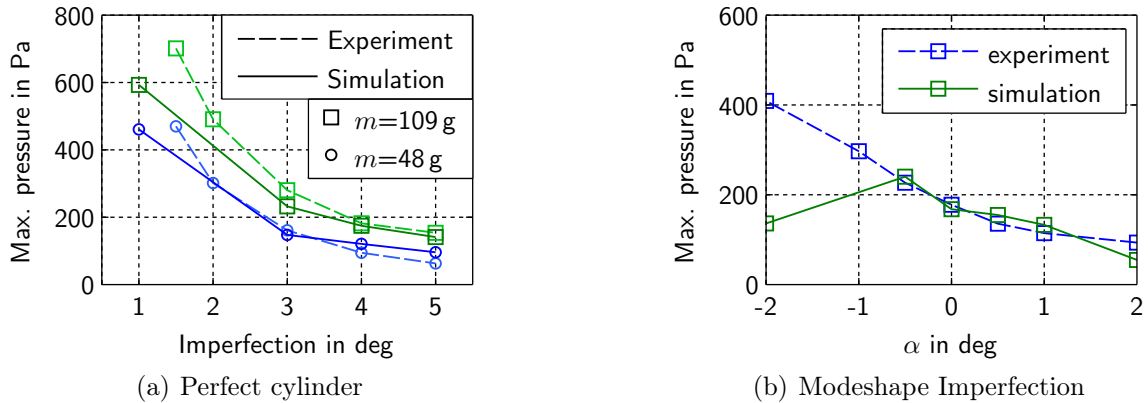


Figure 3.13: Critical pressure depending on the angle of inclination. The water line was at 155 mm from the top. Experiments were carried out for perfectly circular cylinders (a), and for cylinders with a mode shape type imperfection defined by mode 2 and mode 3 linearly combined at a ratio of 5:1 and then scaled to $0.03R$ (b). The skirt was ballasted with different masses at the bottom.

The bifurcation from the trivial equilibrium path can be recognized in the load displacement diagrams of Fig. 3.14. The initial slope of the curves is the same, but the bifurcation pressure decreases with larger inclinations of the cylinder. A larger mass at the bottom end of the skirt increases the bifurcation pressure.

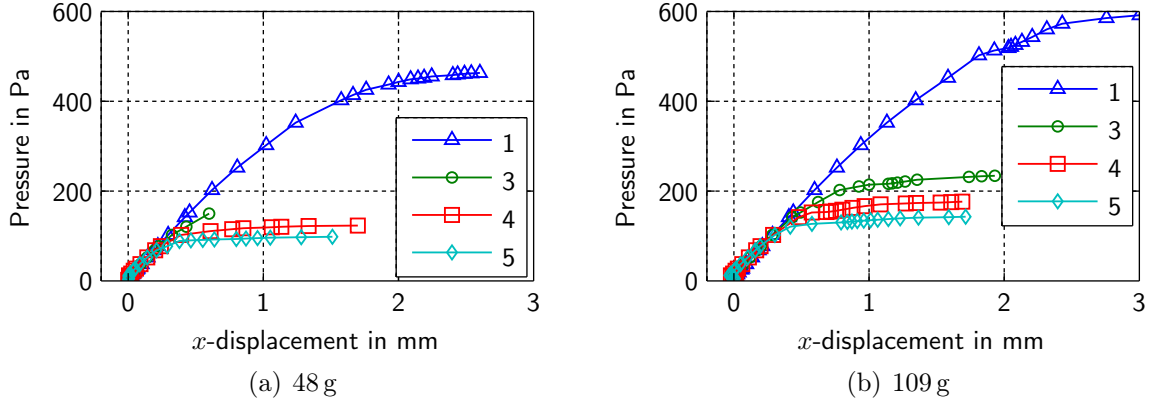


Figure 3.14: Load displacement curves for perfect cylinders with different masses at the lower edge and inclinations of 1, 3, 4, and 5°. The displacement is taken from the position marked by N in Fig. 3.15.

3.4.3 Critical Bending Moment

The global instability, i.e. the sideways bending of the cylinder, is caused by the unsymmetrical pressure distribution at the water line. Fig. 3.15 shows a sketch of the considered geometry. Due to the unsymmetrical geometry the internal pressure creates a bending moment with respect to the centre of the calmed upper edge of the air chamber. The constant internal pressure acting on the small wedge determined by the inclination angle α creates the main part of the bending moment. The linearly decreasing pressure below the water line has a comparatively small contribution. A counteracting bending moment is created by the mass at the end of the skirt.

The bending moment can be computed for a circular cylinder inclined by an angle α by integrating the moment of the pressure distribution on a differential area element over the unsymmetrical surface area. The moment of force of the pressure distribution $p(\mathbf{x})$ onto a surface \mathbf{x} with respect to an arbitrary location \mathbf{p} is computed by

$$\mathbf{m} = \iint_A (\mathbf{x} - \mathbf{p}) \times p \mathbf{n} dA, \quad (3.7)$$

where \mathbf{n} denotes the normalized normal vector onto the surface. The pressure distribution p is piecewise linear, as shown in Fig. 3.15. Therefore, the integration is split into two parts, one for the area above the outer water level, and one for the area between inner and outer water level. Due to the symmetry of the surface with respect to the ξ - ζ -plane only a moment in η -direction, and y -direction, respectively, will arise. The moment will be computed with respect to the centre of the upper support of the cylinder $\mathbf{p} = [0, h_u, 0]^T$, denoted by P in Fig. 3.15.

For the first area, above the outer water level, the surface $\boldsymbol{\psi}$ of the cylinder can be parametrized by cylindrical coordinates in the ξ, η, ζ -system

$$\boldsymbol{\psi}(\varphi, \zeta) = \begin{bmatrix} \xi \\ \eta \\ \zeta \end{bmatrix} = \begin{bmatrix} r \cos(\varphi) \\ r \sin(\varphi) \\ \zeta \end{bmatrix}, \quad (3.8)$$

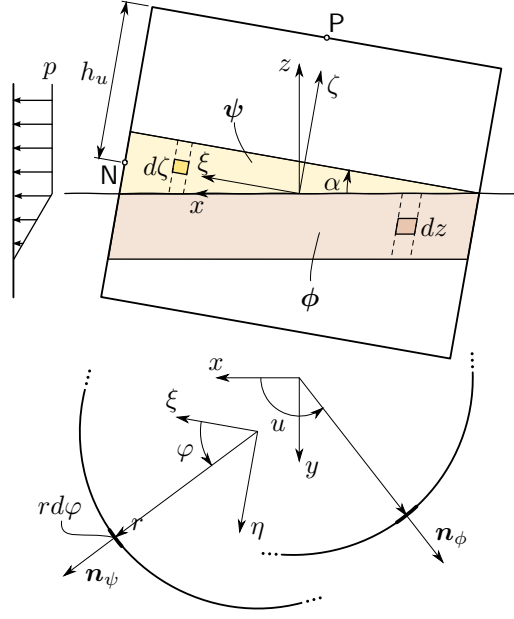


Figure 3.15: Bending Moment

and hence, the normal vector onto the surface is obtained by

$$\mathbf{n}_\psi = \frac{\partial \psi}{\partial \varphi} \times \frac{\partial \psi}{\partial \zeta} = \begin{bmatrix} r \cos(\varphi) \\ r \sin(\varphi) \\ 0 \end{bmatrix}. \quad (3.9)$$

The internal pressure distribution is constant and the integral for the η -component of the bending moment takes the form

$$\begin{aligned} m_{\eta,u} &= \int_{-\pi}^{\pi} pr \int_{-r \cos \varphi \tan \alpha}^{r \tan \alpha} (\zeta - h_u) \cos \varphi d\zeta d\varphi = \\ &= pr^2 \int_{-\pi}^{\pi} h_u (\cos \varphi - \cos^2 \varphi) \tan \alpha + \frac{r}{2} (\cos^3 \varphi - \cos \varphi) \tan^2 \alpha d\varphi = \\ &= -\pi h_u pr^2 \tan \alpha \end{aligned} \quad (3.10)$$

which can be solved by elementary functions.

Considering the area below the outer water surface the linearly decreasing internal pressure must be taken into account. A useful parametrisation for the surface is

$$\phi = \begin{bmatrix} x \\ y \\ z \end{bmatrix} = z \begin{bmatrix} -\frac{\sin \alpha}{\cos \alpha} \\ 0 \\ 1 \end{bmatrix} + \begin{bmatrix} \frac{r \cos u}{\cos \alpha} \\ r \sin u \\ 0 \end{bmatrix}, \quad (3.11)$$

with $u \in [0, 2\pi]$. The normalized normal vector onto the surface is hence computed by

$$\mathbf{n}_\phi = \frac{\phi_u \times \phi_z}{|\phi_u \times \phi_z|} = \begin{bmatrix} \cos \alpha \cos u \\ \sin u \\ \sin \alpha \cos u \end{bmatrix}, \quad (3.12)$$

where the indices u and z donate the partial derivative with respect to the respective parameter. The area element is computed as

$$dA_\phi = |\phi_u \times \phi_z| = \frac{r}{\cos \alpha}. \quad (3.13)$$

The integral for the bending moment of the lower surface is therefore

$$\begin{aligned} m_{y,l} &= \frac{r}{\cos^2 \alpha} \int_{-\frac{p}{\rho_w g}}^0 \int_0^{2\pi} (\rho_w g z + p) (z - h_u \cos \alpha - r \sin \alpha \cos u) \cos u \, du \, dz = \\ &= -\frac{\pi r^2 \sin \alpha}{\cos^2 \alpha} \int_{-\frac{p}{\rho_w g}}^0 (\rho_w g z + p) \, dz = \\ &= -\frac{\pi p^2 r^2 \sin \alpha}{2 \rho_w g \cos^2 \alpha}. \end{aligned} \quad (3.14)$$

Finally, the contribution of an equally distributed mass along the lower end of the skirt should be taken into account. In order to gain a conservative estimate for the reduction of the bending moment it is assumed that the vertical force acts in the centre of the upper waterline. This assumption is chosen because the lower part of the membrane will deform considerably in areas without internal pressure. The mass then exerts a bending moment

$$m_{y,m} = m \left(1 - \frac{\rho_w}{\rho_m} \right) g h_u \sin \alpha, \quad (3.15)$$

with respect to the centre of the upper support. In the above equation g denotes the acceleration of gravity.

Summing up all term yields the total bending moment

$$\begin{aligned} m_y &= m_{y,u} + m_{y,l} + m_{y,m} = \\ &= -\pi h_u p r^2 \tan \alpha - \frac{\pi p^2 r^2 \sin \alpha}{2 \rho_w g \cos^2 \alpha} + m \left(1 - \frac{\rho_w}{\rho_m} \right) g h_u \sin \alpha. \end{aligned} \quad (3.16)$$

This result can be compared with the reaction moment computed by the FE model, which is obtained by reducing the nodal reaction forces into the centre of the upper support. The comparison shows excellent agreement between the analytical formulation and the FE computation, as can be seen in Fig. 3.16. The total bending moment is dominated by the contribution of the internal pressure above the outer water surface. This term increases linearly with the internal pressure. The slope depends on the inclination angle of the cylinder and the height of the water line. Larger values lead to larger slopes.

The x -displacement of the reference node (marked N in Fig. 3.15) is displayed in relation to the total reaction moment at the upper support in Fig. 3.17. It can be seen that for inclinations larger than 2° a critical bending moment is present. The bending moment caused by the unsymmetrical pressure distribution is the reason for the global instability. The stabilizing effect of the internal pressure can be seen when comparing the deformation figures at the upper edge. The deformation figure of the cylinder with lower

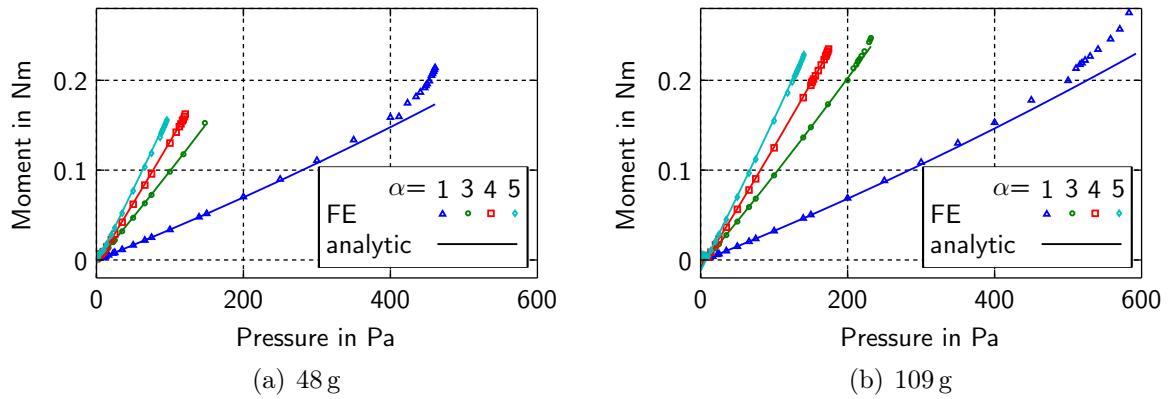


Figure 3.16: Bending Moment at the upper support versus internal pressure for circular cylinders with different inclinations and different masses at the lower edge (waterline 155 mm).

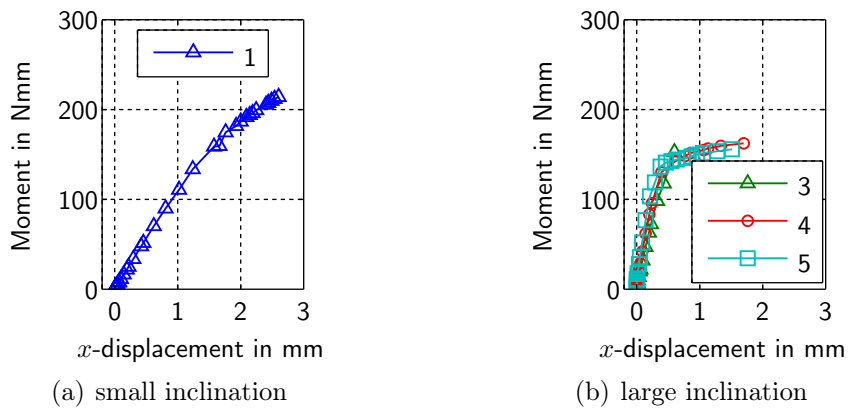


Figure 3.17: Load displacement curves for perfect cylinders with different inclinations at a waterline of 155 mm and a mass of 48 g at the bottom. The internal pressure has a stabilizing effect, the possible bending moment is higher.

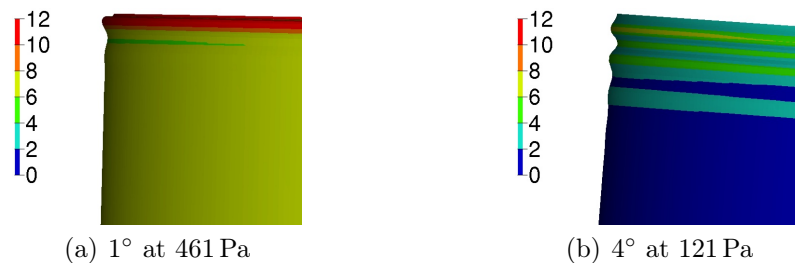


Figure 3.18: Deformation figures of inclined perfect circular cylinders at the critical pressure (155 mm waterline, 48 g at the bottom). The fringe color indicates the maximum von-Mises equivalent stress in MPa.

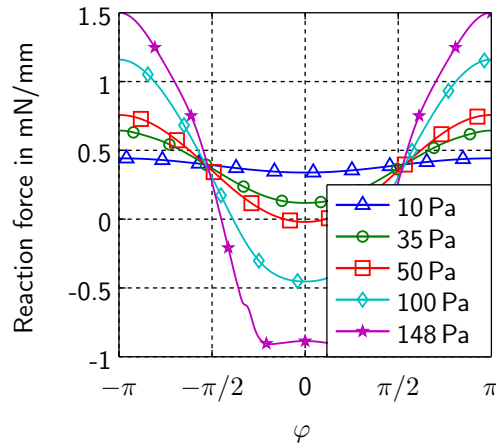


Figure 3.19: Axial reaction force at the upper edge along the circumference for the model of a perfect cylinder inclined 3° at a waterline of 155 mm at different values of the internal pressure.

inclination (Fig. 3.18a) shows only one large wrinkle, whereas the one for the cylinder with larger inclination (Fig. 3.18b) shows three wrinkles with decreasing amplitude and constant wave length. The stabilizing effect of the internal pressure can also be observed by looking at the distribution of the axial reaction force at the upper support along the circumference. Fig. 3.19 shows the reaction force for different values of the internal pressure. Thanks to the stabilizing internal pressure compressive stresses are possible and the cosine distribution can be maintained. The appearance of wrinkles can be clearly recognized as a deviation from the cosine distribution.

3.5 Conclusion

The developed modelling strategy is able to predict the stability behaviour of the considered cylindrical, open air chambers. The reason for the global bending type instability was found to be a bending moment caused by the unsymmetrical pressure distribution at the waterline. This bending moment leads to compressive stresses in the membrane which cause local wrinkling, and subsequently global buckling of the cylindrical air chamber. A stabilizing effect of the internal pressure could be observed.

Imperfections, like the inclination of the upper support dramatically decrease the critical load. As the post buckling behaviour of the air chamber is unstable, the prescribed instability of the supporting structure can cause catastrophic failure of an air chamber supported floating platform. Therefore, the described instability phenomenon should be carefully investigated in the design process. In general lower chambers with larger diameters are less likely to exhibit global buckling. As a mass located at the lower edge of the skirt creates a counteracting bending moment, increasing the ballast can also improve the stability behaviour.

Chapter 4

Treatment of the Periodic Platform Structure by Homogenisation and Localisation

The main load bearing structure of the floating platform is plate like. In order to achieve a low structural weight at the required dimension of several hundred meters side length, the structure is designed as a plain-periodic framework, i.e. the periodicity encompasses two spacial directions. The global behaviour of such a periodic structure is defined by the smallest periodic entity, i.e. a unit cell or representative volume element (RVE), of the structure [66]. Figure 4.1 shows a sketch of the proposed framework. As the structure is plane-periodic, it can be modelled globally by an equivalent plate structure.

A simple method to obtain global properties for a given periodic structure is to analyse a sub-part of the structure. Constant tractions or displacements are then applied on the boundaries of the sub-part to compute the resulting macroscopic strain or stress, respectively. From results from a sufficient number of linearly independent load cases the macroscopic stiffness properties can be computed. This method, termed windowing in the following, delivers the more accurate results the larger the analysed sub-part gets [44]. Generally the macroscopic parameters determined by windowing will underestimate or overestimate the true macroscopic properties, depending on the use of constant traction or constant deformation boundary conditions, respectively [39]. Windowing will be used to determine the transverse shear stiffness of the periodic plate structure. While more complex theories based on second-order homogenisation [37, 38] exist to obtain the transverse shear properties of plain-periodic structures [20], windowing provides sufficient

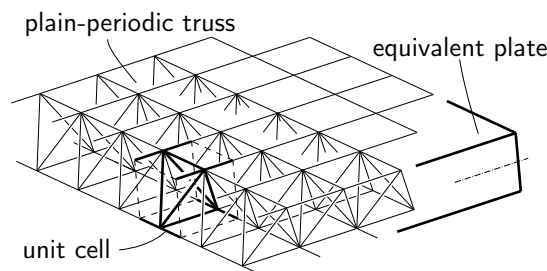


Figure 4.1: Periodic frame structure with unit cell and equivalent plate.

accuracy in the present case.

The in-plane and bending properties of the equivalent plate structure will be generated by using previously developed computational homogenisation algorithms based on unit cells with periodic boundary conditions [47, 48, 58]. In the following only a brief explanation of these algorithms necessary for their application is given.

Once the stiffness properties of an equivalent plate structure are obtained, this structure can be analysed by standard FE methods under global loading. The resulting local stresses in the unit cell(s) can be computed from the section force combinations arising in the global model. This process is commonly termed localisation in the following. For the design of a structure appropriate load cases and failure criteria must be defined. Failure criteria like the exceedance of the yield limit must be evaluated in all material points of every unit cell. To reduce the computational expense, a computational method to define a global failure criterion, i.e. one formulated in terms of section forces, based on local criteria is introduced.

4.1 Plate Theory

The principal difference between shell and plate is that the latter has no initial curvature. A plate can, therefore, be considered as a special case of a shell. Shell theory is applicable for structures with one dimension, the thickness, much smaller than the other dimensions. The structure may then be described by a reference surface. The deformation of the reference surface, expressed as the three in-plane strain components in the reference surface $\boldsymbol{\gamma}$ and three changes of curvature $\boldsymbol{\kappa}$, can be calculated from the displacements and rotations of the reference surface [45].

The relation between shell section forces and reference surface deformation for a thin shell can be written in the form

$$\begin{bmatrix} n_{11} \\ n_{22} \\ n_{12} \\ m_{11} \\ m_{22} \\ m_{12} \end{bmatrix} = \begin{bmatrix} A_{11} & A_{12} & A_{13} & B_{11} & B_{12} & B_{13} \\ & A_{22} & A_{23} & B_{21} & B_{22} & B_{23} \\ & & A_{33} & B_{31} & B_{32} & B_{33} \\ & & & D_{11} & D_{12} & D_{13} \\ & \text{sym.} & & & D_{22} & D_{23} \\ & & & & & D_{33} \end{bmatrix} \begin{bmatrix} \gamma_{11} \\ \gamma_{22} \\ \gamma_{12} \\ \kappa_{11} \\ \kappa_{22} \\ \kappa_{12} \end{bmatrix}, \quad (4.1)$$

or equivalently in matrix notation

$$\begin{bmatrix} \mathbf{n} \\ \mathbf{m} \end{bmatrix} = \begin{bmatrix} \mathbf{A} & \mathbf{B} \\ \text{sym.} & \mathbf{D} \end{bmatrix} \begin{bmatrix} \boldsymbol{\gamma} \\ \boldsymbol{\kappa} \end{bmatrix}, \quad (4.2)$$

where the vectors \mathbf{n} and \mathbf{m} contain the section forces per unit length, and section moments per unit length, respectively [57]. For thick shells the above relations are augmented by the relation between transverse section forces and shear deformations

$$\begin{bmatrix} n_{13} \\ n_{23} \end{bmatrix} = \begin{bmatrix} K_{11}^{ts} & K_{12}^{ts} \\ \text{sym.} & K_{22}^{ts} \end{bmatrix} \begin{bmatrix} \gamma_{13} \\ \gamma_{23} \end{bmatrix}, \quad (4.3)$$

where for a symmetric structure, the off-diagonal terms are zero [12]. Figure 4.2 shows the section forces acting on a shell element.

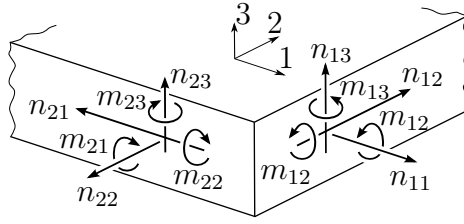


Figure 4.2: Section forces of a general shell element.

4.2 Equivalent Stiffness Properties for Plain Periodic Structures

The stiffness properties of a plate mechanically equivalent to the periodic frame structure can be obtained from the unit cell by the use of computational homogenisation. In general Eqs. (4.1) and (4.3) contain 24 independent parameters. However, for the considered unit cell, depicted in Fig. 4.3, only eight independent parameters arise due to symmetry.

A finite element model (for the software ABAQUS) of the unit cell was created. The input generation was fully automatised in order to allow for rapid changes of discretisation, unit cell size (l_1, l_2, l_3), beam cross sectional parameters (R, t), or different material properties (E, ν). Different cross sectional parameters for the pipe like cross section of the top/bottom and diagonal beams are possible. The structure was discretised by 3-noded, second-order, shear flexible beam elements*. If desired 8-noded, bi-quadratic, general shell elements with reduced integration† can be added at the top and bottom face of the unit cell.

4.2.1 Unit Cells with Periodic Boundaries

Periodic boundary conditions are applied automatically to the unit cell boundary nodes. Six independent load cases need to be calculated in order to determine the effective plate properties. The load cases correspond to the three in plane section forces and the three section moments (in Eq. (4.1)) and are depicted in Fig. 4.4. To simplify the localisation procedure, section forces of unit magnitude are applied in the homogenisation load cases.

*ABAQUS element type: B32

†ABAQUS element type: S8R

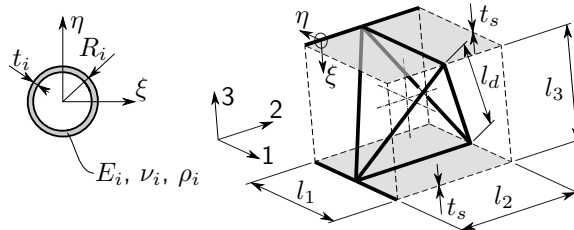


Figure 4.3: Unit cell geometry: Two different pipe-like cross sections are used for the diagonal beams and for the beams in the top/bottom faces. Plates of uniform thickness (depicted in gray) may be added in the top and bottom faces.

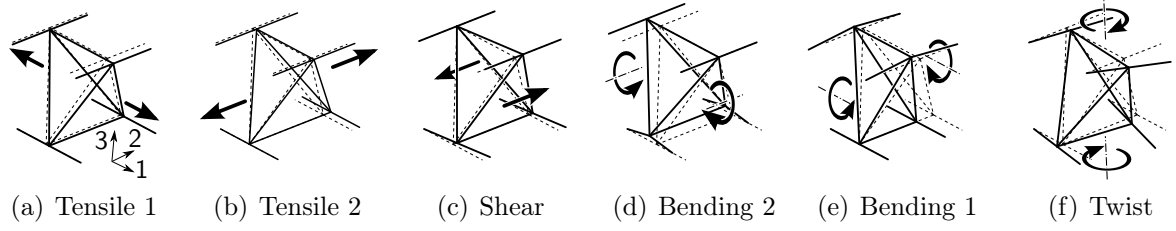


Figure 4.4: Load cases for determination of the effective thin-plate properties.

4.2.2 Transverse Shear Stiffness

The equivalent transverse shear stiffness of the framework structure is obtained by windowing. The corner nodes of the unit cell are constrained to ensure periodicity during deformation, i.e. they are forced to form a parallelepiped. Additionally, constraints are imposed on the nodes on the boundary faces, forcing them to remain in their corresponding parallel planes. Unit section forces $n_{13} = \frac{N_{13}}{l_2} = n_{23} = \frac{N_{23}}{l_1} = 1$ are applied to the reference nodes of the respective faces. Approximating the transverse shear angle by $\gamma_{i3} \approx \frac{u_{i3}}{l_i}$ leads to

$$K_{ii}^{ts} = N_{i3} \frac{l_i}{u_{i3}}, \tag{4.4}$$

from which the stiffness terms in Eq. (4.3) can be calculated. The above used symbols are depicted in Fig. 4.5. Due to the symmetry of the unit cell the coupling term (off-diagonal element) of the transverse shear stiffness matrix is zero, and only two load cases are necessary to compute the remaining terms.

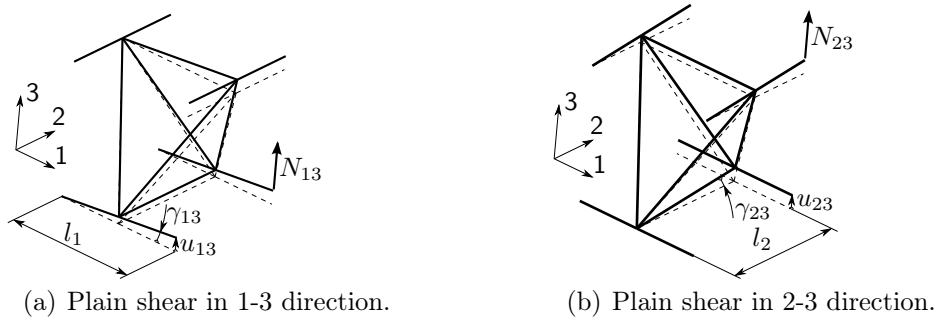


Figure 4.5: Load cases to calculate the equivalent transverse shear stiffness.

4.3 Localisation

Each cell in the global truss structure was represented by a single equivalent, i.e. homogeneous, shell element with effective stiffness properties. The FE analysis of the homogenised shell structure then gives the global structural deformations, as well as the acting shell

section forces. These eight shell section forces are calculated at the integration points of the equivalent shell elements and can simply be averaged to get a single value for each shell section force in each element.

Assuming linear theory, the value of any field variable x in the unit cell can be calculated by linearly superimposing the field values x_i from the homogenisation FE analyses according to

$$x = \sum_{i=1}^n s_i x_i, \quad (4.5)$$

where n donates the number of homogenisation load cases, and s_i are the shell section force values obtained from the analysis of the shell structure. Care has to be taken, that the corresponding field values x_i are obtained from unit cells loaded with unit section forces. This procedure can be applied for unit cell fields like displacements, member section forces, stresses or strains. It is important to note, that the prescribed superposition is not applicable for fields which are not linearly dependent on the section forces. For example, the field of the von-Mises equivalent stress, can not be computed directly by superposition. It must be obtained by superimposing all stress components, and then computing the equivalent stress.

If the value of a field variable x should be computed in all k points of the unit cell, the above relationship can be efficiently written in matrix form

$$\mathbf{x} = \mathbf{X} \mathbf{s}, \quad (4.6)$$

where $\mathbf{x} = [x_1, \dots, x_m]^T$ is the field of quantity x for all m points of the unit cell, and the vector $\mathbf{s} = [s_1, \dots, s_n]^T$ defines the combination of section forces. The columns of the matrix $\mathbf{X} = [\mathbf{x}_1, \dots, \mathbf{x}_n]$ are formed by fields of the quantity x computed from the homogenisation load cases, and is hence of dimension $m \times n$.

4.4 Failure Criteria Defined in Terms of Global Section Forces

For the design of a homogenised structure under certain loading, one needs to translate the arising combination of section forces to the localised field variables in the unit cell. This, so called, localisation procedure is possible for any variable computed in the unit cell for which linear superposition is allowed, e.g. stress components at the integration- or section-points, nodal displacements, or section forces of continuum elements, and was explained in the above section. The localised fields must then be evaluated based on appropriate failure criteria.

For the strength design of the structure, a yield criterion is the appropriate failure criterion. The field variable of interest is an equivalent stress (e.g. the von-Mises equivalent stress), which may not be linearly superimposed – it must be computed from the localised stress fields of the stress components, obtained by the above described localisation procedure. The failure criterion, i.e. localised equivalent stress being smaller than the allowable value, must be evaluated for the whole structure at every time instance. This means that the direct localisation must be done for every arising combination of section forces, i.e. every point at every time instance, in the homogenized structure. For the assessment of

the global structure a failure criterion formulated in terms of section forces would be desirable.

The failure criterion defines the set of section force combinations for which failure occurs in the unit cell. It can be imagined as an $n - 1$ dimensional surface, that splits the n dimensional space of section force combinations in two subspaces. One made up by the section forces combinations which can be tolerated by the unit cell (i.e. points inside the failure surface) and the other one composed of the section force combinations leading to failure of the unit cell (i.e. outside of the failure surface). This is analogous to the definition of the yield-surface describing the yield limit in the stress-space.

An analytical expression for the yield surface in the space of the unit cell section forces, can be obtained by inserting the linear relation between section forces and unit cell stresses into the yield criterion. This would represent a yield criterion for a single point in the unit cell. This analytical expression must be derived and analysed for every point in the unit cell. Therefore, no improvements in computational efficiency can be expected.

In order to make the assessment of a section force combination more efficient one needs a quickly evaluable failure criterion for the unit cell defined in the space of the section forces. If a set of points (i.e. section force combinations) on the failure surface was known, an assessment could be done in form of an interpolation procedure. Of course, the yield criterion used above as an example may not be the only failure criterion by which the structure must be designed. Other criteria, like buckling of individual unit cell elements or excessive displacements may be evaluated on the computed localised fields. By combining all failure criteria in a straight forward manner an overall failure surface for multiple failure criteria may be computed.

4.4.1 Using Radial Paths to Determine Points of the Failure Surface

A point on the failure surface can be obtained by considering a single combination of section forces $\mathbf{s} = [s_1, \dots, s_n]^T$. The stress state in the unit cell for this section force combination can be computed by

$$\sigma_{ij} = \sum_{k=1}^n \sigma_{ij,k} s_k = \boldsymbol{\sigma}_{ij}^T \mathbf{s}, \quad (4.7)$$

where the vector $\boldsymbol{\sigma}_{ij} = [\sigma_{ij,1}, \dots, \sigma_{ij,n}]^T$ contains values of the stress state in the unit cell homogenisation load cases. The von-Mises equivalent stress is computed according to

$$\sigma_v = \sqrt{\sigma_{11}^2 + \sigma_{22}^2 + \sigma_{33}^2 - \sigma_{11}\sigma_{22} - \sigma_{22}\sigma_{33} - \sigma_{33}\sigma_{11} + 3(\sigma_{12}^2 + \sigma_{23}^2 + \sigma_{31}^2)}. \quad (4.8)$$

For the sake of brevity the case of a plane stress state (i.e. $\sigma_{33} = \sigma_{23} = \sigma_{13} = 0$) will be considered. Inserting the localised stress expressions into the von-Mises yield criterion for a plane stress state yields

$$\begin{aligned} \sigma_v &= \sqrt{(\boldsymbol{\sigma}_{11}^T \mathbf{s})(\boldsymbol{\sigma}_{11}^T \mathbf{s}) - (\boldsymbol{\sigma}_{11}^T \mathbf{s})(\boldsymbol{\sigma}_{22}^T \mathbf{s}) + (\boldsymbol{\sigma}_{22}^T \mathbf{s})(\boldsymbol{\sigma}_{22}^T \mathbf{s}) + 3(\boldsymbol{\sigma}_{12}^T \mathbf{s})(\boldsymbol{\sigma}_{12}^T \mathbf{s})} \\ &= \sqrt{\mathbf{s}^T (\boldsymbol{\sigma}_{11} \boldsymbol{\sigma}_{11}^T - \boldsymbol{\sigma}_{11} \boldsymbol{\sigma}_{22}^T + \boldsymbol{\sigma}_{22} \boldsymbol{\sigma}_{22}^T + 3\boldsymbol{\sigma}_{12} \boldsymbol{\sigma}_{12}^T) \mathbf{s}} \end{aligned} \quad (4.9)$$

It can be seen, that if the section force combination is scaled by an arbitrary factor, the resulting equivalent stress will be scaled by the same factor. The value of the highest equivalent stress in the unit cell for a certain section force combination, $\sigma_{v,\max}$, determines the failure of the unit cell. The safety factor for a section force combination \mathbf{s} is then computed by

$$s_{\text{yield}} = \frac{\sigma_{v,\text{lim}}}{\sigma_{v,\max}}, \quad (4.10)$$

where $\sigma_{v,\text{lim}}$ denotes the yield limit. The safety factor can be seen as the factor, by which the vector representing the section force combination must be multiplied in order to represent a point located exactly on the failure surface of the unit cell. Hence, the point on the failure surface is

$$\mathbf{p} = s_{\text{yield}} \mathbf{s}. \quad (4.11)$$

4.4.2 Assessment of the Failure Criterion for a Section Force Combination

Let us assume we are considering the space of n section forces, and we have already determined a set of points \mathbf{p}_i located on the failure surface. We now want to obtain the safety factor for a particular section force combination $\mathbf{s} = [s_1, \dots, s_n]^T$. Geometrically this question corresponds to finding the intersection of the line defined by $\mathbf{x} = t\mathbf{s}$ with the surface Ω defined by the points \mathbf{p}_i . One approach for finding the intersection would be to fit an analytical expression describing the surface to the data points, and then to compute the intersection. However, finding a suitable form for the analytical expression seems difficult. Additionally, the computation of the intersection would require an iterative procedure if no closed form solution for the intersection can be found.

Two different approaches for computing the intersection are presented below. The first one treats the surface as piecewise flat and is suitable for arbitrarily distributed points. The second one is based on the transformation into polar coordinates and a multivariate spline interpolation of the radius. It is only applicable to point sets \mathbf{p}_i whose polar angles form a regular grid.

4.4.2.1 Arbitrarily Distributed Points

The surface defined by the points $\mathbf{p} = [p_1, p_2, \dots, p_n]^T$ will be approximated by a hyperplane spanned by n points. The considered line is then intersected with this approximating hyperplane. The challenge in this approach is to suitably choose the n points defining the approximating hyperplane. They should correspond to those points which most closely surround the direction \mathbf{s} . In the following the developed intersection procedure will be explained. Figure 4.6 shows a visualization of the different steps in the intersection procedure for the three-dimensional case. We consider the straight line with direction vector $\mathbf{s} = [s_1, \dots, s_n]^T$ (in the three-dimensional example: $n=3$) defined by

$$\mathbf{x} = t\mathbf{s}, \quad t \in \mathbb{R}. \quad (4.12)$$

The normal plane, Ψ , to the considered straight line is a hyperplane (or a plane in space in the three-dimensional example) defined by the linear equation

$$\mathbf{x}^T \mathbf{s} = 0. \quad (4.13)$$

It splits the n dimensional space of section forces into two parts: one above and one below the hyperplane (see Fig. 4.6a). All points satisfying

$$\mathbf{p}_i^T \mathbf{s} \geq 0, \quad (4.14)$$

lie above the hyperplane and must be considered to find the intersection, all other points can be discarded. The task now is to find those n points which most tightly surround the straight line. The unit vectors describing the direction to the point \mathbf{p} is defined by

$$\mathbf{p}_0 = \frac{\mathbf{p}}{\|\mathbf{p}\|}, \quad \text{with } \|\mathbf{p}\| = \sqrt{\mathbf{p}^T \mathbf{p}}. \quad (4.15)$$

These normalized directional vectors are projected into the hyperplane Ψ yielding the points

$$\mathbf{p}' = \mathbf{p}_0 - \mathbf{s}^T \mathbf{p}_0 \mathbf{s}. \quad (4.16)$$

The projected points lie in a $n - 1$ dimensional subspace of the space of section forces, defined by the normal plane Ψ via Eq. (4.13). More precisely, the subspace is the nullspace or kernel of \mathbf{s}^T , i.e. the solution of $\mathbf{s}^T \mathbf{x} = 0$. The basis vectors of the nullspace can be computed by using the single value decomposition of the matrix \mathbf{s}^T . The projected points are then transformed into the new, $n - 1$ dimensional, basis where a Delaunay triangulation of the points is performed. The n vertices of the simplex containing the origin correspond to the n directions most closely surrounding the straight line.

The Delaunay triangulation can be obtained by a convex hull algorithm with a performance of the order $k \log k$, where k is the number of points to triangulate [2]. For many cases it is more efficient to triangulate the points incrementally. For this procedure the points are sorted by their direction from the origin. The triangulation is started with the $N > n$ points closest to the origin; N points are added to the triangulation until a simplex containing the origin can be found.

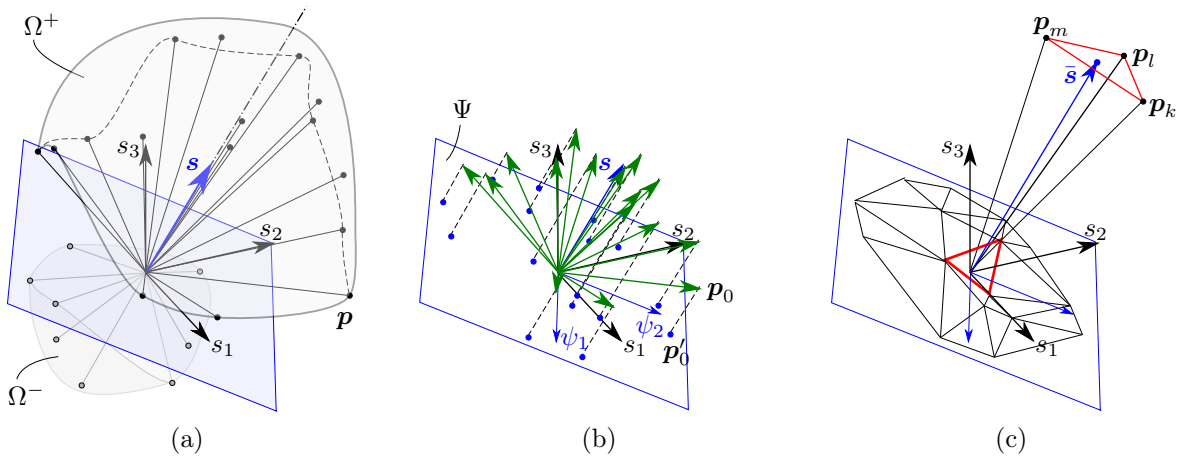


Figure 4.6: Steps of the intersection procedure for irregularly distributed points in a three-dimensional example: (a) Selection of points above the normal plane; (b) projection of the point directions onto the normal plane; (c) triangulation of the projected points to find the closest directions.

Having identified the n failure surface points \mathbf{p}_i with directions most closely surrounding the direction of the straight line, one can construct a hyperplane containing these n points. The hyperplane is formed by the points $\mathbf{x} = [x_1, \dots, x_n]^T$ satisfying the equation

$$\mathbf{x}^T \mathbf{n} = d, \quad (4.17)$$

where \mathbf{n} denotes the normal vector of the hyperplane and d the distance to the origin. The coefficients of the normal vector and the parameter d are obtained by solving the linear system

$$\underbrace{\begin{bmatrix} p_{1,1} & p_{1,2} & \cdots & p_{1,n} & -1 \\ p_{2,1} & p_{2,2} & \cdots & p_{2,n} & -1 \\ \vdots & \vdots & & \vdots & \vdots \\ p_{n,1} & p_{n,2} & \cdots & p_{n,n} & -1 \end{bmatrix}}_{\mathbf{A}} \begin{bmatrix} n_1 \\ n_2 \\ \vdots \\ n_n \\ d \end{bmatrix} = \mathbf{0}, \quad (4.18)$$

where the rows in the coefficient matrix \mathbf{A} contain the coordinates of the n selected closest points $\mathbf{p}_i = [p_{i,1}, \dots, p_{i,n}]^T$. The solution of (4.18) is obtained by computing the nullspace[‡] of \mathbf{A} . Finally the intersection of the straight line and the now known hyperplane can be computed. Combining (4.12) and (4.17) and yields the intersection point

$$\bar{\mathbf{s}} = \frac{b}{\underbrace{\mathbf{n}^T \mathbf{s}}_t} \mathbf{s}. \quad (4.19)$$

It can be seen, that the parameter $t = b/(\mathbf{n}^T \mathbf{s})$ is the safety factor for the considered section force combination.

Significant improvements in terms of accuracy can be obtained if a geometric scaling is employed. Instead of working in the space of section forces, the above computations can be done in equivalent manner in a normalized space. The coordinates of a point, $\mathbf{p}_i = [p_{i,1}, \dots, p_{i,n}]^T$, in the normalized space, $\tilde{p}_{i,j}$, are obtained by scaling the spacial coordinates, $p_{i,j}$, with respect to the extent of the failure surface in the respective coordinate directions, l_j , according to

$$\tilde{p}_{i,j} = \frac{p_{i,j}}{l_j}, \quad \text{for } j = 1, \dots, n. \quad (4.20)$$

The extent of the failure surface in the coordinate direction j is computed by

$$l_j = \frac{\max(p_j) - \min(p_j)}{2}, \quad (4.21)$$

where $\max(p_j)$ and $\min(p_j)$ denote the maximum and minimum, respectively, of the j -coordinate of all known failure surface points. The geometric scaling is particularly useful if the extent of the failure surface varies over several orders of magnitude between different section forces and moments.

The above described interpolation procedure works well even for surfaces defined by very few points. However, for typical unit cell geometries with about 3000 integration

[‡]see Appendix D.9 for details

points and 5 considered section forces ($n = 5$), calculating a single intersection is computationally more expensive than the direct computation of the failure surface point for a given direction. The main part of the computation time is taken up by the Delaunay-triangulation. Efficiency improvements of a factor of approximately 100 can be achieved by an incremental procedure: The data points are sorted with respect to their distance from the origin (see Fig. 4.6b); Only the $3n$ closest points are used for the triangulation; If a surrounding triangle is found the computation can be terminated, otherwise more points must be used for the triangulation. Even with incremental triangulation in normalized space the intersection procedure is approximately 25 times more expensive than the direct computation. Therefore, the intersection procedure will only be applied in special cases: for example for a combined load case of a static base load, manifesting in a constant section force combination at the considered location, and an superimposed dynamic load, represented by an oscillating section force combination. To compute a safety-factor for the amplitude of the dynamic load it is necessary to intersect a straight line going through the point defined by the static load and the direction of the oscillating load with the failure surface. This can be done by the above described procedure, if the failure surface points are shifted to a new origin represented by the static section force combination. Then intersections must be computed for a sufficient number of oscillating section force combinations within one oscillation period.

4.4.2.2 Regular Point Distribution

If points with a regular distribution are used to define the failure surface the efficiency of the intersection procedure can be dramatically improved. The polar angles of the points defining the failure surface must form a structured grid. Then the intersection of an arbitrary direction, represented by its polar angles, with the failure surface can be computed by an n-dimensional interpolation in the dataset of the radii of the failure surface points.

Every point in n-dimensional space may be represented by n-dimensional polar coordinates, described in more detail in Appendix D.11. A point on the failure surface is then defined by $n - 1$ polar angles, $\phi_1, \dots, \phi_{n-1}$, and a radius, r . A structured grid is built by discretising the $n - 1$ dimensional hyperrectangle which encompasses the space of polar angles by

$$\tilde{\phi}_i = \frac{k\pi}{N_\pi}, \quad \text{with } N_\pi \in \mathbb{N}, \quad \text{and } k = \begin{cases} 0, 1, \dots, N_\pi & \text{for } i = 1, \dots, n - 2 \\ 0, 1, \dots, 2N_\pi & \text{for } i = n - 1 \end{cases}. \quad (4.22)$$

The full grid of direction vectors, $\tilde{\phi} = [\tilde{\phi}_1, \dots, \tilde{\phi}_{n-1}]^T$, must be computed. This makes a total of

$$N_c = (2N_\pi - 1)(N_\pi + 1)^{n-2}, \quad (4.23)$$

combinations, for which points on the failure surface have to be obtained. Each grid point corresponds to one radial path, and by setting $\tilde{r} = 1$ defines one point on a hypersphere.

Typically the shape of the failure surface will deviate strongly from a perfect hypersphere due to the different nature of section forces, e.g. in plane tension, bending, out of plane shear. Therefore, a regular grid of polar angles can lead to a very poor characterisation of the shape of the failure surface. This is visualized for a case of three section forces

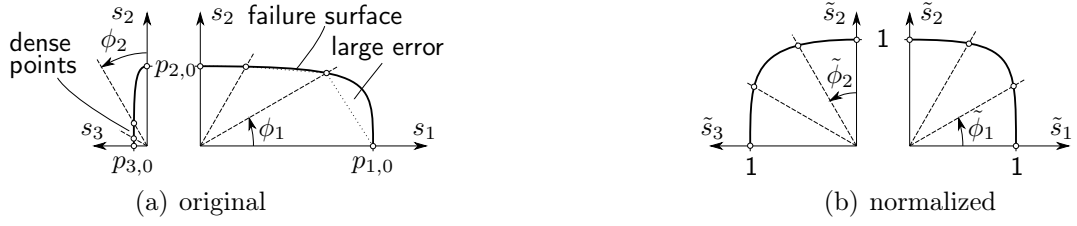


Figure 4.7: Transformation into normalized space for three considered section forces.

in Fig. 4.7 and can also be seen in Fig. 4.11. In some areas the density of points is unnecessarily large, whereas in other areas points are missing, leading to large interpolation errors. This can be remedied by defining the structured grid in the space of normalised section forces. The normalised coordinates of a failure surface point, $p = [p_1, p_2, \dots, p_n]^T$, are defined by

$$\tilde{p}_j = \frac{p_j}{p_{j,0}}, \quad (4.24)$$

where $p_{j,0}$ denotes the failure surface coordinate in the direction of the j^{th} section force, subsequently termed *pole distance*. The pole distance for direction j , $p_{j,0}$, is equal to the safety-factor for the section force combination $\mathbf{s}_j = [\delta_{1j}, \dots, \delta_{nj}]^T$, where δ_{ij} denotes the Kronecker delta. Hence, it can be computed according to Section 4.4.1. The shape of the failure surface in normalised space is much closer to a hypersphere. Therefore, the regular grid of polar angles defined in the normalised space gives a good approximation of the shape of the failure surface. The radial paths in the space of section forces, $\mathbf{s}_i = [s_{i,1}, \dots, s_{i,n}]^T$, must be computed through the geometric transformation

$$s_{i,j} = \tilde{s}_{i,j} s_{j,0}, \quad (4.25)$$

from the points of the hypersphere in the normalised space, $\tilde{\mathbf{s}} = [\tilde{s}_{i,1}, \dots, \tilde{s}_{i,n}]^T$. The points of the hypersphere in Cartesian coordinates are obtained from the grid points of polar angles by the transformation described in Appendix D.11. The polar angles of the radial paths still form a structured grid, but the grid is not equidistant any more (see

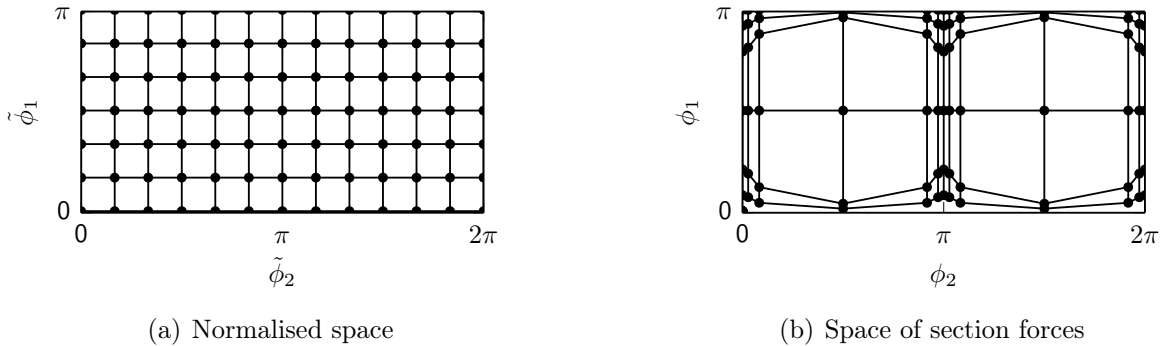


Figure 4.8: Shape of the grid of polar angles: Regular and equidistant as defined in normalized space (a); Regular, but non-equidistant after transformation into the space of section forces (b).

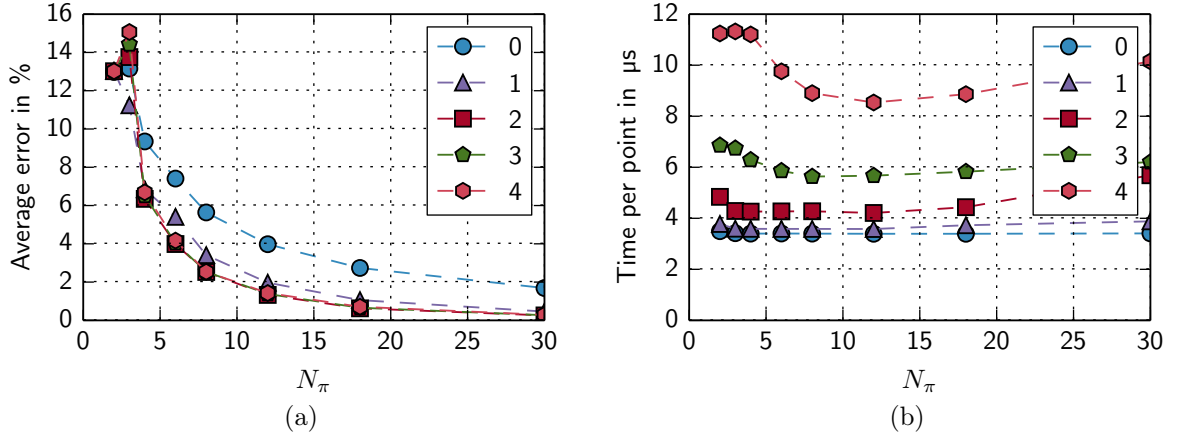


Figure 4.9: Average interpolation error (a), and computational cost of the interpolation (b) for a 5-dimensional (considered section moments and transverse shear forces) failure surface for different discretisations.

Fig. 4.8). In total the failure surface will be defined by N_c radial paths, for which safety-factors can be evaluated according to Section 4.4.1. The distance from the origin of each failure surface point, i.e. its radius, is saved in the appropriate grid-location in an $n - 1$ dimensional matrix. The failure surface is now defined by N_c regularly distributed points.

In order to find the intersection of an arbitrary radial path defined by a section force combination with the failure surface, the section force combination, \mathbf{s} , is first normalized according to (4.25) to obtain a corresponding combination, $\tilde{\mathbf{s}}$, in normalised space. This combination is then transformed into polar coordinates yielding a set of $n - 1$ polar angles $\tilde{\phi}$. A multivariate spline interpolation in the previously computed, $n - 1$ dimensional matrix of radii will yield the distance of the failure surface from the origin in the direction defined by $\tilde{\phi}$, $\tilde{\mathbf{s}}$ and \mathbf{s} . The multivariate spline interpolation can be used because the pre-computed radii are defined on a regular, equally spaced grid of polar angles in the normalised space. The used interpolation algorithm is part of the *ndimage.interpolation* module of *numpy* [36]. Further details about multivariate spline interpolation are given, for example, in the work of Unser [74]. Finally, the safety-factor, s , is computed by

$$s = \frac{r}{\|\mathbf{s}\|}, \quad (4.26)$$

where r donates the radius obtained by interpolation.

Several tests of the interpolation for failure surfaces in different dimensions were conducted. Generally a higher interpolation order yields more accurate interpolation results, as can be seen in Fig. 4.9a. However, the accuracy improvements are marginal for interpolation orders larger than two. The computational cost on the other hand increases dramatically, as can be seen in Fig. 4.9b. Therefore, an interpolation order of 2 is deemed the optimal choice. All interpolation errors were computed as the mean error in the interpolated safety-factor with respect to the directly computed safety-factor for 300,000 randomly distributed points. The interpolation error depends on the resolution of the interpolation basis and on the dimensionality of the failure surface. The resolution of

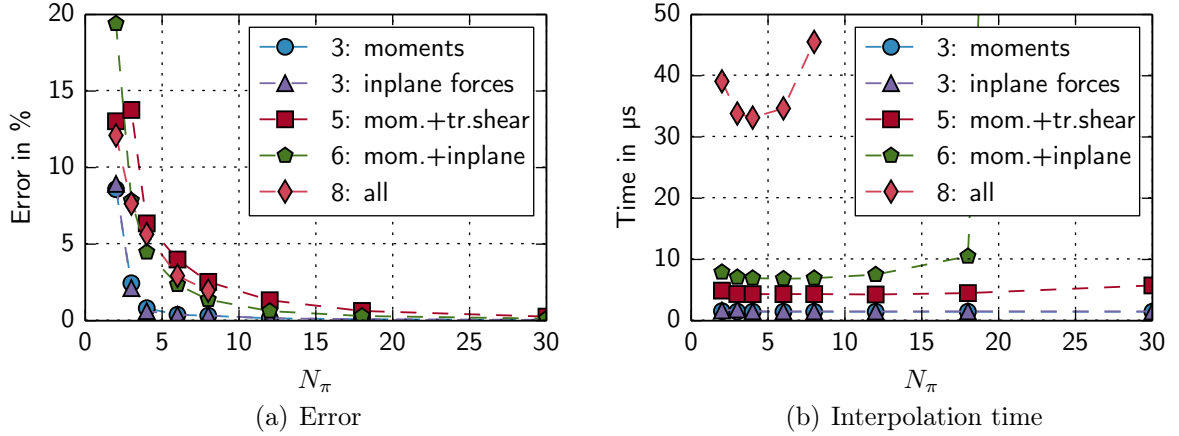


Figure 4.10: Performance of the 2nd order spline interpolation for different considered section forces in dependence of the failure surface resolution: Mean interpolation error with respect to exact computation of the safety-factor (a) and interpolation time per section force combination (b).

the interpolation base, i.e. the discretisation of the hyperrectangle of polar coordinates is defined by N_π . Considering more section forces in the failure surface, i.e. a higher dimension, requires a larger resolution, i.e. higher N_π , to maintain the same interpolation accuracy. Figure 4.10a shows the dependence of the interpolation error on the resolution and the dimension of the failure surface.

Table 4.0a compares computational effort for direct computation and interpolation. For the investigated unit cell with about 3000 integration points the evaluation of the safety-factor by interpolation in the failure surface can be up to 300 times faster compared to the direct computation. The effort for direct computation of a failure surface point, or equivalently, for the safety-factor for a single section force combination depends almost linearly on the number of integration points and increases with increasing dimensionality of the failure surface.

The interpolation procedure is computationally very efficient with speed-up factors of several orders of magnitude. It can be seen, that the effort for the multivariate spline interpolation increases strongly with increasing dimension. For the assessment of the

(a) Computational effort				(b) Break-even point N			
n	t_p in ms	t_i in μ s	speed-up t_p/t_i	n	$N_\pi = 6$	$N_\pi = 8$	$N_\pi = 12$
3	0.441	1.376	320	3	77	135	300
5	0.463	4.515	102	5	381	11,043	51,029
6	0.487	7.590	64	6	26,829	99,973	667,303
8	0.506	37.2	13	8	1,396,831	8,604,175	119,825,945

Table 4.1: Comparison of the computational effort for direct computation and interpolation of order 2 (a), and break-even points for different resolutions of the failure surface (b). Results obtained for a unit cell of about 3000 integration points.

usefulness of the failure surface one must take into account the effort needed to pre-compute the N_c failure surface points. The break-even point of section force combinations, N , after which the speed-up of the interpolation outweighs the additional effort for the computation of the interpolation base consisting of N_c points is computed by

$$N = \frac{t_p}{t_p - t_i} N_c, \quad (4.27)$$

where t_p denotes the computation time for the direct calculation, and t_i for the interpolation, respectively, of one point. In Table 4.0b the break-even point for different failure surface resolutions is computed using (4.27) and the numerical values from Table 4.0a. For large speed-up factors the break-even point effectively equals the size of the interpolation data base. For low dimensional failure surfaces (up to $n = 5$) using the failure surface makes sense if more than a few thousand section force combinations need to be evaluated. On the other hand, if higher dimensional failure surfaces are required, the speed-up decreases due to the larger effort for interpolation, and additionally more points are required in the interpolation base. In the case of eight considered section forces already several million section force combinations must be of interest in order to justify the use of the failure surface. However, the demand to check so many section force combinations can easily arise in the dynamic analysis of a large FE-model.

Figure 4.11 is provided to emphasise the importance of the definition of the equally spaced grid in normalised space. It shows the failure surface for three considered section forces for two different discretisations. Additionally, failure surface points for 30 random directions were evaluated exactly and by interpolation. The true shape of the failure surface is captured very poorly if the grid is defined in the space of section forces (Fig. 4.11a) even if a very fine discretisation is used (Fig. 4.11c). If the regular grid is defined in the normalised space, the shape of the failure surface is captured quite well even for coarse grids (Fig. 4.11b) and the interpolation error is acceptable.

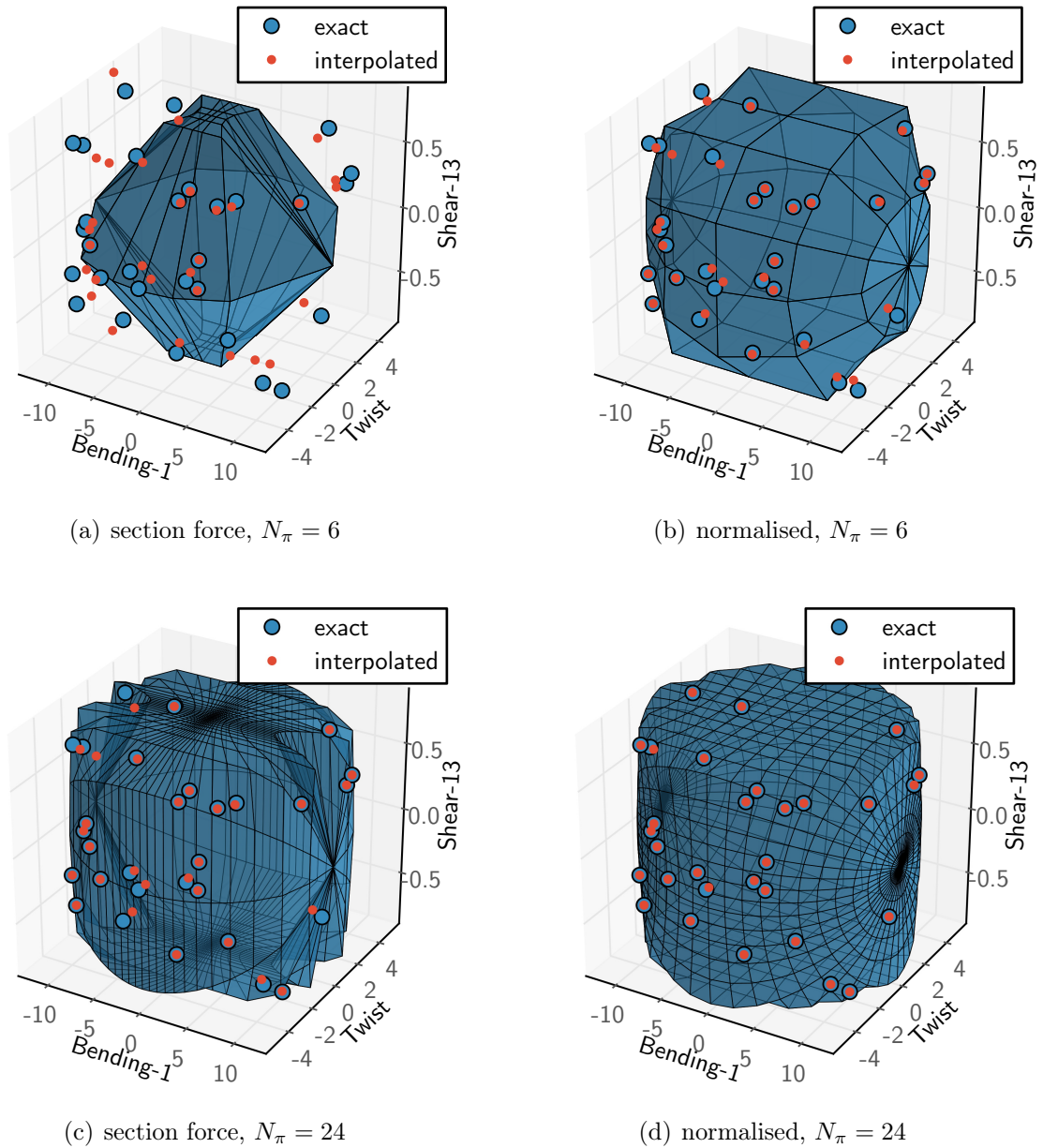


Figure 4.11: Failure surface for three considered section forces in different discretisations; The equally spaced grid was defined in the space of section forces and in normalised space. Based on 30 random directions, points on the failure surface were computed exactly and by interpolation.

Symbol	Value in m	Description
l_1	10.0	cell size in 1-direction
l_2	10.0	cell size in 2-direction
l_3	7.071	cell size in 3-direction
R_1	0.135	radius of the top/bottom beam cross section
t_1	0.004	thickness of the top/bottom beam cross section
R_2	0.135	radius of the diagonal beam cross section
t_2	0.001	thickness of the diagonal beam cross section
t_s		no plate-faces used

Table 4.2: Dimensions of the unit cell geometry. The unit cell is depicted in Fig. 4.3.

4.5 Validation of the Homogenisation Method

To validate the above presented method, an analysis of the detailed, global frame structure is compared with the analysis of a homogenised equivalent model and localised results in the unit cells. The test case corresponds to a typical target application of the method; a 300x300 m plate formed by 900, 10x10x7.07 m sized cells. The edges of the structure are simply supported. Uniform gravity loading is applied in a linear load step. The unit cell geometry is chosen according to Fig. 4.3, and no plates in the top and bottom faces of the cell were used. The used dimensions are given in Table 4.2. As material, a linear-elastic, isotropic model for steel with Young's modulus of 210 GPa, Poisson's ratio of 0.3 and density of 7860 kg/m³ was used.

The homogenised shell model consists of four-node, linearly interpolated, shell elements with reduced integration. Each unit cell is represented by one shell element. Equivalent boundary conditions and loading is applied to the homogenised model.

4.5.1 Global Displacements

Figure 4.12 shows a comparison of the vertical displacement between the full model and the homogenised model. The deformation shape shows excellent agreement. A more

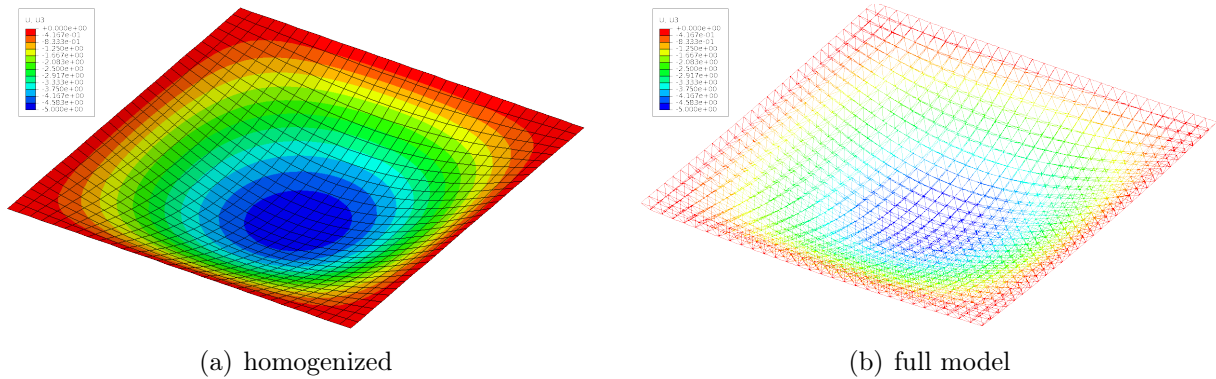


Figure 4.12: Comparison of the vertical displacement (in m) of homogenized and full model.

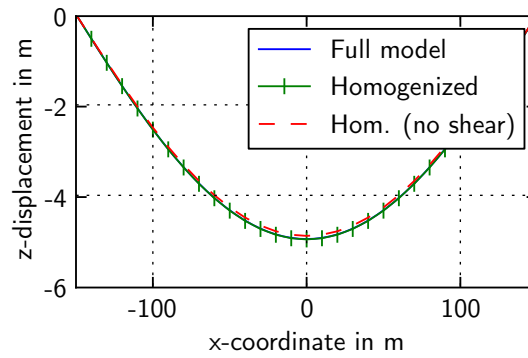


Figure 4.13: Comparison of deformed shape in the symmetry plane of the plate.

detailed comparison of the deformation of the structure in its symmetry plane is given in Fig. 4.13. The deformations of homogenised model and full model match excellently. However, if the transverse shear stiffness is not taken into account, the homogenised structure is slightly too stiff.

4.5.2 Stress Localisation

The stress localisation procedure is validated by a comparison between the von-Mises equivalent stress calculated with the full model and the homogenised model. For the full model the stress values are reported directly in eight section points in the three integration points of the beam elements. The corresponding values for the homogenised structure are computed by the previously described localisation procedure. The maximum arising stresses in the symmetry plane of the plate are compared. For the full model the maximum stress is obtained by taking the maximum stress value found in any point up to the distance of one half unit cell width from the symmetry plane. A plot of the stress field is provided in Fig. 4.14. The maximum stress arises in the top/bottom beams at the centre of the plate. Towards the edges of the structure, the stress in the top/bottom beams decreases due to the lower bending moment in the plate. Close to the simply supported

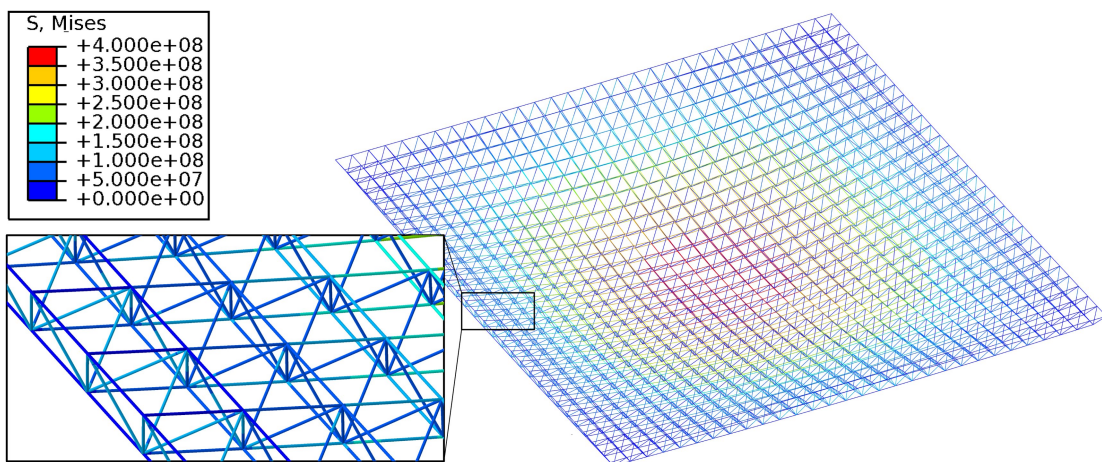


Figure 4.14: von-Mises equivalent stress (in Pa) in the full model.

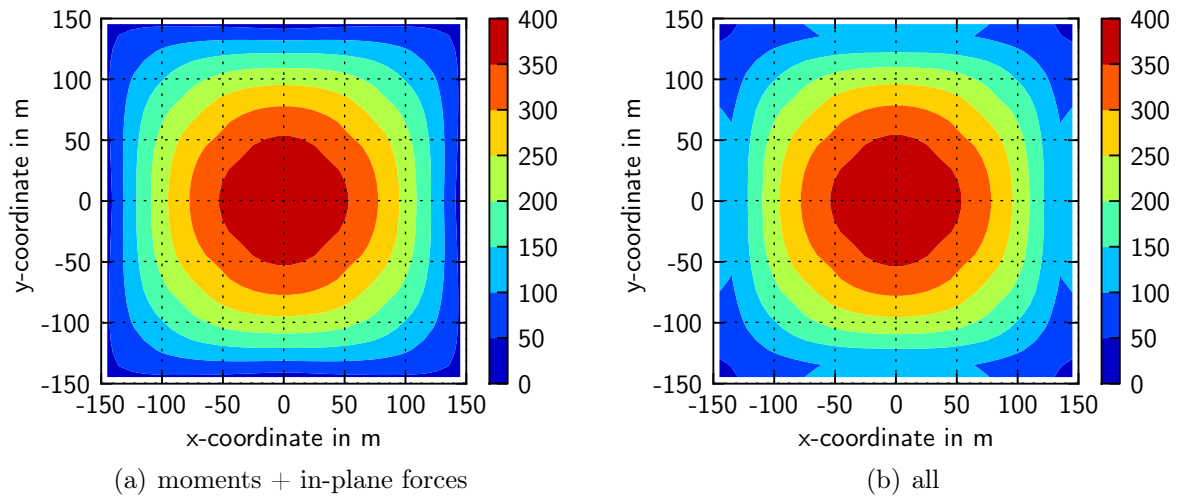


Figure 4.15: Maximum von-Mises stress in the unit cell obtained by localisation with different considered section forces. Values are in MPa

edges, the maximum stresses arise in the diagonal beams, due to the dominating effect of the transverse shear forces.

The maximum stress for the homogenised model is obtained by taking the maximum von-Mises stress in the unit cell stress field obtained by localisation with the appropriate section force combination. Different combinations of section forces are considered. Figure 4.15 shows a comparison between the field of the maximum localised stress in each unit cell for different considered section forces. Considering only in-plane forces and section moments, as in thin-plate theory, captures the maximum stress in the centre of the plate well. However, the stresses close to the edges, which are dominated by the transverse shear forces are not accurately represented. Including the transverse shear forces in the localisation procedure leads to much better results in this area. A more detailed comparison is offered in Fig. 4.16 for the maximum stresses around the symmetry plane of the structure. The error in the stress values obtained by localisation with respect to the full model is minimal (around 2%) in areas where the stress is dominated by bending. In areas where the stresses are dominated by transverse shear, the transverse shear section forces must be taken into account in the localisation procedure in order for the error to remain small (<5%). If transverse shear forces are not taken into account, the error can get very large (see Fig. 4.16a). The graphs also show, that disregarding in-plane section forces leads to equivalent results. This can be explained by the absence of in-plane loading.

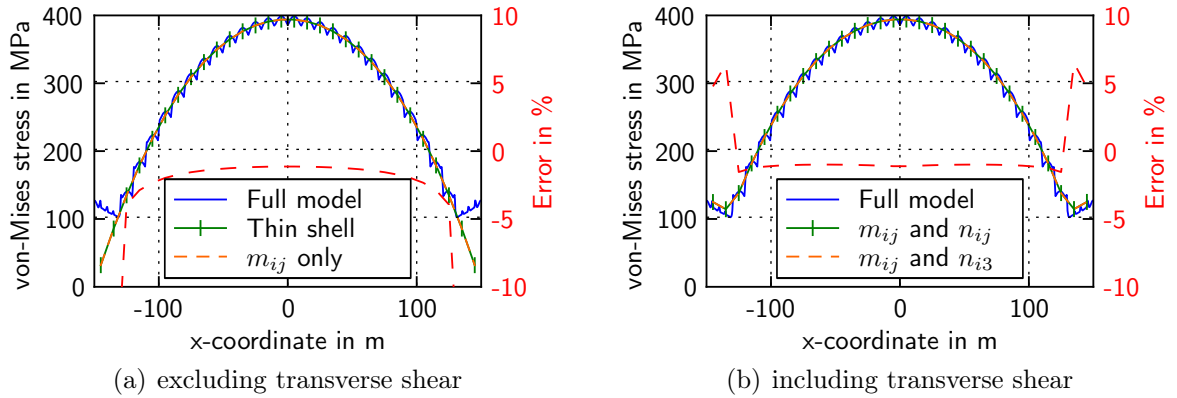


Figure 4.16: Comparison of the maximum von-Mises equivalent stress around the symmetry plane computed by the full model, and the maximum von-Mises stress in the corresponding unit cells obtained by the localization procedure, with different combinations of section forces (a) excluding, and (b) including, transverse shear forces.

4.6 Conclusion

The presented computational homogenisation theory is useful to model a complex, plain-periodic structure by an equivalent shell model. Such shell models can significantly reduce the number of degrees of freedom in a discretised model and, hence, the computational effort. Additionally, the application of boundary conditions can be simplified. Localisation can be used to obtain stress fields in the unit cells at arbitrary location in the global structure.

A method to obtain a failure criterion defined in the space of the global, i.e. plate, section forces, the so called failure surface, was presented. It was shown that the use of such a failure surface to evaluate a failure criterion can offer significant reduction of the computational effort if many different section force combinations have to be evaluated.

Chapter 5

Experimental Testing

5.1 Froude's Scaling Law

In the case of water flow with a free surface Froude's scaling law is most applicable, because the gravitational effect predominates over viscous, surface tension, or other effects [9]. The Froude number defined as

$$\text{Fr} = \frac{v^2}{gl}, \quad (5.1)$$

where v is a characteristic velocity, l is a characteristic dimension, and g is the acceleration of gravity. It can be interpreted as the ratio between gravitational and inertial force acting on a fluid element [9].

In order to preserve geometric similitude between the prototype and the scale model, all dimensions are scaled by a scale factor c , relating the dimensions by

$$l_p = cl_m, \quad (5.2)$$

where the indices p and m denote prototype and model quantities. Maintaining a constant Froude number for prototype and model under the constraint of constant gravitational acceleration ($g_p = g_m = g$) requires the model speed to be

$$v_m = \frac{v_p}{\sqrt{c}}. \quad (5.3)$$

The correct scaling of the model mass can be obtained by requiring the shape of the displaced volume, equal to m/ρ , to be geometrically similar: The displaced volume will be proportional to l^3 ; The constraint of water with the same density in both model and prototype environment, hence, requires:

$$m_m = c^{-3}m_p. \quad (5.4)$$

Table 5.1 sows the correct Froude scaling for selected quantities. It can be seen, that the correct scaling for any derived quantity must follow from the scaling of the fundamental quantities mass, length and time.

Quantity	Dimension	Scaling
Length	L	c
Mass	M	c^3
Time	T	$c^{\frac{1}{2}}$
Velocity	LT^{-1}	$c^{\frac{1}{2}}$
Frequency	T^{-1}	$c^{-\frac{1}{2}}$
Pressure	$ML^{-1}T^{-2}$	c
Density	ML^{-3}	1
Energy	ML^2T^{-2}	c^4
Spring stiffness	MT^{-2}	c^2
Mass per area	ML^{-2}	c

Table 5.1: Scale factors for Froude scaling of different quantities.

5.2 Scale Models

5.2.1 Design of Equivalent Models

Building a Froude scale test model of the desired prototype structure, i.e. an air chamber supported floating platform in a size range of 50-300 m, requires rather high scale factors for model tanks allowing model widths of several meters. The construction of an exact scale model of the original frame structure would be very difficult due to this large scaling factor.

As only the overall behaviour of the structure should be studied, a resolution of the framework detail is not of interest in the model tests. Therefore, only the main properties, bending stiffness and mass per area, have to be correctly reproduced by an equivalent model structure. The design values for bending stiffness D , transverse shear stiffness K^{ts} , and mass per area w , of prototype framework can be computed from the geometry of the unit cell by the homogenisation procedure described in Chapter 4. Values obtained for two different prototype cells, which will be used in the following are given in Table 5.2. The properties of the model plate can then be calculated from the prototype values according to Froude's law by

$$K_m^{ts} = c^{-2} K_p^{ts}, \quad (5.5a)$$

$$D_m = c^{-4} D_p, \quad (5.5b)$$

$$w_m = c^{-1} w_p. \quad (5.5c)$$

A sandwich composed of a core and thin faces of equal thickness allows the designer to

	Prototype 1	Prototype 2
D in Nm	$130.0 \cdot 10^6$	$140.42 \cdot 10^6$
K^{ts} in N/m	$35.4 \cdot 10^6$	$8.893 \cdot 10^6$
w in kg/m ²	20.0	13.166

Table 5.2: Homogenised plate properties of the prototypes.

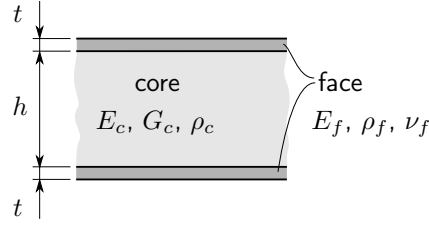


Figure 5.1: Sandwich dimensions

choose two independent materials and their thickness. As the material density and the Young's modulus are determined for specified materials, the geometric dimensions remain the only free parameters. The properties for a sandwich with thin faces ($t \ll h$), depicted in Fig. 5.1, are calculated by

$$K^{ts} = G_c h, \quad (5.6a)$$

$$D = \frac{E_f h^2 t}{2(1 - \nu_f^2)}, \quad (5.6b)$$

$$w = 2t\rho_f + h\rho_c. \quad (5.6c)$$

The above equations were derived under the assumption that the transverse shear stiffness is determined only by the core, and the bending stiffness only by the faces [57]. To take the bending stiffness contribution of the core into account one can add the corresponding term to Eq. (5.6b) giving

$$D = \frac{E_c h^3}{12(1 - \nu_c^2)} + \frac{E_f t h^2}{2(1 - \nu_f^2)}. \quad (5.7)$$

To match the model properties to the desired values the three conditions, Eqs. (5.6a), (5.6c) and (5.7), need to be satisfied, which is not possible with only two free parameters. Matching the transverse shear stiffness of the model is considered less important. Therefore, the condition Eq. (5.6a) is neglected in the following. A database containing the properties of available face and core materials was set up. This allows the computation of the bending stiffness and mass per area, by Eqs. (5.6c) and (5.7), for all possible material combinations. The results can then be ranked according to the cumulative relative error with respect to the desired values, identifying the best sandwich.

The axial stiffness of the air chambers is determined by the membrane stiffness of the skirt and by the compressibility of the gas in the chamber, as derived in Section 2.2. Recalling Eq. (2.7) the axial stiffness is

$$k_c = p_c \gamma \left(1 + \frac{2\gamma r p_c}{tE} \right)^{-1} \frac{r^2 \pi}{h}, \quad (5.8)$$

where p_c denotes the absolute air pressure in the chamber, r the radius and h the height of the chamber, E the Young's modulus and t the thickness of the membrane. The pressure difference between internal chamber pressure and the atmospheric pressure is determined by the mass of the platform and the geometry of the air chambers. It is several orders of magnitude smaller than the atmospheric pressure (ca. 50 Pa vs. 101.325 Pa). Therefore, the absolute pressure in the air chamber will be almost the same for the prototype and

the model. The axial stiffness of the air chamber then does not scale like the Froude scale requirement of c^2 , if the skirt is scaled geometrically. The axial stiffness of the air chambers in the model will be generally too large. A possibility to achieve a correctly scaled axial stiffness is to adjust the membrane stiffness of the model skirt accordingly: The desired, i.e. Froude scaled, ratio between axial air chamber stiffness of prototype and model is

$$\frac{k_{c,p}}{k_{c,m}} = c^2 \quad (5.9)$$

To enforce above condition the membrane stiffness of the model skirt

$$E_m t_m = \frac{2\gamma r_m p_c}{\frac{2\gamma r_m p_c}{E_p t_p} c^2 + c - 1}, \quad (5.10)$$

must be realised. For typical skirt materials and scale factors this condition leads to very thin ($<20 \mu\text{m}$) membranes. Therefore, in practice the axial stiffness of the air chamber will be too high. To come close to the desired stiffness, the skirt membrane should be as thin and flexible as possible.

5.2.2 Description of the Scale Models

Two different models of different prototypes were built and tested. Both have an arrangement of four cylindrical air chambers with circular cross section. The centres of the air chambers coincide with the centres of the quarters of the quadratic plate. The main dimensions of the two models are noted in Table 5.3. Different composite sandwiches were used as plates to obtain the desired plate properties [71, 72]. The skirt was manufactured from polyethylene (PE) foil.

		Model 1 (small)	Model 2 (large)
Scale factor		60	75
Plate	Size in m	0.98	4.0
	Bending stiffness in Nm	9.994	191.6
	mass per area in kg/m^2	0.448	0.864
Skirt	Diameter in m	0.169	1.8
	Length in m	0.320	0.323
	Chamber height in m	0.125–0.208	0.2
	Membrane thickness in μm	13.0	10.0
	Ballast per chamber in kg	0.096–0.448	0.848

Table 5.3: Data of the scale models.

5.3 Behaviour of the Platform in Waves

One of simplest methods to determine the steady state response of a system to harmonic forcing, i.e. its transfer function, is to measure it directly: The system is excited with a

single, harmonic input signal of known amplitude and frequency, and the steady state output is measured. From this measurement one point of the transfer function can be computed. This experiment needs to be repeated for all frequencies of interest. A disadvantage of this method is, that it may take a long time to determine the transfer function in high resolution. On the other hand, the generation of harmonic forcing is simple, and no assumptions about the model must be made in order to allow for its identification.

Another method to determine the transfer function is to use spectral analysis. Here a linear system is excited with a signal with broadband frequency content. The frequency content of the output signal, i.e. the output spectrum, is then compared to the input spectrum yielding an estimate of the transfer function of the system. While this method ideally only requires one experiment to determine the transfer function, in practise the generation of a sufficiently broadband wave spectrum is difficult. Furthermore, the frequency resolution of the transfer function estimate depends on the length of the measurement, requiring long measurement runs, which typically lead to reflections in a wave tank.

Both methods were applied to determine the transfer functions of platform models. Details of the analysis procedure will be given in the following.

5.3.1 Test Setup

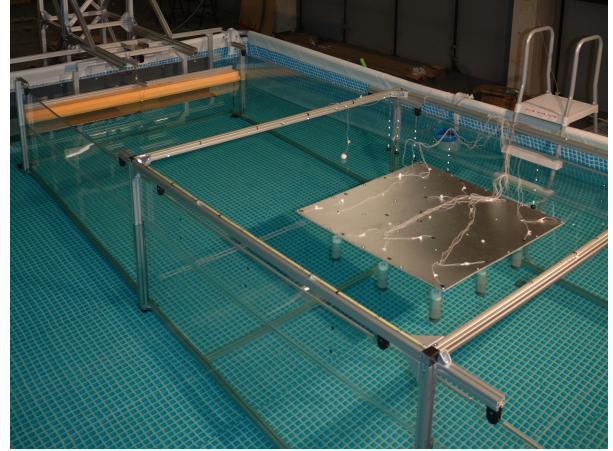
A typical two-dimensional wave tank consists of a long channel and a wave making device capable of producing waves travelling in one direction [9]. At the end of the channel, an active or passive wave absorbing structure may be installed to prevent reflected waves from impacting the measurement. The floating structure can be towed through the tank in order to test its behaviour in the combination of forward speed and waves. However, for the stationary floating platform under investigation here, towing is not necessary.

A test facility was built to test the small model. Two parallel separation walls were inserted into a commercial swimming pool, creating a 2 m wide, 9 m long and 1 m deep wave tank. At one end a plunger type wave maker was created by a floating body across the channel width. The body is excited to oscillate vertically by forces introduced by an elastic connection to a electromechanical shaker. The side of the body facing into the tank is inclined at 45° with respect to the water surface, thereby maximising the height of the produced waves [73, 79]. In this way it is possible to exploit the natural frequency of the floating body. Regular waves with a frequency range of 1.2 to 5 Hz can be produced by this system. The lower limit in the frequency range is given by the operation range of the shaker, and the upper by the response characteristic of the floating body. At the other end of the channel an inclined (ca. 15°) plate was installed, creating a wave absorbing beach. Figure 5.2 shows some photos of the test facility.

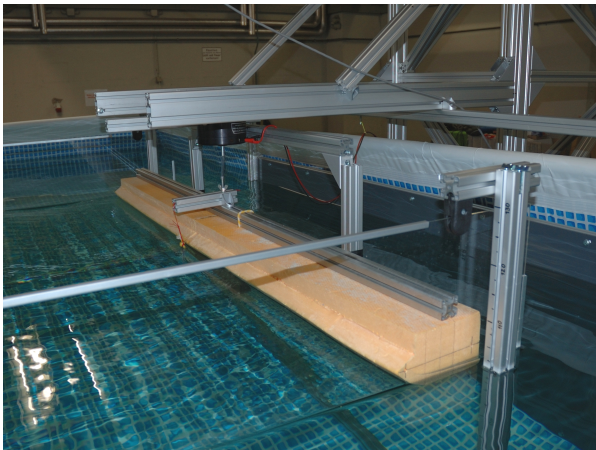
The large model was tested in the 180 m long 10 m wide and 5 m deep towing tank of the Vienna Model Basin [76]. The tank was equipped with a flapper type wave maker capable of producing both regular and irregular waves [76]. The water elevation was measured at the side of the tank (approximately 30 cm from the wall) at one location before the waves hit the model with a capacitive wave probe. Figure 5.3 shows a picture of the model in the tank.



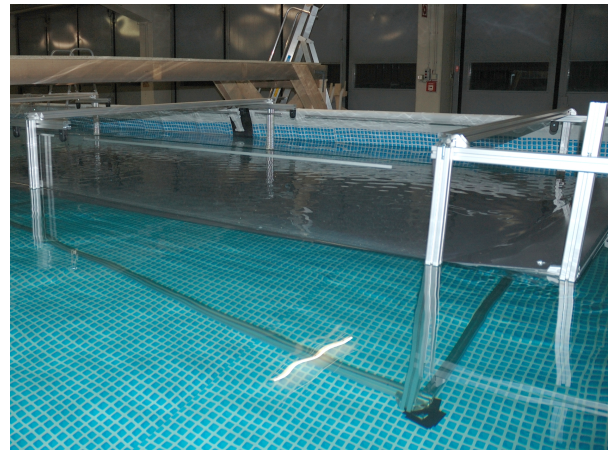
(a) Water basin



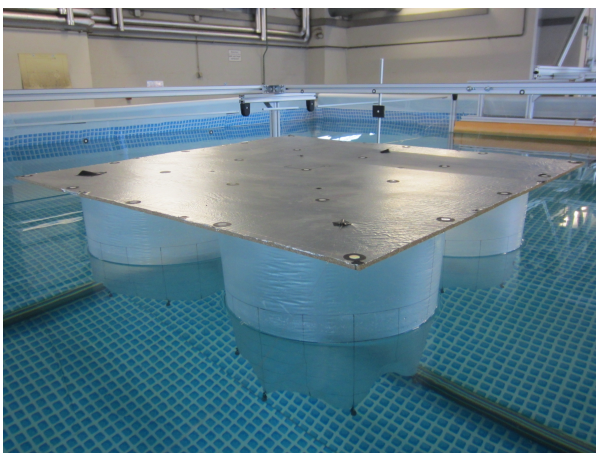
(b) Separation walls



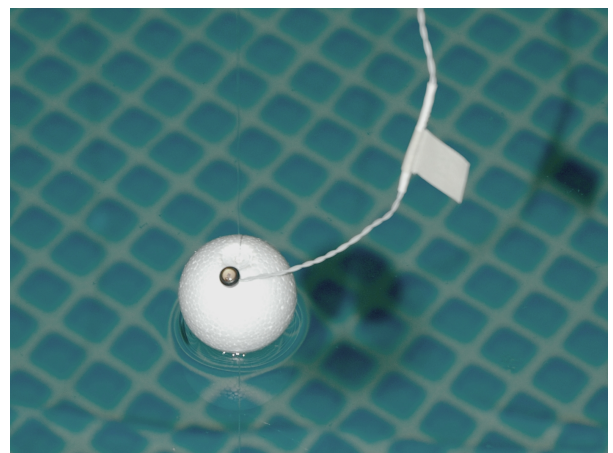
(c) Wave maker



(d) Beach



(e) Model



(f) Wave probe

Figure 5.2: Images of the testing tank for the small model.

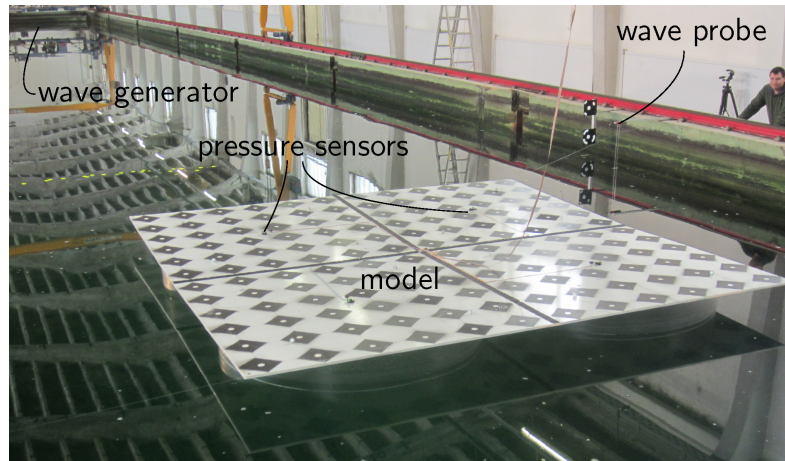


Figure 5.3: Picture of the model in the towing tank. The wave generator is visible at the end of the tank, the wave probe close to the right tank wall.

5.3.2 Measurement of Displacements and Deformations

In order to minimise the impact of the measurement system on the system behaviour, optical measurement systems are employed to record the spacial position of markers fixed to the platform. Two different commercially available 3D motion capture system using infra-red markers were used [46, 56]. A third measurement system offering a larger spacial resolution, i.e. a larger number of targets, developed by Rupnik and Jansa [60] was used alongside the commercial systems.

All measurement systems output the spacial position of every target point at every measured time frame. The output coordinates are defined in the frame of reference of the measurement system, subsequently called camera frame and denoted with 0. The camera frame might not be convenient for further processing of the data, because it might not relate to the physical surroundings. Therefore, the data points are transformed into a Cartesian coordinate system aligned with the water surface and wave direction. This coordinate system will be termed *ground frame*, and denoted with g , in the following. In order to define the position and orientation of the observed structure a coordinate system moving with the structure, subsequently termed *body frame* and denoted with 2, will be used. Figure 5.4a shows the different coordinate systems.

In general a Cartesian coordinate system can be defined by three, non-collinear points in space, as described in detail in Appendix D.6. In order to define the relation of the ground frame with respect to the camera frame the coordinates of this three defining points must be known. They can, for example, be specified by markers placed in the measurement space at physical points of interest. Now the transformation relation between the two systems can be defined, as described in Appendix D.7. The body frame should move with the observed floating platform and represent it's rigid body motion. For the case of a deformable body, the definition of a coordinate system by three points poses the problem of coupling of deformation and rigid body movements. Therefore, all markers located at the ideally plane plate are used to define the moving frame: The x - y plane of the body frame is defined the plane

$$z_g = k_{00} + k_{10}x_g + k_{01}y_g, \quad (5.11)$$

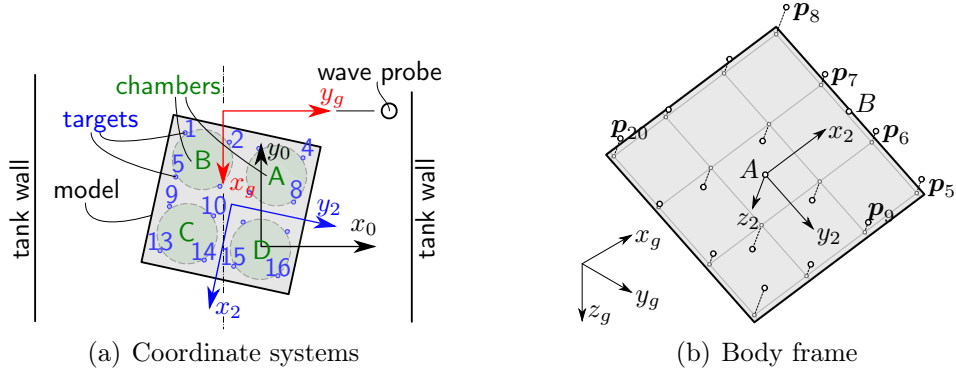


Figure 5.4: Sketch showing the different coordinate systems (a) and the definition of the body frame by a surface fit to the platform markers (b).

with coefficients k_{mn} obtained by a least squares fit to the marker positions ${}^g\mathbf{p}_i$ of the platform. The origin of the body frame is the normal projection of the centre of all markers of the platform onto the interpolation surface. By the vector from the origin to the projection of an arbitrary marker of the platform onto the interpolation surface, the x_2 -direction is defined. The z_2 -direction is defined by the normal vector of the interpolation surface $\mathbf{n} = [-k_{10}, -k_{01}, 1]^T$. The whole process is visualized in Fig. 5.4b. The orientation of the body frame with respect to the ground frame can be described by the three Euler angles, defined in detail in Appendix D.8.

The measured positions of the platform markers displayed in the moving frame describe the deformation of the structure. However, this description is somewhat extensive, especially if a lot of markers are measured on the platform. An efficient description can be achieved if a model approach is used. In order to characterise the deformation figure a set of arbitrary deformation modes are chosen. The modal basis comprises the six rigid body displacement modes, two plate bending modes and one plate twist mode. The rigid body rotation modes are included to check if the moving coordinate system indeed follows the rotation of the plate. The modes are displayed in Fig. 5.5. In order to compute the modal coordinates corresponding to a deformation vector $\mathbf{m}_e = [m_{x_1}, m_{x_2}, \dots, m_{x_M}, m_{y_1}, \dots, m_{y_M}, m_{z_1}, \dots, m_{z_M}]^T$, the linear system of equations

$$\mathbf{V}\boldsymbol{\eta} = \mathbf{m}_e, \quad (5.12)$$

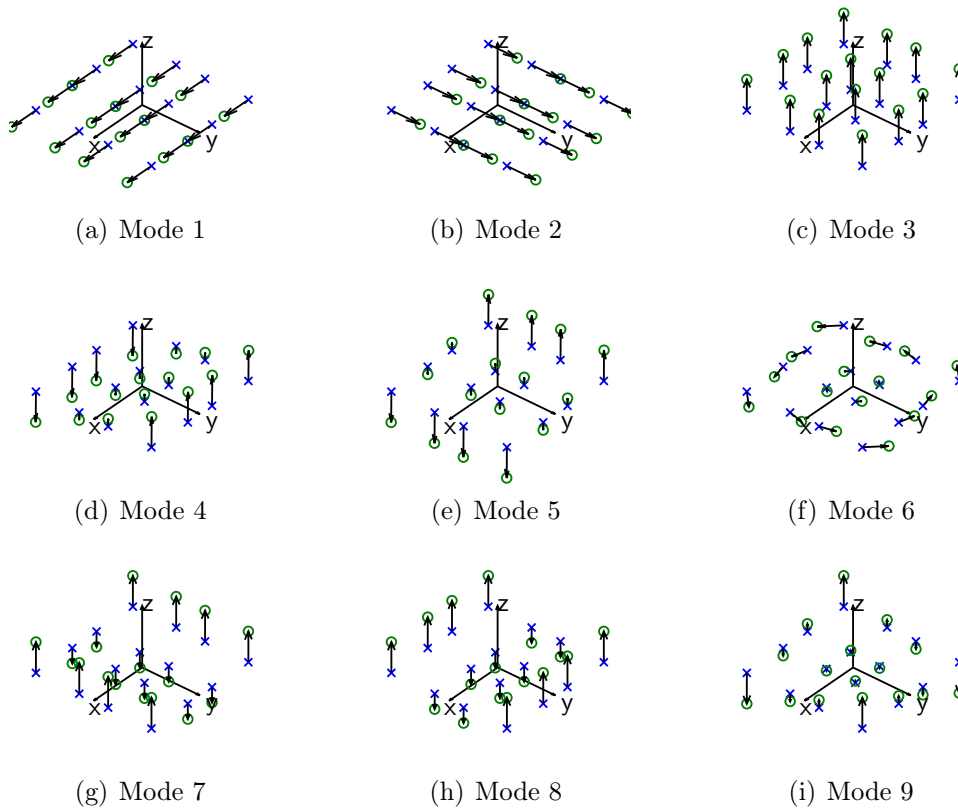


Figure 5.5: Modal basis used to characterise the deformation: (a) translation in the x -direction; (b) translation in the y -direction; (c) translation in the z -direction; (d) rotation around the x -axis; (e) rotation around the y -axis; (f) rotation around the z -axis; (g) bending around the y -axis; (h) bending around the x -axis; (i) twist. The displaced points (green circles) are connected with the original points (blue crosses) by the displacement vectors (black arrows).

has to be solved. The columns of the system matrix

$$\mathbf{V} = \begin{bmatrix} v_{1x_1} & v_{2x_1} & \dots & v_{Mx_1} \\ v_{1x_2} & v_{2x_2} & \dots & v_{Mx_2} \\ \vdots & \vdots & & \vdots \\ v_{1x_N} & v_{2x_N} & \dots & v_{Mx_N} \\ v_{1y_1} & v_{2y_1} & \dots & v_{My_1} \\ \vdots & \vdots & & \vdots \\ v_{1y_N} & v_{2y_N} & \dots & v_{My_N} \\ v_{1z_1} & v_{2z_1} & \dots & v_{Mz_1} \\ \vdots & \vdots & & \vdots \\ v_{1z_N} & v_{2z_N} & \dots & v_{Mz_N} \end{bmatrix}, \quad (5.13)$$

contain the modal displacement vectors of the M arbitrary deformation modes $\mathbf{v}_i = [v_{ix_1}, v_{ix_2}, \dots, v_{ix_N}, v_{iy_1}, \dots, v_{iy_N}, v_{iz_1}, \dots, v_{iz_N}]^T$, which describe the modal displacements of the N platform points. The modal displacement vectors are normalized to a maximum point displacement of 1 m. The vector of modal coordinates $\boldsymbol{\eta} = [\eta_1, \eta_2, \dots, \eta_M]^T$ contains the M modal coordinates.

If the number of modes M is smaller than the number of degrees of freedom $3N$ the linear system of equations (Eq. (5.12)) is overdetermined. It is then solved in the least squares sense. The least square solution is unique if the system matrix is of full rank, i.e. $\text{rank}(\mathbf{V}) = M$. This is the case for a set of linearly independent deformation modes. The solution is computed in Matlab by the "\"-operator [67]. The experimentally determined deformation figure \mathbf{m}_e is approximated by the corresponding modal coordinates determined by the least squares solution of Eq. (5.12). The shape of the residual mode \mathbf{m}_r defined by

$$\mathbf{m}_r = \mathbf{m}_e - \mathbf{V}\boldsymbol{\eta}, \quad (5.14)$$

can be used to determine the quality of the modal approximation. If significant deformation modes were not included in the modal basis, they would show up in the residual mode shape. Figure 5.6 shows the experimentally determined deformation at wave frequency, the modal approximation, and the residual mode. It can be seen that the modal

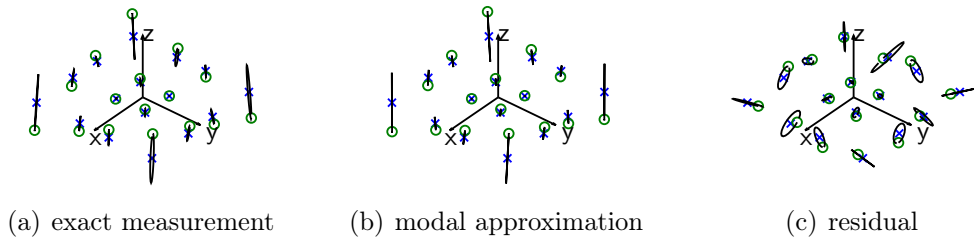


Figure 5.6: Comparison of the steady state deformation figures. The maximum displacements of the deformation figures (a) 7.338 mm, (b) 7.431 mm, and (c) 0.845 mm are scaled to the same value for all cases to better visualize the deformation figure. The displaced points (green circles) move on trajectories (black lines) around the original points (blue crosses).

Mode	1	2	3	4	5	6	7	8	9
participation in %	0.0	0.0	2.2	0.1	0.2	3.5	3.1	5.7	85.2

Table 5.4: Modal participation in the modal approximation of the deformation shown in Fig. 5.6b. The corresponding modes are depicted in Fig. 5.5.

approximation is of very good quality. The total displacement is almost the same for the modal approximation and the experimentally measured shape. The residual is very small in comparison (ca. 11.5%), and its shape looks more or less random.

The participation of the individual modes in the modal approximation can be evaluated by computing their modal participation factors

$$p_{\eta_i} = \frac{|\eta_i|}{\sum_{j=1}^M |\eta_j|}. \quad (5.15)$$

The modal participation factors for the deformation mode depicted in Fig. 5.6b are denoted in Tab. 5.4.

5.3.3 Regular Wave Experiments

Each point of the transfer function is determined by one measurement run in regular waves, where wave excitation and platform response are recorded over the measurement time. Therefore, a sufficiently high number of experiments is necessary to obtain transfer functions with acceptable frequency resolution. The transfer functions are defined by the steady state amplitude and phasing of every measured quantity. Because the length of the transient phase after starting the wave generator is not a priori known, and may differ slightly from experiment to experiment, a sufficiently large time interval must be measured. The system is assumed to be linear. A simple, one dimensional example for the expected system behaviour is the damped spring mass system with harmonic forcing with the equation of motion

$$m\ddot{x} + c\dot{x} + kx = \hat{f}e^{i\omega t}, \quad (5.16)$$

where m denotes the oscillating mass, c the damping and k the spring constant. The general solution of this linear ordinary differential equation is obtained as the sum of its homogeneous and particular solution [21]. In Fig. 5.7a the exponentially decaying oscillation of the transient phase as well as the steady state time interval can be clearly recognized.

As the steady state signals are harmonic it appears straightforward to employ Fourier analysis, which is briefly summarised in Appendix D.1. Fourier transformation offers an efficient and robust way to extract the steady state oscillation amplitude as well as the oscillation frequency and phase from the time signal. In the practical implementation the discrete form of the Fourier transform, described in detail in Appendix D.2, is used. The signal $x(t_j) = x_j$ with N data points, equally spaced in time from $t = 0$ to $t = (N - 1)\Delta t$ is sampled with the sampling frequency $1/\Delta t$. The maximum frequency which may be present in the sampled signal is $f_c = 1/(2\Delta t)$, the so called Nyquist frequency, which equals half the sampling frequency [61]. If higher frequencies are present aliasing occurs. The frequency resolution $\Delta f = 1/(N\Delta t)$ obtainable with the discrete Fourier

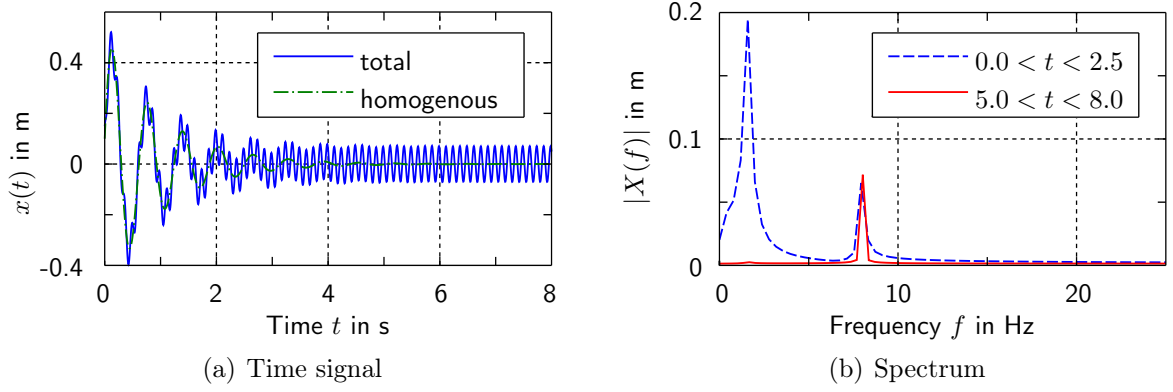


Figure 5.7: Total and homogeneous solution of Eq. (5.16) for $m=1$ kg, $k=100$ N/m, $c=2$ kg/s, $\hat{f}=10$ N, $\omega_f=50.266$ s $^{-1}$ (a), and the absolute value of the Fourier coefficients computed from different parts of the total solution (b).

transform (DFT) depends on the length of the signal. To determine the amplitude of a harmonic with a specific frequency most accurately, the signal length should correspond to an integer multiple of this frequency. Frequencies in the signal which do not lie exactly on the discrete DFT frequencies cause leakage. Figure 5.7b shows the amplitude spectra of two different parts of the signal depicted in Fig. 5.7a. The spectrum of the transient phase shows a peak at the system's natural frequency in addition to the smaller peak caused by the harmonic forcing.

The phase difference between the wave signal and the output signals depends on the relative position at which the water elevation is measured. In order to achieve comparable measurements the position dependent phase difference must be accounted for. The phase difference of the platform response should always be measured with respect to a reference wave located in the centre of the platform. The geometry is depicted in Fig. 5.8. For the sake of simplicity the x_g -direction coincides with the propagation direction of the waves. For a regular wave measurement the wave signal can be approximated by good accuracy with a single harmonic. The phase velocity of this harmonic can be computed by

$$c_p = \lambda f = \frac{g}{2\pi f}, \quad (5.17)$$

according to linear wave theory. In Eq. (5.17) g denotes the gravitational acceleration, f the frequency of the harmonic, and λ the wave length. A wave measured at a position Δx before the model position will arrive at the model with a time lag $\Delta t = \Delta x/c_p$. The

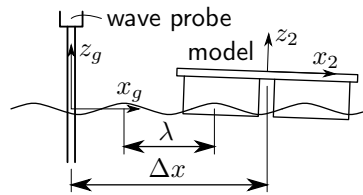


Figure 5.8: Phase difference

signal at the model position can be written as

$$\begin{aligned}
 w_n(t) &\approx |W_n| \cos \left(-\arctan \frac{\text{Im}(W_n)}{\text{Re}(W_n)} - \omega_n (t - \Delta t) \right) \\
 &= |W_n| \cos \left(-\arctan \frac{\text{Im}(W_n)}{\text{Re}(W_n)} + \underbrace{\frac{\omega_n^2 \Delta x}{g}}_{\varphi_x} - \omega_n t \right), \\
 &= \text{Re} \left(W_n e^{-i\varphi_x} e^{i\omega_n t} \right)
 \end{aligned} \tag{5.18}$$

where $\omega_n = 2\pi f_n$ is the angular frequency of the considered harmonic. In order to correct the phase of the Fourier coefficients of the measured wave signal they have to be multiplied by $e^{-i\varphi_x}$, where φ_x is the position dependent phase angle computed by

$$\varphi_x = \frac{(2\pi f_n)^2 \Delta x}{g}. \tag{5.19}$$

The value of the transfer function for a single regular wave measurement is obtained by dividing the Fourier coefficient of the output signal by the phase-corrected Fourier coefficient of the wave signal. The so called response amplitude operator (RAO) is the absolute value of the transfer function and describes the ratio between output and input amplitude. The response amplitude operators for the translational degrees of freedom should be normalised to the wave amplitude. For the rotational degrees of freedom the response amplitude operators should be normalised to the wave slope [34]. The pressure response is normalized to the dynamic pressure at the water surface, which can be computed from the water elevation by multiplying by $\rho_w g$, where ρ_w is the water density. The modal displacements are normalized to the wave amplitude. Regardless of the quantity of normalization, i.e. wave amplitude, wave slope, and dynamic pressure, all phase differences are computed with respect to the phase-corrected water elevation signal. This is important for the wave slope signal, which has in fact a phase shift of π with respect to the wave elevation signal.

5.3.4 Experiments in Irregular Waves

In an irregular wave measurement the model is excited by a defined superposition of regular waves. The excitation follows a predefined wave spectrum. Time signals of excitation and system response are recorded. Spectral estimates of the time signals can then used to determine the transfer function of a linear system.

5.3.4.1 Spectral Analysis

Converting the measured time records of excitation $x(t)$ and response $y(t)$ into the frequency domain, one can determine the transfer function of a linear system. The estimate for the transfer function is

$$H(\omega) = \frac{S_{xy}(\omega)}{S_{xx}(\omega)}, \tag{5.20}$$

where $S_{xx}(\omega)$ is the (autospectral) energy density spectrum of the input, and $S_{xy}(\omega)$ is the cross spectral density function between input and output. The absolute value of the

transfer function, i.e. the RAO, can be estimated using only autospectral energy density spectra of in- and output by

$$RAO(\omega) = |H(\omega)| = \sqrt{\frac{S_{yy}(\omega)}{S_{xx}(\omega)}}, \quad (5.21)$$

where all phase information is lost. The energy density spectrum of the measured signal can be obtained using different estimation methods.

5.3.4.2 Spectral Estimation

The mean square spectral density of a time signal can be estimated in various ways. The different estimation methods can be categorized into

- Non-parametric methods,
- Parametric methods, and
- Subspace methods.

In non-parametric methods the mean square spectral density, or power spectral density (PSD), is estimated directly from the time signal. The simplest non-parametric method is the periodogram. The variance of the estimation can be reduced by more complex methods like Welch's method [81] or multitaper methods [68].

Parametric methods are built on the assumption that the signal is the output of a linear system with white noise as input. The spectrum estimate is the generated by means of system identification. This methods will not be treated in the following.

Subspace methods, also known as high-resolution methods or super-resolution methods, generate frequency component estimates for a signal based on an eigenanalysis or eigendecomposition of the autocorrelation matrix. They are especially useful for the estimation of line-spectra [67].

In the following different estimators are explained and tested on an example signal. As an example a short term wave record of a sea state with Pierson-Moskowitz spectrum with $H_s=3.06$ cm and $T_m=0.7$ s is used. The signal is the sum of 2991 harmonics, equally spaced in frequencies between 0.1 Hz and 30 Hz. The amplitudes are computed from the spectrum according to Eq. (A.15). The phase angles are taken from a uniform distribution between $-\pi$ and π . The signal is then computed according to Eq. (A.14). Figure 5.9 shows the total, 106 s long signal, and a detail. It can be seen that the sampling frequency of 60 Hz is sufficient.

Periodogram: The periodogram of a realization of a random process, i.e. the discrete series $x_n = x_1, \dots, x_N$, is computed by

$$\hat{P}_{xx}(f_k) = \frac{1}{N} \left| \sum_{n=1}^N x_n e^{-i2\pi n f_k} \right|^2, \quad (5.22)$$

where the sum can be identified as the discrete Fourier transform (DFT) of the series (compare Eq. (D.6)). For real valued signals the one-sided periodogram is computed, i.e. the DFT is evaluated at the frequencies $f_k = f_s k/N$ where f_s donates the sampling

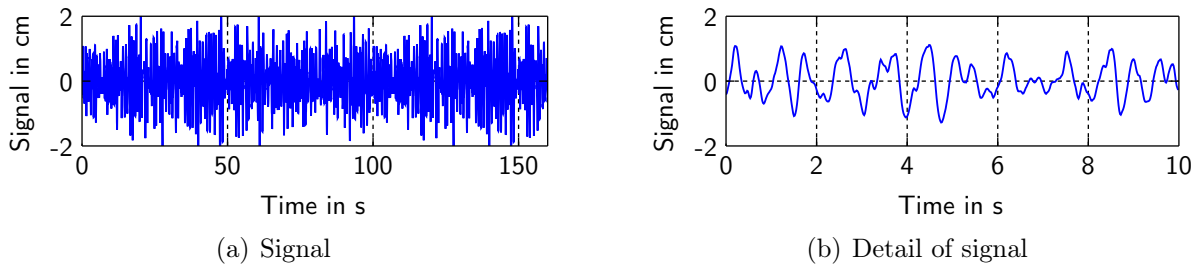


Figure 5.9: Time signal computed from 2991 harmonics with amplitudes generated from a Pierson-Moskowitz spectrum with $H_s=3.06$ cm and $T_m=0.7$ s for equally spaced frequencies between 0.1 Hz and 30 Hz and random phase angles. The sampling frequency is 60 Hz and the signal length 160 s.

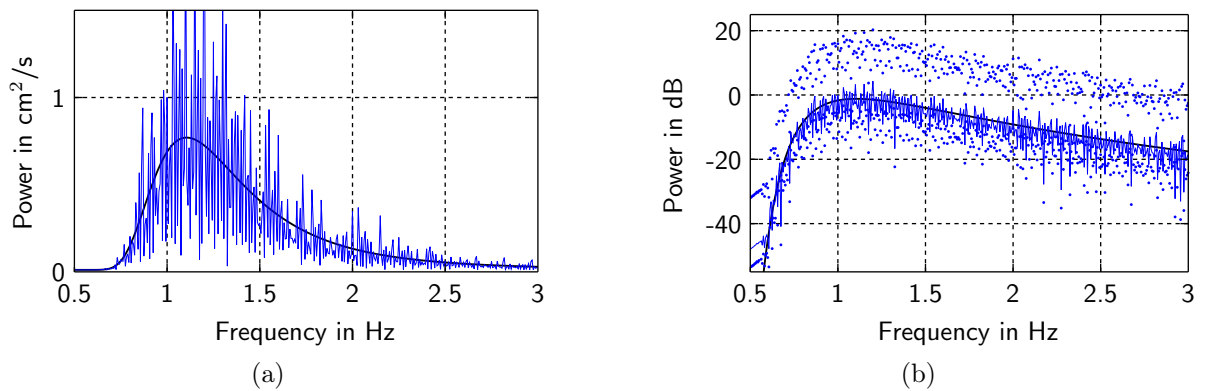


Figure 5.10: Periodogram of the signal in Fig. 5.9 (a); the 95%-confidence interval can only be shown in logarithmic scale (b).

frequency of the data in x_n , and $k = 0, \dots, N/2$. The periodogram is an asymptotically unbiased estimator for the true PSD. For finite signals the estimate is biased. The periodogram is not a consistent estimator of the true spectral density because the variance of the periodogram does not decay to zero regardless of the sample size [67]. Furthermore, the variability of the periodogram is very high. Figure 5.10 shows a periodogram computed from the example signal described above. It can be seen that the true PSD is very badly estimated. Furthermore the 95% confidence bounds are very high, i.e. they can only be displayed in logarithmic scale.

A possibility to decrease the bias of the periodogram is to use windowing [24]. The data is multiplied by a suitable window function prior to computation of the so called modified periodogram. Figure 5.11 shows different window functions for 21 samples as well as their Fourier transforms. The rectangular window corresponds to no window at all, i.e. the original periodogram. The resolution of a periodogram is determined by the width of the main lobe of the Fourier transform of the used window. In order to distinguish two distinct harmonics, their frequency spacing must be greater than the width of the main lobe. Figure 5.12 shows modified periodograms computed with different window functions from the example signal described above. It can be seen that the prediction of the true PSD is still very bad. The confidence levels are comparable to the periodogram.

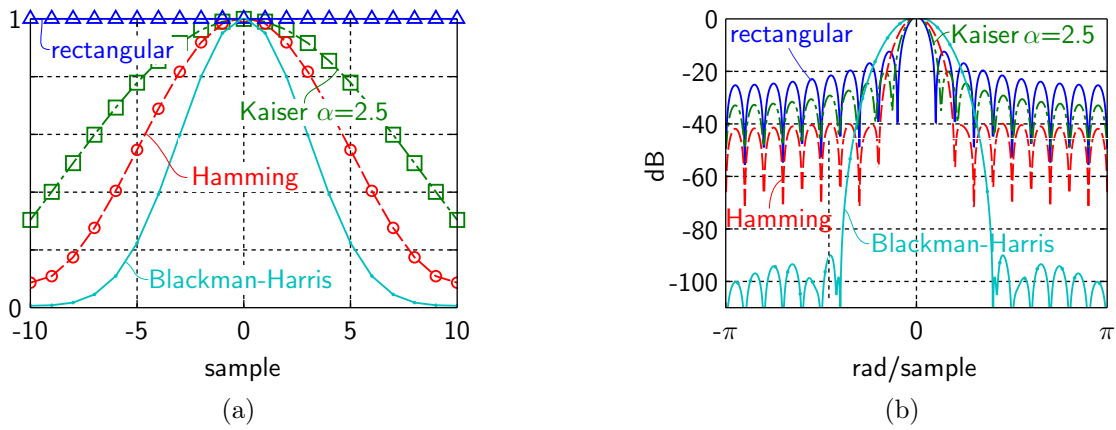


Figure 5.11: Different window functions (a) and their Fourier-transformation (b).

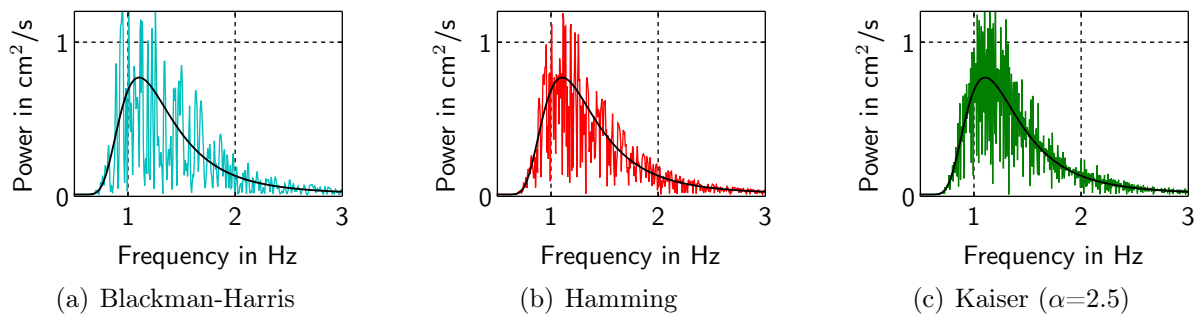


Figure 5.12: Modified periodogram of the signal in Fig. 5.9 using different windows.

Welch's Method: A method to decrease the variance of the spectral estimator is Welch's method. The data is split into overlapping segments from which modified periodograms are computed. These modified periodograms are then averaged, thereby creating a consistent estimator for the true PSD [81]. The overlap should not exceed 30% of the segment length. The segment length N_s can be computed by $N_s = N(100 - p)/100$ where N is the total number of data points and p is the overlap in percent. A small segment length yields bad frequency resolution but low variance, whereas estimations from a few, long segments have better frequency resolution but high variance. For a practical application this trade off must be considered. A possible approach is to try several segment lengths, beginning with short segments, and to compare the results. This procedure is visualized in Fig. 5.13 for the example signal described above. For segments which are too short, excessive frequency leakage occurs (see Fig. 5.13a). If the segments are chosen too long the variance increases and the estimate becomes jagged (see Fig. 5.13d). A suitable number of segments for the estimation of the PSD of the example signal seems to be around 30. It can also be seen that the type of window does not have a major impact. The Blackman-Harris window shows the largest leakage for short segments (see Fig. 5.13a).

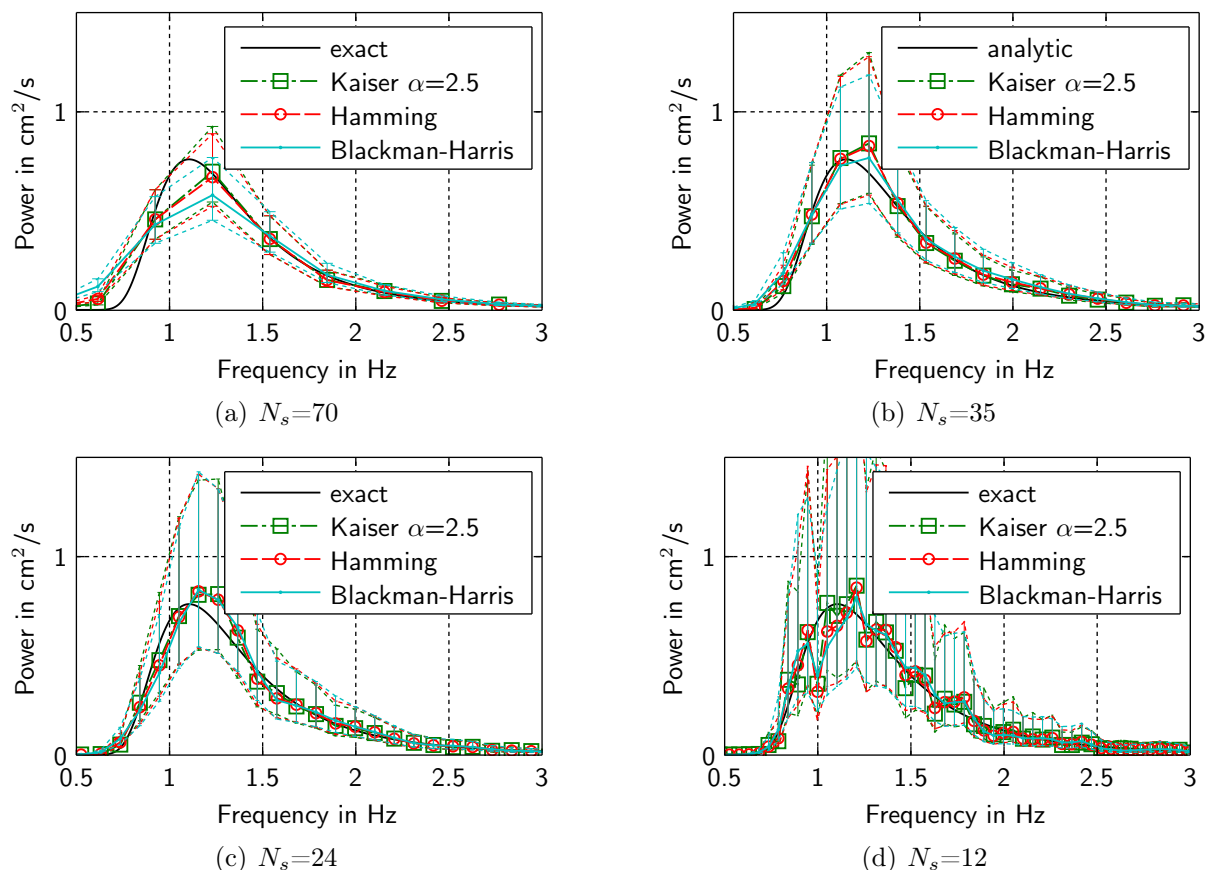


Figure 5.13: Spectral estimation of the signal in Fig. 5.9 by Welch's method: comparison of different segment lengths and window functions. The total signal is split into N_s segments which overlap 30%. The errorbars show the 95% confidence bounds.

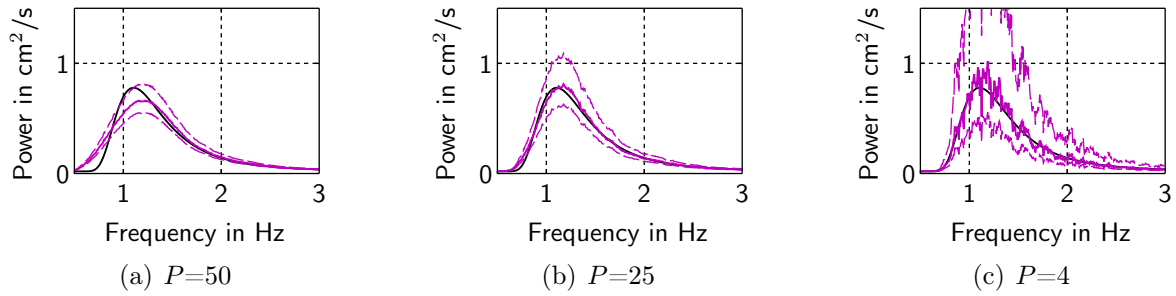


Figure 5.14: Spectral estimation of the signal in Fig. 5.9 by the Thomson multitaper method: Comparison of different time-bandwidth products P . The 95% confidence bounds are shown.

Thomson Multitaper Method: Another method for reducing the variance of a spectral estimator is to use multitaper methods first introduced by Thomson [68]. Here multiple data tapers (i.e. windows), are used to compute a number of modified periodograms, which are then averaged. It is possible to use an weighted average, so called adaptive frequency-dependent average, to reduce the effects of frequency leakage [49, 68]. If data tapers used are mutually orthogonal, the individual spectral estimates are approximately uncorrelated, which efficiently decreases the variance of the estimate [50]. Furthermore, tapers with minimal leakage are desired [49]. Both above requirements are fulfilled by discrete prolate spheroidal sequences described by Slepian and Pollak [62] as tapers, also referred to as prolate eigentapers. A prolate eigentaper with a time-bandwidth product of $P = NW$ is called a $P\pi$ prolate taper; it concentrates spectral energy in frequency bands of width $2W = 2P/N$ [49]. If a higher time-bandwidth product is used, more tapers with wider main lobes can be used. It, therefore, represents a trade-off between variance decrease and resolution increase. Figure 5.14 shows spectral estimates by the Thomson multitaper method of the example signal described above for different values of the time-bandwidth product. It can be seen that, for the analysed signal, an optimal value of P is around 25. For too high values excessive frequency leaking occurs (see Fig. 5.14a), whereas for too low values the estimate becomes jagged and the variance is large (see Fig. 5.14c). Compared to Welch's method, the multitaper method offers a much better frequency resolution with lower variance at the same time (compare Fig. 5.13c and Fig. 5.14b).

5.4 Measurement of Natural Frequencies and Oscillation Modes

The natural frequencies of a structure are an inherent system property and of great importance when the dynamics of the system are investigated. For freely floating structures, the natural frequencies, and especially the corresponding damping factors play an important role when the structure's response to waves is considered. Therefore, it is desirable to measure the natural frequencies and mode shapes of the platform. Most of the experimental methods for estimating oscillation modes involve the the construction

of transfer functions, which requires the measurement of excitation and response simultaneously [1, 16]. If no excitation data is available, the free response can be analysed by the so called Ibrahim time domain method (ITD) [19, 29], which was originally proposed by Ibrahim and Mikulcik [28]. The method allows the calculation of natural frequencies, together with their corresponding damping factors and mode shapes.

In the following the concept of the ITD method is outlined, closely following Ibrahim and Pappa [29]. Different strategies for the assessment of the identification accuracy are presented. Finally, a new method for automatic processing and sorting of results obtained from multiple experiments is presented.

5.4.1 Theory of the Ibrahim Time Domain Method

The equations of motion for a linear dynamic system are commonly written in the form

$$\mathbf{M}\ddot{\mathbf{x}} + \mathbf{C}\dot{\mathbf{x}} + \mathbf{K}\mathbf{x} = \mathbf{0}, \quad (5.23)$$

with \mathbf{M} , \mathbf{C} and \mathbf{K} as the mass, damping, and stiffness matrix, respectively. The response of each degree of freedom contained in \mathbf{x} if m modes are excited can be written as

$$\mathbf{x}(t_j) = \sum_{k=1}^{2m} \boldsymbol{\psi}_k e^{\lambda_k t_j}, \quad (5.24)$$

where λ_k are the $2m$ eigenvalues of the characteristic equation of Eq. (5.23) and $\boldsymbol{\psi}_k$ are the corresponding complex eigenvectors.

The response of a freely oscillating structure $\mathbf{x}(t)$ can be measured at n positions. The signal is commonly sampled, which gives a matrix of measurement data which can be related to the eigenvectors by Eq. (5.24) to form

$$\begin{bmatrix} x_1(t_1) & x_1(t_2) & \cdots & x_1(t_p) \\ x_2(t_1) & x_2(t_2) & \cdots & x_2(t_p) \\ \vdots & \vdots & & \vdots \\ x_n(t_1) & x_n(t_2) & \cdots & x_n(t_p) \end{bmatrix} = \begin{bmatrix} \psi_{11} & \psi_{12} & \cdots & \psi_{1,2m} \\ \psi_{21} & \psi_{22} & \cdots & \psi_{2,2m} \\ \vdots & \vdots & & \vdots \\ \psi_{n,1} & \psi_{n,2} & \cdots & \psi_{n,2m} \end{bmatrix} \begin{bmatrix} e^{\lambda_1 t_1} & \cdots & e^{\lambda_1 t_p} \\ e^{\lambda_2 t_1} & \cdots & e^{\lambda_2 t_p} \\ \vdots & & \vdots \\ e^{\lambda_{2m} t_1} & \cdots & e^{\lambda_{2m} t_p} \end{bmatrix}, \quad (5.25)$$

or simply

$$\mathbf{X} = \boldsymbol{\Psi}\boldsymbol{\Lambda}. \quad (5.26)$$

Writing the above relation for response data that occurs Δt_1 later in time yields

$$x_i(t_j + \Delta t_1) = \sum_{k=1}^{2m} \psi_{ik} e^{\lambda_k(t_j + \Delta t_1)} = \sum_{k=1}^{2m} [\psi_{ik} e^{\lambda_k \Delta t_1}] e^{\lambda_k t_j} = \sum_{k=1}^{2m} \hat{\psi}_{ik} e^{\lambda_k t_j}, \quad (5.27)$$

or again in matrix form

$$\hat{\mathbf{X}} = \hat{\boldsymbol{\Psi}}\boldsymbol{\Lambda}. \quad (5.28)$$

It may be seen that, in the case of $p \geq 2m$, the matrices $\boldsymbol{\Psi}$ and $\hat{\boldsymbol{\Psi}}$ are related through Eq. (5.26) and Eq. (5.28) by

$$\mathbf{A}\boldsymbol{\Psi} = \hat{\boldsymbol{\Psi}}. \quad (5.29)$$

The so called system matrix \mathbf{A} can be obtained by solving

$$\mathbf{X}^T \mathbf{A}^T = \hat{\mathbf{X}}^T, \quad (5.30)$$

where the superscript T donates the matrix transpose. This can be done for example by computing $\mathbf{A} = \hat{\mathbf{X}} \mathbf{X}^T (\hat{\mathbf{X}} \mathbf{X}^T)^{-1}$ or, in a least squares sense, by single value decomposition of the coefficient matrix of Eq. (5.30). Recalling Eq. (5.27) it can be seen, that the columns $\boldsymbol{\psi}_k$ of $\boldsymbol{\Psi}$ and the corresponding columns of $\hat{\boldsymbol{\Psi}}$ are related by $\hat{\boldsymbol{\psi}}_k = e^{\lambda_k \Delta t_1} \boldsymbol{\psi}_k$. Therefore, using Eq. (5.29), one can write

$$\mathbf{A} \boldsymbol{\psi}_k = \underbrace{e^{\lambda_k \Delta t_1}}_{s_k} \boldsymbol{\psi}_k, \quad (5.31)$$

which can be recognised as a standard eigenvalue problem. It can be seen that the eigenvectors $\boldsymbol{\psi}_k$ of \mathbf{A} are the same as the eigenvectors of the dynamic system (described by Eq. (5.23)). The eigenvalues $s_k = a_k + ib_k$ of \mathbf{A} and the desired eigenvalues $\lambda_k = -\delta_k \pm i\omega_{d,k}$ of the dynamic system are related by

$$\delta_k = -\frac{1}{2\Delta t_1} \ln(a_r^2 + b_r^2) \quad (5.32a)$$

$$\omega_{d,k} = \frac{1}{\Delta t_1} \arctan\left(\frac{b_r}{a_r}\right) \quad (5.32b)$$

from which the un-damped natural frequencies $\omega_{n,k} = \sqrt{\omega_{d,k}^2 + \delta_k^2}$ and corresponding damping ratios $\zeta_k = \delta_k / \omega_{n,k}$ can be computed.

5.4.2 Assessment of the Identification Quality

The ITD algorithm produces as many modes as measurement stations are used. Most of these modes are not physical modes of the structure, but so called computational modes. The computational modes can be easily identified by visual inspection, as can be seen in Fig. 5.15. Because visual inspection is very time consuming, it is desired to sort out computational modes automatically. To separate the computational modes from the desired structural modes the system matrix can be further enlarged by using so called transformed measurement stations in the measurement matrix, which are created by time shifting the actual measurement data by time Δt_2 and Δt_3 . The assembly of the measurement matrices is visualized in Fig. 5.16. The real measurement stations are denoted a , b , and c . They can be time shifted by Δt_2 to create artificial measurement stations to increase the number of degrees of freedom of the mathematical system in case the number of structural modes contained in the response is higher than the number of available measurement stations. The time shift Δt_3 is used to create the lower half of the measurement matrices. It, therefore, only contains transformed measurement stations and is used to distinguish between computational and structural modes, as well as to calculate the modal damping in an alternative way.

The assessment of the calculated mode shapes is not always easy and various techniques have been developed to help assessing the quality of identified modes. All of these techniques rely on the fundamental time-shift relationship for perfect identification

$${}^l \boldsymbol{\psi}_{ik} = {}^u \boldsymbol{\psi}_{ik} e^{\lambda_k \Delta t_3}, \quad (5.33)$$

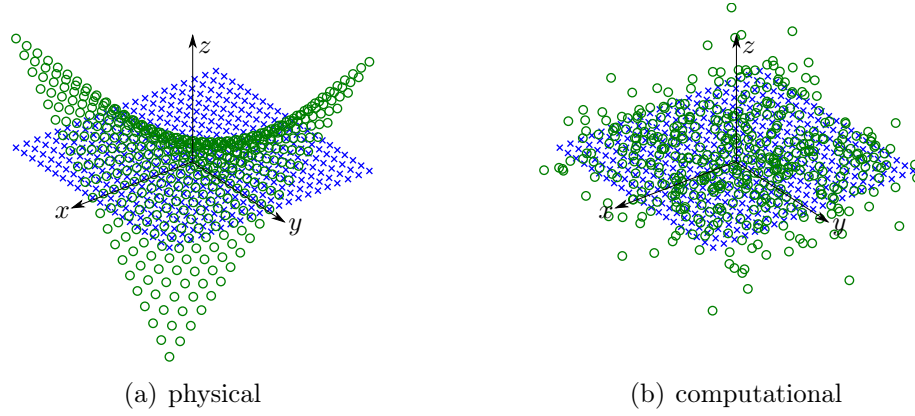


Figure 5.15: Comparison between physical (a) and computational (b) modes extracted by the ITD algorithm.

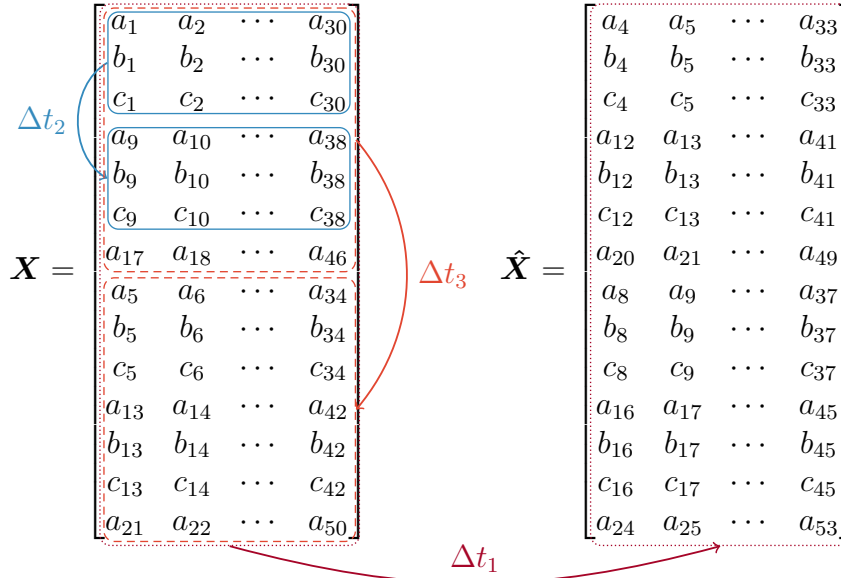


Figure 5.16: Assembly of the measurement matrices.

which relates the time shifted elements in the lower half of the response matrix with the original data in the upper half connected with the calculated eigenvalues. In reality Eq. (5.33) will not be exactly satisfied, and the ratio between expected values (right hand side of Eq. (5.33)) and actually measured values (left hand side of Eq. (5.33)) is the (complex valued) *modal confidence factor* MCF [27]. For well identified modes the absolute value of the MCF will cluster around unity and its phase angle around 0. For computational modes, absolute value and phase of are randomly distributed. A more compact formulation, only one value per mode, is the so called *overall modal confidence factor* OAMCF, which is the percentage of MCF values whose absolute value is at least 0.95 and whose phase difference is a maximum of 10° [27].

Similarly one can use the complex valued *mode shape coherence and confidence factor*

$$\text{MSCCF}_k = \frac{u \boldsymbol{\psi}_k^T l \boldsymbol{\psi}_k^* e^{\lambda_k \Delta t_3}}{l \boldsymbol{\psi}_k^T l \boldsymbol{\psi}_k^*}, \quad (5.34)$$

introduced by Gao and Randall [19] which has an absolute value of unity for a perfectly identified mode.

Additionally to the straightforward method of calculating the damping from the eigenvalues of the system matrix (see Eq. (5.32)), the damping factors can be estimated by the comparison of estimated eigenvectors (upper half) with the corresponding time-shifted eigenvector (lower half). This is done via the so called *modal amplitude ratio* MAR

$$\text{MAR}_k = \frac{|{}^u\boldsymbol{\psi}_k^T {}^l\boldsymbol{\psi}_k^*|}{{}^u\boldsymbol{\psi}_k^T {}^u\boldsymbol{\psi}_k^*}, \quad (5.35)$$

from which an alternate modal damping value,

$$\delta_{2,k} = \frac{\ln(\text{MAR}_k)}{\Delta t_3}, \quad (5.36)$$

can be calculated [29]. The damping ratios calculated in this alternative way, $\zeta_{2,k} = \delta_{2,k}/\omega_{n,k}$, should generally agree well with the ones calculated via the eigenvalues for correctly identified modes. Comparison of both values can be used to assess to identify computational modes.

5.4.3 Automatic Mode Sorting

Often it is necessary to conduct numerous free oscillation experiments of the same structure, for example with different excitations, to determine all structural modes. In theory analysis of every single experiment should yield the same mode shapes at the natural frequencies and damping ratios, providing they were sufficiently excited. Visually comparing the modes of all experiments can be very time consuming. Mathematically the correlations between two mode shapes $\boldsymbol{\psi}_1$ and $\boldsymbol{\psi}_2$ can be described by the so called *mode shape correlation constant* MSCC computed by

$$\text{MSCC} = \frac{|\boldsymbol{\psi}_1^T \boldsymbol{\psi}_2^*|^2}{(\boldsymbol{\psi}_1^T \boldsymbol{\psi}_1^*) (\boldsymbol{\psi}_2^T \boldsymbol{\psi}_2^*)} \quad (5.37)$$

which corresponds to the square of the correlation coefficient computed between two sequences of complex numbers [29]. Sometimes also the term *modal assurance criterion* MAC is used for the above factor [16].

The MSCCs for all computed modes can be arranged in a symmetric matrix. By observing this matrix corresponding mode shapes can be found. For example, summing all MSCC values greater than 0.75 column wise, gives a vector with the number of similar mode shapes for every mode. The matrix of MSCCs can be combined with matrices describing the difference in natural frequency, or damping between modes, to achieve more complex criteria on mode similarity. By picking modes that are detected at least n times as 'master modes', and searching for all similar modes, graphs like Fig. 5.17 can be produced automatically. It can be seen that all modes found by visual inspection were also identified by the automatic grouping mechanism. The already grouped modes can be further classified by visual inspection. The automatic sorting procedure makes the post processing of measurements about 10 times faster.

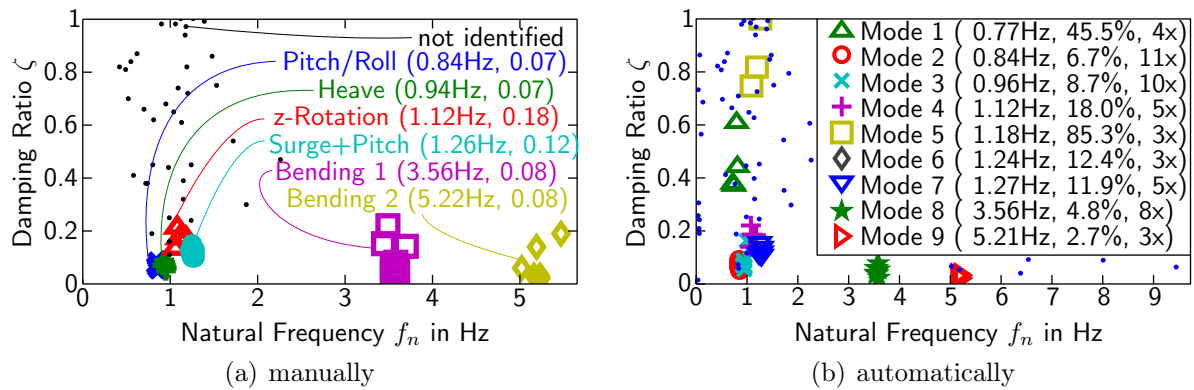


Figure 5.17: Comparison of modes assembled by visual inspection (a) and by automatic grouping (b).

5.5 Summary

Two different approaches were described to determine the transfer functions of a linear system. They were tailored towards the use for wave excited floating platform. A modal approach, allowing a concise description of the deformation of the platform-plate was presented. The described methods were applied to two different scale models. The obtained results were used to validate the computational model described in Chapter 2 and are presented in Section 2.7.3 and Appendices B.1 and B.2.

The Ibrahim time domain method was employed to experimentally determine the modes including corresponding natural frequencies and damping factors of a free floating platform. An algorithm to efficiently process results obtained from numerous measurements was presented above. Results from the conducted measurement campaigns are presented in Section 2.7.2 where they were used to validate the developed computational model.

Chapter 6

Geometric Non-Linear Effects in Plates

Linear theory may be applied to problems where the displacements and rotations remain small. For plate like-structures linear plate theory is applicable if the displacements are small with respect to the dimensions of the plate [7]. For homogeneous, isotropic plates precise limits for the applicability of linear theory can be made. However, for plates made from anisotropic material, or inhomogeneous plate-like structures the definition of such limits is not straight-forward. Especially when plate-like structures are deformed such that the deformed shape is non-developable with respect to the original shape, non-linear effects may play an important role.

6.1 Equations for Large Deflections of Plates

A plate theory taking large deflections of the reference surface into account is von Karman theory. It is briefly outlined here in order to illustrate the effect of geometric non-linearities. The theory uses a non-linear strain measure to account for the in-plane stretching that results from finite transverse displacements and rotations [7]. However, the in plane strains are still assumed small such that second order terms can be neglected, and the transverse displacements are assumed small enough to use a linearised measure of curvature. The in plane strain tensor and the curvature change tensor are then

$$\gamma_{\alpha\beta} = \frac{1}{2} \left(\frac{\partial u_\alpha}{\partial x_\beta} + \frac{\partial u_\beta}{\partial x_\alpha} + \frac{\partial u_3}{\partial x_\alpha} \frac{\partial u_3}{\partial x_\beta} \right), \quad (6.1a)$$

$$\kappa_{\alpha\beta} = -\frac{\partial^2 u_3}{\partial u_\alpha \partial u_\beta}, \quad (6.1b)$$

where u denotes the displacements with the indices α and β determining the in-plane directions 1 and 2, respectively [7]. Using the Kirchhoff hypothesis the strain field in the plate can be approximated by

$$\epsilon_{\alpha\beta} = \gamma_{\alpha\beta} + x_3 \kappa_{\alpha\beta}. \quad (6.2)$$

Integrating above equation over the plate thickness h and using the stress strain relations for a linear elastic, isotropic material with Young's modulus E and Poisson's ratio ν one

obtains the relation between section forces and reference surface deformation

$$n_{\alpha\beta} = \frac{Eh}{1-\nu^2} [(1-\nu)\gamma_{\alpha\beta} + \nu\gamma_{\lambda\lambda}\delta_{\alpha\beta}], \quad (6.3a)$$

$$m_{\alpha\beta} = \frac{Eh^3}{12(1-\nu^2)} [(1-\nu)\kappa_{\alpha\beta} + \nu\kappa_{\lambda\lambda}\delta_{\alpha\beta}], \quad (6.3b)$$

where $\delta_{\alpha\beta}$ denotes the Kronecker-delta [7, 70]. The directions of the section forces and moments are depicted in Fig. 4.2. A corresponding matrix equation is given in Eq. (C.13).

The balance of forces in vertical direction posed for a plate element together with the strain compatibility equation yield the von Karman plate equations

$$\frac{\partial^4 u_3}{\partial x_1^4} + 2\frac{\partial^4 u_3}{\partial x_1^2 \partial x_2^2} + \frac{\partial^4 u_3}{\partial x_2^4} = \frac{p}{A} + \frac{\partial^2 \phi}{\partial x_2^2} \frac{\partial^2 u_3}{\partial x_1^2} + \frac{\partial^2 \phi}{\partial x_1^2} \frac{\partial^2 u_3}{\partial x_2^2} - 2\frac{\partial^2 \phi}{\partial x_1 \partial x_2} \frac{\partial^2 u_3}{\partial x_1 \partial x_2}, \quad (6.4a)$$

$$\frac{\partial^4 \phi}{\partial x_1^4} + 2\frac{\partial^4 \phi}{\partial x_1^2 \partial x_2^2} + \frac{\partial^4 \phi}{\partial x_2^4} = Eh \left[\left(\frac{\partial^2 u_3}{\partial x_1 \partial x_2} \right)^2 - \frac{\partial^2 u_3}{\partial x_1^2} \frac{\partial^2 u_3}{\partial x_2^2} \right], \quad (6.4b)$$

in which p denotes a force per area acting perpendicularly to the plate and $A = \frac{Eh^3}{12(1-\nu^2)}$ the bending stiffness of the plate [57, 70]. The two coupled equations can be solved for the out-of-plane displacements u_3 and the stress function ϕ which is related to the section forces by

$$n_{\alpha\beta} = (2\delta_{\alpha\beta} - 1) \frac{\partial^2 \phi}{\partial x_\alpha \partial x_\beta}. \quad (6.5)$$

The stains in the plate can subsequently be obtained from Eq. (6.2) by inserting the solutions into Eqs. (6.1b), (6.3a) and (6.5).

The von Karman plate equations as posed in the above form take into account membrane forces due to out of plate deformations. If the second order term in Eq. (6.1a) is neglected one directly arrives at a linear plate theory, in which out-of-plane deformations have no influence on membrane forces. While some analytic results exist for the solution of the von Karman plate equations [70] a geometrically non-linear finite element formulation is used to solve a plate problem related to floating platforms with four chambers in the following.

6.2 Homogeneous, Isotropic Plates

In order to illustrate the impact of geometric non-linearities the simple example of an isotropic, homogeneous plate is chosen. The plate is loaded similarly to a loadcase typically arising for a floating platform with four air chambers: Four reference nodes at the centres of the chambers are coupled to the plate nodes such that a vertical displacement of the reference node leads to a constant pressure onto the plate in the chamber area. Two diagonal chambers are displaced downwards and the other two are displaced upwards.

Figure 6.1 shows a sketch of the dimensions of the model. The air chamber centres are located at $\pm 0.25l$, and the radius of the chambers is $0.225l$, where the reference length l was chosen as 1 m. The plate material is homogeneous, isotropic and linear elastic with a Young's modulus of 120 GPa and a Poisson's ratio of 0.3. Plates with different thickness h

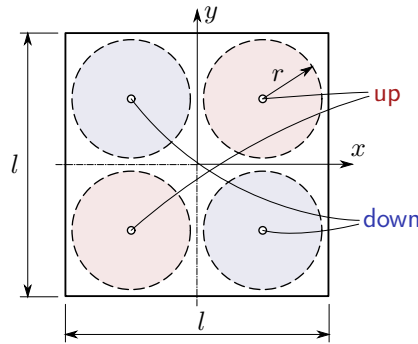


Figure 6.1: Sketch of the model geometry.

of $l/1000$, $l/200$, $l/100$, $l/50$, and $l/20$ were investigated. These plates can all be assumed as thin plates because the thickness is smaller than $1/16$ of the characteristic dimension [12].

The problem is treated by the finite element method in a formulation including geometrically non-linear effects. 900 shell elements with linear interpolation and reduced integration* are used. The equilibrium is computed in an incremental iterative procedure for prescribed z -displacements of the reference nodes.

Figure 6.2 shows the computed section forces in the plate. The section forces are related to the deformation of the reference surface of the shell via the shell's stiffness matrix, as detailed in Section 6.1. The deformation of the reference surface is characterised by the in-plane strain and the change of curvature. Observing Eq. (C.13) one notices that in-plane strains are coupled to the section forces, and the changes of curvature are coupled to the section moments. Due to geometrically non-linear effects, out of plane deformations lead to in plane-strains and, therefore, membrane forces. The twist like deformation induced by the anticipated load case creates membrane tension along the edges of the plate and membrane compression in the centre (see Figs. 6.2a and 6.2b). Additionally, membrane shear is induced in the quarters of the plate (see Fig. 6.2a). In a geometrically linear analysis these membrane forces would not occur. The section moments on the other hand can be accurately predicted by geometrically linear analysis, provided the curvature remains small.

The membrane forces are intrinsically non-linear while the section moments remain linear in until the transverse displacements reach about $3h$. In Fig. 6.3 the maximum membrane force (in 1-direction) and the maximum section moment (in 1-direction) are displayed for plates of different thickness. The maximum membrane force is proportional to the square of the transverse displacement, as it is the product of the geometrically non-linear effects. A slight deviation of this behaviour is visible for the thinnest plate at the point at which plate buckling occurs due to membrane compression in the centre of the plate.

Observing the load displacement curve of the structure depicted in Fig. 6.4a one can see that the model behaves linearly up to displacements equalling the plate thickness. In a linear formulation membrane forces due to transverse deformations are not taken into

* Reduced integration is chosen to simplify post-processing. Checking displacement results against fully integrated elements shows good agreement.

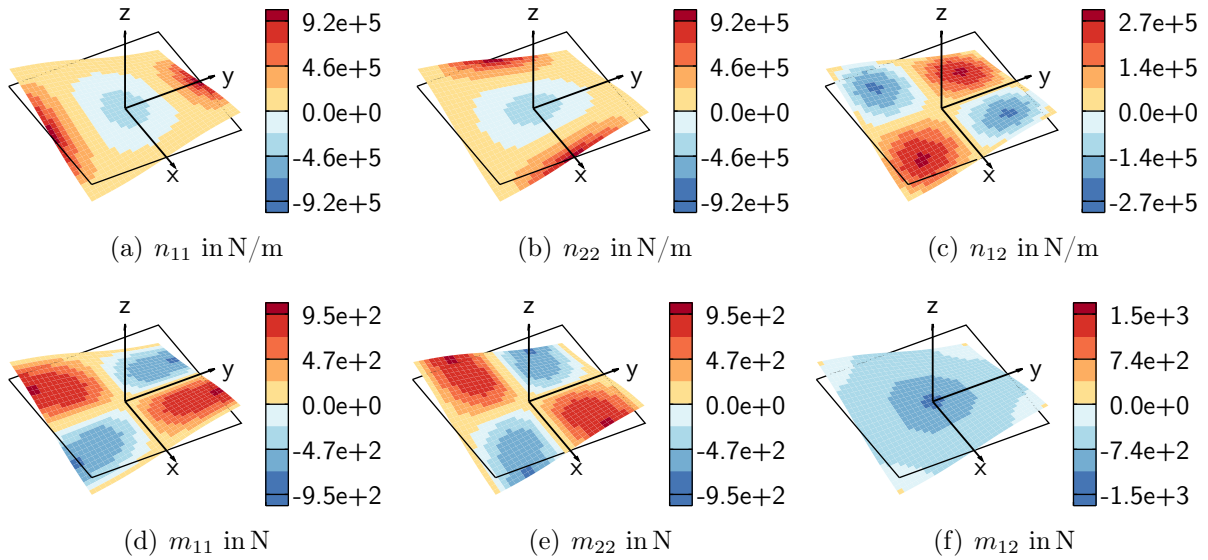


Figure 6.2: Section forces and moments in the plate for the model with $h = l/100$ at a reference node displacement of $0.00875l = 0.875h$. The deformation is displayed scaled by a factor of 5. The 1 and 2-axes coincide with x and z , respectively.

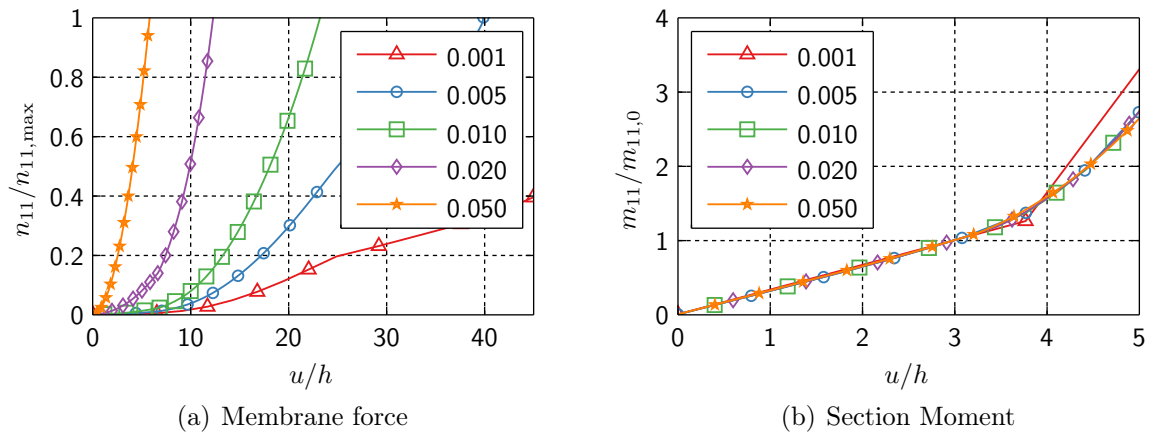


Figure 6.3: Maximum membrane force (a) and bending moment (b) in the plate depending on the maximum transverse displacement u for plates of different thickness. The section moment is normalised by $m_{11,0} = m_{11}|_{u/h=3}$ in order to show the proportionality.

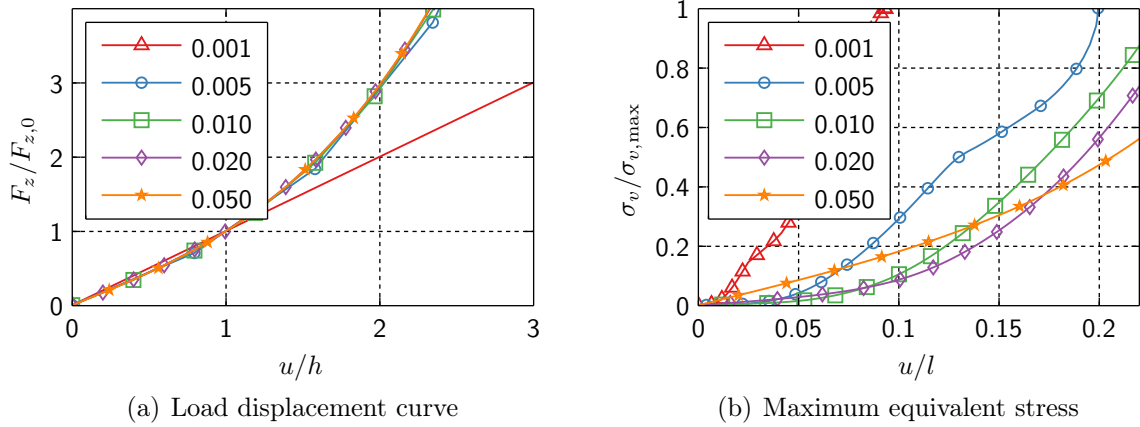


Figure 6.4: Vertical reaction force (a) and maximum von Mises equivalent stress (b) in dependence of the maximum displacement u for plates of different thickness. The load displacement curves show the vertical reaction force at the displaced reference node normalised by the value at $u = h$; The von Mises stress is normalised by the absolute maximum for each plate.

account. This can lead to a serious underestimation of the occurring stresses. A linear stress prediction for the investigated load case is accurate for transverse displacements up to $3h$. For larger displacements, in-plane stresses due to transverse deformation start to have an impact. The thicker the plate the larger the transverse deformations can be until non-linear effects play a role (see Fig. 6.4b).

6.3 Periodic Plate-Like Structures

For periodic plate like structures it is difficult to determine up to which transverse displacement magnitude linear theory is applicable. Generally, linear theory is applicable if the stresses due to plate section moments dominate over stresses due to plate membrane forces [45]. Thus, the determining quantity is the ratio of bending to membrane stiffness. For homogeneous, isotropic plates this is equivalent to h^2 , and linear theory is applicable for small transverse displacements compared to h [45, 70]. For plate like structure the height of the structure can not be used to estimate a limit for the applicability of linear theory.

In order to illustrate how deceiving the physical height of a structure can be, an example is presented in the following. Quadratic, plate-like structures with a dimension l of 300 m based on the unit cell presented in Chapter 4 are considered. The centres of the four supporting air chambers are located at $\pm 0.25l = 75$ m, and the radius of the chambers is $0.225l = 67.5$ m (see Fig. 6.1 for a sketch of the geometry). The boundary conditions are chosen as for the homogeneous, isotropic plates above, i.e. the reference nodes of the four air chambers are constrained.

In a first load case gravity loading is applied to the plate structure. The nodes modelling the position of the water plane are constrained to 0. In a subsequent load step the nodes modelling the water plane are displaced by the expected maximum wave amplitude

Name	l_1 in m	l_2 in m	l_3 in m	r_1 in m	t_1 in m	r_2 in m	t_2 in m	β in $^\circ$
Thin	10.0	10.0	7.071	0.135	0.004	0.135	0.001	0
Thick	10.0	10.0	15.0	0.3	0.01	0.3	0.01	45

Table 6.1: Dimensions of the unit cells as depicted in Fig. 4.3. The angle β defines the orientation of the unit cell.

of 7.5 m. The most critical wave heading of 45° is assumed, displacing the water-plane nodes of two diagonal chambers upwards and the other two nodes downwards, as depicted in Fig. 6.1.

Two different unit cells with dimensions given in Table 6.1 are considered. The thin cell has a mass per area of 13.17 kg/m^2 and the thick cell has a mass of 154.9 kg/m^2 . The thick cell is considered with its top and bottom beams oriented in the direction of the plate diagonals. This is achieved by specifying an appropriate orientation for the homogenised stiffness properties: The homogenised plate properties are defined with respect to the unit cell's local 1-2-3 coordinate system. For the shell elements of the plate the orientation of the unit cell with respect to the global x - y - z system needs to be specified. The unit cell's 1-2-3 system is defined by rotating the x - y - z system by an angle β around the z -axis. The section forces are reported by ABAQUS with respect to the 1-2-3 system [12]. Therefore, they can be directly used for the localisation procedure without any coordinate transformations.

The gravity load specified in the first load step is not critical in comparison to the forces displacement in the second step. This can be explained by the continuous support by the air chambers. Figure 6.5 shows the maximum von Mises equivalent stress in any beam element of the thin model in dependence of the maximum deformation of the plate. The stresses obtained by the localisation procedure are compared against stress values from a full model, already used in Section 4.5. Excellent agreement is obtained for both models up to the point at which beam buckling of diagonal beams occurs in the full model, which leads to a sudden increase of the equivalent stress. The good agreement suggests the

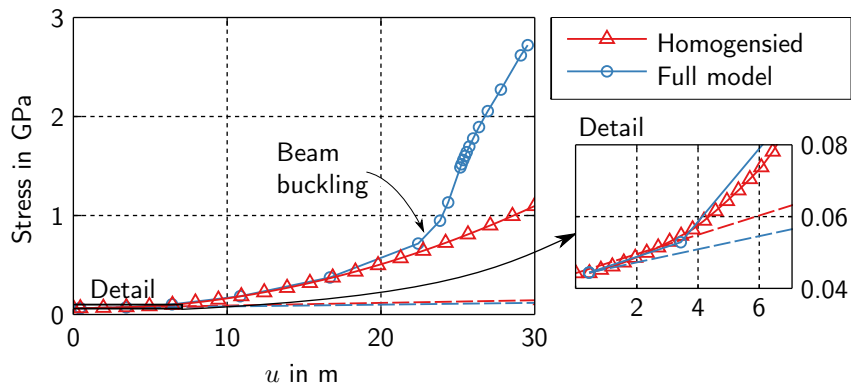


Figure 6.5: Maximum von Mises equivalent stress in any beam element for the wave-type load step in dependence of the maximum plate displacement. Stresses obtained from a homogenised model are compared to stresses from a full beam model. Dashed lines show the prediction of a geometrically linear model.

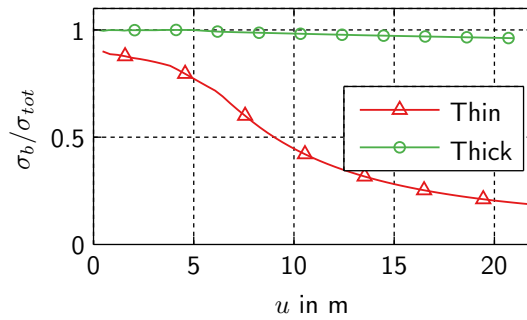


Figure 6.6: Ratio of maximum equivalent stress computed using only section moments to maximum equivalent stress computed from all section forces in dependence of the maximum plate displacement u for the wave-type load case.

usability of the linear homogenisation approach even for geometrically non-linear analyses on the global level. Of course, geometrically linear unit cells can only be used as long as the local deformations remain sufficiently small. The stress predictions of geometrically linear models seriously underestimate the actual stress, because they neglect membrane forces due to transverse displacements. For the thin model, membrane forces become significant already for transverse displacements of about 1.5 m, which is only about 1/5th of the structure height.

The significance of membrane forces can be visualized if the stress fields obtained from homogenisation considering only bending moments are compared to the stress fields obtained from all section forces. The so computed ratio of von Mises equivalent stresses is displayed for both models in Fig. 6.6. The maximum stress in the thick model is dominated by the stress originating from plate bending moments even up to large twist deformations. For the thin model membrane forces have a significant impact (ca. 10%) even for no twist deformation, i.e. at the start of the second load step. As the twist deformation is increased the impact grows and eventually becomes the dominating factor.

A comparison of the maximum equivalent stress in each unit cell for the gravity load step of the thin plate model obtained through geometrically linear and non-linear analyses is shown in Fig. 6.7. While the stress levels are still in an acceptable range the linear model seriously underestimates the arising stress state.

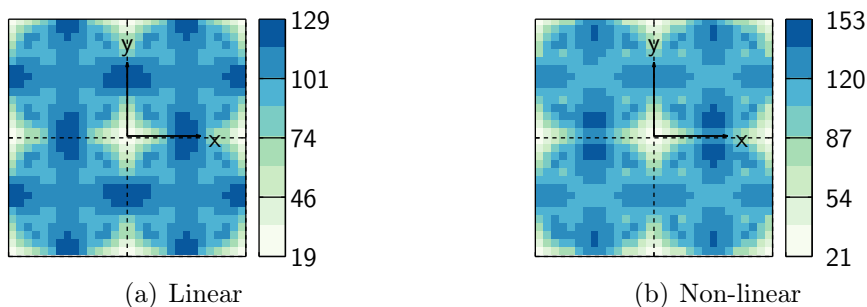


Figure 6.7: Maximum von Mises equivalent stress in each unit cell of the homogenised model of the thin plate for the gravity load step. Values are in in MPa.

6.4 Conclusion

In plate-like structures membrane forces arising due to transverse displacements can only be predicted by a geometrically non-linear treatment. The significance of these membrane forces depends on the magnitude of the transverse displacements in relation to an effective thickness of the structure. The effective thickness represents the ratio between bending and membrane stiffness of the plate structure. The higher this ratio the more important are stresses due to section moments, while stresses due to membrane forces decrease in importance. Thus, within certain limits, higher transverse displacements can be accurately predicted with linear theory only if the effective structure thickness is higher. Especially for structures with anisotropic effective plate properties the prediction of the effective thickness is difficult and may vary depending on load case. In such cases a geometrically non-linear computation is highly recommended as the physical size of the plate-like structure may be very misleading.

Chapter 7

Design of a Prototype Platform

In this chapter a possible design for a platform supported by four cylindrical air chambers will be presented as an example. The previously developed and experimentally validated computational models will be applied to determine the dynamical behaviour of the platform in waves, and, subsequently, to describe the behaviour of the platform under the expected environmental conditions. For these conditions, expected stress, displacement and force amplitudes are computed based on probabilistic theory and compared with the allowable limits, demonstrating the feasibility of the design.

7.1 Environmental Conditions

Loads on offshore floating platforms may result from environmental impacts like wind, water waves and currents as described by DNV [14]. Wind and currents are not taken into account in the current analysis, mainly due to the focus of the project to deliver information on the motion of the platform as a basis to the efficiency calculation of a concentrator system. Forces originating from wind or currents, as well as the resulting forces from mooring lines, may be modelled as static forces and incorporated into the current model in a straightforward matter.

Wave conditions can be described by wave spectra (for more detail see Appendices A.2 and A.4). Typical input parameters for wave spectra are the wind speed (as a single parameter) or a mean wave period and significant wave height (for two-parameter spectra). Wave conditions vary from day to day and throughout the year. A typical description of this so called metocean conditions involves the probability for certain combinations of significant wave height, mean wave period, and possibly wave direction.

Data for the Mediterranean Sea, used as an input to the following computations was collected by Diendorfer [13] and, for the sake of completeness, is presented in Fig. 7.1 and Table 7.1 in concentrated form. The most probable sea state which is observed 25% of the time has a significant wave height of 1–2 m and a mean wave period of 3–4 s. The most severe sea state in terms of wave height has a significant wave height of 8–9 m with a mean wave period of 7–9 s and arises with a probability of 0.3%.

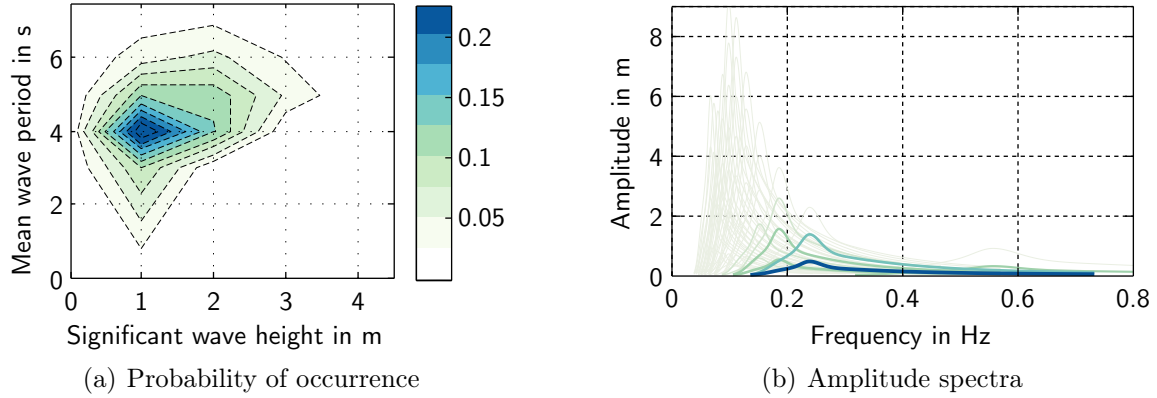


Figure 7.1: Probability for a specific sea state in the Mediterranean Sea (a) and corresponding JONSWAP spectra (b). Graphic based on the data in Table 7.1

T_m / H_s	0–1 m	1–2 m	2–3 m	3–4 m	4–5 m	5–6 m	6–7 m
0–3 s	0.0990	0.0034	0	0	0	0	0
3–4 s	0.2515	0.1288	0.0027	0	0	0	0
4–5 s	0.1185	0.1157	0.0464	0.0022	0	0	0
5–6 s	0.0393	0.0574	0.0232	0.0156	0.0013	0	0
6–7 s	0.0127	0.0211	0.0078	0.0050	0.0038	0.0006	0
7–8 s	0.0052	0.0106	0.0021	0.0010	0.0006	0.0006	0.0002
8–9 s	0.0023	0.0077	0.0010	0.0002	0.0001	0.0000	0.0001
9–10 s	0.0008	0.0054	0.0011	0.0001	0.0000	0	0
10–11 s	0.0002	0.0023	0.0011	0.0002	0	0	0
11–12 s	0	0.0004	0.0007	0.0001	0	0	0
12–13 s	0	0.0001	0.0001	0.0000	0	0	0
13–33 s	0	0	0	0	0	0	0

Table 7.1: Probability of occurrence of particular sea states classified by mean wave period, T_m , and significant wave height, H_s , in the Mediterranean Sea. A graphical representation of the data is given in Fig. 7.1.

7.2 Overall Dimensions of the Floating Platform

The general dimensions of the platform are based on the calculation of the optical efficiency in dependence of the wave excitation by Diendorfer [13], where a platform size of 300 m was determined as the smallest size with acceptable efficiency. The unit cell for the truss is chosen according to the unit cell presented earlier (see Fig. 4.3). The two unit cell geometries given in Table 6.1 are used. For the thin cell the length of all beams l was fixed to 10 m, which determines the dimensions of the unit cell by

$$l_1 = l_2 = l_d = l, \quad (7.1a)$$

$$l_3 = \sqrt{l_d^2 - \frac{1}{4}(l_1^2 + l_2^2)} = \frac{\sqrt{2}}{2}l. \quad (7.1b)$$

The dimensions of the thin cell are the same as used before in the validation of the homogenisation procedure in Section 4.5. The thick cell is considerably higher in order to obtain a higher bending stiffness. Additionally, the thick cell is considered rotated by 45° such that the top and bottom beams are oriented in the diagonal directions of the plate.

As a material steel was selected, modelled by a linear elastic, isotropic material with a Young's modulus E of 210 GPa, Poisson's ratio ν of 0.3, and density ρ of 7860 kg/m³. The areal mass of the plate structure can be directly computed by

$$w = \frac{2\rho}{l_1 l_2} \left[A_1 (l_1 + l_2) + 2A_2 \sqrt{\frac{1}{4}(l_1^2 + l_2^2) + l_3^2} \right], \quad (7.2)$$

where the cross sectional area of the beam is

$$A_i = [R_i^2 - (R_i - t_i)^2] \pi, \quad (7.3)$$

with the index 1 for the top and bottom beams and the index 2 for beams oriented diagonally. The proposed design has an areal mass of 13.166 kg/m² for the thin cell and 154.9 kg/m² for the thick cell. Hence, the total mass of the plate framework is 1,184,940 kg and 13,941,000 kg, respectively.

The centre points of the cylindrical air chambers are located at the centres of the quarters of the plate. For the radii of the chambers a value of 67.5 m was selected, leaving reasonable gaps between the air chambers themselves and also to the edge of the plate. The total length of the skirt was selected to be 25 m. With the design height of the air chamber of 15 m the skirt extends 10 m below the water surface. This leaves rather large safety margins even with the maximum expected wave height of 15 m*.

The membrane stiffness of the skirt in circumferential direction is an important parameter for the dynamic model, as it governs the axial stiffness of the air chambers. For the thin plate model a membrane stiffness of 4,200 kN/m was assumed. This could for example be achieved by a 6 mm thick polymer foil with a typical Young's modulus of 0.7 GPa. Assuming a skirt density of 1100 kg/m³ the total skirt mass of per chamber is 69,979 kg. For the thick plate model a membrane stiffness of 500 kN/m was assumed. This value could be obtained with elastomer membranes or by geometric effects (e.g. wavy structures). For the thick model a mass of 20,000 kg was assumed for the skirt.

*Estimated height of the 100-year return period wave in the Mediterranean sea.

The static pressure in the skirt can now be estimated based on total platform mass (including a payload of 30 kg/m^2) and the cross sectional area of the chambers. This gives a static pressure of 714 Pa for the thin plate model and 2865 Pa for the thick plate model. As the membrane forces and, hence, stresses in the skirt are directly related to the chamber pressure (as described in detail in Section 2.2) values for skirt will not be explicitly reported in the following.

7.3 Load Cases

The different investigated load cases are described in the following. The same model was used for static as well as dynamic load cases. In all cases the rotation around the z -axis of one plate node was constrained in order to disable the corresponding rigid body mode.

For all load cases the arising plate deformations, normal stresses, beam normal forces, and chamber pressures were computed. The stress state in all beam elements is dominated by the normal forces, with a small contribution from bending moments. The shear stresses originating for torsion moments are negligible. Therefore, only the normal stress component is taken into account when evaluating the yield criterion. A yield stress of 250 MPa will be assumed for computing safety factors.

The normal forces in the beams are computed in order to compute the buckling safety. A conservative estimate for the buckling load is given by

$$F_i^* = \frac{\pi^3 E_i R_i^3 t_i}{l_i}, \quad (7.4)$$

where l is the length of the beam, E the Young's modulus, and R the radius of the pipe-like cross section with small wall thickness t [57]. The index i emphasises that there may exist multiple buckling loads depending on material, cross section, and beam length. For the current unit cell two different buckling loads exist. The top and bottom beams have a critical load of 613 kN and the diagonal beams have a critical load of 158 kN for the thin plate model. For the thick plate model the respective values are $16,721 \text{ kN}$ and $6,080 \text{ kN}$. In both cases both critical loads lie below the normal force leading to yielding in the cross section, hence elastic buckling is expected.

7.3.1 Static Equilibrium

Here the vertical displacement of the upper air chamber reference nodes were constrained in vertical direction. Gravity loading was applied to the plate. An additional pressure load was specified in order to take into account a payload amounting to 30 kg/m^2 . The weight of the skirt as well as its buoyancy were taken into account by specifying an appropriately adapted gravity loading. This load step is also used as an initial step for the steady state dynamic analyses used to compute the transfer functions for the dynamic model. Hence it is of importance for computing the total loading.

7.3.2 Quasi-Static Wave

For a first approximation of the wave loading a quasi-static approach is used. This load case corresponds to a wave with amplitude a , travelling at 45° heading. The displacement

of the waterplane nodes is set to $\pm a$ depending on their location, resulting in a twist-type deformation of the plate. The amplitude is chosen to resemble the assumed maximum wave height of 15 m. This resembles the expected maximum wave height in the most serious conditions, i.e. significant wave heights of about 7 m, reported in the Mediterranean Sea. The analysis is conducted geometrically non-linear with two subsequent load steps: A load step to apply the gravity loading, and a subsequent step in which the waterplane nodes are displaced. The springs modelling the air chambers are defined as non-linear springs with zero stiffness in the tensional regime. Therefore, the plate might only be supported by two chambers while the two other chambers are 'hanging free' and don't transmit tensional forces as linear springs would.

7.3.3 Irregular Wave Spectrum

Real ocean waves may be described as a superposition of an infinite number of regular waves according to a wave spectrum $S_\eta(\omega)$. For completeness, a more detailed description of the representation of an irregular seaway is given in Appendix A.2, and commonly used sea spectra are described in Appendix A.4.

The floating platform is modelled as a linear, single-input (wave), multi-output (plate displacements and section forces, chamber pressures, etc.) system, as described in detail in Chapter 2. The output for a single output variable x can then be given in terms of the output spectrum

$$S_x(\omega) = |H_{x\eta}(\omega)|^2 S_\eta(\omega), \quad (7.5)$$

where $H_{x\eta}$ is the transfer function for output x with respect to the wave signal η [9, 55]. As the input for the system may be regarded as a random process with its properties defined by the wave spectrum, the output may be similarly regarded as the realisation of a random process with its properties defined by the response spectrum. Using probabilistic theory, predictions about the response can be made based on the response spectrum. Most useful for design purposes is the statistic of the expected response maxima. For a time signal following a narrow band spectrum, the peaks of the response follow the Rayleigh probability density function

$$f(x) = \frac{x}{m_0} e^{-\frac{x^2}{2m_0}}, \quad (7.6)$$

where m_0 is the zero order moment of the output spectrum[†], i.e. the variance of the output time signal [6, 55]. For some quantities, e.g. displacements, the dynamic model delivers the transfer functions directly. Transfer functions for quantities on unit cell level, on the other hand, have to be computed by the localisation procedure described in Section 4.3.

As common wave spectra are narrow band, Rayleigh statistics are applicable [55]. Figure 7.2 shows an example wave signal computed from a Pierson-Moskowitz wave spectrum (depicted in Fig. A.1c). It also compares the statistics computed directly from the peaks with the Rayleigh distribution according to Eq. (7.6). It can be seen that the direct peak statistics are matched very well by the Rayleigh distribution. The agreement gets better the more narrow-band the spectrum is.

[†] The n^{th} order moment of a spectrum $S(\omega)$ is defined as $m_n = \int_0^\infty \omega^n S(\omega) d\omega$.

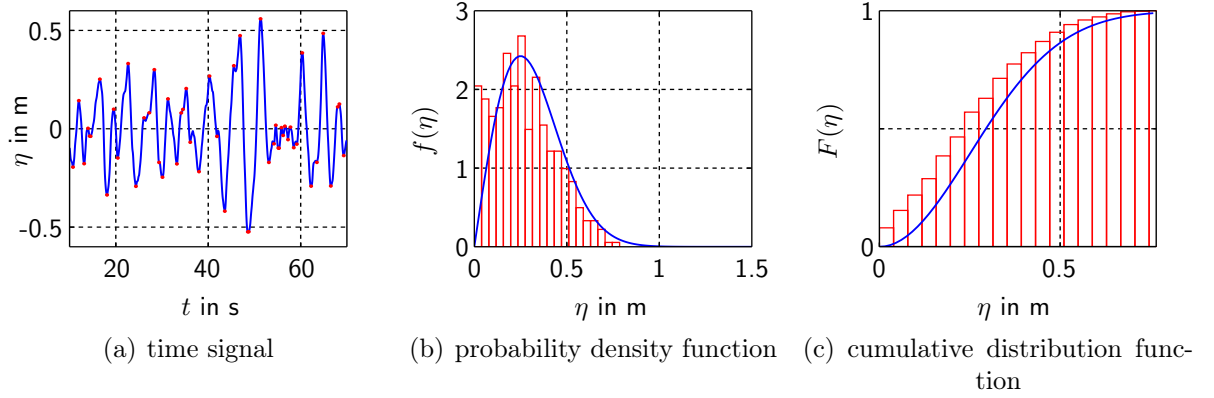


Figure 7.2: Statistics of the peaks of the wave signal: (a) part of the wave signal with peaks; (b) probability density function; (c) cumulative distribution function. Statistics computed directly from the peaks are displayed as bar-plots (red); Rayleigh statistics as continuous lines (blue).

A design criterion for the quantity x may now be defined in a statistical sense. The amplitude x which is not exceeded by a probability of p may be computed from the Rayleigh distribution's cumulative distribution function

$$F(x) = 1 - e^{-\frac{x^2}{2m_0}}, \quad (7.7)$$

by setting $F(x) = p$ and solving for η . The so obtained amplitude value x_p must then be combined with the static value of the quantity x_0 to compute the total value

$$x_t = x_0 \pm x_p, \quad (7.8)$$

which must lie within the design limits, i.e. it must pass an appropriate failure criterion like a yield criterion or critical buckling load.

In order to evaluate Eq. (7.7) for a single quantity the output spectrum must be computed and numerically integrated in order to obtain the zero order moment. For a numerically efficient integration the points along the frequency axis should be well chosen: due to the narrow-band nature of the excitation spectrum the output spectrum is narrow-band as well, which allows for a rather small frequency interval. Intelligent choice of the integration points can provide substantial computational improvements at constant accuracy. A possible procedure to obtain integration points, also used in the current computation, is described in detail in Appendix D.5. The output spectrum must only be computed for the frequencies of the integration points. The numerical efficiency of above described integration procedure is especially important as it needs to be carried out for many points. It is necessary for every point in every unit cell at which some value should be evaluated. To give an example: In the unit cell each beam element has two integration points with eight section points each; for a platform model with 30x30 shell elements representing homogenised unit cells with 88 beam elements each, this makes a total of 1,267,200 points to evaluate. Of course, a similar amount of points needs to be evaluated in order to check the safety factors against beam buckling. A separate evaluation of each point is necessary because the transfer functions, and hence the output spectra, of all

points are different. A remedy to reduce the computational cost would be to group the points in groups of transfer functions of similar shape and then only evaluate the integral for the most critical, i.e. the one with the largest amplitude, transfer function of each group. Unfortunately grouping the transfer functions by similarity is computationally rather expensive because a similarity measure must be computed for each combination of transfer functions.

Above described procedure was carried out for every wave spectrum with non-zero probability given in Table 7.1. As the orientation of the platform with respect to the wave direction is not known, each spectrum is evaluated for a range of 10 wave directions from 0–45°, for which platform transfer functions were pre-computed as described in Chapter 2. This results in a total of 411 different sea states to evaluate.

7.4 Results and Discussion

7.4.1 Gravity Loading

Both models show a similar deformation figure under gravity loading as depicted in Fig. 7.3. The deformation shape with the edges curved downwards results from the overpressure in the chambers, which leads to the bending of the plate. As the individual modules (one chamber with plate on top) are connected by the continuous plate, this local curvature leads to a global curvature of the plate. This global curvature also leads to a slight inclination of the air chambers, which will lead to an additional bending moment on the plate, as described in Chapter 3. The additional bending moment is not taken into account in the current analysis.

Figure 7.4 shows the maximum normal stresses and normal forces in each unit cell of the thick plate model for the gravity load step. The stress values are in an acceptable range and the normal forces are far below the critical buckling loads. Results from the static load case will form the basis on which the dynamic amplitudes will be superimposed.

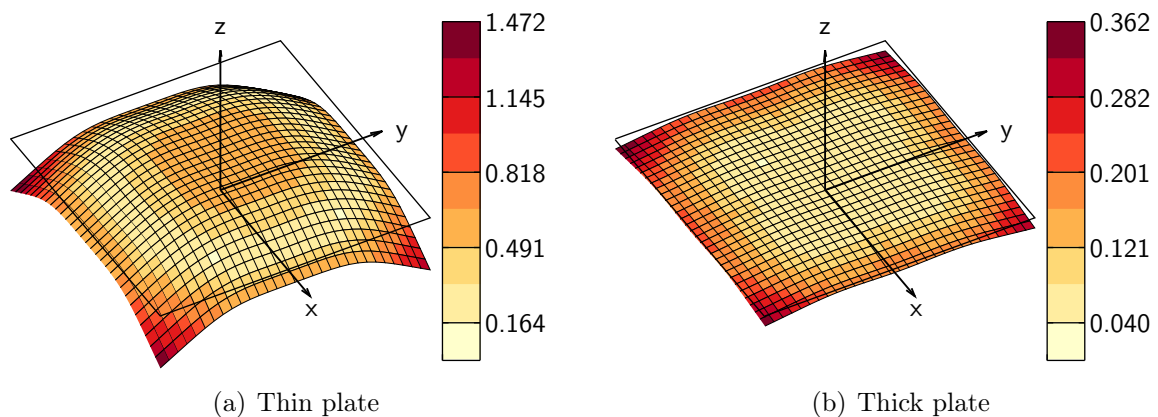


Figure 7.3: Static deformation of the models under gravity loading. The deformation is scaled by a factor of 50; scale bar values are in m.

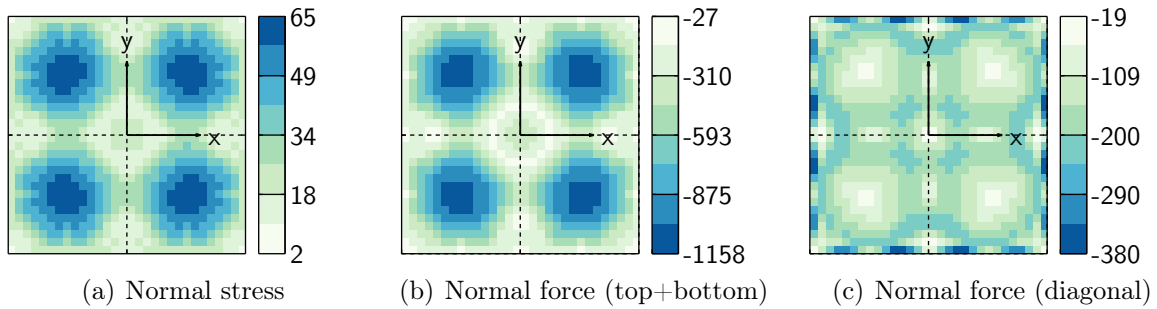


Figure 7.4: Maximum normal stress and beam normal normal forces in each unit cell of the thick plate model for the gravity load case. Stress in MPa and force in kN.

7.4.2 Evaluation of the Irregular Wave Load Cases

The irregular wave load case was computed for all spectra with non-zero probability and for 10 wave directions in the the range of $0-45^\circ$. Oscillation amplitudes not exceeded by a certain probability were computed for normal stress and beam normal force of all elements of all unit cells. This large amount of data was automatically processed and significant results are presented in the following.

7.4.2.1 Impact of the p -Value on the Oscillation Amplitude

The amplitude which is not exceeded by a certain probability p , for brevity just termed *oscillation amplitude* in the following, is computed from the Rayleigh distribution via Eq. (7.7). The higher the p value is chosen the higher the oscillation amplitudes get. The dependence of a single oscillation amplitude on the required required probability of not-exceedance can be best seen from Fig. 7.2c. It is highly non-linear. For design purposes one needs to require reasonably high p -values, to ensure safe operation of the platform at all times. Therefore, a probability of not-exceedance of 0.9999 is chosen. This means that the computed oscillation amplitudes will only be exceeded with a probability of 0.01%.

7.4.2.2 Motions and Deformations

The expected motions and deformations can be computed from the modal transfer functions by the above described procedure. Maximum expected amplitudes of the modal coordinates are then obtained via probabilistic theory. The same modal basis was used to evaluate the modal transfer functions for both model. The modal basis is composed of the six rigid body plate modes and the first 20 plate deformation modes obtained via natural frequency extraction from the thick plate model. The most active deformation modes are displayed in Fig. 7.5.

Figure 7.6 shows the maximum amplitudes of the first five modes with maximum average response. Large differences are visible between the thick and the thin plate model. The rigid body response for waves shorter than 50 m is not significant. The heave response remains smaller than the maximum wave hight for all wave conditions, thus no heave natural mode is excited. Amplitudes of the pitch/roll modes can reach up to 12 m depending on the wave direction. For a wave heading on 0° only the pitch mode has it's highest amplitude while the roll mode has zero amplitude. If the wave angle increases

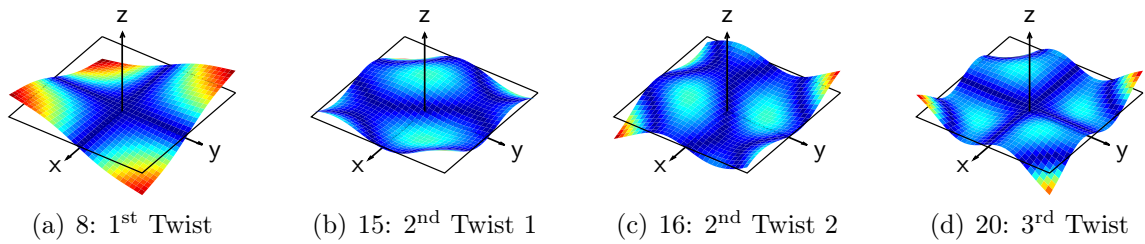


Figure 7.5: Most active deformation modes of the modal basis used to evaluate the plate deformations.

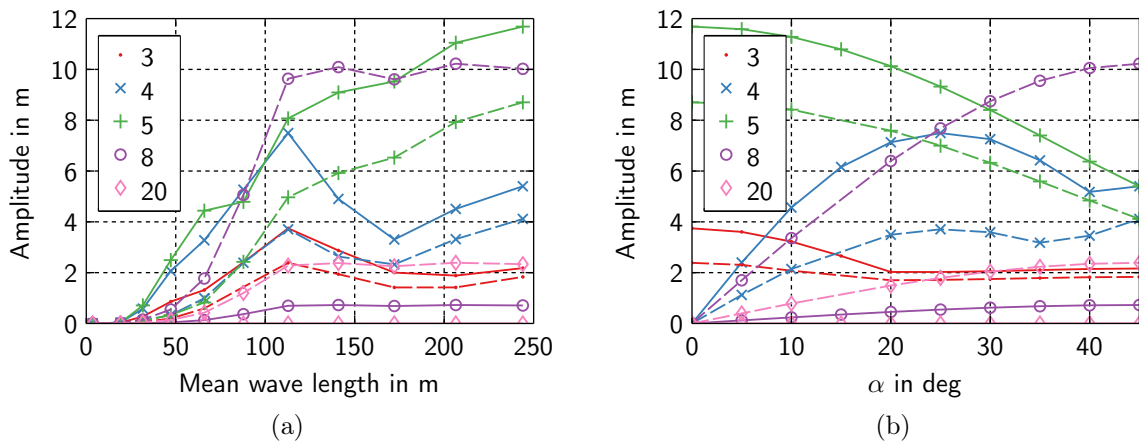


Figure 7.6: Amplitudes ($p=0.9999$) of the modes with the highest average response in dependance of wave length (a) and wave heading (b). Full lines used for the thick, and dashed lines for the thin plate model. Modes 3, 4, and 5 are rigid body heave, roll, and pitch, respectively; Deformation modes are depicted in Fig. 7.5.

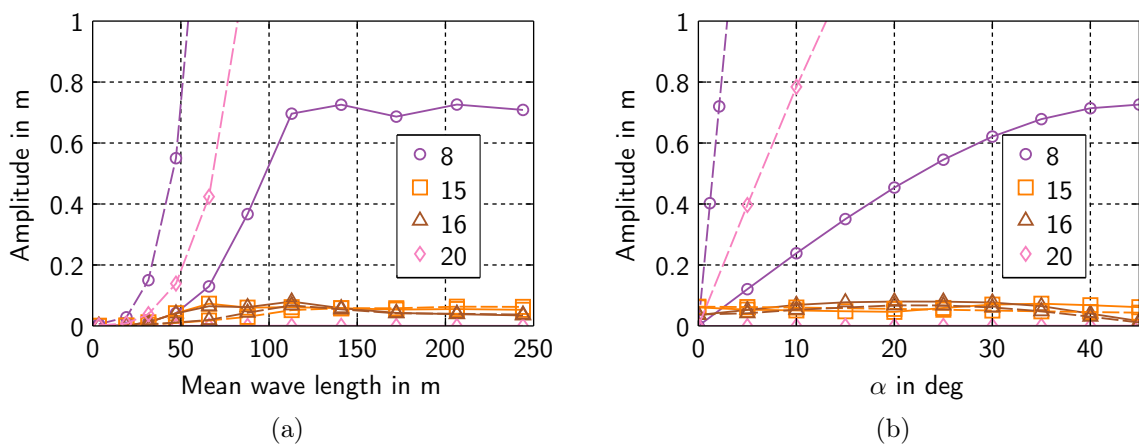


Figure 7.7: Amplitudes ($p=0.9999$) of the deformation modes with the highest average response in dependance of wave length (a) and wave heading (b). Full lines used for the thick, and dashed lines for the thin plate model. Modes 3, 4, and 5 are rigid body heave, roll, and pitch, respectively; Deformation modes are depicted in Fig. 7.5.

the roll amplitude grows and the pitch amplitude declines until, at a wave heading of 45° , both amplitudes are equal. Although the phase information is lost, the rotation axis of the plate must be parallel to the wave crests in this case. Combining the amplitudes, one can compute a maximum angle of inclination of the plate yielding 3.2° .

While the rigid body response of the thick plate model is slightly higher, the thin plate model undergoes significant twist-type deformations with amplitudes up to 10 m. Such high deformations cannot be treated by geometrically linear theory for the thin plate as was shown in Chapter 6. Thus, the linear dynamic model is not applicable for the thin plate model. Therefore, only results for the thick plate model are shown in the further discussion. The deformations of the thick plate model remain in an acceptable range with a maximum amplitude of the first twist mode of about 0.8 m, as shown in Fig. 7.7. This is well within the applicability limit of geometrically linear theory. In fact, the first twist mode (maximum amplitude <0.8 m) is the only mode with significant deformation; all other modes show a much smaller response.

7.4.2.3 Combination of Static and Wave Loading

Due to the application of the homogenisation technique a large reduction in the number of degrees of freedom was achieved on the model level. The localisation procedure however recreates the original amount of information, e.g. one stress value in every integration point in every unit cell. This can lead to a large amount of data to be processed. Although this task is easy to parallelise the question remains if all this information needs to be processed. A compact visualization of the arising maximum field-value values in every unit cell is given in Fig. 7.8 for the normal stress.

In order to evaluate the dynamic load case the superposition of the static load and the dynamic load must be computed. This can be done exactly based on the localised field values in the unit cell, possibly resulting in a large amount of data. The maximum value for each unit cell can then be found from the total field in the each unit cell. A conservative estimation of the total load can be obtained by an evaluation on the level of the homogenised plate elements: The maximum amplitude per unit cell is added to the maximum static value per unit cell. This allows a large reduction in the amount of data to be handled. Figure 7.9 shows a comparison of results from both evaluation methods, as well as the magnitude of the relative error. For the current case both methods agree quite well. The maximum total loads are very similar, indicating that maximum static loads

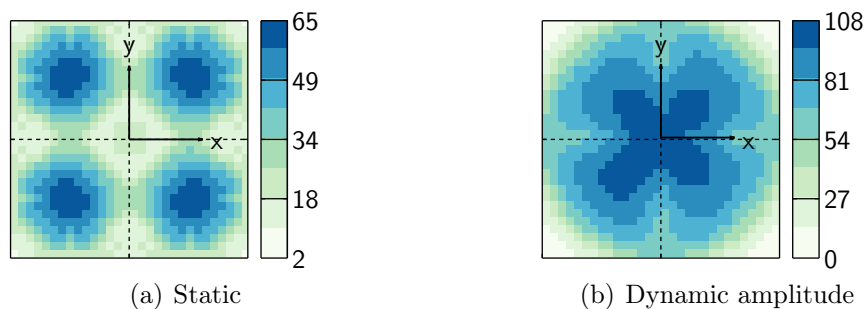


Figure 7.8: Maximum normal stress per unit cell for static load (a), and oscillation amplitudes for a spectrum with $H_s=3.5$ m, $T_m=11.5$ s, and wave heading of 45° (b).

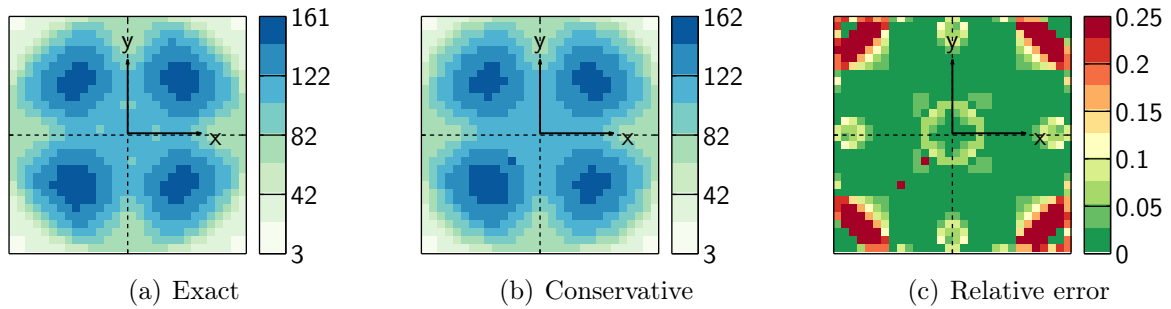


Figure 7.9: Maximum total normal stress in each unit cell: (a) Evaluated exactly, on each element in each unit cell; (b) Conservative estimate by combining maximum static values and maximum amplitudes of each unit cell on the homogenised level; (c) Magnitude of the relative error.

and maximum amplitudes arise in the same parts of the unit cells. Hence, the conservative estimation can be applied without being over-conservative. Large errors only arise in areas with low total loads, which are not critical. As the current model could be evaluated in an exact manner on the available computational resources, the exact formulation was chosen.

Special care should be taken when combining static loads and oscillation amplitudes of signed quantities like the beam normal force. In this case the largest total compressive, i.e. negative, force must be compared to the buckling load. The largest total compressive force is obtained by finding the minimum total force per unit cell, where the total force is obtained by subtracting the amplitude from the static force.

7.4.2.4 Critical Wave Conditions

In order to evaluate which wave conditions are most critical for the structure the maximum values of the field variables over the whole structure were computed in dependence of the two parameters of the wave spectrum, significant wave height and mean wave period. Figure 7.10 shows the maximum value in the whole structure for the oscillation amplitude of the normal stress and the total normal stress. As expected the critical values appear in the same area of wave conditions. The critical areas are the similar for the normal forces shown in Fig. 7.11, the chamber pressures shown in Fig. 7.12a, and the vertical plate displacements shown in Fig. 7.12b.

Large values (both amplitude and total) appear for mean wave periods larger than 8 s (which corresponds to a mean wave length of 100 m) and significant wave heights larger than 3 m. The limit based on the wave period is much more pronounced than the limit based on the wave height. This can be best seen in Fig. 7.13, where the maximum oscillation amplitudes in dependence of wave height and wave period, i.e. the projections of Fig. 7.10a onto its coordinate axes, are depicted. Here an important phenomenon can be observed: Wave conditions with mean wave periods shorter than 8 s are never critical. This limit is due to the ratio between chamber size and mean wave length (computed from the mean wave period via the dispersion relation for deep water waves). If the wave length is shorter than the chamber radius even high waves have a small impact, because they do not change the volume of the air chamber significantly. The maximum amplitude of the normal stress depends linearly on the significant wave height. The non-linear behaviour

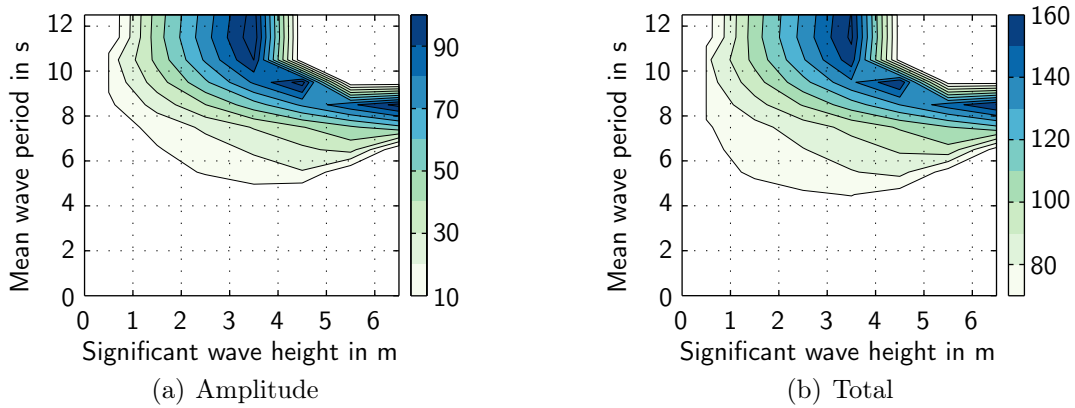


Figure 7.10: Maximum normal stress (in MPa) in the whole plate in dependence of the wave conditions: (a) Dynamic stress amplitude; (b) Total stress.

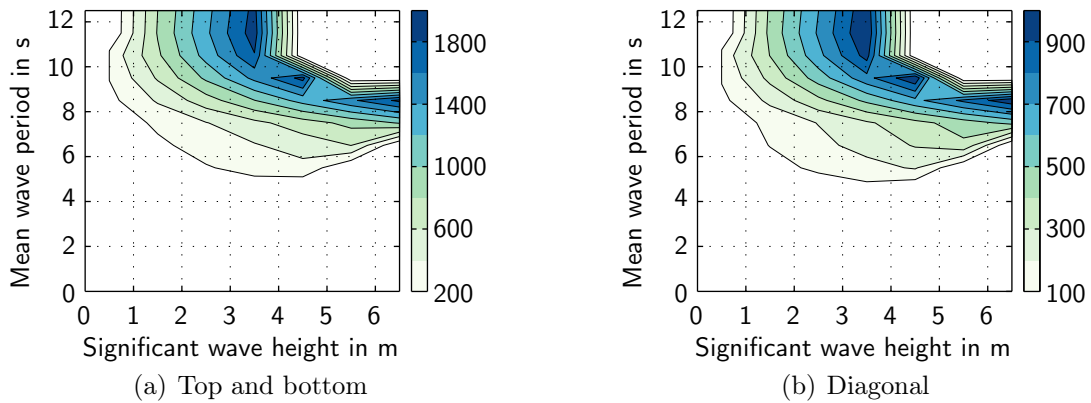


Figure 7.11: Maximum normal force oscillation amplitude (in kN) in the whole plate in dependence of the wave conditions for different types of beams: (a) Top and bottom beams; (b) Diagonal beams.

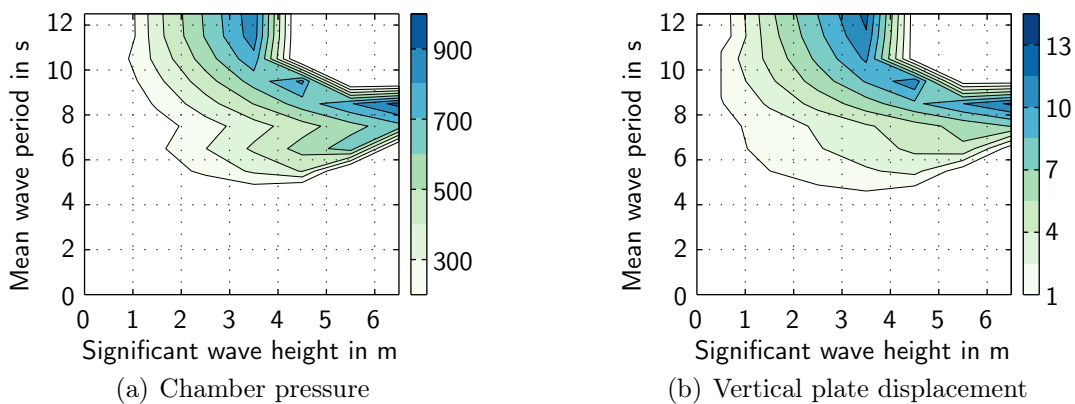


Figure 7.12: Maximum oscillation amplitudes in dependence of the wave conditions: (a) Chamber pressure (in Pa); (b) Vertical plate displacement (in m).

in Fig. 7.13a is due to the fact that only wave conditions with non-zero probability were incorporated in the analysis.

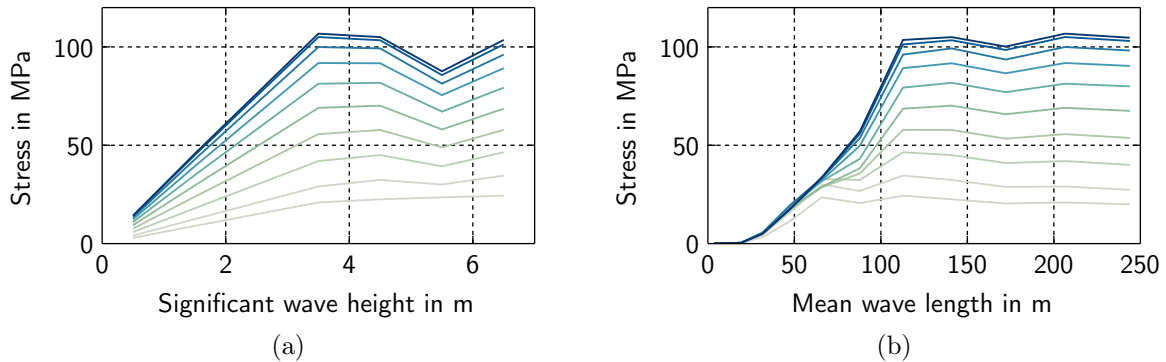


Figure 7.13: Maximum value of the oscillation amplitude of the normal stress in the whole plate in dependence of the significant wave height (a) and on the mean wave length (b). The different lines indicate the different wave headings (from $0-45^\circ$) with darker lines corresponding to higher angles.

The maximum amplitudes of stresses and normal forces in the unit cell always appear at a wave heading of 45° , i.e. for waves propagating in the direction of a diagonal of the square platform. This can be seen in Fig. 7.14. This is due to the resulting twist-like deformation of the plate. When the wave propagates in the diagonal direction two diagonal chambers are lifted up resulting in a twisting of the plate (i.e. bending around a vertical axis).

Observing the maximum occurring pressure amplitudes in the air chamber, as depicted in Fig. 7.15, shows that the oscillation amplitudes remain lower than the static pressure in the chambers for the assumed wave conditions, resulting in a positive internal pressure. Thus, the validity of the linear spring model for the air chambers can be confirmed. The difference of the oscillation amplitudes of the four chambers suggests a dynamic interaction between the comparatively stiff platform and the flexible air chambers. The curves show a similar trend for diagonally opposite chamber pairs, i.e. chambers 1 and 3, and chambers

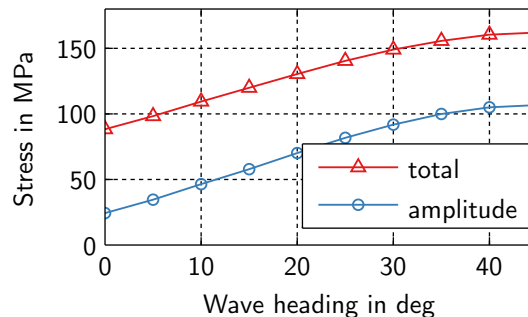


Figure 7.14: Dependence of the maximum normal stress (total values and oscillation amplitudes) in the whole structure on the wave heading. Values obtained by taking all wave conditions with non-zero probability into account.

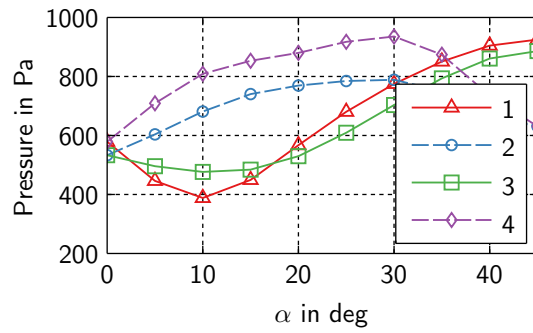


Figure 7.15: Dependence of maximum pressure amplitude in each chamber on the wave heading. The maximum amplitudes appear for the wave spectrum with $H_s=6.5$ m and $T_m=8.5$ s.

2 and 4, respectively. For a wave heading of 45° the wave crest is parallel to the diagonal on which chambers 2 and 4 are located, thus the plate rotates around this axis, creating higher dynamic pressure oscillations in chambers 1 and 3. A similar explanation can be given for the location of the maximum of the pressure amplitudes in chambers 2 and 4 at a wave heading of 30° . Here, the rolling motion of the plate is strongest (see Fig. 7.6).

7.4.2.5 Selected Results

An important case is obviously the wave condition at which the maximum total values appear. Figure 7.16 shows the vertical displacement amplitudes for the sea states at which the largest displacements and the largest stresses occur. The largest total displacements occur at the spectrum with the longest waves at 0° heading. The largest stresses occur when the deformations are highest; at a wave heading of 45° (compare Fig. 7.7).

The arising oscillation amplitudes, total values, and resulting safety factors for the field variables of normal stress and beam normal force are depicted in Figs. 7.17 to 7.19. The maximum total values arise at the same wave conditions as the maximum amplitude values. The sea states leading to maxima in the field variables arise only with very low probability ($<0.5\%$) and correspond to serious storms. Because the platform is moored offshore at a fixed location, it cannot be moved in the case of such an event, and must withstand these harsh conditions. Observing the computed safety factors shows that the

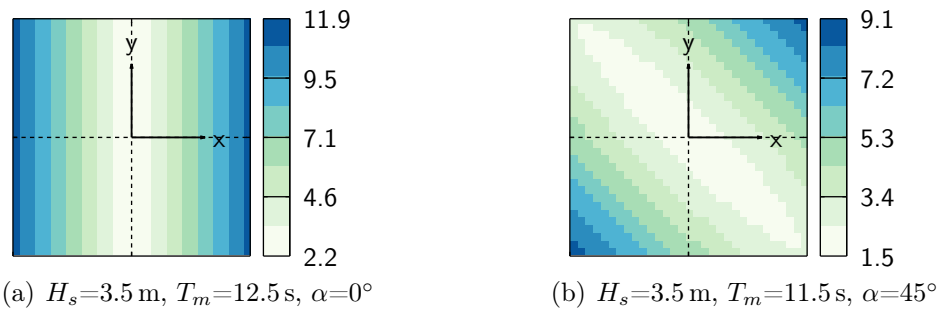


Figure 7.16: Vertical displacement amplitudes (in m) for the wave condition with maximum displacement amplitudes (a) and maximum total normal stress (b).

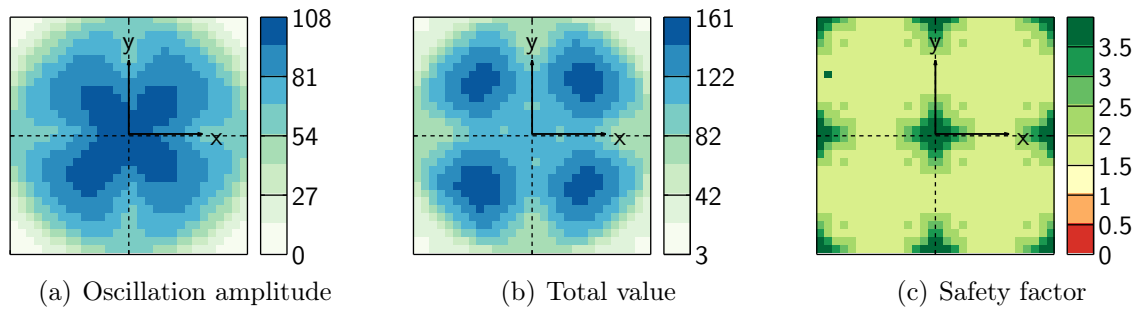


Figure 7.17: Maximum normal stress amplitudes (a), total values (b) in each homogenised unit cell, and corresponding safety factors for an assumed yield limit of 250 MPa (b), for a wave spectrum with $H_s=4.5$ m, $T_m=9.5$ s, and a wave heading of 45° . Stress values are in MPa.

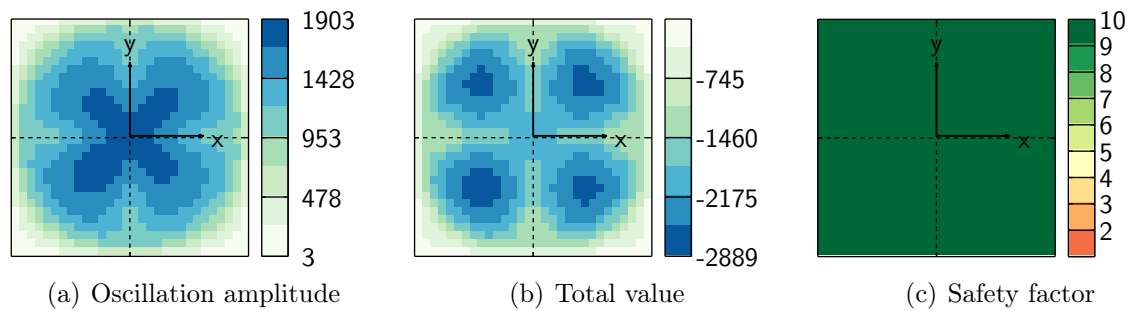


Figure 7.18: Maximum normal force amplitude (a), total normal force (b), and corresponding safety factors against buckling (c) in the top or bottom beams of each homogenised unit cell for a wave spectrum with $H_s=6.5$ m, $T_m=8.5$ s, and a wave heading of 45° . Forces are in kN.

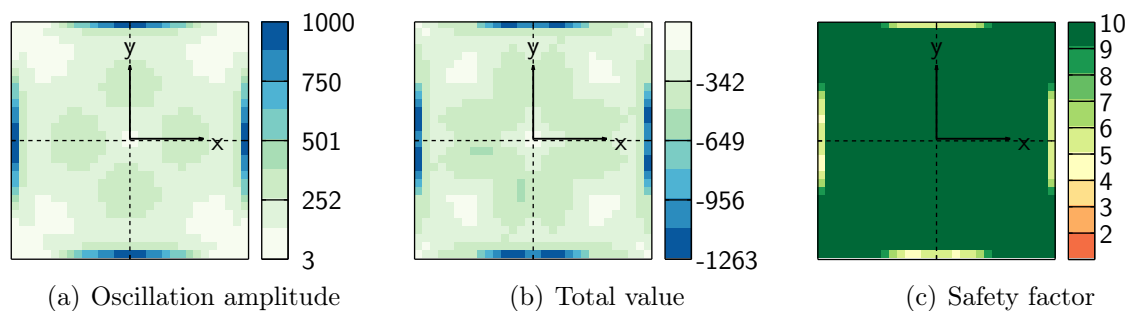


Figure 7.19: Maximum normal force amplitude (a), total normal force (b), and corresponding safety factors against buckling (c) in the diagonal beams of each homogenised unit cell for a wave spectrum with $H_s=6.5$ m, $T_m=8.5$ s, and a wave heading of 45° . Forces are in kN.

computed values lie within acceptable limits.

Another interesting sea state is the one arising with the highest probability. The spectrum with a significant wave height of 0–1 m and mean wave period of 3–4 s arises with a probability of about 25% and thus describes a typical operation condition of the platform. Figures 7.20 and 7.21 show the oscillation amplitudes of normal stress and vertical plate displacement, respectively, for this wave spectrum under different wave headings. The amplitudes of the stresses is very small. Therefore, fatigue damage does not seem critical for the truss structure. Arising displacement amplitudes are so small that the efficiency of the concentrator system is not significantly impacted by the wave induced motion.

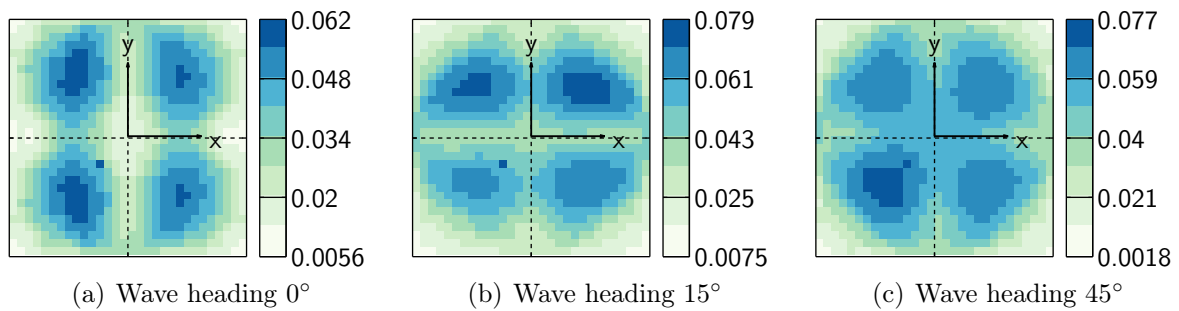


Figure 7.20: Maximum normal stress amplitudes (in MPa) in each homogenised unit cell for the most probable wave spectrum with $H_s=0.5$ m, $T_m=3.5$ s, and different wave headings.

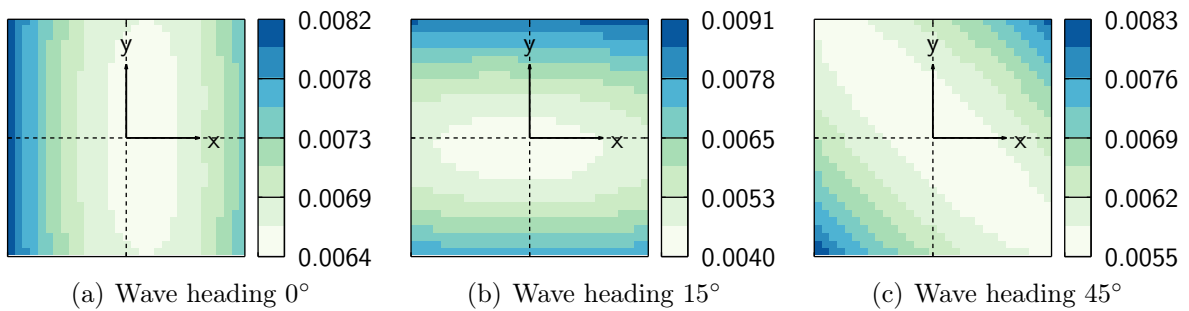


Figure 7.21: Oscillation amplitudes of the vertical plate displacement (in m) for the most probable wave spectrum with $H_s=0.5$ m, $T_m=3.5$ s, and different wave headings.

7.4.3 Quasi-Static Wave Load Case

The quasi-static wave load case assumes a wave of 7.5 m amplitude, which corresponds to the maximum expected wave heights in a wave spectrum with a significant wave height of about 7 m. The resulting twist-type deformation of the plate is the most critical for the structure. A main influence factor on the intensity of the twist-type deformation is the axial stiffness of the air chambers (governed by the membrane stiffness of the skirt material). If the chambers are too stiff, the plate will only be supported by two chambers,

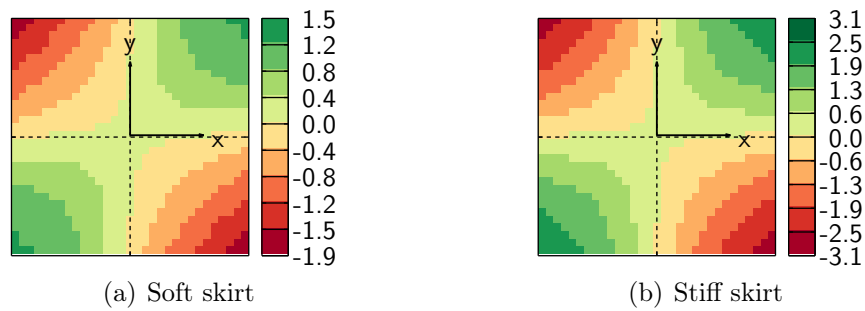


Figure 7.22: Vertical plate deformation (in m) of the quasi-static wave load case for models with different circumferential skirt stiffness.

leading to the most critical situation. An estimation of this limit stiffness based on the assumption of a stiff plate is given in Appendix C.2. The quasi-static wave load case was evaluated for two models with different circumferential membrane stiffness of the skirt. The first one, subsequently denoted soft skirt, corresponds to the value used in the dynamic calculation (500 kN/m). For the other model, termed stiff skirt, a value of 2,500 kN/m is chosen; This value is close to the limit case at which the plate is only carried by two chambers. Figure 7.22 shows a comparison between the computed vertical deformations between the two models. For both models the quasi-static wave load case overestimates the maximum deformation computed via the irregular wave load case (0.8 m amplitude in the twist-mode). This can be explained by the wave length of the expected waves: They are longer than the distance between the centres of two diagonal chambers, which means that the maximum amplitudes occur not at the same time but with a phase difference. Furthermore, the change in the effective surface elevation, i.e. the change in air volume of the chamber, is smaller than the wave amplitude due to the shape of the wave.

The von-Mises equivalent stresses in different parts of the unit cell are depicted in Figs. 7.23 and 7.24 for the soft and the stiff skirt model, respectively. In both cases the overall maximum equivalent stress is dominated by the stress in the top and bottom beams. Substantially larger values arise for the stiff skirt model, because large bending moments are created by the weight of the plate only supported on two chambers. It can be seen that more flexible chambers can reduce this load. The stresses computed in the quasi-static case are overestimations compared to the maxima obtained in the analysis of the irregular wave spectra (see Fig. 7.17). Therefore, the load case is conservative and may be used to obtain a first estimate for the design of the structure.

The maximum compressive normal forces in the beams show the same pattern as the equivalent stress and are, therefore, not explicitly given. All compressive normal forces are, for both models, well below the critical buckling loads.

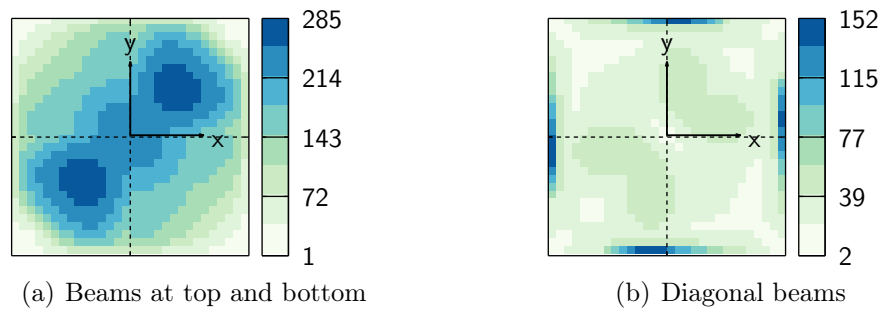


Figure 7.23: Maximum von-Mises equivalent stress (in MPa) in different areas of the unit cell for the soft skirt model.

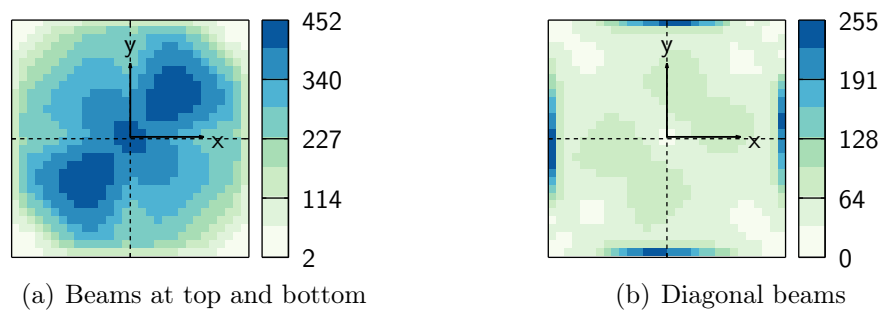


Figure 7.24: Maximum von-Mises equivalent stress (in MPa) in different areas of the unit cell for the stiff skirt model.

7.5 Conclusion

The developed dynamic model was used together with probabilistic theory to describe the behaviour of a floating platform supported by flexible air chambers in real wave conditions defined by wave spectra encountered in the Mediterranean Sea. Two different designs were analysed with the linear dynamic model. Arising loads in static as well as dynamic load cases were computed and evaluated. One of the designs, i.e. the thinner structure, showed excessive deformations in some of the expected sea spectra. While the forces predicted by the linear dynamic model remain in acceptable limits, the predicted deformations exceed the applicability limits of geometrically linear theory. Large in-plane-forces would arise due to geometrically non-linear effects, leading to failure of the structure. The linear dynamic model is, therefore, not applicable for the thin model. The predicted deformations for the other investigated design, the thick model, remain within the applicability limits of linear theory.

Evaluation of the dynamic load cases identified the most critical wave conditions for the structure. While the most critical significant wave height and mean wave period differ for the different field variables like stresses, normal forces or displacements, the largest amplitudes always arise at a wave heading of 45° . Thus, the most critical wave condition are waves travelling in the direction of a diagonal of the square platform. A quasi-static load case resembling such wave conditions was presented and compared to the fully dynamic computations. Due to the simplicity of this load case it is especially useful for a quick pre-design. While the results of the quasi-static wave load case were

conservative with respect to the fully dynamic model in the present case, this may not be true for all models. Therefore, a fully dynamic computation should be carried out for detailed analysis. This is especially important for wave conditions with wave lengths differing from the distance between two diagonal chambers.

The computed values for normal stresses and beam normal forces were evaluated by yield and buckling criteria, respectively. Computed values for the typical operating conditions showed that dynamic effects can be a substantial part of the total load in severe wave conditions. In the typical operation conditions the dynamic amplitudes remain negligible, so fatigue seems to be no major concern. Acceptable safety factors were obtained for the presented design, even in the most severe storm conditions, showing the feasibility of such or similar designs for offshore applications.

Bibliography

- [1] R. Allemang and D. Brown. A Unified Matrix Polynomial Approach to Modal Identification. *Journal of Sound and Vibration*, 211(3):301 – 322, 1998.
- [2] C. B. Barber, D. P. Dobkin, and H. Huhdanpaa. The Quickhull Algorithm for Convex Hulls. *ACM Trans. Math. Softw.*, 22(4):469–483, December 1996.
- [3] N. D. P. Barltrop. *Floating Structures: a guide for design and analysis*, volume 1. CMPT, 1998.
- [4] N. D. P. Barltrop and A. J. Adams. *Dynamics of fixed marine structures*. Butterworth-Heinemann, 1991.
- [5] Y. Başar and W. B. Krätzig. *Mechanik der Flächentragwerke*. Vieweg, 1985.
- [6] J. S. Bendat and A. G. Piersol. *Engineering Applications of Correlation and Spectral Analysis, 2nd Edition*. Wiley-Interscience, 1993.
- [7] A. F. Bower. *Applied Mechanics of Solids*. CRC Press, 2009.
- [8] C. L. Bretschneider. *Wave Variability and Wave Spectra for Wind Generated Gravity Waves*. PhD thesis, Agricultural and Mechanical College of Texas, 1959.
- [9] S. K. Chakrabarti. *Offshore Structure Modeling*, volume 9 of *Advanced Series on Ocean Engineering*. World Scientific, 1994.
- [10] K. Cheung, A. Phadke, D. Smith, S. Lee, and L. Seidl. Hydrodynamic response of a pneumatic floating platform. *Ocean Engineering*, 27(12):1407 – 1440, 2000.
- [11] J. W. Cooley and J. W. Tukey. An Algorithm for the Machine Calculation of Complex Fourier Series. *Mathematics of Computation*, 19(90):pp. 297–301, 1965.
- [12] Dassault Systèmes. *Abaqus Analysis User’s Manual*, 6.10-2 edition, 2010.
- [13] C. M. Diendorfer. *System Design and Analysis of Floating Offshore Solar Power Plants*. PhD thesis, Vienna University of Technology, 2014.
- [14] DNV. Recommended Practice DNV-RP-C205, Environmental Conditions and Environmental Loads. Technical report, Det Norske Veritas, 2010.
- [15] L. Euler. Formulae generales pro translatione quacunque corporum rigidorum. *Novi Commentarii academiae scientiarum Petropolitanae*, 20:189–207, 1776.

- [16] D. J. Ewins. *Modal Testing: Theory and Practice*. Research Studies Press, 1986.
- [17] O. Faltinsen. *Sea Loads on Ships and Offshore Structures*. Cambridge Ocean Technology Series. Cambridge University Press, 1993.
- [18] M. Frigo and S. G. Johnson. The Fastest Fourier Transform in the West. Technical Report MIT-LCS-TR-728, Massachusetts Institute of Technology, September 1997.
- [19] Y. Gao and R. B. Randall. The ITD Mode-Shape Coherence and Confidence Factor and its Application to Separating Eigenvalue Positions in the Z-Plane. *Mechanical Systems and Signal Processing*, 14(2):167 – 180, 2000.
- [20] M. G. D. Geers, E. W. C. Coenen, and V. G. Kouznetsova. Multi-scale computational homogenization of structured thin sheets. *Modelling and Simulation in Materials Science and Engineering*, 15(4):S393, 2007.
- [21] N. Gershenfeld. *The Nature of Mathematical Modeling*. Cambridge University Press, 1999.
- [22] H. Goldstein, C. P. Poole Jr., and J. L. Safko. *Classical Mechanics*. Addison-Wesley, 3 edition, 2001.
- [23] M. Haider, F. G. Rammerstorfer, H. J. Böhm, C. M. Diendorfer, and F. Toth. *Floating Platform*. Patent, European Union, EP2731859, 2014.
- [24] F. J. Harris. On the use of windows for harmonic analysis with the discrete Fourier transform. *Proceedings of the IEEE*, 66(1):51–83, 1978.
- [25] C. Hedegaard. A Roadmap for moving to a competitive low carbon economy in 2050. Technical report, European Commission, 2011.
- [26] L. H. Holthuijsen. *Waves in Oceanic and Coastal Waters*. Cambridge University Press, 2007.
- [27] S. R. Ibrahim. Modal Confidence Factor in Vibration Testing. *Journal of Spacecraft and Rockets*, 15(5), sep/oct 1978.
- [28] S. R. Ibrahim and E. C. Mikulcik. A time domain modal vibration test technique. *The Shock and Vibration Bulletin*, 43:21–37, 1973.
- [29] S. R. Ibrahim and R. S. Pappa. A Parametric Study of the Ibrahim Time Domain Modal Identification Algorithm. *The Shock and Vibration Bulletin*, 1981.
- [30] T. Ikoma, K. Masuda, H. Maeda, and C.-K. Rheem. Effects of Aircushion Division to Hydroelastic Responses of an Aircushion Type Very Large Floating Structure. *ASME Conference Proceedings*, 2003(36819):755–763, 2003.
- [31] International Energy Agency. *Solar Energy Perspectives*. OECD Publishing, 2011.
- [32] International Energy Agency. *World Energy Outlook 2012*. Organization for Economic Cooperation & Development, 2013.

- [33] ITTC. 7.5-02-07-02.1 Seakeeping Experiments. In *ITTC Recommendend Procedures and Guidelines*. International Towing Tank Conference, 2011.
- [34] ITTC. 7.5-02-07-03.2 Analysis Procedure for Model Tests in Regular Waves. In *ITTC Recommendend Procedures and Guidelines*. International Towing Tank Conference, 2002.
- [35] S. G. Johnson and M. Frigo. Implementing FFTs in Practice. In C. S. Burrus, editor, *Fast Fourier Transforms*, chapter 11. Connexions, Rice University, Houston TX, September 2008.
- [36] E. Jones, T. Oliphant, P. Peterson, et al. SciPy: Open source scientific tools for Python, 2001–. <http://www.scipy.org/>.
- [37] Ł. Kaczmarczyk, C. J. Pearce, and N. Bićanić. Scale transition and enforcement of RVE boundary conditions in second-order computational homogenization. *International Journal for Numerical Methods in Engineering*, 74(3):506–522, 2008.
- [38] V. G. Kouznetsova, M. G. D. Geers, and W. A. M. Brekelmans. Multi-scale constitutive modelling of heterogeneous materials with a gradient-enhanced computational homogenization scheme. *International Journal for Numerical Methods in Engineering*, 54(8):1235–1260, 2002.
- [39] V. G. Kouznetsova. *Computational homogenization for the multi-scale analysis of multi-phase materials*. Proefschrift, Technische Universiteit Eindhoven, 2002.
- [40] H. Lamb. *Hydrodynamics*. Cambridge University Press, 1895.
- [41] C.-H. Lee and J. Newman. Wave effects on large floating structures with air cushions. *Marine Structures*, 13(4-5):315 – 330, 2000.
- [42] A. W. Leissa. *Vibration of shells*, volume 288 of *NASA SP*. Scientific and Technical Information Office, National Aeronautics and Space Administration, 1973.
- [43] J. Lighthill. *Waves in Fluids (Cambridge Mathematical Library)*. Cambridge University Press, 2001.
- [44] S. Nasser and M. Hori. *Micromechanics: Overall Properties of Heterogeneous Materials*. Applied Mathematics and Mechanics Series. North-Holland Publ., 1993.
- [45] F. I. Niordson. *Shell Theory*. North-Holland Series in Applied Mathematics and Mechanics. North Holland, 1985.
- [46] Northern Digital Inc. Optotrak Certus. online. <http://www.ndigital.com>, 3 2014.
- [47] D. H. Pahr. *Experimental and Numerical Investigations of Perforated FRP-laminates*. Fortschrittberichte VDI / 18. VDI-Verlag, 2003.
- [48] D. H. Pahr and F. G. Rammerstorfer. Buckling of Honeycomb Sandwiches: Periodic Finite Element Considerations. *Computer Modeling in Engineering & Sciences*, 12: 229–241, 2006.

- [49] J. Park, C. R. Lindberg, and F. L. Vernon, III. Multitaper spectral analysis of high-frequency seismograms. *Journal of Geophysical Research*, 92:12675, November 1987.
- [50] D. B. Percival and A. T. Walden. *Spectral Analysis for Physical Applications*. Cambridge University Press, 1993.
- [51] S. P. Philipps and A. W. Bett. Photovoltaik: Technologien und Märkte - Quo Vadis? In *11. Österreichische Photovoltaik-Tagung 2013*, 2013.
- [52] W. J. Pierson and L. Moskowitz. A proposed spectral form for fully developed wind seas based on the similarity theory of S. A. Kitaigorodskii. *Journal of Geophysical Research*, 69(24):5181–5190, 1964.
- [53] J. Pinkster and E. M. Scholte. The behaviour of a large air-supported MOB at sea. *Marine Structures*, 14(1-2):163 – 179, 2001.
- [54] R. L. Pio. Euler angle transformations. *IEEE Transactions On Automatic Control*, 11(4):707–715, 1966.
- [55] W. G. Price and R. E. D. Bishop. *Probabilistic Theory of Ship Dynamics*. Chapman and Hall, 1974.
- [56] Qualisys AB. Oqus camera series. online. <http://www.qualisys.com>, 3 2014.
- [57] F. G. Rammerstorfer. *Repetitorium Leichtbau*. Oldenbourg, 1992.
- [58] F. G. Rammerstorfer, D. H. Pahr, T. Daxner, and W. K. Vonach. Buckling in Thin Walled Micro and Meso Structures of Lightweight Materials and Material Compounds. *Computational Mechanics*, 37(6):470–478, 2006.
- [59] B. Riemann. *Abhandlungen der Königlich-Gesellschaft der Wissenschaften zu Göttingen*, volume 13, chapter Ueber die Darstellbarkeit einer Function durch eine trigonometrische Reihe. Dedekind, Richard, 1867.
- [60] E. Rupnik and J. Jansa. Experiences in determination of non-rigid body motion in industrial environment using low-cost photogrammetry. *Videometrics, Range Imaging, and Applications XII; and Automated Visual Inspection*, 8791:87910I–87910I–11, May 2013.
- [61] C. E. Shannon. Communication in the Presence of Noise. *Proceedings of the IRE*, 37(1):10–21, 1949.
- [62] D. Slepian and H. O. Pollak. Prolate Spheroidal Wave Functions, Fourier Analysis and Uncertainty - I. *Bell System Technical Journal*, 40, 1961.
- [63] A. Sommerfeld. Die Greensche Funktion der Schwingungsgleichung. *Jahresbericht der Deutschen Mathematiker-Vereinigung*, 21:309–353, 1912.
- [64] R. H. Stewart. *Introduction to Physical Oceanography*. Orange Grove Books, september 2008 edition, 2009.

- [65] E. Stoeger and G. Munzenrieder. *Device for concentrating solar radiation in an absorber*. Patent, United States of America, US20140071551 A1, March 2014.
- [66] P. Suquet. Local and global aspects in the mathematical theory of Plasticity. In A. Sawczuk and G. Bianchi, editors, *Plasticity Today*. Elsevier Appl. Sc. Pub., London, 1985.
- [67] The MathWorks Inc. *MATLAB Documentation*, 8.0.0.783 (R2012b) edition, 2012.
- [68] D. J. Thomson. Spectrum estimation and harmonic analysis. *Proceedings of the IEEE*, 70(9):1055–1096, 1982.
- [69] F. Tiefenbacher and J. Höfler. *Kissenförmiger Konzentrador*. Patent, European Union, EP 2 542 841 B1, 2013.
- [70] S. Timoshenko and S. Woinowsky-Krieger. *Theory of Plates and Shells*. Engineering Societies Monographs. McGraw-Hill College, 1959.
- [71] F. Toth. Model Tests of a Floating Platform at the Vienna Model Basin. Technical Report 278, Institute of Lightweight Design and Structural Biomechanics, Vienna University of Technology, 2013.
- [72] F. Toth. Design of an Equivalent Model for Hydrodynamic Model Tests. Technical Report 274, Institute of Lightweight Design and Structural Biomechanics, Vienna University of Technology, 2012.
- [73] F. Tsai. Measurement of wave hight produced by the forced heaving of cylinders. Report vol. viii, No. 29, Research Intitute for Applied Mechanics, Kyushu University, 1960.
- [74] M. Unser. Splines: A perfect fit for signal and image processing. *Signal Processing Magazine, IEEE*, 16(6):22–38, 1999.
- [75] J. L. F. van Kessel. *Aircushion Supported Mega-Floaters*. PhD thesis, Delft University of Technology, 2010.
- [76] Vienna Model Basin Ltd. online. <http://www.sva.at>, 3 2014.
- [77] C. M. Wang, Z. Y. Tay, K. Takagi, and T. Utsunomiya. Literature Review of Methods for Mitigating Hydroelastic Response of VLFS Under Wave Action. *Applied Mechanics Reviews*, 63(3):030802, 2010.
- [78] C. Wang and C. Wang. Computation of the stress resultants of a floating Mindlin plate in response to linear wave forces. *Journal of Fluids and Structures*, 24(7):1042 – 1057, 2008.
- [79] S. Wang. Plunger-Type Wavemakers: Theory and Experiment. *Journal of Hydraulic Research*, 12(3):pp. 375–388, 1974.
- [80] E. Watanabe, C. M. Wang, T. Utsunomiya, and T. Moan. Very Lange Floating Structures: Applications, Analysis and Design. Technical report, Centre for Offshore Research and Engineering, National University of Singapore, 2004.

- [81] P. D. Welch. The use of fast Fourier transform for the estimation of power spectra: A method based on time averaging over short, modified periodograms. *Audio and Electroacoustics, IEEE Transactions on*, 15(2):70–73, 1967.
- [82] G. Wempner and D. Talaslidis. *Mechanics of Solids and Shells*. CRC Press, 2003.
- [83] I. M. Winogradow. Parseval equality. In M. Hazewinkel, editor, *Encyclopedia of Mathematics*. Springer, 1987-1994.
- [84] J. T. Xing. Natural vibration of two-dimensional slender structure–water interaction systems subject to Sommerfeld radiation condition. *Journal of Sound and Vibration*, 308(1–2):67 – 79, 2007.

Appendix A

Water Waves

A.1 Linear Surface Gravity Waves

Let us consider a domain of water with infinite depth. The x and y -axis are located in the plane of the undisturbed water surface, i.e. in its equilibrium position, and the z -axis points vertically upwards. The acceleration of gravity points in negative z direction. Air with an ambient pressure of p_0 is located above the water domain. The hydrostatic pressure in the water, p_h , can then be obtained by solving the static equilibrium equation

$$\nabla p_h = \rho \mathbf{g}, \quad (\text{A.1})$$

where ρ denotes the density of the water [43]. Integration and insertion of the boundary condition $p_h = p_0$ at $z = 0$ yields

$$p_h(z) = p_0 - \rho g z. \quad (\text{A.2})$$

In the presence of water waves an excess pressure due to the disturbance, for brevity denoted just p , will arise in the fluid. The total pressure in the water domain is then

$$p_t = p_h + p. \quad (\text{A.3})$$

Considering only small disturbances the momentum equation may be linearised yielding

$$-\nabla p = \rho \frac{\partial \mathbf{v}}{\partial t}, \quad (\text{A.4})$$

where \mathbf{v} denotes the velocity vector. The continuity equation for incompressible media reduces to

$$\nabla^2 \phi = 0, \quad (\text{A.5})$$

where the velocity potential ϕ is used to prescribe the velocity field by $\nabla \phi = \mathbf{v}$. Equation (A.5) is recognised as the Laplace equation for the velocity potential. For domains entirely bounded by stationary walls it cannot describe the propagation of waves. However, for the problem at hand we are dealing with a free surface.

The position of the free surface is defined by the function $\eta(x, y)$. The total pressure in the fluid at the free surface must equal the atmospheric pressure. This gives the dynamic boundary condition

$$p = \rho g \eta \quad \text{on } \eta. \quad (\text{A.6})$$

Additionally, the kinematic boundary condition at the free surface constrains the evolution of the free surface to the motion of a liquid particle at the free surface, giving

$$\frac{\partial \eta}{\partial t} + \mathbf{v} \cdot \nabla \eta = \left[\frac{\partial \phi}{\partial z} \right]_{z=\eta}. \quad (\text{A.7})$$

Both boundary conditions can be linearized. Taking the gradient of Eq. (A.6) and combining with Eq. (A.4) yields

$$\left[\frac{\partial \phi}{\partial t} \right]_{z=\eta} = -g\eta \quad (\text{A.8})$$

Taking the time derivative and insertion into the linearised form of Eq. (A.7) finally gives

$$\frac{\partial^2 \phi}{\partial t^2} = -g \frac{\partial \phi}{\partial z} \quad \text{on } z = 0, \quad (\text{A.9})$$

which is the free surface condition formulated in terms of the velocity potential.

Considering the two-dimensional case, i.e. $\phi = \phi(x, z, t)$ one solution to Eq. (A.5) fulfilling the boundary condition Eq. (A.9) is

$$\phi(x, z, t) = a \frac{\omega}{k} e^{kz} \sin(kx - \omega t), \quad (\text{A.10})$$

where a denotes the wave amplitude, $k = 2\pi/\lambda$ the wave number, and ω the angular wave frequency. Inserting above solution into the boundary condition Eq. (A.9) yields the dispersion relation for deep water waves

$$\omega^2 = gk. \quad (\text{A.11})$$

The pressure field is related to the velocity potential directly by the momentum equation, Eq. (A.4), yielding

$$p(x, z, t) = -\rho \frac{\partial \phi}{\partial t} = \rho g a e^{kz} \cos(kx - \omega t). \quad (\text{A.12})$$

The velocity of a fluid particle can be computed by its relation to the velocity potential by

$$\mathbf{v}(x, z, t) = \nabla \phi = \left[\frac{\partial \phi}{\partial x} \right]_{\frac{\partial \phi}{\partial z}} = a \omega e^{kz} \begin{bmatrix} \cos(kx - \omega t) \\ \sin(kx - \omega t) \end{bmatrix}. \quad (\text{A.13})$$

A.2 Representation of an Irregular Seaway

An immediately recognisable property of real ocean waves is their irregularity. In the following only two-dimensional waves are considered due to simplicity. However the general concept may be extended in a straightforward matter by considering a distribution of the wave direction as give by Price and Bishop [55], or DNV [14]. For the mathematical treatment an irregular sea state is can be assumed as the sum of a large number of regular waves, i.e. solutions of the linearised hydrodynamic equations for water waves, according to

$$\eta(t) = \sum_{j=1}^{\infty} a_j \cos(\varphi_j - \omega_j t). \quad (\text{A.14})$$

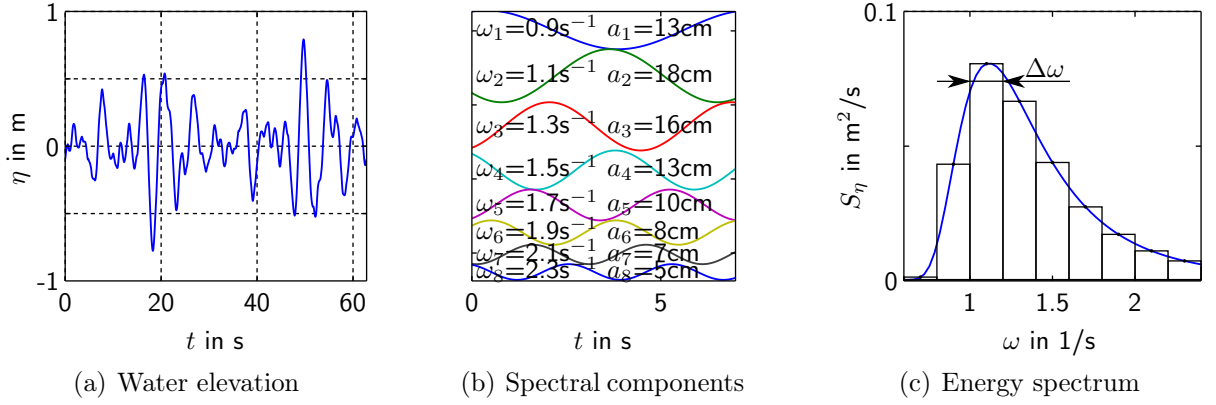


Figure A.1: Example of a short term wave record (a), its components with the largest amplitudes (b), and the corresponding energy spectrum (c).

The amplitudes a_j and corresponding angular frequencies ω_j are deterministic and related by the wave energy spectrum. The phase angles $\varphi_j \in [0, 2\pi[$ are considered as a random variable with uniform probability density function [55]. Hence, the water elevation may be thought of as the realisation of a random process. It can be shown that the so defined random process of the wave height is ergodic in the mean, mean square and autocorrelation function statistics [55].

Some wave energy spectra for real sea conditions are presented in Appendix A.4. When computing an example wave signal (see Fig. A.1a) for a specified wave spectrum $S_\eta(\omega)$ only a finite number of harmonics can be taken into account. Doing so, care has to be taken that the total energy is conserved (see also Appendix A.3 for a more concise description of wave energy). The frequency axis is discretised into N intervals of width $\Delta\omega$. The amplitudes are computed by

$$a_i = \sqrt{2S_\eta(\omega_i) \Delta\omega}. \quad (\text{A.15})$$

The process is illustrated in Fig. A.1c.

A.3 Wave Energy

The wave energy per surface area

$$E = \frac{\rho g}{2} \langle \eta^2 \rangle, \quad (\text{A.16})$$

is related to the variance of sea surface displacement $\langle \eta^2 \rangle$, which can be obtained by averaging in time or space [64]. In Eq. (A.16) g denotes the acceleration of gravity and ρ the fluid density. The energy relation can be obtained from the wave energy of a single harmonic

$$E_j = \frac{\rho g}{2} a_j^2, \quad (\text{A.17})$$

by using Parseval's equality, which states

$$\int_{-\infty}^{\infty} |\eta(t)|^2 dt = \int_{-\infty}^{\infty} |\mathcal{F}\{\eta(t)\}|^2 df, \quad (\text{A.18})$$

where \mathcal{F} denotes the Fourier transform [83].

The area under the spectrum curve

$$\sigma^2 = \int_0^{\infty} S_{\eta}(\omega) d\omega, \quad (\text{A.19})$$

is equivalent to the variance σ^2 of the surface elevation. Because the variance of the surface elevation determines the wave energy care has to be taken when expressions for the spectrum given in terms of angular frequency are converted to expressions in terms of frequency. To conserve the wave energy the relation

$$S_{\eta}(f) = 2\pi S_{\eta}(\omega), \quad (\text{A.20})$$

must hold.

A.4 Commonly Used Wave Spectra

A general form applicable to most sea spectra, sometimes termed Bretschneider spectrum [8], is

$$S_B(\omega) = \frac{A}{\omega^5} e^{\frac{B}{\omega^4}}. \quad (\text{A.21})$$

The international towing tank conference (ITTC) recommends using $A = 173H_s^2/T_1$ and $B = 691/T_1$ with the average wave period T_1 and significant wave height H_s of the sea state. This is equivalent to the *Pierson-Moskowitz* (PM) spectrum [52] for fully developed seas

$$S_{PM}(\omega) = \frac{5}{16} H_s^2 \omega_p^4 \omega^{-5} \exp\left(-\frac{5}{4} \left(\frac{\omega}{\omega_p}\right)^{-4}\right), \quad (\text{A.22})$$

where $\omega_p = 2\pi/T_p$ is the angular spectral peak frequency.

An extension of the above spectra was developed in the *joint north sea wave atmosphere program* (JONSWAP). The, so called, JONSWAP spectrum describes a developing sea state in a fetch limited condition[14]. In the notation of Barltrop and Adams [4], it is calculated by

$$S_J(f) = \frac{k_b^4 H_s^2 k_{\gamma}}{4\pi(k_p T_z)^4 f^5} \exp\left(-\frac{1}{\pi f^4} \left(\frac{k_b}{k_p T_z}\right)^4\right) \gamma^a, \quad (\text{A.23})$$

with

$$k_b = 1.4085, \quad (\text{A.24a})$$

$$k_p = 0.327 \exp(-0.315\gamma) + 1.17, \quad (\text{A.24b})$$

$$k_{\gamma} = 1 - 0.285 \ln(\gamma), \quad (\text{A.24c})$$

$$\sigma = \begin{cases} 0.07 & \text{for } f \leq \frac{1}{k_p T_z} \\ 0.09 & \text{for } f > \frac{1}{k_p T_z} \end{cases}, \quad (\text{A.24d})$$

$$a = \exp\left(-\frac{(k_p T_z f - 1)^2}{2\sigma^2}\right). \quad (\text{A.24e})$$

The ITTC recommends using a peak shape parameter of $\gamma = 3.3$ [33], which was obtained from measurements in the north sea [55].

The significant wave height H_s is defined as the average height of the highest one-third waves in the indicated time period. The zero-up-crossing period T_z is the average time interval between two successive up-crossings of the mean sea level [14].

Appendix B

Additional Experimental Results

B.1 Small Model

For the sake of completeness the test results for the small model are presented here. Details of test conditions are given by Diendorfer [13]. The results in Fig. B.1 are an average of all conducted test campaigns.

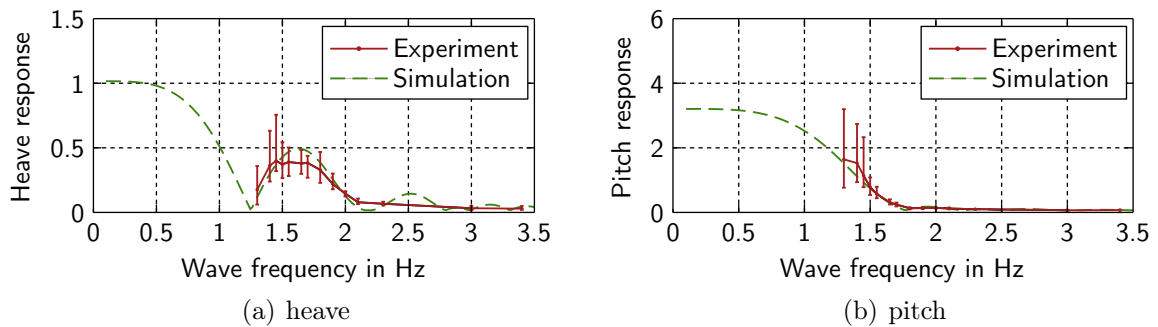


Figure B.1: Experimentally obtained and simulated response amplitude operators for the small model at a wave heading on 0° . The error bars indicate the 0.05 and 0.95 quantiles of all experiments.

B.2 Large Model

The large model was tested in the Vienna Model Basin. Tests in regular and irregular waves were performed to determine the transfer functions for three different wave headings. Two different wave spectra were modelled. The following test results are included here for the sake of completeness. For more details the reader is referred to the test report[71].

B.2.1 Wave Heading 0°

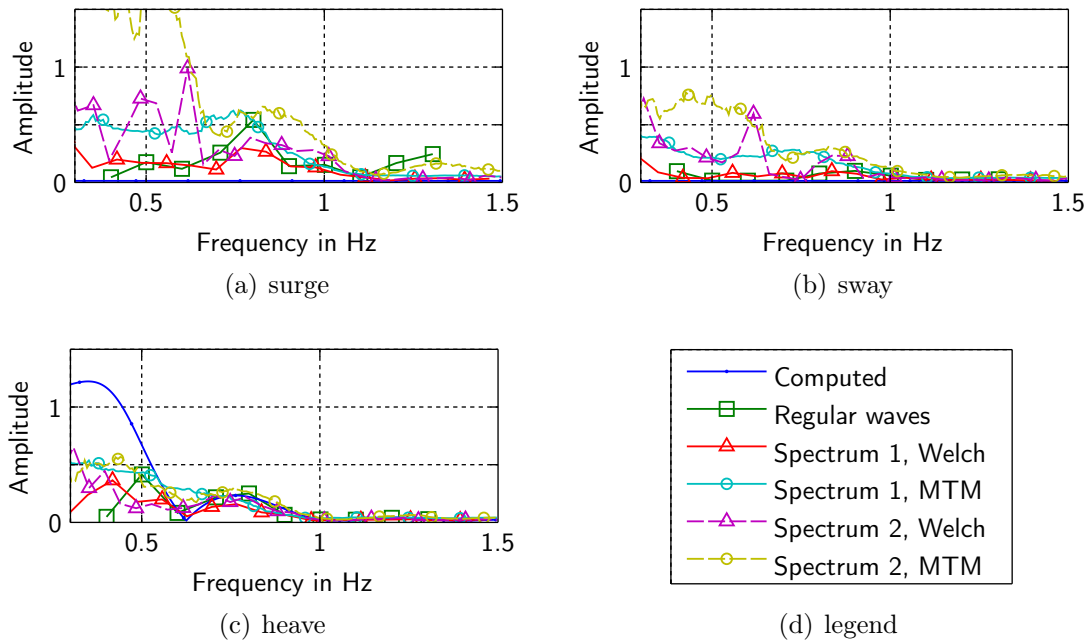


Figure B.2: Translational RAOs for a wave heading of 0° generated by a computational model, regular wave experiments, and irregular wave experiments with two different spectra. The response amplitude is normalized by the wave amplitude.

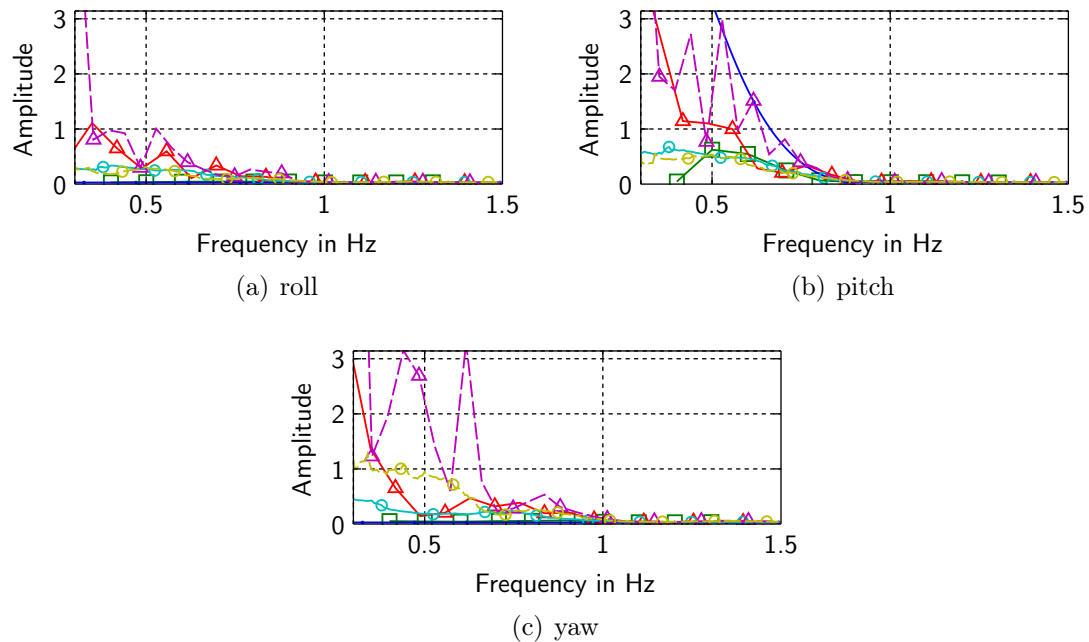


Figure B.3: Rotational RAOs for a wave heading of 0° generated by a computational model, regular wave experiments, and irregular wave experiments with two different spectra. The response amplitude is normalized by the wave slope. For a legend see Fig. B.2.

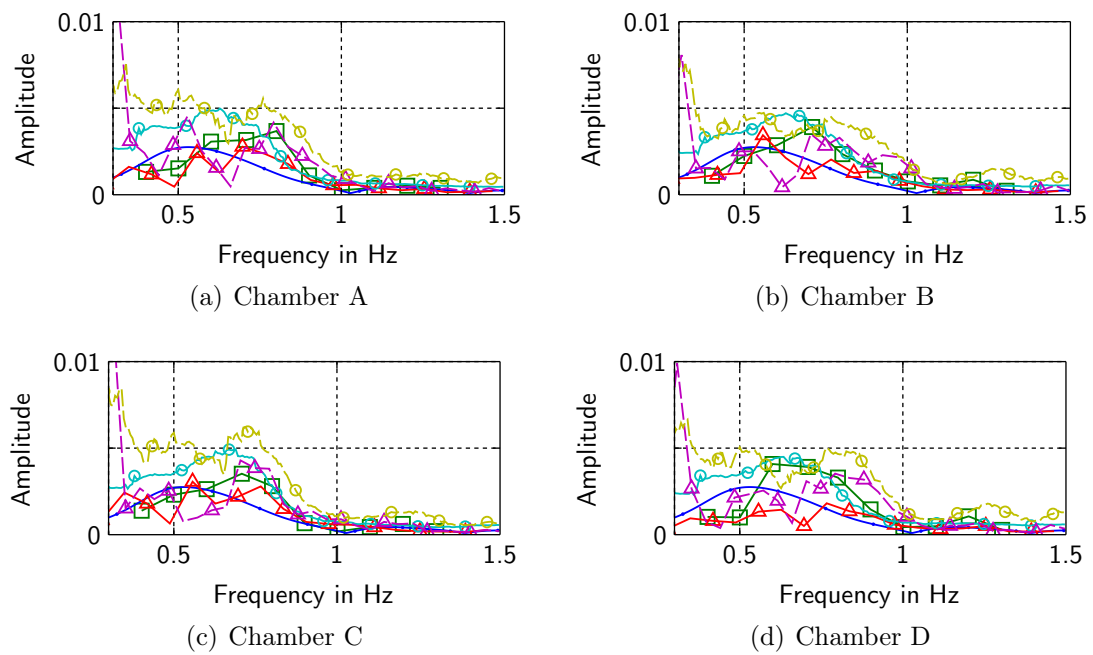


Figure B.4: Pressure RAOs for a wave heading of 0° generated by a computational model, regular wave experiments, and irregular wave experiments with two different spectra. The response amplitude is normalized by the dynamic pressure at the water surface. For a legend see Fig. B.2.

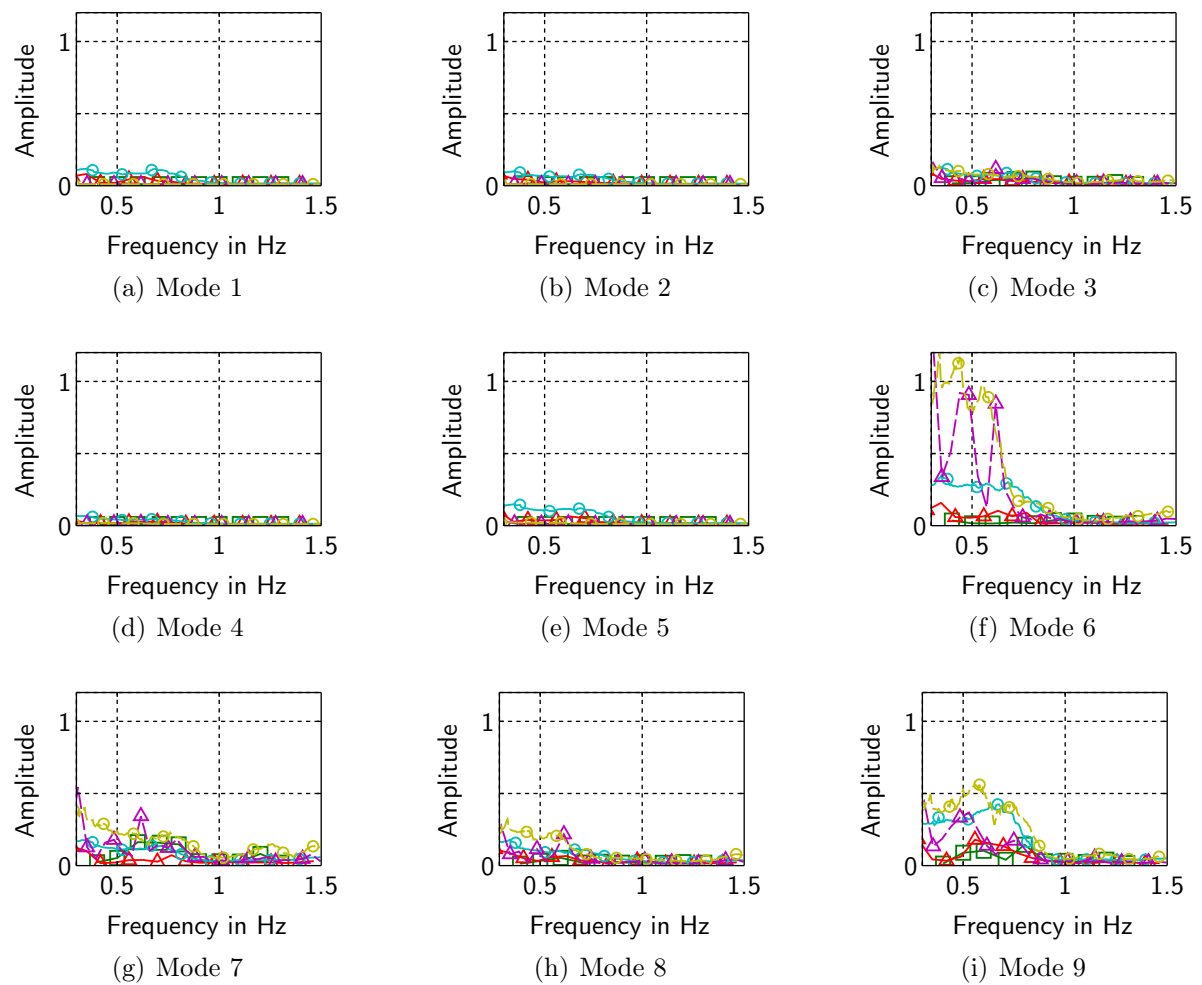


Figure B.5: Deformation RAOs for a wave heading of 0° generated by regular wave experiments, and irregular wave experiments with two different spectra. The response amplitude is normalized by the wave amplitude. For a legend see Fig. B.2.

B.2.2 Wave Heading 22.5°

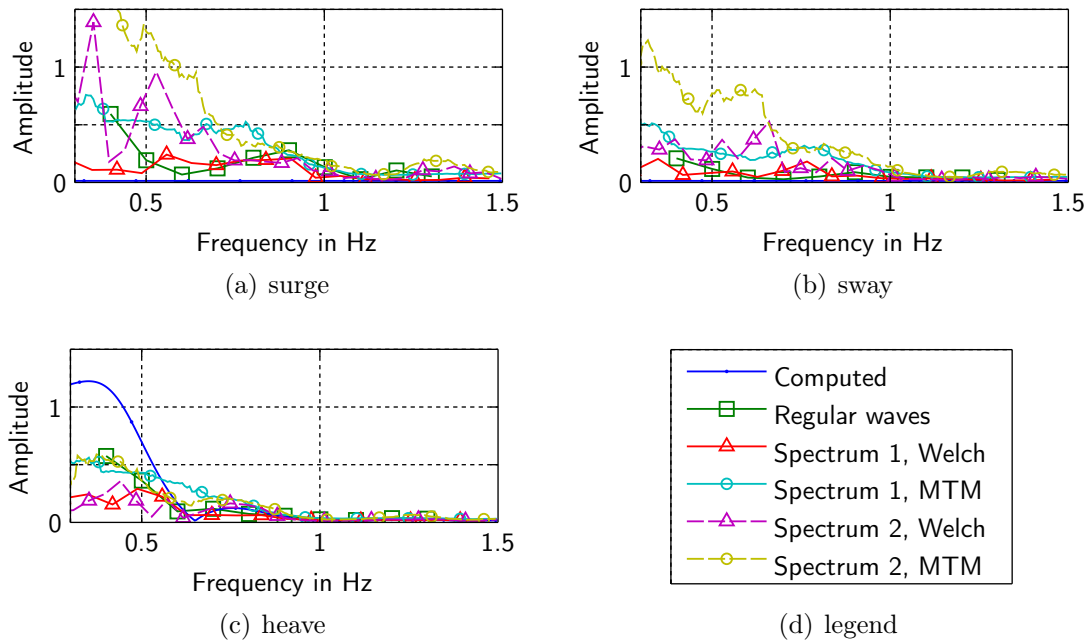


Figure B.6: Translational RAOs for a wave heading of 22,5° generated by a computational model, regular wave experiments, and irregular wave experiments with two different spectra. The response amplitude is normalized by the wave amplitude.

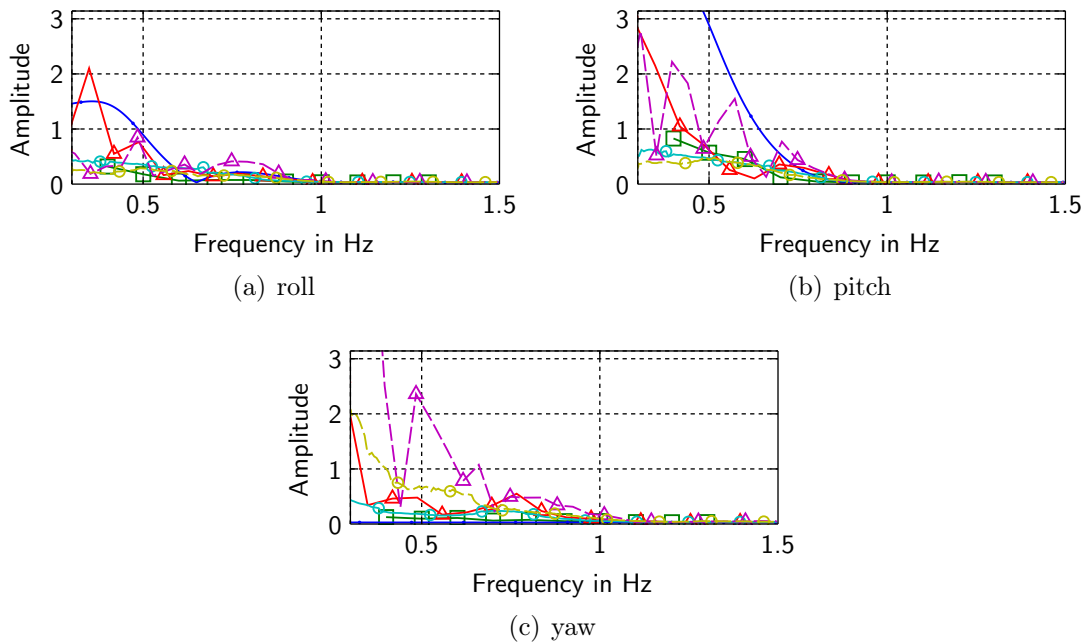


Figure B.7: Rotational RAOs for a wave heading of 22,5° generated by a computational model, regular wave experiments, and irregular wave experiments with two different spectra. The response amplitude is normalized by the wave slope. For a legend see Fig. B.6.

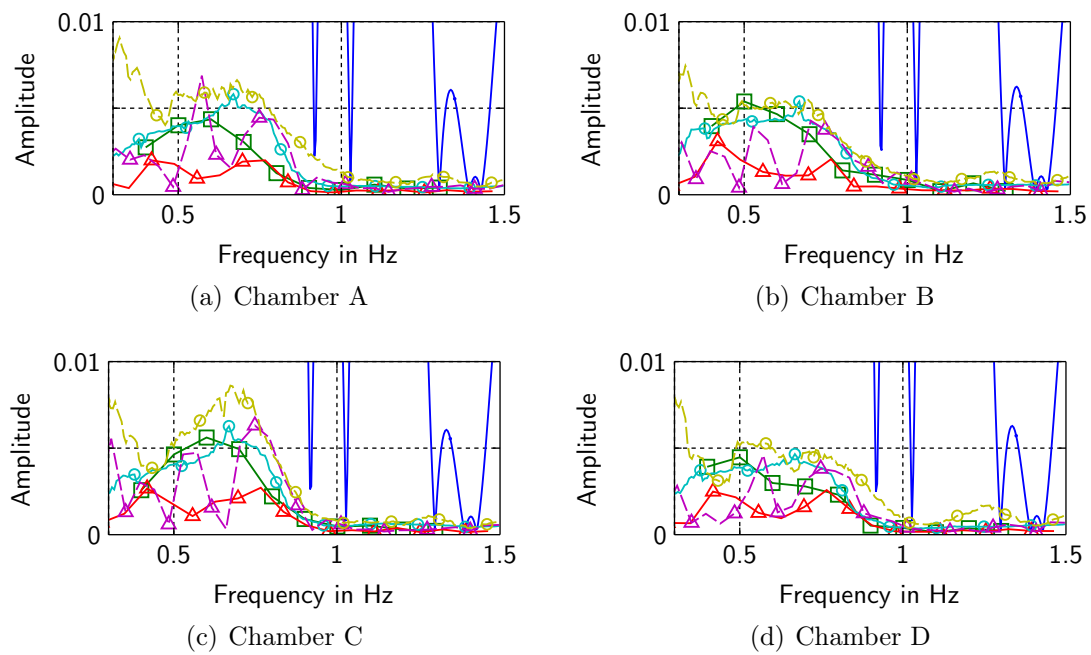


Figure B.8: Pressure RAOs for a wave heading of 22.5° generated by a computational model, regular wave experiments, and irregular wave experiments with two different spectra. The response amplitude is normalized by the dynamic pressure at the water surface. For a legend see Fig. B.6.

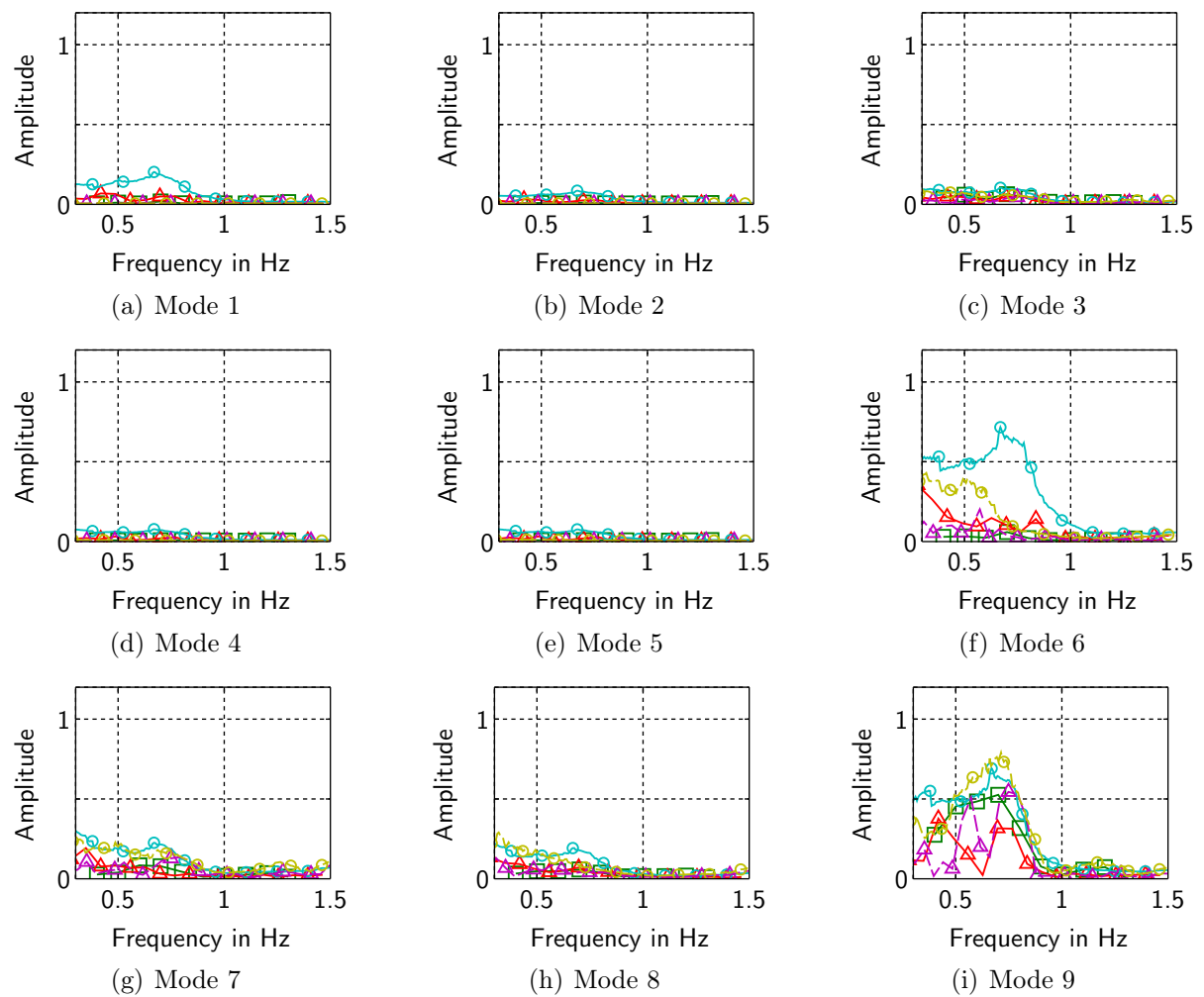


Figure B.9: Deformation RAOs for a wave heading of $22,5^\circ$ generated by regular wave experiments, and irregular wave experiments with two different spectra. The response amplitude is normalized by the wave amplitude. For a legend see Fig. B.6.

B.2.3 Wave Heading 45°

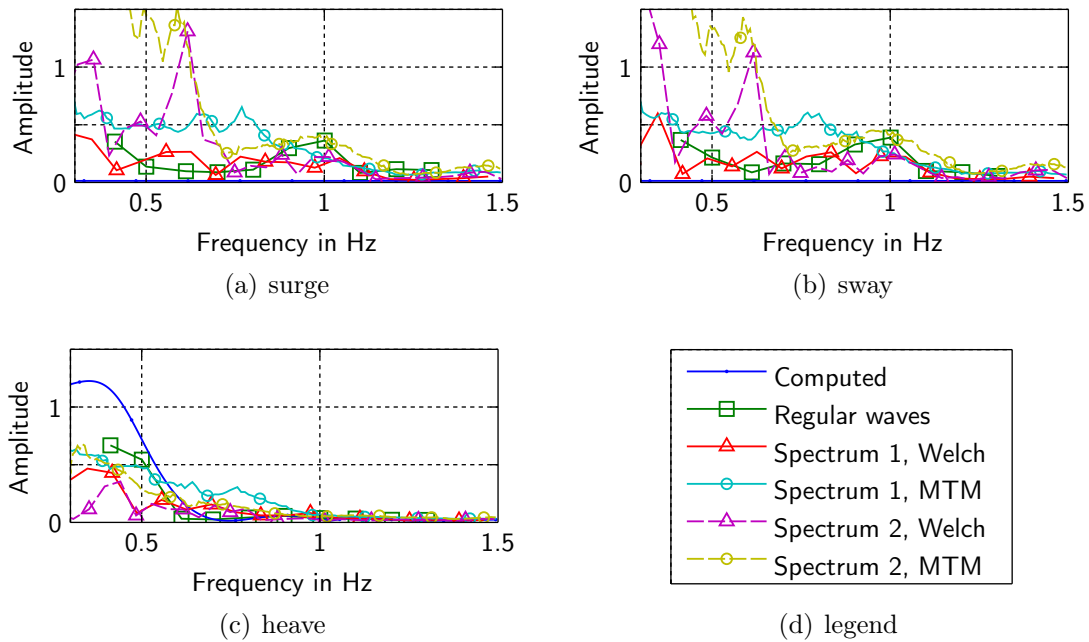


Figure B.10: Translational RAOs for a wave heading of 45° generated by a computational model, regular wave experiments, and irregular wave experiments with two different spectra. The response amplitude is normalized by the wave amplitude.

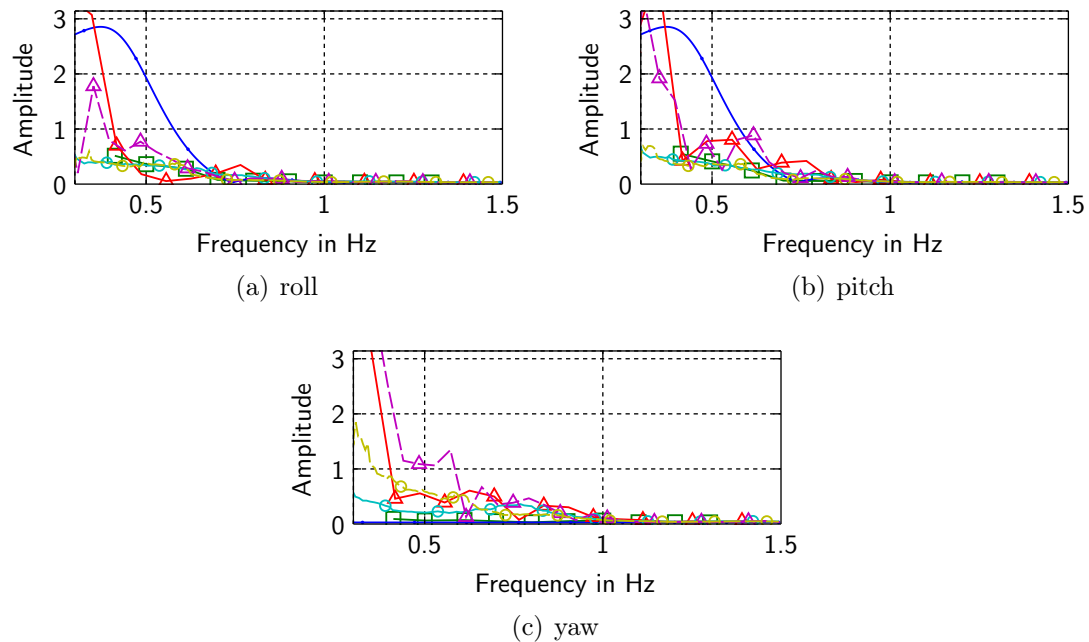


Figure B.11: Rotational RAOs for a wave heading of 45° generated by a computational model, regular wave experiments, and irregular wave experiments with two different spectra. The response amplitude is normalized by the wave slope. For a legend see Fig. B.10.

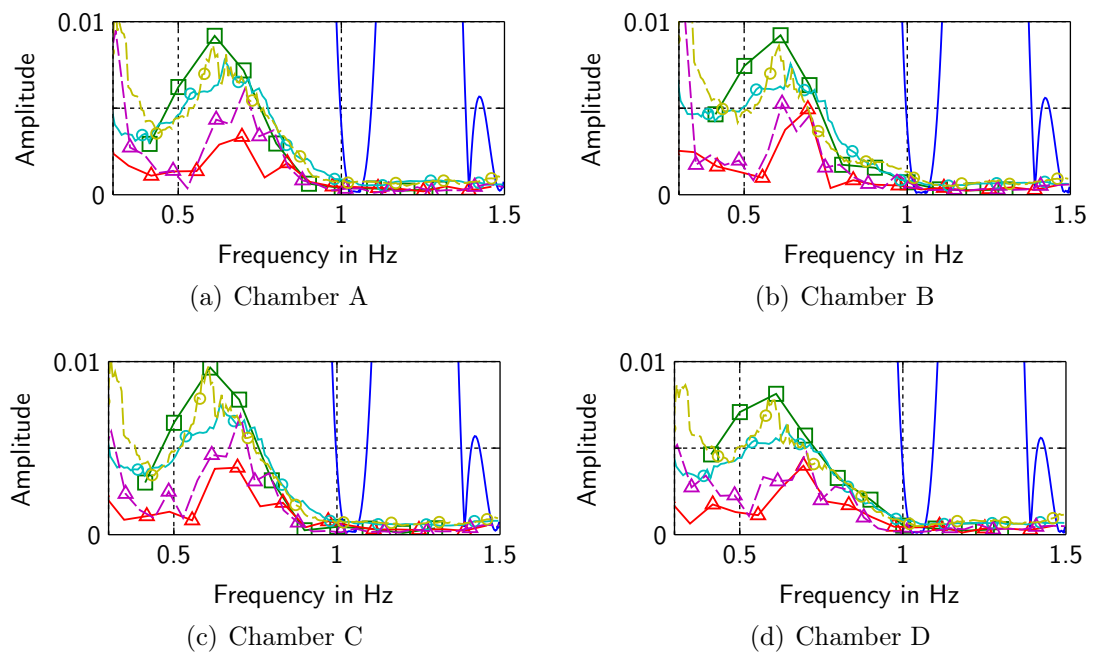


Figure B.12: Pressure RAOs for a wave heading of 45° generated by a computational model, regular wave experiments, and irregular wave experiments with two different spectra. The response amplitude is normalized by the dynamic pressure at the water surface. For a legend see Fig. B.10.

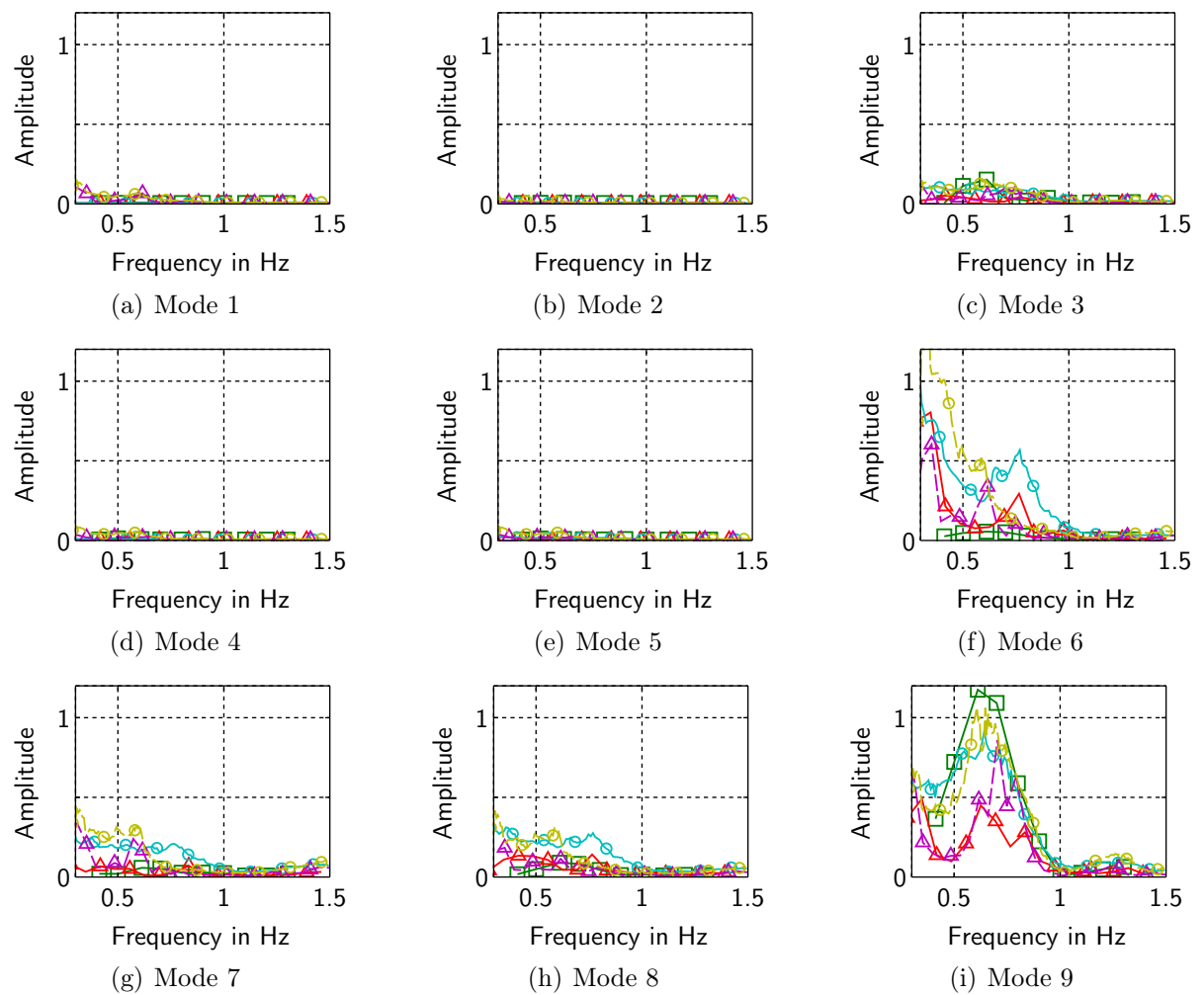


Figure B.13: Deformation RAOs for a wave heading of 45° generated by regular wave experiments, and irregular wave experiments with two different spectra. The response amplitude is normalized by the wave amplitude. For a legend see Fig. B.10.

Appendix C

Miscellaneous Mechanics

C.1 Static Air Pressure in the Chambers

To calculate the static pressure in the chambers of an air chamber supported floating platform the mass of the platform and the acting buoyancy forces must be considered. The total mass is divided into parts for the plate, m , for the skirt, m_s , and the ballast weights at the lower end of the skirt, m_b , and can be calculated by

$$m_t = m + \sum_i \underbrace{2r_i\pi h_{s,i} t_{s,i} \rho_s}_{m_{s,i}} + \sum_i m_{b,i}, \quad (\text{C.1})$$

where r is the radius of the chamber, h_s is the total height of the cylindrical skirt membrane, t_s is the thickness of the membrane, and ρ_s is the density of the skirt material. The index i denotes the number of the air chamber. The total buoyancy force can be computed by

$$B = \sum_i 2r_i\pi h_{l,i} t_s \rho_w g + \sum_i m_{b,i} \frac{\rho_w}{\rho_b} g, \quad (\text{C.2})$$

where h_l is the submerged depth of skirt and ρ_b is the density of the ballast material.

The static pressure in the chambers needs to carry the total weight of the whole platform less the buoyancy of submerged elements and can, hence, be calculated by

$$p_c = \frac{m_t g - B}{\sum_i r_i^2 \pi} = \frac{g}{\sum_i r_i^2 \pi} \left[m + \sum_i m_{s,i} \left(1 - \frac{h_{l,i} \rho_w}{h_{s,i} \rho_s} \right) + \left(1 - \frac{\rho_w}{\rho_b} \right) \sum_i m_{b,i} \right]. \quad (\text{C.3})$$

The terms in round parentheses take into account the buoyancy effects. For a typical platform configuration, this effect is small for the skirt, due to the low share of submerged skirt mass in the total mass and due to the density ratio of about one. The buoyancy of the ballast weight at the end of the skirt should be taken into account, because even for lead ballast the buoyancy force is about 9% of its weight.

C.2 Chamber Stiffness and Wave Height

In order to describe the platform dynamics by a linear system, the forces in the linear springs modelling the air chambers must remain compressive at all times, because the

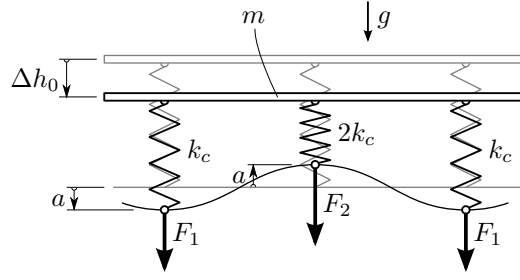


Figure C.1: Wave travelling along the diagonal of a platform with 4 chambers.

flecible air chambers cannot transmit tensional forces. This will be the case if the wave amplitudes are sufficiently small. The allowable wave amplitude can be estimated based on a quasi-static model. As a further simplification the plate is assumed as rigid. The most critical load case, a wave travelling along the diagonal of the quadratic platform with four chambers, is considered. The mechanical system is depicted in Fig. C.1.

The displacements of the water surface, i.e. the lower end of the chamber, equals the wave amplitude a . The forces in the springs modelling the air chambers are

$$F_1 = k_c(a - \Delta h_0), \quad (\text{C.4a})$$

$$F_2 = -2k_c(a + \Delta h_0), \quad (\text{C.4b})$$

where k_c denotes the axial stiffness of the air chamber. The static depression of the plate onto the air chambers due to its weight, denoted by Δh_0 in the above equation, can be obtained by a balance of forces in vertical direction giving

$$\Delta h_0 = \frac{mg}{4k_c}, \quad (\text{C.5})$$

where g denotes the acceleration of gravity, and m the total mass of the plate. The condition for the springs to remain in compression is $F_i < 0$. Inserting Eq. (C.5) into Eq. (C.4) thus gives

$$|a| < \frac{mg}{4k_c} \quad (\text{C.6})$$

as the condition for all springs to remain in tension. It can be seen that the allowable wave amplitude can be increased by lowering the axial stiffness of the air chamber, or by increasing the platform mass.

C.3 Pressure Measurement by a Water Column

The pressure difference Δp between a pressure vessel, i.e. a chamber, and the ambient air is related to the water level difference Δh in the connecting water column by

$$p_2 - p_1 = \Delta p = \rho_w g \Delta h, \quad (\text{C.7})$$

where p_2 is the pressure in the air chamber, p_1 is the pressure in the surrounding air, ρ_w is the density of the fluid, i.e. water, and g is the gravitational acceleration. For a description of the used symbols see the sketch of the water column in Fig. C.2. Measuring the water

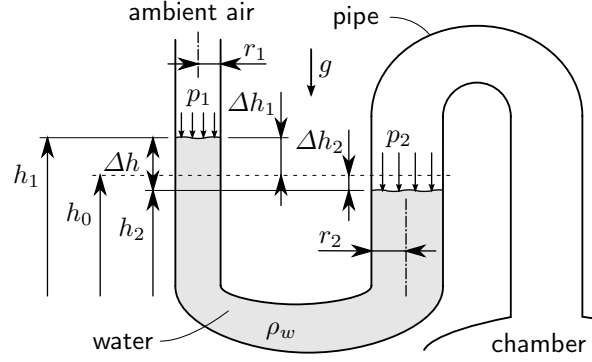


Figure C.2: Sketch of the water column.

level distance is inconvenient, because two water levels must be observed simultaneously. Using the assumption of an incompressible fluid

$$\underbrace{(h_1 - h_0)}_{\Delta h_1} A_1 = \underbrace{(h_0 - h_2)}_{\Delta h_2} A_2, \quad (\text{C.8})$$

the total level difference can be related to the level difference in the column with the smaller cross section via

$$h_1 - h_2 = \Delta h = \Delta h_1 + \Delta h_2 = \Delta h_1 \left(1 + \frac{A_1}{A_2} \right), \quad (\text{C.9})$$

where Δh_i is the water level difference in column i with respect to the initial water level, i.e. the water level for the same pressure in both columns. Combining above equations and assuming circular cross sections one finally obtains

$$\Delta p = \rho_w g \left[1 + \left(\frac{r_1}{r_2} \right)^2 \right] \Delta h_1, \quad (\text{C.10})$$

which reveals the usefulness of different diameters of the columns: it increases the measurement resolution. For the same measured water level distance Δp_1 the pressure difference is smaller for larger radius ratios.

When using different column diameters capillary effects can impact the measurement result. The difference of the water level in a vertical pipe with radius r with respect to an infinite basin can be calculated by

$$h = \frac{2\sigma \cos \Theta}{\rho_w g r}, \quad (\text{C.11})$$

where σ is the surface tension and Θ is the contact angle between water and pipe. The level difference between columns with different radii is hence calculated by

$$\Delta h = \frac{2\sigma \cos \Theta}{\rho_w g} \frac{r_2 - r_1}{r_1 r_2} \quad (\text{C.12})$$

which yields a difference of 0.765 mm for the used water column ($r_1=6.25$ mm, $r_2=9.5$ mm). In the calculation a surface tension of 0.0728 J/m² and a contact angle of 20° were assumed.

The water level difference due to capillary effects can, therefore, lead to an error of 7.49 Pa if it were not taken into account and the measurement was based on the absolute water level difference. If the pressure measurement is based on the water level difference between the current water level and the one for equal pressure, surface tension has no effect on the measurement.

C.4 Homogeneous, Isotropic, Linear-Elastic Shells

For a homogeneous shell of isotropic, linear elastic material with Young's modulus E and Poisson's ratio ν and uniform thickness h the stiffness matrix takes the form

$$\begin{bmatrix} n_{11} \\ n_{22} \\ n_{12} \\ m_{11} \\ m_{22} \\ m_{12} \end{bmatrix} = \begin{bmatrix} \frac{Eh}{1-\nu^2} & \frac{\nu Eh}{1-\nu^2} & 0 & 0 & 0 & 0 \\ & \frac{Eh}{1-\nu^2} & 0 & 0 & 0 & 0 \\ & & Gh & 0 & 0 & 0 \\ & & & \frac{Eh^3}{12(1-\nu^2)} & \frac{\nu Eh^3}{12(1-\nu^2)} & 0 \\ & sym. & & \frac{Eh^3}{12(1-\nu^2)} & 0 & 0 \\ & & & & \frac{Gh^3}{12} & 0 \end{bmatrix} \begin{bmatrix} \gamma_{11} \\ \gamma_{22} \\ \gamma_{12} \\ \kappa_{11} \\ \kappa_{22} \\ \kappa_{12} \end{bmatrix}, \quad (\text{C.13})$$

where the expression $\frac{Eh}{1-\nu^2}$ is termed membrane stiffness, and $\frac{Eh^3}{12(1-\nu^2)}$ bending stiffness [5, 82].

The transverse shear stiffness K^{ts} is direction independent and calculated by

$$K^{ts} = \frac{Eh}{2(1+\nu)} = Gh, \quad (\text{C.14})$$

with G denoting the shear modulus of the shell material [82]. In the original publication by Reissner, a value of $\frac{5}{6}Gh$ is found. This value is also used by ABAQUS [12].

C.5 Natural Frequencies of a Cylindrical Domain

The low amplitude sloshing modes for fluid in a circular cylinder with radius R , height h and vertical axis can be computed analytically [40]. The surface elevation ξ of the natural modes take the form

$$\xi(r, \varphi, t) = AJ_m(kr) \cos(m\varphi) \cos(\omega t), \quad (\text{C.15})$$

where J_m donates the Bessel function of the first kind of order m . The amplitudes A are arbitrary, and the admissible values of the wave number $k = 2\pi/\lambda$ are obtained as the solutions of

$$J'_m(kR) = 0. \quad (\text{C.16})$$

The corresponding natural frequencies are obtained from

$$\omega^2 = gk \tanh(kh). \quad (\text{C.17})$$

Eq. (C.17) is recognised as the dispersion relation for surface gravity waves. The first ten roots of Eq. (C.16) for $m = 0, 1, \dots, 5$ are given in Table C.1. A number of mode shapes is depicted in Fig. C.3. The mode shapes for $m = 0$ show axial symmetry. Their surface elevation with respect to the radius is depicted in Fig. C.4.

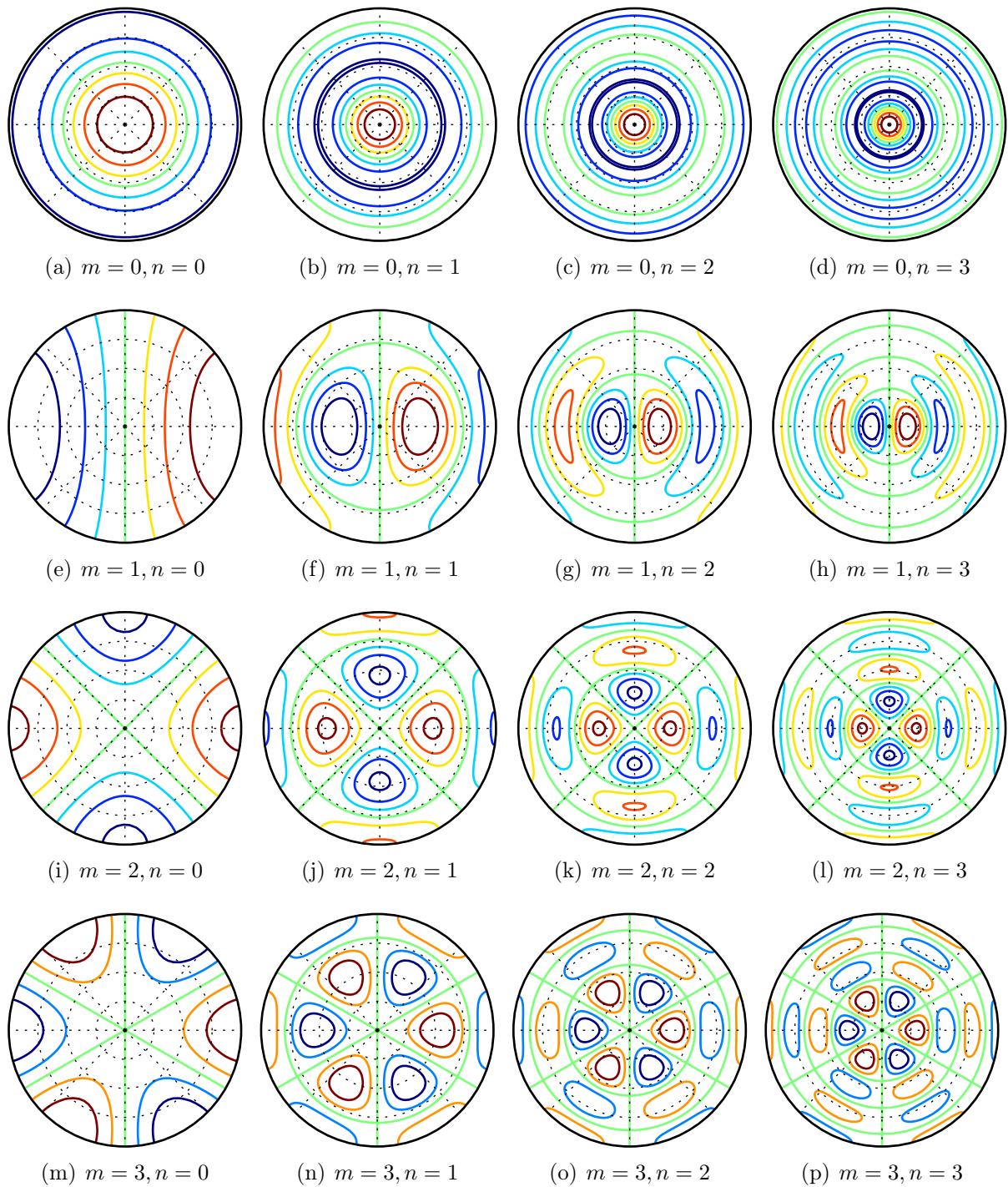


Figure C.3: Mode shapes: The order of the Bessel function (m) governs the number of nodal diameters whereas the number of the root of Eq. (C.16) governs the number of nodal circles (n). Nodal diameters, and circles, respectively, are plotted in green in the diagrams.

m	$n=0$	$n=1$	$n=2$	$n=3$	$n=4$	$n=5$	$n=6$	$n=7$	$n=8$	$n=9$
0	0.610	1.117	1.619	2.121	2.621	3.122	3.622	4.123	4.623	5.123
1	0.293	0.849	1.359	1.863	2.366	2.867	3.368	3.869	4.370	4.870
2	0.486	1.067	1.587	2.096	2.602	3.106	3.608	4.110	4.612	5.113
3	0.669	1.276	1.806	2.321	2.831	3.338	3.843	4.347	4.849	5.352
4	0.846	1.477	2.018	2.541	3.055	3.565	4.073	4.579	5.083	5.587
5	1.021	1.674	2.226	2.755	3.275	3.788	4.299	4.807	5.313	5.819

Table C.1: Roots of Eq. (C.16) for different orders m of the Bessel function of the first kind given as values of $R/\lambda = \frac{kR}{2\pi}$.

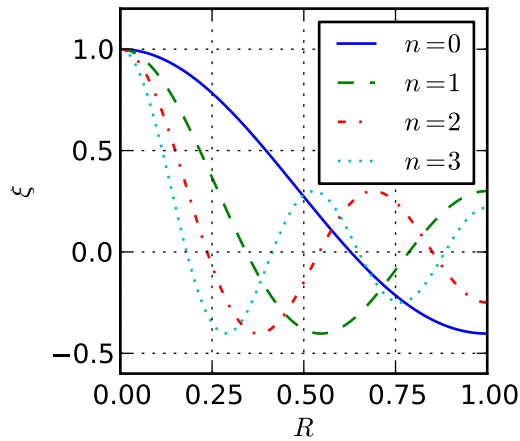


Figure C.4: Elevation profile for the first four axially symmetric modes.

Appendix D

Miscellaneous Mathematics

D.1 Fourier Series and Fourier Transform

In general, the periodic function $x(t)$ with period $T > 0$ can be expressed as an infinite sum of harmonics

$$x(t) = \frac{a_0}{2} + \sum_{n=1}^{\infty} a_n \cos n\omega t + \sum_{n=1}^{\infty} b_n \sin n\omega t = \sum_{-\infty}^{\infty} c_n e^{in\omega t}, \quad (\text{D.1})$$

with $\omega = 2\pi/T$ [59]. Usually the complex notation is used and the coefficients are determined by

$$c_n = \frac{1}{T} \int_{-T/2}^{T/2} x(t) e^{-in\omega t} dt. \quad (\text{D.2})$$

A non-periodic function $f(t)$ can only be represented as a Fourier series if the period tends to infinity. Inserting Eq. (D.2) into Eq. (D.1) and remembering $\omega = 2\pi/T$ one obtains

$$\begin{aligned} f(t) &= \sum_{n=-\infty}^{\infty} \left(\frac{1}{T} \int_{-T/2}^{T/2} f(u) e^{-in\omega u} du \right) e^{in\omega t} \\ &= \frac{1}{2\pi} \sum_{n=-\infty}^{\infty} e^{in\omega t} \int_{-T/2}^{T/2} f(u) e^{-in\omega u} du \omega. \end{aligned} \quad (\text{D.3})$$

As the period T tends to infinity the previous fundamental angular frequency ω becomes the differential parameter ds and the product $n\omega$ becomes the continuous frequency parameter s . Hence the sum in Eq. (D.3) becomes a Riemann integral and one can write

$$f(t) = \frac{1}{2\pi} \int_{-\infty}^{\infty} F(s) e^{ist} ds, \quad (\text{D.4})$$

with

$$F(s) = \int_{-\infty}^{\infty} f(t) e^{-ist} dt, \quad (\text{D.5})$$

being the Fourier transform. Care has to be taken as to where the factor 2π is placed in the definition as different conventions appear in the literature. The Fourier transform of a function exists if $\int_{-\infty}^{\infty} |f(t)| dt$ is finite [55].

D.2 Discrete Form of the Fourier Transform

The discrete form of the Fourier transform is useful for the precessing of data in computer programs. Most implementations are based on the fast Fourier transform (FFT) algorithm by Cooley and Tukey [11] which is especially easy to implement for series lengths of powers of 2 [35]. In MATLAB the publicly available FFTW library by Frigo and Johnson [18] is used [67].

For a signal $x(t_j) = x_j$ with N data points, equally spaced in time from $t = 0$ to $t = (N - 1) \Delta t$ the coefficients of the discrete Fourier transform (DFT) are computed by

$$X_k = \sum_{j=1}^N x_j e^{-\frac{2\pi i}{N}(j-1)(k-1)}. \quad (\text{D.6})$$

The original signal can then again be obtained by the inverse transform defined by

$$x_j = \frac{1}{N} \sum_{k=1}^N X_k e^{\frac{2\pi i}{N}(j-1)(k-1)}. \quad (\text{D.7})$$

The frequencies corresponding to the Fourier coefficients X_k are computed by

$$f_k = \frac{1}{\Delta t} \frac{k-1}{N}. \quad (\text{D.8})$$

For a real valued input signal the Fourier coefficients are conjugate complex. Therefore, only one half of the coefficients* contain the complete information. These single-sided coefficients are conveniently scaled according to

$$C_m = \begin{cases} \frac{1}{N} X_m, & \text{for } m = 1, \\ \frac{2}{N} X_m, & \text{otherwise,} \end{cases} \quad (\text{D.9})$$

so the original signal can be obtained by computing

$$x(t) = \sum_{m=1}^{N/2+1} |C_m| \cos \left(\arctan \frac{\text{Im}(C_m)}{\text{Re}(C_m)} + 2\pi f_m t \right). \quad (\text{D.10})$$

From Eq. (D.10) it can be seen that the amplitudes of the single harmonics correspond to the absolute values of the scaled Fourier coefficients, and that the phase of the harmonic follows from their argument. The values $|C_m|$ can, therefore, be regarded as the single sided amplitude spectrum of the signal. In contrast the double sided amplitudes are X_k/N .

* More precisely: The coefficient $X_1 = \sum_{k=1}^N x_j$ is always real and corresponds to zero frequency; The last non-redundant coefficient is the one for $M = \text{floor}(N/2) + 1$, corresponding to frequency $1/(2\Delta t)$.

The discrete, single sided mean square spectral density is obtained from the FFT coefficients by

$$\Phi_m = \begin{cases} \frac{\Delta t}{N} |X_m|^2, & \text{for } m = 1, \\ \frac{2\Delta t}{N} X_m, & \text{otherwise.} \end{cases} \quad (\text{D.11})$$

For signals with zeros mean, the area under the mean square spectral density, in discrete form written as,

$$\frac{1}{N\Delta t} \sum_{m=1}^M \Phi_m = \frac{1}{N} \sum_{k=1}^N X_k^2, \quad (\text{D.12})$$

equals the mean square value. Sometimes the mean square spectral density is termed power spectral density (PSD), because of the relation of power and the mean square value of a signal [55]. The power in the signal transmitted in a particular frequency band can, therefore, be determined by the sum of the respective terms of the power spectral density times the frequency spacing. In the continuous formulation, the power would equal the definite integral over the PSD with limits defined by the frequency band of interest.

D.3 Power Spectral Density

If one wants to investigate a signal or random process in terms of frequency content, it seems straightforward to employ the Fourier transform. However, this poses the problem that a general signal might not possess a Fourier transform, because the criteria for its existence are not fulfilled[†]. This can be overcome by considering the truncated signal

$$x_T(t) = \begin{cases} x(t) & \text{for } -T/2 < t < T/2, \\ 0 & \text{otherwise} \end{cases}, \quad (\text{D.13})$$

which has the Fourier transform

$$X_T(\omega) = \int_{-\infty}^{\infty} x_T(t) e^{-i\omega t} dt. \quad (\text{D.14})$$

The mean value of the signal is thus obtained by

$$\langle x_T(t) \rangle = \frac{1}{T} \int_{-T/2}^{T/2} x_T(t) dt = \frac{X_T(0)}{T}. \quad (\text{D.15})$$

[†] For example: If the signal $x(t)$ is regarded as the realisation of a stationary random process, $\int_{-\infty}^{\infty} |x(t)| dt$ is not finite [55].

The mean square value of the signal is

$$\begin{aligned}
\langle x_T^2(t) \rangle &= \frac{1}{T} \int_{-T/2}^{T/2} x_T^2(t) dt \\
&= \frac{1}{T} \int_{-\infty}^{\infty} x_T(t) \frac{1}{2\pi} \int_{-\infty}^{\infty} X_T(\omega) e^{i\omega t} d\omega dt \\
&= \frac{1}{T} \int_{-\infty}^{\infty} X_T(\omega) \frac{1}{2\pi} \int_{-\infty}^{\infty} x_T(t) e^{i\omega t} dt d\omega \\
&= \frac{1}{2\pi T} \int_{-\infty}^{\infty} X_T(\omega) X_T^*(\omega) d\omega,
\end{aligned} \tag{D.16}$$

where X_T^* is the complex conjugate of X_T . The mean square spectral density defined as

$$S_{xx}(\omega) = \lim_{T \rightarrow \infty} \left\{ \frac{|X_T(\omega)|^2}{2\pi T} \right\}, \tag{D.17}$$

is related to the mean square value of the signal by

$$\langle x_T^2(t) \rangle = \int_{-\infty}^{\infty} S_{xx}(\omega) d\omega. \tag{D.18}$$

D.4 Integral over One Oscillation Period

An integral of the form

$$\int_0^T f(t)v(t) dt, \tag{D.19}$$

is often of interest for computing quantities like work. If the integrands are harmonics they can be written in the form

$$f(t) = \operatorname{Re} \left\{ \hat{f} e^{i\omega t} \right\}, \tag{D.20}$$

$$v(t) = \operatorname{Re} \left\{ \hat{v} e^{i\omega t} \right\}, \tag{D.21}$$

where

$$\hat{f} = a_f + ib_f, \tag{D.22}$$

$$\hat{v} = a_v + ib_v, \tag{D.23}$$

with $a_f, b_f, a_v, b_v \in \mathbb{R}$ and $\omega = 2\pi/T \in \mathbb{R}$. Inserting into the integral equation one obtains

$$\begin{aligned}
\int_0^T f(t)v(t) dt &= \int_0^T (a_f \cos \omega t - b_f \sin \omega t) (a_v \cos \omega t - b_v \sin \omega t) dt \\
&= a_f a_v \underbrace{\int_0^T \cos^2 \omega t dt}_{=T/2} + b_f b_v \underbrace{\int_0^T \sin^2 \omega t dt}_{=T/2} - (a_f b_v + a_v b_f) \underbrace{\int_0^T \cos \omega t \sin \omega t dt}_{=0} \\
&= (a_f a_v + b_f b_v) \frac{T}{2}. \tag{D.24}
\end{aligned}$$

Hence the integral of the product of two harmonics over one oscillation period is obtained by the sum of the product of the real and imaginary parts, multiplied with the half oscillation period.

D.5 Numerical Integration of Narrow-Band Spectra

If the moments of a spectrum should be computed the spectrum must be numerically integrated. For narrow-band spectra a clever choice of the integration points can lead to large increases in computational performance. Typical wave spectra (e.g. the ones described in Appendix A.4) are narrow band. A good procedure for the determination of N_f integration points, suitable typical wave spectra is:

1. Compute a vector of pseudo-frequencies

$$f_{0,n} = \int_0^n \left| \frac{2}{1 + e^{n/N_f - a}} - 1 \right| dn, \quad \text{with } 0 < a < 1 \quad \text{and } n = 0, 1, \dots, N_f. \tag{D.25}$$

2. From the pseudo-frequencies an efficient vector of integration points may be computed by

$$f_n = f_p \left(1 + b \frac{f_{0,n} - f_{0,c}}{\max(f_0)} \right), \quad \text{with } b > 0, \tag{D.26}$$

where f_p is the peak frequency of the spectrum and $f_{0,c}$ is the centre value of the pseudo-frequency vector, i.e. the value at which the spacing between adjacent values is minimal.

The parameter a governs the location of the peak in the frequency interval, and the parameter b controls the length of the frequency interval. The so obtained integration points ensure a good resolution of the spectral peak. The length of the frequency interval must be chosen sufficient to cover the significant part of the total spectral energy. Parameters suitable for a JONSWAP spectrum with a peak enhancement factor of 3.3 are $a = 0.3$ and $b = 2.5$.

D.6 Definition of a Cartesian Coordinate System

A coordinate system "1" can be defined by three points A , B and C in space, which must not be located on the same straight line. The coordinates of this points in the ground coordinate system (denoted with g) are known. The coordinates of the unit vectors of the "1"-system are then computed by

$${}^g\mathbf{x}_1 = \frac{\overrightarrow{AB}}{\|\overrightarrow{AB}\|}, \quad (\text{D.27})$$

$${}^g\mathbf{z}_1 = \frac{\overrightarrow{AB} \times \overrightarrow{AC}}{\|\overrightarrow{AB} \times \overrightarrow{AC}\|}, \quad (\text{D.28})$$

$${}^g\mathbf{y}_1 = {}^g\mathbf{z}_1 \times {}^g\mathbf{x}_1. \quad (\text{D.29})$$

As visualized in Fig. D.1, the unit vector for the x_1 -direction points from A to B , and together with C the three points span the x_1 - y_1 plane.

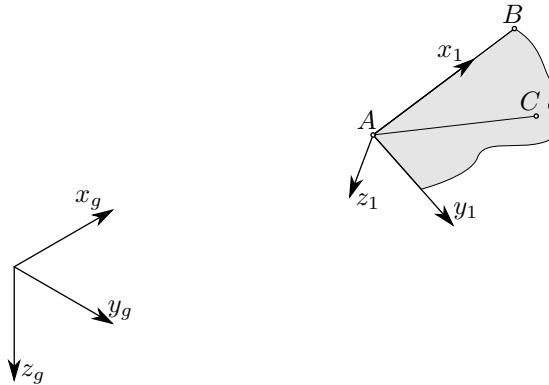


Figure D.1: Points defining the reference frame.

D.7 Coordinate Transformation

The change between two right handed coordinate systems "0" and "1", with coinciding origins is accomplished via the matrix multiplication

$${}^0\mathbf{p} = {}^{01}\mathbf{T} {}^1\mathbf{p} \quad (\text{D.30})$$

where the ${}^i\mathbf{p} = [{}^i p_1, {}^i p_2, {}^i p_3]^T$ is the same vector represented in coordinates of the system $i = 0, 1$. The columns of the transformation matrix \mathbf{T}_{01} contain the unit vectors of the system "1" represented in coordinates of the system "0". The transformation matrix \mathbf{T} is orthogonal, i.e. $\mathbf{T}\mathbf{T}^T = \mathbf{T}^T\mathbf{T} = \mathbf{E}$, and $\det \mathbf{T} = 1$. The transformation is, therefore, a rotation in space. The rotation matrix for changing coordinate system in the other direction is simply obtained by inverting Eq. (D.30).

In general, the two coordinate systems may not have the same origin (see Fig. D.2). In this case the coordinate transformation from the "0"-system into the "1"-system is done

in two steps. First points in coordinates of the "0"-system are translated to the origin of the "1"-system, and then the system is rotated. This is done by

$${}^1\mathbf{p} = {}^{10}\mathbf{T} ({}^0\mathbf{p} - {}^0\mathbf{o}_1) \tag{D.31}$$

where ${}^{10}\mathbf{T} = {}^{01}\mathbf{T}^T$.

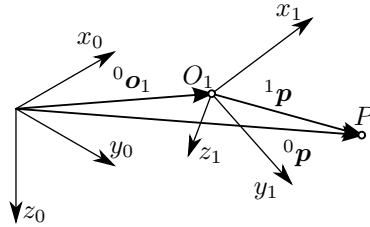


Figure D.2: Change of reference frame.

D.8 Euler Angles

To better visualize a general rotation in space, the so called Euler angles can be used. According to Euler's rotation theorem, any rotation may be described using three angles [15, 54]. The general rotation matrix is the product of the rotation matrices of the successive rotations around the coordinate axes. The three rotation angles are called the Euler-angles of the transformation. If the successive rotations are executed around the new axes obtained by a preceding rotation, the rotation is called intrinsic. In the scope of this text, intrinsic rotations will be used. In general there exist 12 different possibilities of successive rotations. Therefore, the definition of the rotation sequence is important to uniquely define the Euler-angles. In the following the rotation sequence z - y - x is used. This is a common method in aerospace and marine engineering [22]. The rotation sequence is explained in the following and depicted in Fig. D.3.

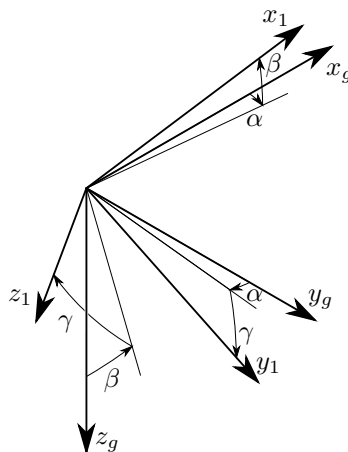


Figure D.3: Euler angles for the intrinsic rotation sequence z - y - x

To rotate the ground system "g" into the position of the body fixed system "1", the ground system is first rotated by $\alpha \in]-\pi, \pi]$ around its z_g -axis until the x -axis coincides

with the projection of the x_1 -axis onto the x_g - y_g plane. The angle α is the so called *heading* or *azimuth angle*. Points in the ground system are then transformed into the new α -system by the relation

$$\begin{bmatrix} {}^\alpha p_1 \\ {}^\alpha p_2 \\ {}^\alpha p_3 \end{bmatrix} = \underbrace{\begin{bmatrix} \cos \alpha & \sin \alpha & 0 \\ -\sin \alpha & \cos \alpha & 0 \\ 0 & 0 & 1 \end{bmatrix}}_{{}^\alpha \mathbf{T}} \begin{bmatrix} {}^g p_1 \\ {}^g p_2 \\ {}^g p_3 \end{bmatrix}. \quad (\text{D.32})$$

Then the new axes are rotated by the angle $\beta \in [-\frac{\pi}{2}, \frac{\pi}{2}]$ around the y_α -axis until the final x_1 axis is reached. The angle β is the so called *inclination angle*. Points in the α -system are transformed into the new β -system by

$$\begin{bmatrix} {}^\beta p_1 \\ {}^\beta p_2 \\ {}^\beta p_3 \end{bmatrix} = \underbrace{\begin{bmatrix} \cos \beta & 0 & -\sin \beta \\ 0 & 1 & 0 \\ \sin \beta & 0 & \cos \beta \end{bmatrix}}_{{}^\beta \mathbf{T}} \begin{bmatrix} {}^\alpha p_1 \\ {}^\alpha p_2 \\ {}^\alpha p_3 \end{bmatrix}. \quad (\text{D.33})$$

To reach the final position the axes are rotated by the so called *bank angle* $\gamma \in]-\pi, \pi[$ around the x_β -axis. Points in the β -system are transformed into the final "1"-system by

$$\begin{bmatrix} {}^1 p_1 \\ {}^1 p_2 \\ {}^1 p_3 \end{bmatrix} = \underbrace{\begin{bmatrix} 1 & 0 & 0 \\ 0 & \cos \gamma & \sin \gamma \\ 0 & -\sin \gamma & \cos \gamma \end{bmatrix}}_{{}^\gamma \mathbf{T}} \begin{bmatrix} {}^\beta p_1 \\ {}^\beta p_2 \\ {}^\beta p_3 \end{bmatrix}. \quad (\text{D.34})$$

The total rotation can now be written as

$${}^1 \mathbf{p} = \underbrace{{}^\gamma \mathbf{T} {}^\beta \mathbf{T} {}^\alpha \mathbf{T}}_{{}^{1g} \mathbf{T}} {}^g \mathbf{p}, \quad (\text{D.35})$$

with

$${}^{1g} \mathbf{T} = \begin{bmatrix} \cos \alpha \cos \beta & \cos \beta \sin \alpha & -\sin \beta \\ \cos \alpha \sin \beta \sin \gamma - \sin \alpha \cos \gamma & \cos \alpha \cos \gamma + \sin \alpha \sin \beta \sin \gamma & \cos \beta \sin \gamma \\ \sin \alpha \sin \gamma + \cos \alpha \sin \beta \cos \gamma & \sin \alpha \sin \beta \cos \gamma - \cos \alpha \sin \gamma & \cos \beta \cos \gamma \end{bmatrix}. \quad (\text{D.36})$$

To extract the euler angles from a given transformation matrix \mathbf{T} the relations

$$\alpha = \arctan_2(T_{12}, T_{11}), \quad (\text{D.37})$$

$$\beta = \arcsin(-T_{13}), \quad (\text{D.38})$$

$$\gamma = \arctan_2(-T_{21}, T_{22}) \quad (\text{D.39})$$

can be used, where the function $\arctan_2(a, b)$ is equivalent to $\arctan(\frac{a}{b})$, but delivering values in the range $]-\pi, \pi]$, depending on the signs of the arguments. In case of a so called *gimbal-lock*, i.e. $\beta = \pm \frac{\pi}{2}$, the transformation matrix takes the form

$$\mathbf{T}' = \begin{bmatrix} 0 & 0 & \mp 1 \\ \pm \cos \alpha \sin \gamma - \sin \alpha \cos \gamma & \cos \alpha \cos \gamma \pm \sin \alpha \sin \gamma & 0 \\ \sin \alpha \sin \gamma \pm \cos \alpha \cos \gamma & \pm \sin \alpha \cos \gamma - \cos \alpha \sin \gamma & 0 \end{bmatrix} \quad (\text{D.40})$$

where the remaining angles cannot be uniquely determined. Therefore, in the gimbal-lock case, one remaining angle can be chosen arbitrarily. Commonly this is done by setting $\alpha = 0$, thereby fixing the three Euler angles to

$$\alpha = 0 \quad (\text{D.41})$$

$$\beta = \arcsin(-T_{13}) = \pm \frac{\pi}{2} \quad (\text{D.42})$$

$$\gamma = \pm \arctan_2(T_{21}, T_{22}), \quad (\text{D.43})$$

depending on the sign of the element T_{13} . In marine engineering, when dealing with ordinary ships, the gimbal-lock is unlikely to occur. It would mean, that the ship's longitudinal axis is in a vertical position.

D.9 Nullspace

The nullspace or kernel of a real valued, $m \times n$ matrix \mathbf{A} is defined as the set of points

$$\mathbf{v} \in \mathbb{R}^n : \mathbf{A}\mathbf{v} = \mathbf{0}, \quad (\text{D.44})$$

where $\mathbf{0}$ denotes the zero vector with m components. The nullspace can be seen as an $(n - m)$ dimensional subspace, in which the m linear constraints defined by

$$\begin{aligned} a_{11}v_1 + a_{12}v_2 + \dots + a_{1n}v_n &= 0 \\ a_{21}v_1 + a_{22}v_2 + \dots + a_{2n}v_n &= 0 \\ \vdots & \\ a_{m1}v_1 + a_{m2}v_2 + \dots + a_{mn}v_n &= 0 \end{aligned} \quad (\text{D.45})$$

are fulfilled. The coefficients a_{ij} in the above system of constraint equations are the components of the matrix \mathbf{A} .

We can now introduce a new set of coordinates, \mathbf{w} , for the nullspace

$$\mathbf{v} = \mathbf{C}\mathbf{w}, \quad (\text{D.46})$$

where \mathbf{C} is an $n \times (n - m)$ matrix containing the $n - m$ right singular vectors corresponding to vanishing singular values of \mathbf{A} . They form an orthogonal basis and can be obtained by computing the singular value decomposition of \mathbf{A} . Due to the orthogonality the backward transformation can be done by

$$\mathbf{w} = \mathbf{C}^T \mathbf{v}. \quad (\text{D.47})$$

When solving a system of equations, for example $\mathbf{K}\mathbf{v} = \mathbf{f}$, under the set of linear constraints $\mathbf{A}\mathbf{v} = \mathbf{0}$. it is convenient to project the system into a subspace where the constraints are enforced, i.e. to solve $\mathbf{C}^T \mathbf{K} \mathbf{C} \mathbf{w} = \mathbf{C}^T \mathbf{f}$.

D.10 Single Value Decomposition

For a real valued, $m \times n$ matrix \mathbf{A} there exists a decomposition

$$\mathbf{U}\mathbf{\Sigma}\mathbf{V}^T = \mathbf{A}, \quad (\text{D.48})$$

such that \mathbf{U} is an $m \times m$ orthogonal matrix, $\mathbf{\Sigma}$ is a $m \times n$ diagonal matrix with non-negative real elements, and \mathbf{V} is an $n \times n$ orthogonal matrix. The diagonal entries of $\mathbf{\Sigma}$ are called the singular values of \mathbf{A} . The columns of \mathbf{U} and \mathbf{V} contain the left and right singular vectors of \mathbf{A} , respectively.

The number of non-zero singular values corresponds to the rank of the matrix \mathbf{A} . The right singular vectors corresponding to vanishing singular values of \mathbf{A} span the nullspace of \mathbf{A} . These vectors are not uniquely defined.

The singular value decomposition (SVD) has many useful applications like the computation of the pseudoinverse for solving least-squares minimization problems, the solution of homogeneous linear equation systems, and the computation of the nullspace.

D.11 N-Dimensional Polar Coordinates

The classical (two-dimensional) polar coordinates can be extended for n dimensions. A point in n -dimensional space may be represented by its radius r together with its $n - 1$ polar angles $\phi_1, \phi_2, \dots, \phi_{n-2} \in [0, \pi]$ and $\phi_{n-1} \in [0, 2\pi[$. The Cartesian coordinates of the point $\mathbf{s} = [s_1, s_2, \dots, s_n]^T$ are then computed according to

$$s_1 = r \cos \phi_1, \quad (\text{D.49a})$$

$$s_2 = r \cos \phi_2 \sin \phi_1, \quad (\text{D.49b})$$

$$s_3 = r \cos \phi_3 \sin \phi_2 \sin \phi_1, \quad (\text{D.49c})$$

$$\vdots \quad (\text{D.49d})$$

$$s_{n-1} = r \cos \phi_{n-1} \sin \phi_{n-2} \dots \sin \phi_1, \quad (\text{D.49e})$$

$$s_n = r \sin \phi_{n-1} \sin \phi_{n-2} \dots \sin \phi_1. \quad (\text{D.49f})$$

The inverse transformation is computed by

$$r = \sqrt{\sum_{k=1}^n s_k^2}, \quad (\text{D.50a})$$

$$\phi_1 = \arccos \frac{s_1}{\sqrt{\sum_{k=1}^n s_k^2}}, \quad (\text{D.50b})$$

$$\vdots \quad (\text{D.50c})$$

$$\phi_{n-2} = \arccos \frac{s_{n-2}}{\sqrt{\sum_{k=n-2}^n s_k^2}}, \quad (\text{D.50d})$$

$$\phi_{n-1} = \begin{cases} \arccos \frac{s_{n-1}}{\sqrt{s_n^2 + s_{n-1}^2}} & \text{if } s_n \geq 0 \\ 2\pi - \arccos \frac{s_{n-1}}{\sqrt{s_n^2 + s_{n-1}^2}} & \text{if } s_n < 0 \end{cases}. \quad (\text{D.50e})$$

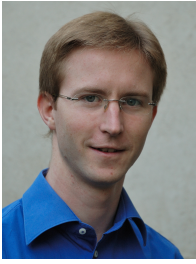
For the case of

$$s_{k+1} = 0 \quad \forall \quad j = k + 1, \dots, n], \quad (\text{D.51})$$

the above relations do not need to be computed. The polar angle is then defined by

$$\phi_k = \begin{cases} \pi & \text{if } s_k < 0 \\ 0 & \text{if } s_k > 0 . \\ \text{ambiguous} & \text{if } s_k = 0 \end{cases} \quad (\text{D.52})$$

For the case of $s_k = 0$ the choice of ϕ_k will be ambiguous, because the transformation is not unique. In this case ϕ_k may be chosen as 0.



Florian TOTH

Mollardgasse 70A/4
1060 Wien
Austria
Tel: +43 664 5557596
Email: floriantoth@silverserver.at

Born: July 5, 1986 in Vienna
Citizenship: Austria
Austrian military duty fulfilled

Professional Experience

since 10/2013	Project assistant at the <i>Institute of Lightweight Design and Structural Biomechanics, Vienna University of Technology</i> , working on fluid structure interaction and structural mechanics
10/2010 – 10/2013	Participation in the ENSYS2030 doctoral college, employed at the <i>Institute of Lightweight Design and Structural Biomechanics, Vienna University of Technology</i>
06/2011 – 11/2011	Participation in a research project investigating thin film buckling (FWF-Project P22648-N20).
07/2010	Temporary employed at the <i>Department of Aeronautical and Vehicle Engineering, Royal Institute of Technology (KTH), Sweden</i> , doing project work, mainly involving material tests. The ply properties of carbon fiber composites were determined by combined off-axis tension tests using a DSP (Digital Speckle Photography) system. Contributions to a study investigating the performance of different Nastran shell elements.
07+08/2007	Summer job at <i>Pörner + Partner Ziviltechniker GmbH</i> , a civil engineers office.
2005 – 2007	Part time employment as tutor in mathematics at <i>ProLern Nachhilfe- und Lerninstitut</i> , a coaching center for high school pupils.
07/2006	summer job at <i>Pörner + Partner Ziviltechniker GmbH</i> .
2004, 2005	Several months of summer internships at <i>Pörner + Partner Ziviltechniker GmbH</i> .

Education

University

25-29/07/2012	participation in the CISM Advanced School on <i>modal analysis of nonlinear mechanical systems</i> in Udine, Italy
07/2011	University of Strathclyde: Stay at the <i>Department of Naval Architecture and Marine Engineering</i> as visiting researcher working on the dynamic wave response of floating structures, funded by a short term scholarship (TU Wien, International Office: Kurzfristige Wissenschaftliche Arbeit im Ausland)
2005 – 2010	Vienna Institute of Technology: Graduation as <i>Diplom-Ingenieur</i> ¹ by completing the program in <i>mechanical engineering</i> , specialized in <i>modeling and simulation</i> , passing the final exam with distinction.
21/01/2011	Receiver of the <i>Preis der Stadt Wien für hervorragende Diplomarbeiten</i> , an award for the best Diploma theses in 2010.
2009/2010	Royal Institute of Technology, (KTH) in Stockholm: ERASMUS stay and writing of diploma thesis <i>Aeroelastic analysis of a Glider Aircraft</i> .
2006 – 2009	Receiver of the <i>TU-Stiftungsstipendium</i> , a merit scholarship.

School

2002 – 2004	Oberstufenrealgymnasium, St. Ursula Wien, high school with emphasis on natural sciences.
1996 – 2002	Gymnasium, St. Ursula Wien, secondary school.
1992 – 1996	Volksschule, St. Ursula Wien, primary school.

¹MSc level degree